

**Mechanistic Investigations of CO₂ Hydrogenation
Reactions Using Homogeneous/Heterogeneous
Catalysts
Ph.D. Thesis**

By

SHYAMA CHARAN MANDAL



**DEPARTMENT OF CHEMISTRY
INDIAN INSTITUTE OF TECHNOLOGY INDORE**

DECEMBER 2021

Mechanistic Investigations of CO₂ Hydrogenation Reactions Using Homogeneous/Heterogeneous Catalysts

A Thesis

*Submitted in partial fulfillment of the
requirements for the award of the degree*

of

DOCTOR OF PHILOSOPHY

by

SHYAMA CHARAN MANDAL

Roll No. 1701131007



**DEPARTMENT OF CHEMISTRY
INDIAN INSTITUTE OF TECHNOLOGY INDORE**

DECEMBER 2021



INDIAN INSTITUTE OF TECHNOLOGY INDORE

CANDIDATE'S DECLARATION

I hereby certify that the work which is being presented in the thesis entitled “**Mechanistic Investigations of CO₂ Hydrogenation Reactions Using Homogeneous/Heterogeneous Catalysts**” in the partial fulfillment of the requirements for the award of the degree of **DOCTOR OF PHILOSOPHY** and submitted in the **DEPARTMENT OF CHEMISTRY, Indian Institute of Technology Indore**, is an authentic record of my own work carried out during the time period from June 2017 to December 2021 under the supervision of **Dr. BISWARUP PATHAK**, Associate Professor, Department of Chemistry, IIT Indore.

The matter presented in this thesis has not been submitted by me for the award of any other degree of this or any other institute.

Shyama Charan Mandal
20/12/2021

Signature of the student with date
(SHYAMA CHARAN MANDAL)

This is to certify that the above statement made by the candidate is correct to the best of my knowledge.

Dr. Biswarup Pathak
20/12/2021

Signature of Thesis Supervisor with date
(Dr. BISWARUP PATHAK)

SHYAMA CHARAN MANDAL has successfully given his Ph.D. Oral Examination held on **04/03/2022**.

Dr. Biswarup Pathak
04/03/2022

Signature of Thesis Supervisor with date
(Dr. BISWARUP PATHAK)

ACKNOWLEDGEMENTS

It is my great pleasure to acknowledge all the individuals who have helped and supported me over last five years for the completion of this thesis. First and foremost, I would like to express my sincere gratitude to my supervisor, **Dr. Biswarup Pathak** for his constant guidance, patience, and motivation throughout my work study and related research. His motivation and faith have always been encouraging for me to achieve the best in all my ups and downs, which has inspired me to thrive for excellence and nothing less.

I am deeply thankful to my PSPC members, Dr. Sanjay K. Singh and Dr. Amrendra Kumar Singh for their guidance and valuable suggestions during my whole research work.

I would also like to thank my experimental collaborators, Dr. Subhadip Neogi, Dr. Sanjay K. Singh, Dr. Gouriprasanna Roy and Dr. Tridib Kumar Sarma for their guidance and scientific discussions during all the collaborative projects.

I am grateful to past and present Directors, IIT Indore, Prof. Pradeep Mathur and Prof. Neelesh Kumar Jain for their endless motivations and providing all the facilities at the institute.

I would like to acknowledge IIT Indore for providing laboratory, computational facilities, and financial support during my research work.

I would also like to thank Prof. Rajneesh Misra, Prof. Suman Mukhopadhyay, Dr. Apurba K. Das, Dr. Anjan Chakraborty, Dr. Sampak Samanta, Dr. Tushar Kanti Mukherjee, Dr. Shaikh M. Mobin, Dr. Satya S. Bulusu, Dr. Chelvam Venkatesh, Dr. Abhinav Raghuvanshi, Dr. Dipak Kumar Roy, Dr. Selvakumar Sermadurai and Dr. Umesh A. Kshirsagar for their guidance during my PhD career.

I extend my deep appreciations to my past and present group members Dr.

Arup Mahata, Dr. Indrani Choudhuri, Dr. Kuber Singh Rawat, Dr. Priyanka Garg, Dr. Preeti Bhauriyal, Dr. Gargee Bhattacharya, Dr. Sourabh Kumar, Dr. Chiranjit Mondal, Dr. Rameshwar Lal Kumawat, Dr. Surajit Nandi, Mr. Akhil S Nair, Mr. Sandeep Das, Mr. Arunendu Das, Mr. Surya Sekhar Manna, Mr. Amitabha Das, Mr. Milan Kumar Jena, Mr. Diptendu Roy, Ms. Nishchal Bharadwaj, Ms. Eti Mahal, Ms. Sneha Mittal, Mr. Souvik Manna, Ms. Harpriya Minhas, Mr. Rahul Kumar Sharma, Mr. Neeraj Kumar Pandit, Mr. Sumit Kumar, Mr. Hariom Saini and Mr. Bhavya Jain for their generous help and co-operation to make my work successful. I would like to thank Ministry of Human Resource Development (MHRD) for the research fellowship. I would also like to thank Mr. Dhiraj Vijayvargiya, Mr. Yogendra Singh, Mr. Manish Kushwaha, Ms. Vinita Kothari, and Mr. Rameshwar Dauhare for their technical support. I would like to acknowledge Ms. Anjali Bandiwadekar, Mr. Rajesh Kumar and other library staffs of IIT Indore for their constant help, whenever required.

I would personally like to extend my admiration to all my dearest friends during various times of my PhD period, Ms. Abira Roy, Mr. Tapas Ghosh, Mr. Rishi Ranjan and Mr. Devraj Singh who were always there to support during my PhD days. I feel extremely grateful to acknowledge Prof. Jnanendranath Mandal for his endless support throughout my educational life and all other teachers who have taught me in some or the other ways since my childhood. I could never achieve anything without their guidance, and support. Most importantly, none of this would have been possible without the support of my lovely family, hence I deeply express my love and gratitude to my parents (Mr. Kalikinkar Mandal and Ms. Sikha Mandal), sister (Ms. Momi Mandal), niece (Ms. Tisam Mandal) and to all my other family members for their love and support throughout my life. Last but not the least, I would also want to extend my appreciation to those who could not be mentioned here but have well played their role in shaping my life. Thank you all for being a part of my life.

SHYAMA CHARAN MANDAL

***DEDICATED TO MY PARENTS,
SISTER AND NIECE***



Abstract

The increasing world's population, industrialization and economic development are rapidly enhancing the worldwide energy demand. Most of the energy demands are fulfilled by conventional fossil fuel-based resources. Therefore, the fossil-fuel sources are decreasing, and these will be depleted by 2060 if it is being used at our current rate. Besides, the uses of fossil fuels increase the amount of greenhouse gases on the environment such as CO, CO₂, NO, NO_x, SO_x among others. Therefore, it is essential to find out renewable and green carbon-neutral fuels. Recently, hydrogen fuel has gained significant attention due to its clean energy resources. But the storage and transportation of H₂ fuel are very difficult. However, H₂ can be stored and transported by converting H₂ into some other useful chemicals known as liquid fuels (HCOOH, CH₃OH, C₂H₅OH, C₂H₄ among others). In this context, CO₂ conversion in the presence of H₂ to value-added products and uses of these products as a liquid fuel can be an important alternate as the process is carbon neutral. Hence, the scientific community is enthusiastic towards CO₂ hydrogenation reactions.

Several catalytic systems have been explored for effective CO₂ hydrogenation reactions. In the case of homogeneous catalysts, noble metal-based systems (Ru, Rh, Ir, and so on) have been comprehensively studied, but these systems cannot be used in the industrial productions of value-added products as the availability of these metals are very less and cost of these metals are very high. To circumvent these drawbacks, non-noble (Mn, Fe, Co, Ni among others) metal catalysts have been introduced. In the case of non-noble metal-based catalysts presence of the bifunctional nature of the ligand helps to activate the reaction. Side by side, Hori and co-workers have examined the uniqueness of Cu based heterogeneous catalysts for the CO₂ hydrogenation to value-added products (CH₃OH, CH₄, C₂H₄, and C₂H₅OH). In this regard, numerous Mn-based bifunctional homogeneous catalysts and Cu-based heterogeneous catalysts have been identified for the practical utilization of various CO₂ hydrogenation reactions in this thesis.

Even though several experimental reports have reported several metal-based catalysts for active CO₂ hydrogenation reactions, the underlying reason behind these reactions is still unclear. Henceforth, all the possible mechanistic pathways have been investigated using computational techniques and identified the most favourable one among all the considered pathways. Moreover, some Mn and Cu-based catalytic systems have been designed and identified to be promising catalysts for CO₂ hydrogenation reactions using various computational techniques.

The contents of each chapter included in the thesis are discussed as follows:

1. **Introduction (Chapter 1)**

In this section of the thesis, a short overview of hydrogen energy as a green energy resource has been discussed. Then, the uses of CO₂ and catalytic hydrogenation of it to useful chemicals using earth-abundant metal-based catalysts have been shown. For a better understanding of catalytic CO₂ hydrogenations, the Mn(I)-based homogeneous as well as Cu-based heterogeneous catalysts have been used for the formation of various useful value-added products such as CO, CH₃OH, HCOOH, C₂H₄, C₂H₅OH and so on. The benefits of these products as a green energy source have also been discussed in this chapter. Furthermore, the main obstacles of CO₂ hydrogenations have been mentioned with some of the recent reports which have tried to solve these problems. Moreover, the role of different ligands/metals, most important steps, rate-determining steps, potential determining steps, microkinetic analysis in the CO₂ hydrogenation has been reviewed in this context.

All these studies are done using the density functional theory (DFT) calculations. Therefore, this chapter contains the basic introduction of DFT from the quantum chemistry perspective and the uses of these methods in the considered catalytic systems. Additionally, the brief introduction of natural bond orbital (NBO), non-covalent interaction (NCI), ab initio molecular dynamics (AIMD) simulation, nudged elastic band (NEB) method, Bader charge, transition state theory and several other

computational tools have been discussed as these tools are very important and highly essential for the understanding of the mechanistic insights of homogeneous and heterogeneous CO₂ hydrogenation reactions.

2. **Electrocatalytic CO₂ Reduction by Mn(I) Half Sandwich Based Catalysts: Role of Substitution and Solvent (Chapter 2)**

In this chapter, a series of Mn(I) half sandwich-based catalysts have been considered for the investigation of CO₂ reduction to CO. The half sandwich-based catalysts were functionalized with various substituents such as NH₂, CH₃, COOH, CMe₃ and OH. Along with these substituents various solvents e.g., water, acetonitrile, and dimethyl sulfoxide (DMSO) have been considered for the investigation of the CO₂ reduction reaction. At first, the considered catalysts were converted to the active catalyst via two-electron reductions and removal of the Br⁻ ion from the ligand sphere of the catalyst. In this step, the first reduction potential values are less influenced by the substituents whereas the second potential values are highly influenced by the substituents. Besides, solvents play a significant role in the active catalyst formations on the reduction potential values. In the next step, there is competitiveness between CO₂ and proton binding on the metal center of the active catalyst. The calculated results show that proton binding is thermodynamically more favourable whereas CO₂ binding is kinetically more favourable. The following mechanism of the CO₂ bonded intermediates are formation and cleavage of C–OH bond for CO formation. Various mechanistic pathways have been considered for the formation and cleavage of C–OH bond and identified the most plausible mechanism. However, the calculated results show that COOH substitution with the phenyl ring of Mn(I) half sandwich-based catalyst can be the most promising catalyst for the efficient CO formation. Further to this, reduction steps are more favourable in the DMSO solvent subsequently water and acetonitrile solvent whereas protonation steps are more favourable in the acetonitrile solvent subsequently water and DMSO solvent. In the case of

electrocatalytic CO₂ reduction reactions, both the reduction and protonation steps are available. Therefore, we conclude that water can be a perfect choice for the solvent during Mn(I) half sandwich-based CO₂ reduction to CO.

3. CO₂ Hydrogenation to HCOOH Using Earth Abundant Homogenous Based Mn-Catalysts (Chapter 3)

The CO₂ hydrogenated products are highly useful due to its applications as useful chemical as well as hydrogen storage materials. One of the simple and useful CO₂ hydrogenated products is HCOOH. Therefore, in this chapter the CO₂ hydrogenation to HCOOH using a series of Mn(I)-aminomethyl based catalysts have been discussed as Mn(I) is inexpensive and highly abundant on the earth crust. Here, the metal center (Mn) and N–H functionality of the aminomethyl ligand sphere can behave as bifunctional catalysts. However, the detailed mechanistic possibilities of CO₂ hydrogenation to HCOOH using bifunctional Mn(I)-based catalysts have been investigated in this chapter. As hydrogenation steps are consists of hydride and proton transfer, at first, hydride transfer from the Mn-metal center and proton transfer from the ligand sphere of the catalyst following Noyori type hydrogenation mechanism. Besides, the revised Noyori type mechanism has also been investigated where N–H functionality of the aminomethyl ligand sphere only assist the reaction without participating in the active reaction mechanism. In this context, the N–H functionality does not prefer to donate the proton to the oxygen of formate rather it assists the reaction vis N–H···O non-covalent interactions. This observation is opposite to the Noyori type hydrogenation mechanism, and it is known as the revised Noyori type mechanism. Specifically, the N–H···O non-covalent interactions stabilize the formate ion and reduce activation barriers of the heterolytic H₂ cleavage step. Therefore, ligand assisted mechanistic pathway is more favourable compared to the ligand participated mechanism for CO₂ hydrogenation to HCOOH using Mn(I)-aminomethyl-based

catalysts. Hence, the Mn(I)-based bifunctional aminomethyl based catalysts can be promising for the CO₂ hydrogenation to HCOOH and the proposed mechanism will be very beneficial for the experimentalists for the advancement of earth-abundant metal-based catalysts for efficient CO₂ hydrogenation to HCOOH.

4. CO₂ Hydrogenation to Methanol Using Earth Abundant Homogenous Based Mn Catalysts (Chapter 4)

Recently various bifunctional earth-abundant metal catalysts have been investigated for efficient CO₂ hydrogenation to methanol. However, the in-depth mechanistic pathways were unexplored for these cases. Therefore, in this chapter, various possible mechanistic pathways have been explored and identified the most favourable one during CO₂ hydrogenation to methanol utilizing PNP based catalysts. As direct hydrogenation of CO₂ to methanol is highly energy demanding, various approaches have been considered to reduce the reaction free energy of CO₂ hydrogenation to methanol. In one case, morpholine base has been considered to make the reaction thermodynamically favourable whereas on the other side CO₂ has been captured first with the help of amino alcohol followed by further hydrogenation of the CO₂ captured product (oxazolidinone) to methanol. In the case of morpholine based hydrogenation, the reaction proceeds via three steps: CO₂ hydrogenation to HCOOH, HCOOH amidation to N-formylmorpholine and N-formylmorpholine hydrogenation to methanol. Besides, the 2-amino-1-propanol can capture CO₂ and hydrogenation of the oxazolidinone can form methanol. However, in both cases various pathways of hydrogenation steps are possible, and all of these have been considered in this chapter. Surprisingly, the N-formylmorpholine can be converted to methanol by following two different pathways (C=O vs. C–N bond hydrogenation) and the calculated reaction free energies show that both the pathways are competitive. Further to these, the microkinetic simulations on the DFT calculations agree well with the earlier experimental results which

suggest that the suggested mechanistic pathway is the most probable for CO₂ hydrogenation. In the case of oxazolidinone to methanol, C–N → C–O → C=O bond hydrogenations or C–O → C–N → C=O bond hydrogenations are the favourable pathways (total reaction free energy barrier of 36.9 kcal/mol) in the presence of Mn(I)–PNP catalyst. The most important hydrogenation steps are the heterolytic H₂ cleavage as well as hydride transfer from the ligand sphere of the catalyst. Moreover, the calculated results discovers that the rate-determining step of the reaction is heterolytic H₂ cleavage. Therefore, the presence of co-catalyst or hydrogenation of the CO₂ captured product can be promising for CO₂ hydrogenation to methanol.

5. Selective CO₂ Hydrogenation to Methanol Using Heterogeneous Based Cu Nanocatalysts (Chapter 5)

Hori and co-workers have shown the unique capability of Cu-based heterogeneous catalysts for CO₂ hydrogenation reactions. Therefore, along with Mn(I)-based homogeneous catalysts, Cu-based heterogeneous catalysts have also been considered for CO₂ hydrogenation reactions. According to them, Cu(111) surface is active of C₁ based products hence, DFT calculations have been accomplished for the in-depth understanding of CO₂ hydrogenation to methanol on Cu(111) monolayer (Cu ML) as monolayers are more active than that of the bulk Cu(111) surface. Different Cu MLs (orthorhombic and hexagonal; Cu(111) and Cu(110)) have been considered and examined the stability of these MLs by considering formation energy, cohesive energy and phono dispersion and investigated the CO₂ hydrogenation reaction on the most stable ML (hexagonal Cu(111) ML). The CO₂ hydrogenation to C₁ based products all the possible mechanistic pathways have been considered and the calculated adsorption energies, reaction free energies as well as activation barriers show that CH₃OH is selective over CH₄. Moreover, Cu(111) ML works at low working potential (0.46 V) than that of periodic Cu(111) surface (0.71 V)

and Cu nanocluster (0.53) catalysts. Besides, the industrially CO₂ hydrogenation to methanol catalyst is Cu/ZnO/Al₂O₃ and several reports show single atom doping can enhance the catalytic activity. Therefore, we have considered the Cu doped ZnO based nanocages (NCs) for the CO₂ hydrogenation to methanol. Two different ZnO based NCs have been taken into consideration and the most stable one has been doped with Cu atom to see the impact of Cu on CO₂ hydrogenation reactions. The calculated adsorption energies and reaction free energies show that ZnO as well as Cu doped ZnO NCs can be effective for methanol formation. The required working potential is less for Cu doped ZnO NC (0.39 V) compared to ZnO NC (0.55 V), bulk Cu(111) (0.71 V), Cu(111) monolayer (0.46 V) and Cu nanocluster (0.53 V) catalysts. Therefore, the Cu(111) ML and Cu doped ZnO based NCs are highly efficient and can be promising for CO₂ hydrogenation for selective CH₃OH formation over CH₄.

6. Electrocatalytic CO₂ Hydrogenation to C₂ Based Products through C–C Coupling over Heterogenous Based Cu Nanocatalysts (Chapter 6)

In this chapter, a (100) facets exposed Cu nanocube (Cu-NC) catalyst has been designed for CO₂ hydrogenation to C₁ and C₂ based products formation. All the possible mechanistic pathways have been considered for the formations of C₁ (CH₃OH, HCOOH and CH₄) as well as C₂ (C₂H₅OH and C₂H₄) based products formation using the density functional theory calculations and identified the most probable pathways. Along with these all the calculated results have been compared with the earlier reports on the periodic Cu(111) and Cu(100) surfaces, and also on the Cu₈₅ nanocluster. The detailed investigation concludes that Cu-NC can be selective for the C₂ based products formation with a lower limiting potential than that of the periodic Cu(100) surfaces. However, the underlying causes for such findings have been described using the density of states and Bader charge analysis and the calculated reaction free energies have been compared with

the periodic surfaces. The calculated results show that formation of *HCO from *CO is the potential determining step and dimerization of *HCO intermediate to *HCO-HCO is the most favourable C–C coupling step among all the considered possible C–C coupling steps (*CO and *HCO coupling as well as *CO and *COH coupling). Therefore, the proposed Cu-NC based catalyst can be more effective for C₂ based products formation from CO₂ than periodic Cu(100) surface.

7. Conclusions

The conclusions of the thesis can be outlined as follows:

- i) The half sandwich Mn(I)-based complexes with COOH substitution at the phenyl ring can be an efficient catalyst for CO₂ reduction to CO. Moreover, water can be the perfect solvent for electroreduction of CO₂ to CO, among water, acetonitrile and DMSO solvents.
- ii) The aminomethyl-based Mn(I) complexes follow the revised Noyori type mechanism via ligand assisted pathways for the hydrogenation of CO₂ to HCOOH. This is due to the presence of N–H functional on the ligand sphere of the catalysts. Therefore, Mn(I) aminomethyl-based catalysts can be efficient for HCOOH formation.
- iii) Identified the most preferable pathways of recent reports for CO₂ hydrogenation to methanol using PNP-based catalysts with morpholine co-catalyst and capturing agent amino alcohol.
- iv) The highly efficient Cu-based heterogeneous catalysts such as hexagonal Cu(111) monolayer and Cu doped ZnO nanocage have been designed for the selective CO₂ hydrogenation to methanol over methane and identified the most favourable pathways.
- v) The detailed mechanistic investigation of CO₂ hydrogenation to C₁ as well as C₂-based products formation on Cu-NC shows that *CO to *HCO is the most important step whereas dimerization of *HCO is the most favourable coupling step. Therefore, Cu nanocube can be efficient for CO₂ hydrogenation reaction to C₂ based product formation.

List of Publications

- 1) **Mandal S. C.**, Pathak B. (2021), Computational Insights into Electrocatalytic CO₂ Reduction Facilitated by Mn(I) Half Sandwich-based Catalysts: Role of Substitution and Solvent, *Electrochim. Acta*, 137463 (DOI: 10.1016/j.electacta.2020.137463)
- 2) **Mandal S. C.**, Rawat K. S., Pathak B. (2019), A computational study on ligand assisted vs. ligand participation mechanisms for CO₂ hydrogenation: importance of bifunctional ligand based catalysts, *Phys. Chem. Chem. Phys.*, 21, 3932-3941 (DOI: 10.1039/C8CP06714G)
- 3) **Mandal S. C.**, Rawat K. S., Nandi S., Pathak B. (2019), Theoretical insights into CO₂ hydrogenation to methanol by a Mn–PNP complex, *Catal. Sci. Technol.*, 9, 1867-1878 (DOI: 10.1039/C9CY00114J)
- 4) **Mandal S. C.**, Pathak B. (2021), Identifying the preferential pathways of CO₂ capture and hydrogenation to methanol over Mn(I)-PNP catalyst: A computational study, *Dalton Trans.*, 50, 9598-9609 (DOI: 10.1039/D1DT01208H)
- 5) **Mandal S. C.**, Rawat K. S., Garg P., Pathak B. (2019), Hexagonal Cu(111) Monolayers for Selective CO₂ Hydrogenation to CH₃OH: Insights from Density Functional Theory, *ACS Appl. Nano Mater.*, 2, 7686-7695 (DOI: 10.1021/acsanm.9b01751)
- 6) **Mandal S. C.**, Pathak B. (2020), Computational insights into selective CO₂ hydrogenation to CH₃OH catalysed by ZnO based nanocages, *Mater. Adv.*, 1, 2300-2309 (DOI: 10.1039/D0MA00208A)
- 7) **Mandal S. C.**, Pathak B. (2021), Density Functional Theory Calculations on Electrocatalytic CO₂ Hydrogenation to C₂-Based Products over Cu(100) Nanocubes, *ACS Appl. Nano Mater.*, 4, 11907–11919 (DOI: 10.1021/acsanm.1c02478)
- 8) Rawat K. S., **Mandal S. C.**, Pathak B. (2019), A computational study of electrocatalytic CO₂ reduction by Mn(I) complexes: Role of bipyridine substituents, *Electrochim. Acta*, 297, 606-612 (DOI: 10.1016/j.electacta.2018.11.210)

- 9) Goswami R., **Mandal S. C.**, Pathak B., Neogi S. (2019), Guest-Induced Ultrasensitive Detection of Multiple Toxic Organics and Fe³⁺ Ions in a Strategically Designed and Regenerative Smart Fluorescent Metal–Organic Framework, *ACS Appl. Mater. Interfaces*, 11, 9042-9053 (DOI: 10.1021/acsami.8b20013)
- 10) Rawat K. S., **Mandal S. C.**, Bhauriyal P., Garg P., Pathak B. (2019), Catalytic upgrading of ethanol to n-butanol using an aliphatic Mn–PNP complex: theoretical insights into reaction mechanisms and product selectivity, *Catal. Sci. Technol.*, 9, 2794-2805 (DOI: 10.1039/C9CY00501C)
- 11) Binnani C., **Mandal S. C.**, Pathak B., Singh S. K. (2019), Ruthenium-Catalyzed C-H Bond Activation/Arylation Accelerated by Biomass-Derived Ligands, *Eur. J. Inorg. Chem.*, 23, 2844-2852 (DOI: 10.1002/ejic.201900218)
- 12) Goswami R., **Mandal S. C.**, Pathak B., Seal N., Neogi S. (2019), Antibiotic-triggered reversible luminescence switching in amine-grafted mixed-linker MOF: exceptional turn-on and ultrafast nanomolar detection of sulfadiazine and adenosine monophosphate with molecular keypad lock functionality, *J. Mater. Chem. A*, 7, 19471–19484 (DOI: 10.1039/C9TA06632B)
- 13) Chalana A., Karri R., **Mandal S. C.**, Pathak B., Roy, G. (2019), Chemical Degradation of Mercury Alkyls Mediated by Copper Selenide Nanosheets, *Chem. Asian J.*, 14, 4582–4587 (DOI: 10.1002/asia.201901077)
- 14) Das A., **Mandal S. C.**, Pathak B. (2021), Unraveling the catalytically preferential pathway between direct and indirect hydrogenation of CO₂ to CH₃OH using N-heterocyclic carbene-based Mn(I) catalysts: A theoretical approach, *Catal. Sci. Technol.*, 11, 1375-1385 (DOI: 10.1039/D0CY02064H)
- 15) Das A., Nair A. S., **Mandal S. C.**, Pathak B. (2021), Current Density Calculations of an Octahedral Fe Nanocluster for Selective

- Electrocatalytic for Nitrogen Reduction, *ACS Appl. Nano Mater.*, 4, 7758–7770 (DOI: 10.1021/acsnm.1c01037)
- 16) Roy D., **Mandal S. C.**, Pathak B. (2021), Machine Learning-Driven High-Throughput Screening of Alloy Based Catalysts for Selective CO₂ Hydrogenation to Methanol, *ACS Appl. Mater. Interfaces*, 13, 56151–56163 (DOI: 10.1021/acсами.1c16696)
- 17) Panigrahi A., **Mandal S. C.**, Pathak B., Sarma T. K. (2022), Discriminative Detection of Aliphatic, Electron-rich and Electron-Deficient Aromatic Volatile Organic Contaminants Using Conjugated Polymeric Fluorescent Nanoaggregates with Aggregation Induced Emission Characteristics, *Macromolecular Chemistry and Physics*, 223, 2100391 (DOI: 10.1002/macp.202100391)
- 18) Das A., **Mandal S. C.**, Nair A. S., Pathak B. (2021), Computational Screening of First-row Transition Metal (TM) Based Alloy Catalysts – Ligand Induced NRR Selectivity, *ACS Phys. Chem Au*, (DOI: 10.1021/acspyschemau.1c00021)
- 19) Mahal E., **Mandal S. C.**, Pathak B. (2022), Understanding the Role of Spacer Cation in 2D Layered Halide Perovskites to Achieve Stable Perovskite Solar Cell, *Materials Advances* (DOI: 10.1039/D1MA01135A)

Table of Contents

1. List of Figures	xxiii
2. List of Schemes	xxxv
3. List of Tables	xli
4. Acronyms	xlvii

Chapter 1: Introduction	Page Number
1.1. Current Scenario of CO ₂ and Disadvantages of Fossil Fuels	3
1.2. CO ₂ as a Raw Material for Fuel Production	5
1.3. Types of Catalysts	7
1.3.1. Homogeneous Catalysts	7
1.3.1.1. Half Sandwich Based Catalysts	7
1.3.1.2. Bifunctional Mn(I) Aminomethyl Type Catalysts	9
1.3.1.3. PNP Based Mn(I) Catalysts	12
1.3.2. Heterogeneous Catalysts	14
1.3.2.1. Cu Based Catalysts for C ₁ Based Products	14
1.3.2.2. Cu Based Catalysts for C ₂ Based Products	17
1.4. Theoretical Methods	18
1.4.1. Schrödinger Equation	18
1.4.2. The Born-Oppenheimer (BO) Approximation	19
1.4.3. Hartree-Fock Theory (HF Theory)	19
1.4.4. Density Functional Theory (DFT)	21
1.4.4.1. The Hohenberg-Kohn theorems	21
1.4.4.2. Kohn-Sham Formulation	22
1.4.4.3. Exchange-correlation Functional	23
1.4.4.4. Local Density Approximation (LDA)	23
1.4.4.5. Generalized Gradient Approximation (GGA)	24
1.4.4.6. Hybrid Functionals	24
1.4.5. Basis Sets	24
1.4.6. Projector Augmented Wave (PAW) Method	27
1.4.7. Dispersion Corrected Density Functional Theory	28

1.4.8. Other Computational Tools	29
1.4.8.1. Natural Bond Orbital (NBO)	29
1.4.8.2. Noncovalent Interaction (NCI) Plots	30
1.4.8.3. Nudged Elastic Band (NEB) Method	30
1.4.8.4. Ab initio Molecular Dynamics (AIMD)	31
1.4.8.5. Bader Charge Analysis	31
1.4.8.6. Phonon Dispersion	32
1.5. References	32

Chapter 2: Electrocatalytic CO₂ Reduction by Mn(I) Half Sandwich Based Catalysts: Role of Substitution and Solvent

2.1. Introduction	59
2.2. Computational Details	61
2.3. Results and Discussion	64
2.3.1. Formation of Active Catalysts	64
2.3.2. CO ₂ vs. Proton Binding	69
2.3.3. Formation and Breaking of C–OH Bond	76
2.4. Conclusions	81
2.5. References	82

Chapter 3: CO₂ Hydrogenation to HCOOH Using Earth Abundant Homogenous Based Mn-Catalysts

3.1. Introduction	93
3.2. Computational Details	95
3.3. Results and Discussion	96
3.3.1. Ligand Participated Mechanism	97
3.3.2. Ligand Assisted Mechanism	101
3.3.3. Formate Anion vs External Base	107
3.4. Effect of N–H Functionality	110
3.5. Conclusions	112
3.6. References	113

Chapter 4: CO₂ Hydrogenation to Methanol Using Earth Abundant Homogenous Based Mn Catalysts

4.1. Introduction	127
4.2. Computational Details	133
4.3. Results and Discussion	135
4.3.1. Morpholine Assisted CO ₂ Hydrogenation to Methanol	135
4.3.1.1. CO ₂ Hydrogenation to HCOOH	136
4.3.1.2. HCOOH to N-formylmorpholine	143
4.3.1.3. N-formylmorpholine Hydrogenation to Methanol	146
4.3.1.3.1. C=O Bond Hydrogenation Followed by C–N Bond Hydrogenation	147
4.3.1.3.2. C–N Bond Hydrogenation Followed by C=O Bond Hydrogenation	150
4.3.1.4. Hydride Transfer Step	153
4.3.1.5. Microkinetic Modelling	155
4.3.1.6. Conclusions	159
4.3.2. CO ₂ Hydrogenation to Methanol via Capturing	160
4.3.2.1. CO ₂ Capture to Oxazolidinone	160
4.3.2.2. Oxazolidinone Hydrogenation to Methanol	163
4.3.2.3. Conclusions	180
4.4. References	181

Chapter 5: Selective CO₂ Hydrogenation to Methanol Using Heterogeneous Based Cu Nanocatalysts

5.1. Introduction	197
5.2. Computational Details	201
5.3. Results and Discussion	203
5.3.1. Cu MLs for CO ₂ Hydrogenation Reaction	203
5.3.1.1. Stability of the Cu MLs	204
5.3.1.2. Adsorption of Intermediates	210

5.3.1.3. CO ₂ Hydrogenation Mechanisms	213
5.3.1.4. Working Potential for CO ₂ Hydrogenation	221
5.3.1.5. Microkinetic Analysis	222
5.3.1.6. Conclusions	227
5.3.2. ZnO Based NCs for CO ₂ Hydrogenation Reaction	228
5.3.2.1. Stability of the NCs	228
5.3.2.2. Adsorption of Different Intermediates	231
5.3.2.3. CO ₂ Hydrogenation Reaction Mechanism	236
5.3.2.4. Comparison between ZnO and Cu@ZnO NCs	240
5.3.2.5. Conclusions	243
5.4. References	244

Chapter 6: Electrocatalytic CO₂ Hydrogenation to C₂ Based Products through C–C Coupling over Heterogenous Based Cu Nanocatalysts

6.1. Introduction	259
6.2. Computational Details	263
6.3. Results and Discussion	265
6.3.1. Stability Analysis	265
6.3.2. Adsorption of Different Intermediates	269
6.3.3. CO ₂ Hydrogenation to C ₁ Based Product Formation	276
6.3.3.1. Formation of HCOOH	276
6.3.3.2. Formation of CH ₃ OH	277
6.3.3.3. Formation of CH ₄	279
6.3.4. CO ₂ Hydrogenation to C ₂ Based Product Formation	282
6.3.4.1. Formation of C ₂ H ₄	282
6.3.4.2. Formation of C ₂ H ₅ OH	286
6.4. Comparison among C ₁ and C ₂ Based Products	287
6.5. Conclusions	290
6.6. References	291

Chapter 7: Scope for Future Work

List of Figures

Chapter 1

- Figure 1.1** Various possible products of CO₂ hydrogenation reaction. 7
- Figure 1.2** Various kinds of macrocyclic, bipyridine and thiolate complexes reported for electrochemical CO₂ reduction reaction. 8
- Figure 1.3** Modelled Mn(I) half sandwich-based catalysts for CO₂ reduction reaction. 9
- Figure 1.4** Various reported noble and non-noble metal-based catalysts for CO₂ hydrogenation reaction to formic acid/ formate. 10
- Figure 1.5** Comparison between classical and revised Noyori type mechanism during hydrogenation reaction. 11
- Figure 1.6** Mn(I) aminomethyl bifunctional catalysts for electrochemical CO₂ reduction reaction. 12
- Figure 1.7** PNP based bifunctional catalysts for CO₂ hydrogenation to methanol. 13
- Figure 1.8** PNP based Mn(I), Fe(II) and Ru(II)-based complexes. 13
- Figure 1.9** Amino alcohol participated CO₂ capture to oxazolidinone, and hydrogenation of CO₂ captured product to methanol. 14
- Figure 1.10** Modelled Cu-MLs for CO₂ hydrogenation reaction. 15
- Figure 1.11** Modelled ZnO and Cu-doped ZnO based nanocages. 16
- Figure 1.12** Modelled Cu(100) facets exposed Cu nanocube (Cu-NC) for CO₂ hydrogenation reaction. 17
-
- Chapter 2**
- Figure 2.1** Modelled Mn(I) half sandwich-based complexes for the electrochemical CO₂ reduction reaction. 60

Figure 2.2	Calculated LUMO energies of intermediate 2 . All the LUMO energies are in eV.	69
Figure 2.3	Occupied d-orbital energies and shapes (HOMO or HOMO-1) of intermediate 3 with antibonding orbital energy and shape (LUMO) of the CO ₂ molecule.	73
Figure 2.4	Structures of intermediates 3 , 4 and 5 with one explicit water molecule for all the modelled catalysts.	75
Figure 2.5	Intermediate 5 for COOH based Mn(I) half sandwich complex.	81
 Chapter 3		
Figure 3.1	Structure of modelled Mn(I) complexes for CO ₂ hydrogenation reaction.	97
Figure 3.2	Optimized geometries of intermediates for CO ₂ hydrogenation catalyzed by Mn-AMP complex. Bond lengths and bond angles are in Å and °, respectively.	99
Figure 3.3	Optimized geometries of transition states for CO ₂ hydrogenation catalyzed by Mn-AMP complex. Bond lengths and bond angles are in Å and °, respectively.	100
Figure 3.4	Reaction free energy profile diagram of CO ₂ hydrogenation <i>via</i> ligand involvement mechanism catalyzed by Mn-AMP complex. $\Delta\Delta G^{\ddagger R}$ and ΔG_{rxn} denote the total free energy barrier and total reaction free energy of the overall catalytic cycle, respectively.	101
Figure 3.5	Reaction free energy profile diagram of CO ₂ hydrogenation catalyzed by Mn-AMP complex <i>via</i>	

	ligand assisted mechanism. $\Delta\Delta G^{\ddagger R}$ and ΔG_{rxn} denote the total free energy barrier and total reaction free energy of the overall catalytic cycle, respectively.	103
Figure 3.6	Structure of Mn-MAMP and Mn-MAMP' (Isomer of each other)	105
Figure 3.7	Reaction free energy profile diagram of CO ₂ hydrogenation via ligand assisted mechanism catalyzed by Mn-MAMP complex. $\Delta\Delta G^{\ddagger R}$ and ΔG_{rxn} denote the total free energy barrier and total reaction free energy, respectively.	105
Figure 3.8	Reaction free energy profile diagram of CO ₂ hydrogenation via ligand assisted mechanism catalyzed by Mn-MAMP' complex. $\Delta\Delta G^{\ddagger R}$ and ΔG_{rxn} denote the total free energy barrier and total reaction free energy, respectively.	106
Figure 3.9	Reaction energy profile diagram of CO ₂ hydrogenation of formate anion vs external base catalyzed by Mn-AMP complex. $\Delta\Delta G^{\ddagger R}$ and ΔG_{rxn} denote the total free energy barrier and total reaction free energy of the overall catalytic cycle, respectively.	109
Figure 3.10	Non-covalent interaction of intermediate 3 and intermediate 10 of Mn-MAMP and Mn-MAMP' . The relative energy (in kcal/mol) values are given in parentheses for Mn-MAMP and Mn-MAMP' . The colours of NCI regions represent the type of interaction present in the intermediate (blue=strong, green=weak, and red=repulsive interaction).	111

Chapter 4

- Figure 4.1** Considered metal catalysts for indirect CO₂ hydrogenation reaction to methanol. 129
- Figure 4.2** Reaction free energy profile diagram of CO₂ hydrogenation to HCOOH *via* ligand assisted mechanism catalyzed by Mn-PNP complex. $\Delta\Delta G^{\ddagger R}$ and ΔG_{rxn} denote the total free energy barrier and total reaction free energy of the catalytic cycle, respectively. 139
- Figure 4.3** Reaction free energy profile diagram of CO₂ hydrogenation to HCOOH *via* ligand participated mechanism catalysed by Mn-PNP complex. $\Delta\Delta G^{\ddagger R}$ and ΔG_{rxn} denote the total free energy barrier and total reaction free energy of the catalytic cycle, respectively. 140
- Figure 4.4** Optimized geometries of intermediates for CO₂ hydrogenation to methanol catalyzed by Mn-PNP complex. Bond lengths and bond angles are in Å and °, respectively. 141
- Figure 4.5** Optimized geometries of transition states for CO₂ hydrogenation to methanol catalyzed by **Mn-PNP** complex. Bond lengths and bond angles are in Å and °, respectively. 142
- Figure 4.6** Reaction free energy profile diagram of HCOOH to N-formylmorpholine (amidation). 144
- Figure 4.7** Reaction free energy profile diagram of N-formylmorpholine hydrogenation to methanol *via* C=O bond hydrogenation followed by C–N bond hydrogenation catalyzed by Mn-PNP complex. $\Delta\Delta G^{\ddagger R}$ and ΔG_{rxn} denote the total free energy

- barrier and total reaction free energy of the catalytic cycle, respectively. 149
- Figure 4.8** Reaction free energy profile diagram of N-formylmorpholine hydrogenation to methanol *via* C–N bond hydrogenation followed by C=O bond hydrogenation catalyzed by Mn-PNP complex. $\Delta\Delta G^{\ddagger R}$ and ΔG_{rxn} denote the total free energy barrier and total reaction free energy of the catalytic cycle, respectively. 152
- Figure 4.9** Frontier molecular orbitals of intermediates **15**, **16**, **21**, and **22** for Mn-PNP complex. 154
- Figure 4.10** **a)** Amine conversion over H_2 and CO_2 concentration for the amide formation. Simulations based-on Scheme 4.3 and 4.5. **(b)** Amine conversion over time for the amide formation. Simulations based-on Scheme 4.3 and 4.5. **(c)** Amide conversion to methanol over H_2 concentration. Simulations based-on Scheme 4.10. **(d)** Amide conversion to methanol over time. Simulations based-on Scheme 4.10. Here reaction time, initial conditions, pressure, and temperature were similar as used in the experiments. 158
- Figure 4.11** Amide conversion to methanol over time. Simulations on the based-on scheme S5. Change of concentration of reactant amide (14), intermediate (HCHO) and products CH_3OH and amine (6). 159
- Figure 4.12** Possible reaction mechanism and corresponding reaction free energy profile diagram of CO_2

- capturing to oxazolidinone using 2-amino-1-propanol amino alcohol in the presence of Et₃N base. 161
- Figure 4.13** Possible reaction mechanism and corresponding reaction free energy profile diagram of CO₂ capturing to oxazolidinone using 2-amino-1-propanol amino alcohol in the presence of Et₃N base and frontier molecular orbitals of intermediates **4** and **5**. 162
- Figure 4.14** Reaction scheme (a) and corresponding reaction free energy profile diagrams of oxazolidinone hydrogenation to various products in the presence of Mn-PNP catalyst through various pathways: (b) Pathway I (via C–N bond cleavage), (c) Pathway II (via C–O bond cleavage), and (d) Pathway III (via C=O bond cleavage). Here $\Delta\Delta G^{\ddagger R}$ denotes the total reaction free energy barrier of the catalytic cycle. 164
- Figure 4.15** (a) Figure of oxazolidinone with NBO charge distribution on C, N, and O atom of C–N, C–O and C=O bonds, (b) electron density diagram of LUMO+4 of oxazolidinone. 168
- Figure 4.16** Reaction free energy profile diagram for C–O bond cleavage (Pathway A) and C=O bond hydrogenation (Pathway B) of 2-aminopropyl formate (**11**) to formaldehyde (**25**) and (2-aminopropoxy)methanol (**29**) using the Mn-PNP catalyst. Here, $\Delta\Delta G^{\ddagger R}$ denotes the total free energy barrier of the catalytic cycle. 172
- Figure 4.17** Reaction free energy profile diagram for C–N bond cleavage (Pathway C) and C=O bond

hydrogenation (Pathway D) of (1-hydroxypropan-2-yl)formamide (**17**) to formaldehyde (**25**) and 2-((hydroxymethyl)amino)propan-1-ol (**36**) using the Mn-PNP catalyst. Here, $\Delta\Delta G^{\ddagger R}$ denotes the total free energy barrier of the catalytic cycle. 172

Figure 4.18 Reaction scheme and corresponding reaction free energy profile diagram for C–N bond cleavage (Pathway E) and C–O bond hydrogenation (Pathway F) of 4-methyloxazolidin-2-ol (**21**) to (2-aminopropoxy)methanol (**29**) and 2-((hydroxymethyl)amino)propan-1-ol (**36**) using the Mn-PNP catalyst. Here, $\Delta\Delta G^{\ddagger R}$ denotes the total free energy barrier of the catalytic cycle. 174

Figure 4.19 Reaction schemes and corresponding reaction free energy profile diagrams of formaldehyde (**25**) hydrogenation to methanol using the Mn-PNP catalyst. Here, $\Delta\Delta G^{\ddagger R}$ denotes the total free energy barrier of the catalytic cycle. 175

Figure 4.20 Reaction schemes and corresponding reaction free energy profile diagrams of (2-aminopropoxy)methanol (**29**) hydrogenation to methanol using the Mn-PNP catalyst. Here, $\Delta\Delta G^{\ddagger R}$ denotes the total free energy barrier of the catalytic cycle. 176

Figure 4.21 Reaction schemes and corresponding reaction free energy profile diagrams of 2-((hydroxymethyl)amino)propan-1-ol (**36**) hydrogenation to methanol using the Mn(I)-PNP catalyst. Here, $\Delta\Delta G^{\ddagger R}$ denotes the total free energy barrier of the catalytic cycle. 177

Figure 4.22 Overall reaction free energy profile diagram for oxazolidinone hydrogenation to methanol via C–O bond hydrogenation followed by C–N/C=O and C=O/C–N bond hydrogenation using the Mn-PNP catalyst. Here, $\Delta\Delta G^{\ddagger R}$ denotes the total free energy barrier of the catalytic cycle. 178

Figure 4.23 Overall reaction free energy profile diagram for oxazolidinone hydrogenation to methanol via C–N bond hydrogenation followed by C–O/C=O and C=O/C–O using Mn-PNP catalyst. Here, $\Delta\Delta G^{\ddagger R}$ denotes the total free energy barrier of the catalytic cycle. 179

Figure 4.24 Overall reaction free energy profile diagram for oxazolidinone hydrogenation to methanol via C=O bond hydrogenation followed by C–N/C–O and C–O/C–N using Mn(I)-PNP catalyst. Here, $\Delta\Delta G^{\ddagger R}$ denotes the total free energy barrier of the catalytic cycle. 179

Figure 4.25 Plot of rate constant (k) of the heterolytic hydrogen cleavage (RDS) for oxazolidinone hydrogenation to methanol at 273–600 K. 180

Chapter 5

Figure 5.1 Different motifs of six coordinated Cu MLs: (a) hexagonal buckled, (b) orthorhombic buckled, (c) hexagonal planar, and (d) orthorhombic planar. The red dashed line indicates the unit cell of the respective monolayer. 199

Figure 5.2 Top and side views of the considered NCs: (i, ii) $Zn_{12}O_{12}$, (iii, iv) $Zn_{24}O_{24}$. 200

Figure 5.3	(a) The phonon dispersion plot of hexagonal Cu(111) ML, (b) top and side views of Cu(111) ML (where red dotted lines show the unit cell of the structure) and (c) the possible adsorption sites on Cu(111) ML.	206
Figure 5.4	Dispersion of phonon modes for six-coordinated (a) orthorhombic planar Cu(111) ML, (b) orthorhombic buckled Cu(110) ML and (c) hexagonal buckled Cu(110) ML.	206
Figure 5.5	(a) The AIMD simulation of the Cu(111) ML at 300-700 K temperature for 20 ps. (b) Stress-strain relationship of the Cu(111) ML under in-plane uniaxial and biaxial direction.	207
Figure 5.6	Snapshots of the Cu(111) ML at the end of the simulation with temperature (a) 300 K, (b) 500 K and (c) 700 K. Snapshots of the Cu(111) ML when the total energy fluctuation of the Cu(111) ML is around 10 eV during the simulation at 500K (d-f), and at 700 K (g-i).	208
Figure 5.7	Strain energy under in plane uniaxial and biaxial strains of the Cu(111) ML.	209
Figure 5.8	Adsorption patterns of the intermediates on the Cu(111) ML surface: (a) *CO ₂ , (b) *COOH, (c) *CO, (d) *CHO, (e) *COH, (f) *CHOH, (g) *CH ₂ O, (h) *CH ₂ OH, (i) *CH ₃ O, (j) *CH ₃ OH, (k) *CH ₂ , (l) *H ₂ O, (m) *HCOO, (n) *HCOOH (o) *H ₂ COOH (p) *H, (q) *O and (r) *OH.	211
Figure 5.9	Potential energy surface for CO ₂ hydrogenation to methanol via different possible pathways on the Cu(111) ML. All the calculated reaction free energies and activation barriers are in eV.	215

- Figure 5.10** Optimized structure of the transition states on the Cu(111) ML: (a) $*CO_2 + *H \rightarrow *COOH$, (b) $*COOH + *H \rightarrow *CO + *H_2O$, (c) $*CO + *H \rightarrow *CHO$, (d) $*CHO + *H \rightarrow *CH_2O$, (e) $*CHO + *H \rightarrow *COH$, (f) $*CH_2O + *H \rightarrow *CH_3O$, (g) $*CH_2O + *H \rightarrow *CH_2OH$, and (h) $*CH_3O + *H \rightarrow *CH_3OH$. 216
- Figure 5.11** Relative reaction free energies and their dependencies on the applied electrode potential. 222
- Figure 5.12** Top and side views of considered Cu doped ZnO NCs: (a, b) first layer Cu doped $Zn_{24}O_{24}$, (c, d) second layer Cu doped $Zn_{24}O_{24}$, (e, f) third layer Cu doped $Zn_{24}O_{24}$. (g, h) Ab initio molecular dynamics simulations of (g) ZnO and (h) Cu@ZnO NCs at 300, 500 and 700 K. 229
- Figure 5.13** Adsorption patterns of the considered CO_2 hydrogenation reaction intermediates on ZnO NC: (a) $*CO_2$, (b) $*COOH$, (c) $*CO$, (d) $*CHO$, (e) $*COH$, (f) $*CHOH$, (g) $*CH_2O$, (h) $*CH_2OH$, (i) $*CH_3O$, (j) $*CH_3OH$, (k) $*CH_2$, (l) $*H_2O$, (m) $*H$, (n) $*O$ and (o) $*OH$. 232
- Figure 5.14** Adsorption patterns of the considered CO_2 hydrogenation reaction intermediates on Cu@ZnO NC: (a) $*CO_2$, (b) $*COOH$, (c) $*CO$, (d) $*CHO$, (e) $*COH$, (f) $*CHOH$, (g) $*CH_2O$, (h) $*CH_2OH$, (i) $*CH_3O$, (j) $*CH_3OH$, (k) $*CH_2$, (l) $*H_2O$, (m) $*H$, (n) $*O$ and (o) $*OH$. 233
- Figure 5.15** Relative CO_2 hydrogenation ZPE corrected reaction energies and their dependencies on the applied electrode potential on (a) ZnO NC, and (b) Cu@ZnO NC. 241

Chapter 6

- Figure 6.1** Modelled Cu nanocube (Cu-NC) exposed with Cu(100) surface for CO₂ hydrogenation reaction. 262
- Figure 6.2** (a) Optimized structures of the Cu-NC and ab initio molecular dynamics (AIMD) simulations of Cu NC at 300, 400 and 500 K. (b) Optimized structures of the Cu-dNC and AIMD simulations of Cu-dNC at 300, 500 and 700 K. 268
- Figure 6.3** The radial distribution functions (g(r)) of (a) Cu-NC and (b) Cu-dNC calculated from AIMD simulation at different temperatures. The structure obtained at the end of the simulation is attached with g(r). 269
- Figure 6.4** (a) Side and (b) top views of the considered Cu-dNC with all possible adsorption sites. 270
- Figure 6.5** Adsorption patterns of the considered CO₂ hydrogenation to C₁ based intermediates on Cu-dNC: (a) *CO₂, (b) *COOH, (c) *HCOO, (d) *HCOOH, (e) *CO, (f) *HCO, (g) *COH, (h) *H₂COOH, (i) *H₂CO, (j) *HCOH, (k) *H₂COH, (l) *H₃CO, (m) *H₃COH, (n) *C, (o) *HC, (p) *H₂C, (q) *H₃C, (r) *H₄C, (s) *H, (t) *O and (u) *H₂O. 271
- Figure 6.6** Adsorption patterns of the considered CO₂ hydrogenation to C₂ based intermediates on Cu-dNC: (a) *HCO-HCO, (b) *HCO-HCOH, (c) *HCO-CO, (d) *COH-CO, (e) *C-CO, (f) *C₂H₄, (g) *HC-CO, (h) *H₂C-CO, (i) *HC-HCO, (j) *H₂C-HCO, (k) *H₂C-H₂CO, (l) *HC-COH, (m)

*C-HC, (n) *C-H₂C, (o) *HC-HC, (p) *HC-H₂C,
(q) *H₂C-HCOH, (r) *H₃C-HCO, (s) *H₃C-H₂CO,
(t) *H₃C-HCOH and (u) *H₃C-H₂COH. 272

Figure 6.7 Projected density of states plot of (a) *COOH, (b) *HCOO, (c) *C-H₂C, and (d) *HC-HC intermediates on Cu-dNC. 275

Figure 6.8 Reaction free energies of CO₂ hydrogenation to (a) CH₃OH, (b) C₂H₄ and (c) C₂H₅OH and their dependencies on the applied potentials. 288

Figure 6.9 Reaction free energies of CO₂ hydrogenation to (a) HCOOH, and (b) CH₄ and their dependencies on the applied potentials. 289

Chapter 7

List of Schemes

Chapter 1

Chapter 2

- Scheme 2.1** Proposed reduction pathways for the active catalyst formation for half sandwich Mn(I) catalysts. 65
- Scheme 2.2** Possible CO₂ vs. proton reduction pathways using the Mn(I) half sandwich-based active catalyst. 70
- Scheme 2.3** Proton reduction pathways using the NH₂ based Mn(I) half sandwich based active catalyst. 76
- Scheme 2.4** Proposed catalytic pathway for the CO₂ reduction reaction to CO catalyzed by the COOH based Mn(I) half sandwich active catalysts **3**. The calculated reaction free energies (ΔG), activation barriers (ΔG^\ddagger) and reduction potential values (E vs. SCE) of COOH substituted Mn(I) half sandwich catalyst in water solvent. 77

Chapter 3

- Scheme 3.1** Proposed ligand participated CO₂ hydrogenation reaction mechanism for **Mn-AMP** complex. 98
- Scheme 3.2** Proposed ligand assisted CO₂ hydrogenation mechanisms by **Mn-AMP** complex. 102
- Scheme 3.3** Formate anion vs external base assisted CO₂ hydrogenation catalyzed by the **Mn-AMP** complex. 108

Chapter 4

- Scheme 4.1** The overall reaction mechanisms of CO₂ capture using 2-amino-1-propanol followed by

	hydrogenation to methanol in the presence of Mn-PNP catalyst.	132
Scheme 4.2	The reaction mechanisms of CO ₂ hydrogenation to methanol in the presence of morpholine.	136
Scheme 4.3	Ligand assisted CO ₂ hydrogenation to HCOOH catalyzed by Mn-PNP catalyst.	137
Scheme 4.4	Ligand participated CO ₂ hydrogenation to HCOOH catalyzed by Mn-PNP.	138
Scheme 4.5	HCOOH to N-formylmorpholine (amidation).	143
Scheme 4.6	Formation of formate and amide intermediates in the presence of morpholine base.	145
Scheme 4.7	Uncatalyzed reaction between two equivalents of morpholine and CO ₂ for the formation of carbamate salt.	145
Scheme 4.8	Expected two different possibilities for N-formylmorpholine hydrogenation to methanol by Mn-PNP catalyst.	147
Scheme 4.9	N-formylmorpholine hydrogenation reaction to methanol <i>via</i> C=O bond hydrogenation followed by C–N bond hydrogenation catalyzed by Mn-PNP complex.	148
Scheme 4.10	N-formylmorpholine hydrogenation to methanol <i>via</i> C–N bond hydrogenation followed by C=O bond hydrogenation catalysed by Mn-PNP complex.	151
Scheme 4.11	Proposed mechanistic pathway of Pathway I for C–N bond cleavage of oxazolidinone by Mn-PNP catalyst.	165
Scheme 4.12	Proposed mechanistic pathway of Pathway II for C–O bond cleavage of oxazolidinone by Mn-PNP catalyst.	165

Scheme 4.13	Proposed mechanistic pathway of Pathway III for C=O bond hydrogenation of oxazolidinone by Mn-PNP catalyst.	166
Scheme 4.14	The reaction mechanisms of C–O bond cleavage (Pathway A) and C=O bond hydrogenation (Pathway B) of 2-aminopropyl formate (11) to formaldehyde (25) and (2-aminopropoxy)methanol (29) in the presence of Mn-PNP catalyst.	170
Scheme 4.15	The reaction mechanisms of C–N bond cleavage (Pathway C) and C=O bond hydrogenation (Pathway D) of (1-hydroxypropan-2-yl)formamide (17) to formaldehyde (25) and 2-((hydroxymethyl)amino)propan-1-ol (36) in the presence of Mn-PNP catalyst.	171
Scheme 4.16	Reaction scheme for C–N bond cleavage (Pathway E) and C–O bond hydrogenation (Pathway F) of 4-methyloxazolidin-2-ol (21) to (2-aminopropoxy)methanol (29) and 2-((hydroxymethyl)amino)propan-1-ol (36) in the presence of Mn-PNP catalyst.	173
Chapter 5		
Scheme 5.1	The calculated reaction free energies (eV) and activation barriers (values in parenthesis, eV) for electrochemical CO ₂ reduction on the Cu(111) ML. Our calculated activation barriers are compared that with the previous reports on the bulk Cu(111) surface. Here (-) represents data is not available for this step.	214

Scheme 5.2 The calculated ZPE corrected reaction energies (eV) for electrochemical CO₂ hydrogenation reaction on ZnO (red) and Cu@ZnO (green) NCs. Our calculated ZPE corrected reaction energies are compared with those of the previous reports on the Cu nanocluster and Cu(111) ML. Here (-) means that the energy is not available for this step and ML stands for Cu(111) ML. The green arrow shows the most favourable pathway for CO₂ hydrogenation reaction to CH₃OH.

236

Chapter 6

Scheme 6.1 All possible mechanistic pathways with reaction free energies (in eV) for CO₂ hydrogenation reaction to HCOOH, CH₃OH and CH₄ on Cu-dNC. The common intermediates of most favourable pathways are highlighted in magenta color and the intermediates determine the selectivity of HCOOH, CH₃OH and CH₄ are highlighted in green, blue and red colors, respectively. The hollow and solid arrow heads represent the endergonic and exergonic steps, respectively.

277

Scheme 6.2 All the possible mechanistic pathways with reaction free energies (in eV) for CO hydrogenation reaction to C₂H₄ and C₂H₅OH on Cu-dNC. The common intermediates of most favourable pathways are highlighted in blue color and the intermediates determine the selectivity of C₂H₄ and C₂H₅OH are highlighted in magenta and green colors, respectively. The hollow and solid

arrow heads represent the endergonic and exergonic steps, respectively. 283

Scheme 6.3 Possible mechanistic pathways of (a) *CO to *HCO vs. *COH formation and (b) C–C coupling steps with reaction free energies (in eV) on Cu-dNC. The values given in the parenthesis are the activation barriers in eV at 0 V vs. RHE. The common favourable intermediates of most favourable pathways are highlighted in blue color. The hollow and solid arrow heads represent the endergonic and exergonic steps, respectively. 285

Chapter 7

List of Tables

Chapter 1

Chapter 2

- Table 2.1** Calculated two separate one-electron reduction potentials (E in V) in three different solvents (acetonitrile, water and DMSO) for all the considered half sandwich Mn(I) complexes calculated at UB3LYP/6-31+G** + LANL2DZ with CPCM solvation model. The calculated values with UB3LYP/6-311++G** + SDD and SMD solvation model are shown in parenthesis. 66
- Table 2.2** The calculated NBO charges of the Mn atom and the ligand part of the intermediates **1**, **2** and **3** for different substitutions in acetonitrile solvent by UB3LYP/6-31+G** + LANL2DZ with CPCM solvation model. The calculated NBO using UB3LYP/6-311++G** + SDD with SMD solvation model values are shown in parenthesis. 68
- Table 2.3** The calculated reaction free energies (ΔG in kcal/mol) and activation barriers (ΔG^\ddagger in kcal/mol) of proton and CO₂ reduction reaction by half sandwich Mn(I) based complexes using UB3LYP/6-31+G** + LANL2DZ with CPCM solvation model. The calculated UB3LYP/6-311++G** + SDD with SMD solvation model values are shown in parenthesis. 71
- Table 2.4** Calculated reaction free energies (ΔG) and activation barriers (ΔG^\ddagger) of proton and CO₂ reduction reaction of all considered Mn(I) half sandwich-based complexes with one explicit solvent molecule. The calculated reaction free energies (ΔG)

and activation barriers (ΔG^\ddagger) of proton and CO₂ reduction reaction without explicit solvent molecule are shown in parenthesis. All these calculated reaction free energies and barriers are in kcal/mol. 75

Table 2.5 Calculated reaction free energies (ΔG in kcal/mol), activation barriers (ΔG^\ddagger in kcal/mol) and reduction potentials (E vs. SCE) of CO₂ reduction reaction to CO by Mn(I) half sandwich-based complexes by considering UB3LYP/6-31+G** + LANL2DZ with CPCM solvation model. The calculated UB3LYP/6-311++G** + SDD with SMD solvation model values are shown in parenthesis. 78

Chapter 3

Table 3.1 The calculated total reaction free energy barriers (in kcal/mol) for CO₂ hydrogenation via Ligand assisted (presence of external base) and ligand participated mechanisms. 104

Table 3.2 Ligand assisted reaction free energy for CO₂ hydrogenation reaction catalyzed by Mn(I) modelled complexes of amply ligands. $\Delta\Delta G^\ddagger$ represents the total reaction free energy barriers for reaction. All free energies are in kcal/mol. 106

Table 3.3 Stepwise reaction kinetic model for all barriers at different temperatures. All the temperatures are in Kelvin (K) and all the rate constants are in M⁻¹S⁻¹. 109

Table 3.4 Overall reaction kinetic model for all possible pathways at different temperatures. All the temperatures are in Kelvin (K) and all the rate constants are in M⁻¹S⁻¹. 110

Chapter 4

Table 4.1	Evaluation of functional, basis sets and solvation model for Mn(I)-PNP based catalyst.	135
Table 4.2	Ligand assisted reaction free energy for CO ₂ hydrogenation reaction to HCOOH by PNP based Mn(I), Fe(II) and Ru(II) complexes. $\Delta\Delta G^\ddagger$ represents the total reaction free energy barriers for reaction. All free energies are in kcal/mol.	143
Table 4.3	N-formylmorpholine hydrogenation to methanol via C=O bond hydrogenation followed by C–N bond hydrogenation reaction by PNP based Mn(I), Fe(II) and Ru(II) complexes. $\Delta\Delta G^{\ddagger R}$ represents the total reaction free energy barriers for reaction. All free energies are in kcal/mol.	150
Table 4.4	N-formylmorpholine hydrogenation to methanol via C–N bond hydrogenation followed by C=O bond hydrogenation reaction by PNP based Mn(I), Fe(II) and Ru(II) complexes. $\Delta\Delta G^{\ddagger R}$ represents the total reaction free energy barriers for reaction. All free energies are in kcal/mol.	153
Table 4.5	Reaction mechanisms elementary step's gibbs free energy and rate constant. $\Delta\Delta G^{\ddagger R}$ represents the total reaction free energy barriers for reaction. All free energies are in kcal/mol and rate constants are in M ⁻¹ S ⁻¹ .	156
Table 4.6	The total energies (in Hartree) of the singlet and triplet states of Mn(I) based intermediates associated in Pathway I and the energy difference (kcal/mol) between the singlet and triplet states of the Mn(I) based intermediates.	167

Chapter 5

Table 5.1	Formation and cohesive energies of Cu MLs and bulk Cu(111) surface. The experimental cohesive energy value of the bulk Cu(111) surface listed for comparison.	204
Table 5.2	Preferred adsorption sites (top, bridge and hollow) and adsorption energies of all the CO ₂ hydrogenation intermediates on Cu(111) ML. The preferred site and adsorption energies of the respective adsorbates are compared with our earlier report on the bulk Cu(111) surfaces.	212
Table 5.3	All imaginary frequencies of the corresponding transition states.	217
Table 5.4	Reaction mechanisms elementary step's reaction free energy barrier and rate constant. All activation energy barriers are in kcal/mol and rate constants are in M ⁻¹ S ⁻¹ .	225
Table 5.5	Formation and cohesive energies of Zn ₁₂ O ₁₂ , Zn ₂₄ O ₂₄ NCs and bulk ZnO. Previously calculated formation energy value for the bulk ZnO is also listed in the parenthesis for comparison.	228
Table 5.6	Adsorption energies of all the intermediates of CO ₂ hydrogenation reaction with their most favourable adsorption sites (in the parenthesis) on ZnO and Cu@ZnO NCs. The adsorption energies of all the considered adsorbates have been compared with the previous reports on the bulk Cu(111), Cu(111) ML and Cu nanocluster.	233
Table 5.7	Average adsorption energies per ZnO unit on the ZnO and Cu@ZnO NCs.	242

Chapter 6

- Table 6.1** The convergence calculation for Cu-NC using various plane wave basis set cutoff. 265
- Table 6.2** Formation and cohesive energies of Cu-NC, Cu-dNC, periodic Cu(100) and Cu(111) surface. The experimental formation and cohesive energy values for the periodic Cu(111) surface are given in parenthesis for comparisons. 267
- Table 6.3** Favored adsorption sites and all the CO₂ hydrogenation related intermediates adsorption energies on the Cu-dNC surface. 273
- Table 6.4** Stepwise CO₂ hydrogenation reaction free energies on Cu-dNC, periodic Cu(100) surface, Cu(111) monolayer and Cu nanocluster based surfaces. All reaction free energies are in eV. Here, (–) means that the reaction free energy is not available for this step. The stepwise reaction free energies of Cu(100) surface, Cu(111) monolayer and Cu₈₅ nanocluster have been taken from references. 279

Chapter 7

Acronyms

Gt	Gigaton
IPCC	International Panel on Climate Change
CCS	Carbon Capture and Storage
CCU	Carbon Capture and Utilization
TEA	triethanolamine
DIPA	diisopropanolamine
DEA	diethanolamine
MDEA	methyldiethanolamine
FTS	Fischer-Tropsch Synthesis
ML	monolayer
NC	nanocage
dNC	distorted Nanocube
BO approximation	Born-Oppenheimer approximation
NHC	N-heterocyclic Carbene
TON	Turnover Number
TOF	Turnover Frequency
THF	Tetrahydrofuran
MLC	Metal-ligand Cooperation
HF	Hartree-Fock
SCF	Self-Consistent Field
DFT	Density Functional Theory
LDA	Local Density Approximation
GGA	Generalized Gradient Approximation
PBE	Perdew-Burke-Ernzerhof
PW91	Perdew and Wang 91
B3LYP	Becke, three-parameter, Lee-Yang-Parr
RPBE	Revised Perdew-Burke-Ernzerhof
STO	Slater Type Orbitals
GTO	Gaussian Type Orbitals
ECP	Effective Core Potential

LANL2DZ	Los Alamos National Laboratory double-zeta
NBO	Natural Bond Orbital
NCI	Noncovalent Interaction
ZPE	Zero-point Energy
AIMD	Ab Initio Molecular Dynamics
NEB	Nudged Elastic Band
MEP	Minimum Energy Path
hTST	harmonic approximation of Transition State Theory
CMD	Classical Molecular Dynamics
Mn-AMP	Mn(I)-2-(aminomethyl)pyridine
Mn-MAMP	Mn(I)-2-(methylaminomethyl)-
Mn-AMI	Mn(I)-2-(aminomethyl)imidazole
Mn-AMIM	Mn(I)-2-(aminomethyl)imidazoline
Mn-AMNHC	Mn(I)-2-(aminomethyl)Nheterocycliccarbene
Mn-MAMI	Mn(I)-2-(methylaminomethyl)imidazole
Mn-MAMIM	Mn(I)-2-(methylaminomethyl)imidazoline
Mn-MAMNHC	Mn(I)-2-(methylaminomethyl)Nheterocycliccarbene

Chapter **1**

Introduction

1.1. Current Scenario of CO₂ and Disadvantages of Fossil Fuels

The natural carbon cycle of the earth atmosphere is balanced by the plants and animals. The concentration of CO₂ was balanced until 17th century after that it has started increasing. Generally, 120 Gt of CO₂ is the balanced amount which is supposed to be used by the plants for the photosynthesis process [1]. However, the amount of CO₂ is rising every year. This emission is very much dependent on the location of the countries and the top ten CO₂ produce countries are China, USA, India, Russia, Germany, Japan, Iran, Canada, South Korea, and Saudi Arabia [2]. These countries emit almost 78% of the total CO₂ emission. The effect of this excess CO₂ on the atmosphere was first noticed by Svante Arrhenius in 1896 and outlined the idea about the CO₂ as a greenhouse gas which can enhance the atmospheric temperature that can cause global warming. The increasing CO₂ emission is very rapid, the first 50 ppm of CO₂ has been increased in 200 years then next 50 ppm has been increased within 33 years whereas the next 20 ppm has increased in the last 11 years [3]. So, the concentration of CO₂ has increased from ~280 ppm to ~390 ppm by 2010 and it is further expected to increase up to ~570 ppm by the end of this century [4]. Moreover, the recent reports have shown that in nature approximately 3.9% excess CO₂ is present in the carbon cycle [5]. Human actions with the advancement of industrialization and growing energy demands are predominantly responsible for this excess CO₂ in the environment. This is further accelerated by the enhanced consumption of fossil fuels such as coal, natural gas, and oil for the fulfilment of human development. Out of all the CO₂ emission sources, coal combustion alone contributes to 43% of its total emissions, whereas oil and gas production release 30% and 27% CO₂, respectively on its total amount [6]. As CO₂ is a greenhouse gas, this increment of CO₂ can enhance the atmospheric temperature by 1.9°C [7]. International Panel on Climate Change (IPCC) has mentioned that all of these can cause increased sea level up to 1 meter by the year 2100 [8]. Therefore, the climate change due to the enhancement of CO₂ is one of the

ferocious challenges of our times. So, the high emission of CO₂ has pushed governments for the implementation of CO₂ reduction strategies. In this context, European Union has set the aim of decreasing the emissions of greenhouse gas by 80-95% within 2050 compared to the CO₂ emission in 1990 levels. It is very strange that CO₂ is a threat for plants and animals even if it is nontoxic. This is due to the sudden increase to a huge amount. However, CO₂ is a thermally stable molecule with high symmetry nature and nonpolar functional even if it is the combination of two polar parts of carbon and oxygen atoms. Between carbon and oxygen atoms, carbon is electron deficient whereas oxygen is electron rich which can makes the molecule bifunctional during the reaction. So, a massive input of scientific knowledge is highly essential to handle CO₂ in the practical scenario.

Besides, the year 2020 is the uses of oil for 52 years, coal for 169 years and 73 years for gas [9,10]. As the amount of these fossil fuels are limited, it is going to diminish very soon. Moreover, these fuels are region dependent that is all these energy sources are highly dependent on the political laws of that place. Moreover, the global energy supply is increasing rapidly such as it has increased by 150% from 1971 to 2013 due to its economic growth and development of the society. Hence, there is an urgent need of the renewable energy resources for clean energy production to fulfill the global energy demand with almost zero CO₂ emission [11,12]. The wind and solar energy can be the potential candidate for this in future application of energy. But these energy resources are dependent on the time and region. Besides, these large-scale applications of energy resources are highly problematic. Therefore, wind and solar energy resources cannot be the alternate energy for the replacement of the fossil fuels. In this context, molecular hydrogen can be the most promising alternate, but storage and transportation of molecular hydrogen is the big issue [13-15]. Several reports have shown the storage of hydrogen on various materials but desorption of the hydrogen molecule from the material surface is very easy as hydrogen molecule is attached via physisorption method with weak bonding [16-18]. Therefore,

there is a need of chemisorption storage for hydrogen molecule [19-22].

1.2. CO₂ as a Raw Material for Fuel Production

Recent investigation shows that the direct storage of CO₂ can reduce only 1% of the overall CO₂ emission whereas formation of chemicals and value-added liquid fuels can reduce 10% of overall CO₂ emission [23]. Therefore, conversion of CO₂ to chemicals and fuels will be more effective rather than CO₂ capture. Besides, the market of fuels is more demanding than chemicals, and the emission of CO₂ is associated with the fossil fuel consumption whereas the produced fuel can replace the conventional fossil fuels. The chemical industries use only 10% of the global crude oil-based fuels consumption whereas rest is used by the fuels such as diesel, gasoline and other heavy oil. So, the net emission of CO₂ can only be reduced by using CO₂ as a feedstock for liquid fuels formation. Nowadays, researchers are highly motivated to investigate the possible ways of the CO₂ conversion to value added products as it can be the key alternate for the development of carbon neutral fuels. However, the emission of CO₂ can be solved as follows:

- i) carbon capture and storage (CCS)
- ii) carbon capture and utilization (CCU)

An effective and robust pathway is highly essential for CCS. One important strategy for the storage of CO₂ is the capturing using various solvents. In case of CO₂ capture, the commonly used solvents are triethanolamine (TEA), diisopropanolamine (DIPA), diethanolamine (DEA), and methyldiethanolamine (MDEA) [24]. The main target of CO₂ capture technologies is in the fuel processing power plants. This CO₂ capture and storage are divided based on the absorption, chemical process and separation. The most important storage technology is captured CO₂ in the empty oil fields. In the next step of the storage, a special care needs to be taken for the maintaining of the reservoirs from any leakage and desorption. Therefore, it requires significant financial strength along with technical

developments. However, these captured products have low enthalpy of absorption and hence very less energy is needed during the removal of CO₂. Therefore, the CO₂ capturing process is not perfect and it should be avoided via transformation of CO₂ to other value-added products. So, the progress in efficient CO₂ conversion to value added products using renewable energy could reduce the pollution as well as generate clean energy resource. So, formation of chemicals, fuels and fuel-alternatives from CO₂ can be one of the most important technologies for large scale reduction of CO₂. So, CCU is the need of the hour and the most important strategy for the reduction of CO₂ as well as carbon neutral fuel cycle. In this context, CO₂ can be utilized directly by the hydrogenation/reduction reaction and/or reverse water gas shift reaction subsequently Fischer-Tropsch synthesis (FTS) for the formation of hydrocarbons, acids, and alcohols [25-30]. To make these conversions meaningful, the converted products should not emit CO₂. Even though various hydrogen sources are available for the hydrogenation reactions the used hydrogen for the CO₂ hydrogenation should be originated from the clean sources such as water splitting using wind, solar, and geothermal energy [31,32]. The development of efficient catalysts by lowering the kinetic barriers of the CO₂ hydrogenation reaction is a crucial factor. To achieve the efficient catalysts with selective products, investigation of mechanistic pathways is highly important. Overall, the conversion of CO₂ to CO, HCOOH, CH₃OH, C₂H₄ and C₂H₅OH (Figure 1.1) can be one of the promising ways of to reduce the presence of CO₂ in the environment. In this perspective, various homogeneous as well as heterogeneous catalysts have been extensively studied for the formation of CO, HCOOH, CH₃OH, CH₄, C₂H₄ and C₂H₅OH. In the next chapters of this thesis the formation of various useful products from CO₂ has been discussed in detail via understanding of the most plausible mechanistic pathways and in the last chapter of this thesis, we have summarized the future direction of this topic with potential scopes.

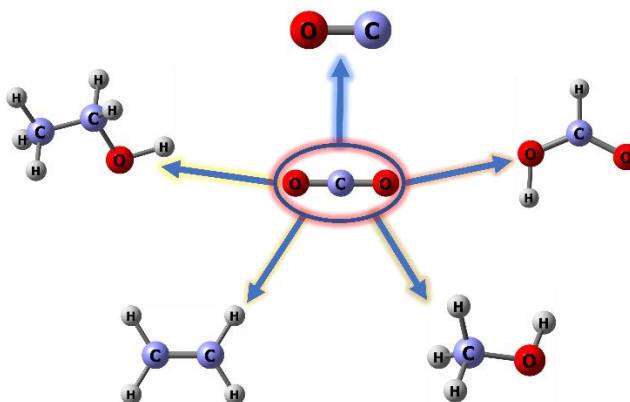


Figure 1.1: Various possible products of CO₂ hydrogenation reaction.

1.3. Types of Catalysts

In 1976, Inoue et al., have stated the very first Rh-based homogeneous catalyst [RhCl(PPh₃)₃] for CO₂ hydrogenation to HCOOH [33]. After that several other groups have started working on homogeneous catalysts for the hydrogenation of CO₂ [34-52]. However, most of the reported catalysts are based on noble metals. Even though, several catalysts have been reported high catalytic activity and the industrialization of the reported catalysts are far from the actual uses. Besides, Hori and co-workers have investigated various metal based heterogeneous catalysts and shown the unique capability of Cu metal based heterogeneous catalysts for CO₂ hydrogenation reactions [53-55]. Even if the Cu-based heterogeneous catalysts are effective for CO₂ hydrogenation the selectivity of the products are the major concern. Therefore, designing of efficient homogeneous and heterogeneous based catalysts and finding out the most favourable pathways of CO₂ hydrogenation reactions to value-added products are highly important. Therefore, based on the nature of the catalysts, the following sections are subdivided into homogeneous and heterogeneous catalysts.

1.3.1. Homogeneous Catalysts

1.3.1.1. Half Sandwich Based Catalysts

The activation of CO₂ requires a potential of -1.90 V during the conversion of linear CO₂ to bent [56]. So, efficient catalysts are essential for the

transformation of CO₂ to other valuable products. Most of the reported active catalysts are noble metal-based complexes [57-67]. So, metal center is very important for the efficient conversion of CO₂ to CO. Some recent reports have revealed that ligand sphere can also play very important role during the improvement of the catalytic activity [68-69]. Therefore, an active catalyst designing can be achieved by proper sequence of the metal and ligand sphere. Along with the above reports several Co, Ni, Fe, Re, Mn-based catalysts were reported for the electrochemical CO₂ reduction reaction (Figure 1.2) [70-72].

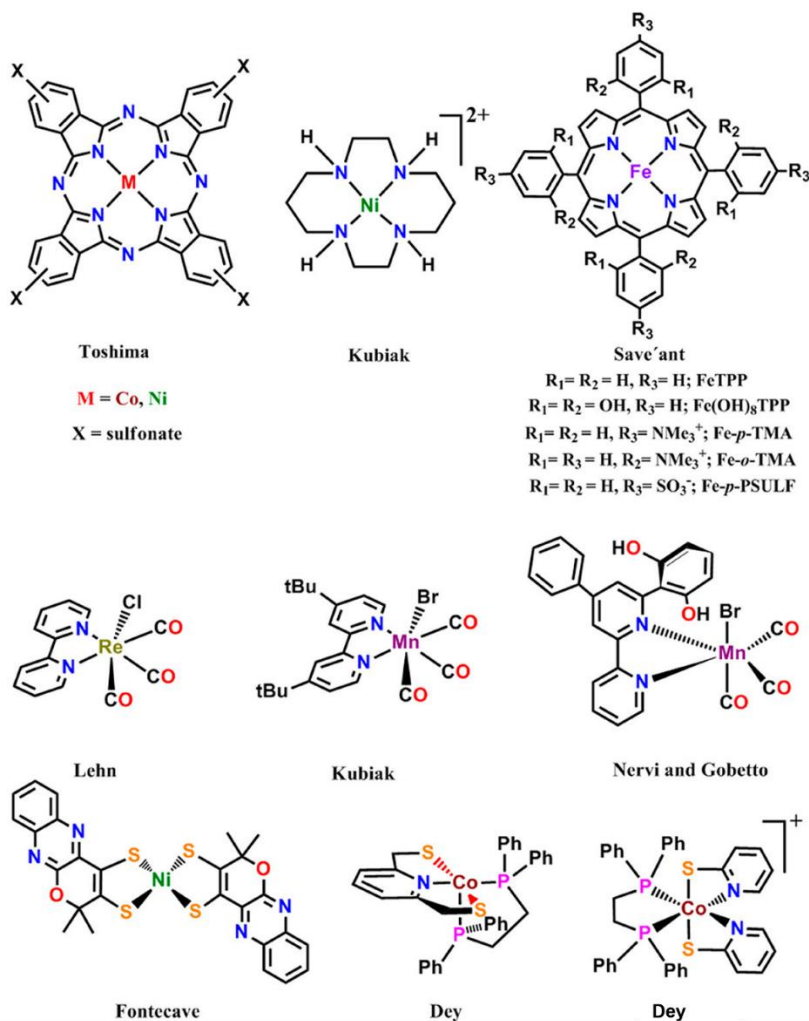


Figure 1.2: Various kinds of macrocyclic, bipyridine and thiolate complexes reported for electrochemical CO₂ reduction reaction. (Reprinted

with permission from Ref. 72; Copyright 2020, American Chemical Society)

Kubiak and his co-workers have revealed that ^tBu functional on the bpy ligand sphere can form selective CO [61]. In general, redox ligand-based homogeneous catalysts are reported to be important for the electrochemical CO₂ reduction reaction because of the reversible electron switch between the ligand sphere and metal center of the catalyst. Besides, Perekalin and co-workers have reported half sandwich-based Mn(I) catalysts during ketone hydrogenation where ligand sphere of the catalyst can behave as a redox ligand due to the delocalization of π -electrons [73]. So, we have modelled Mn(I) half sandwich-based complexes for CO₂ reduction reaction. Moreover, phenyl ring of the ligand sphere has been substituted with various substituents (CH₃, CMe₃, OH, NH₂ and COOH) to understand the role of substituents during the reaction (Figure 1.3).

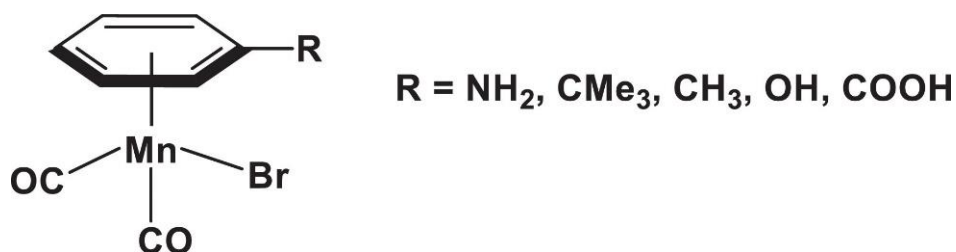


Figure 1.3: Modelled Mn(I) half sandwich-based catalysts for CO₂ reduction reaction.

1.3.1.2. Bifunctional Mn(I) Aminomethyl Type Catalysts

Recently, several highly active as well as selective homogeneous catalysts were mentioned for the efficient hydrogenation of CO₂ to a hydrogen storage material such as formic acid/formate anion [74-86]. However, it is still essential to model an inexpensive catalyst for the industrial purpose. The hydride transfer as well as heterolytic H₂ cleavage are very significant

steps for the CO₂ hydrogenation reaction. Based on the reports of Hazari and co-workers Ir(III)-PNP [PNP = 2,6-bis(dialkylphosphinomethyl)pyridine] complexes can benefit heterolytic H₂ cleavage by following a metal–ligand cooperation (MLC) mechanism [86]. Besides, several groups have shown pincer-based complexes of Ir, Co, Fe, Mn and Ru where heterolytic H₂ cleavage is performed utilizing an external base (Figure 1.4). In this context, Gonsalvi and co-workers have shown highly effective Mn-PNP complex which shows a TON of 30000 for formate formation with LiOTf co-catalyst [85].

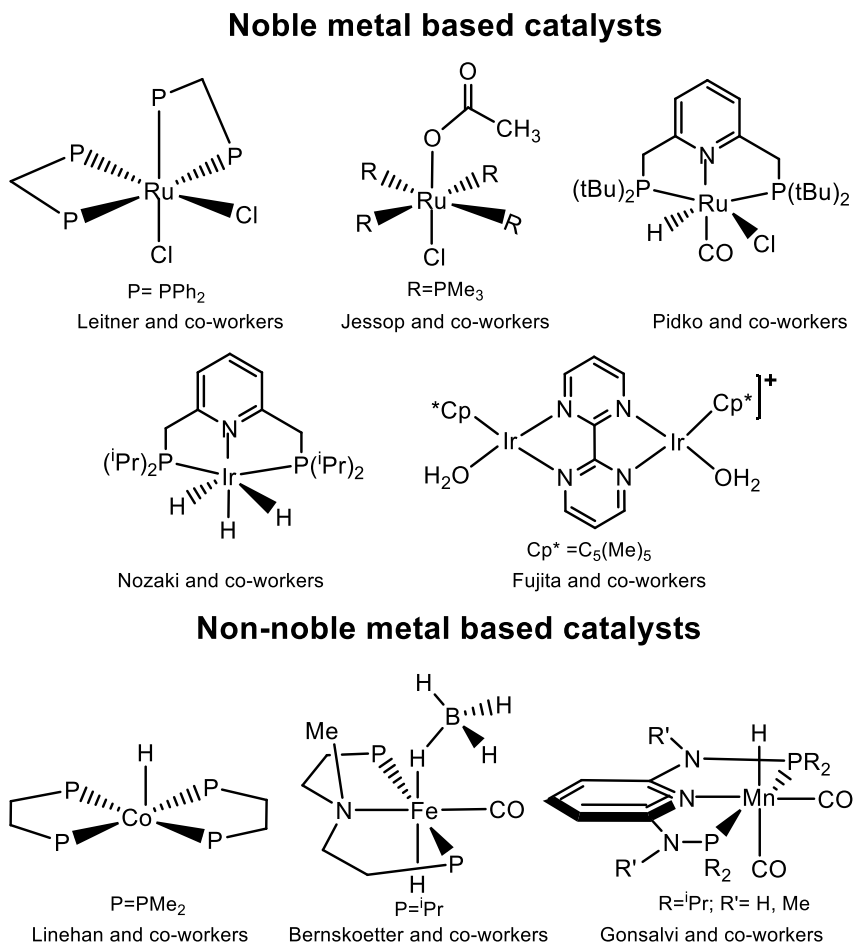


Figure 1.4: Various reported noble and non-noble metal-based catalysts for CO₂ hydrogenation reaction to formic acid/ formate.

These studies indicate that the involvement of the ligand sphere is crucial

during CO₂ hydrogenation reaction. However, there are few reports which show the importance of the N–H functionality during hydride/proton transfer [87,88]. This functionality plays a crucial part during the reaction by formation or cleavage of N–H bond through MLC as indicated by Noyori, Ikariya, and co-workers. Similarly, Dub et al. have reported revised Noyori type mechanism and propose that the N–H functionality of the ligand sphere does not involve actively during the reaction (Figure 1.5) [89-93]. In this case, the N–H functionality of the ligand sphere stabilizes the oxyanions via N–H···O hydrogen-bonding interactions by following heterolytic H₂ cleavage.

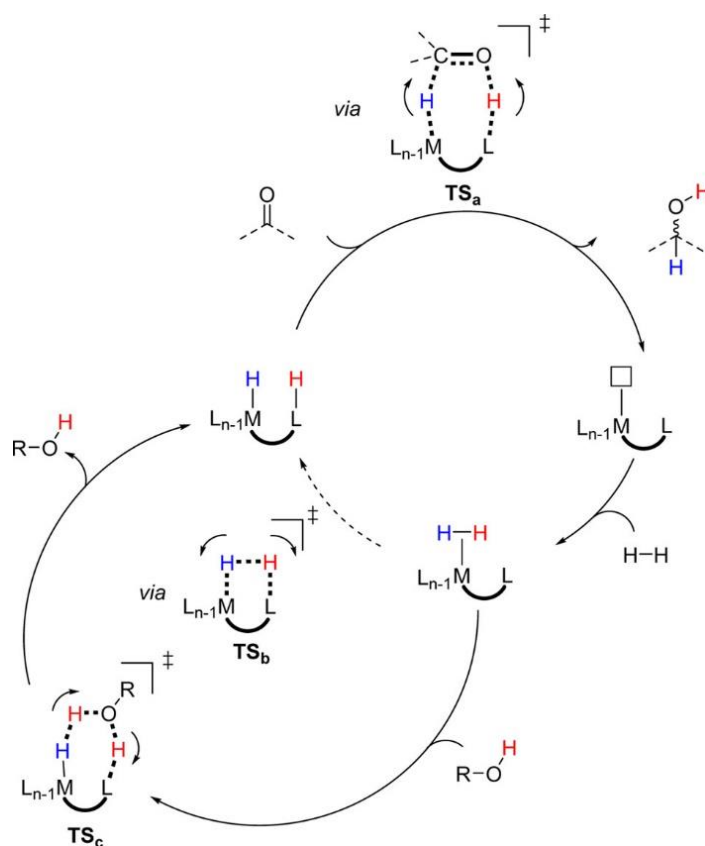


Figure 1.5: Comparison between classical and revised Noyori type mechanism during hydrogenation reaction. (Reprinted with permission from Ref. 91; Copyright 2017, American Chemical Society)

Inspired by all the above studies, we have attempted to know the importance

of the N–H functionality during CO₂ hydrogenation reaction. Recently Bruneau–Voisine et al. have shown that Mn(I)-2-(aminomethyl)pyridine as well as Mn(I)-2-(methylaminomethyl)pyridine complexes can have potential for hydrogenation reaction [94]. Hence, we suppose that the bifunctional Mn(I)-aminomethyl catalysts can be active during CO₂ hydrogenation reaction. So, to understand the N–H functionality during CO₂ hydrogenation, we have designed 2-aminomethylpyridine ligand-based Mn(I) complexes (Figure 1.6).

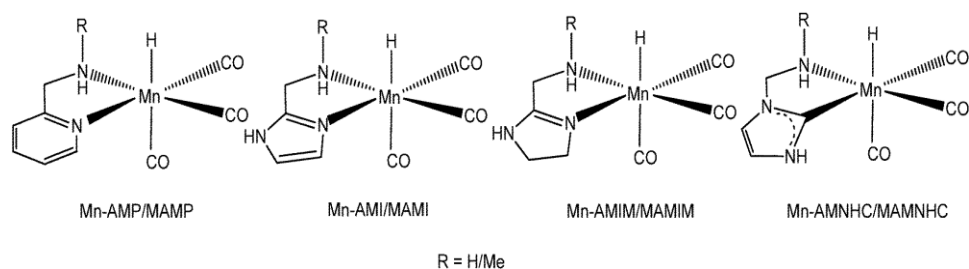


Figure 1.6: Mn(I) aminomethyl bifunctional catalysts for electrochemical CO₂ reduction reaction.

1.3.1.3. PNP Based Mn(I) Catalysts

The first Ru₃(CO)₁₂ homogeneous catalyst and N-methyl-2-pyrrolidone have been reported by Tominaga et al. for CO₂ hydrogenation reaction to methanol at 240°C at 9 MPa pressure [95]. In this report, CO₂ first converted to CO, which is hydrogenated further to methanol. After that, several other effective homogeneous catalysts were mentioned for CO₂ hydrogenation to methanol (Figure 1.7) [96]. Sanford and co-workers have examined three-step CO₂ hydrogenation approach to methanol [97]. At first, CO₂ and H₂ is converted to HCOOH in the presence of Ru(II) and Fe(II) catalysts. Then, HCOOH is esterified and form formate ester which is hydrogenated further to methanol in the presence of catalyst. Further to this, Milstein and coworkers have used [(PNN)Ru–(CO)(H)] complex and established a different approach for methanol formation [98]. Zhang et al. have shown methanol formation from CO₂ using Ru–PNP as well as Mn–

PNP catalysts with morpholine co-catalyst [99].

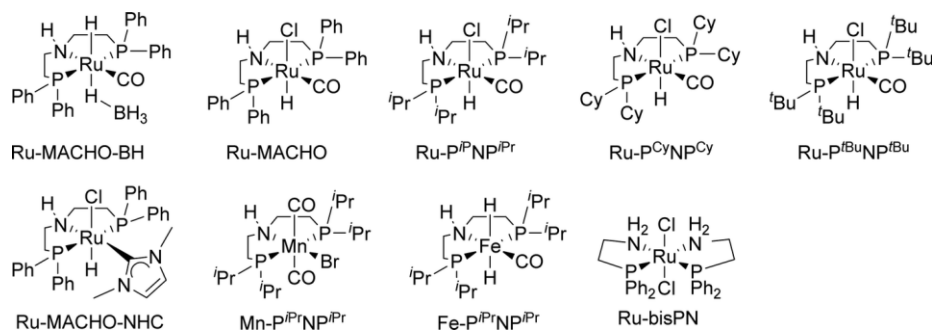


Figure 1.7: PNP based bifunctional catalysts for CO₂ hydrogenation to methanol. (Reprinted with permission from Ref. 96; Copyright 2021, Royal Society of Chemistry)

Very recently, Prakash and his group have made important role in CO₂ hydrogenation reaction and described that non-noble metal-based catalysts (Fe and Mn) can be used for methanol formation in the presence of morpholine [100-103]. Therefore, we have investigated N-H functionalized PNP-based Mn, Fe and Ru catalysts (Figure 1.8) along with morpholine co-catalyst for our CO₂ hydrogenation to methanol study.

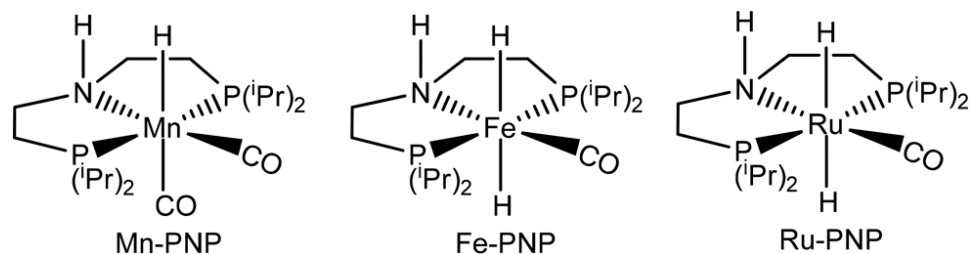


Figure 1.8: PNP based Mn(I), Fe(II) and Ru(II)-based complexes.

On the other hand, CO₂ can be captured with amino alcohols and the captured product can be converted further to other useful product. Amines as well as amino alcohols are extremely useful CO₂ capturing agents where amino alcohols can capture CO₂ to oxazolidinone [104-106]. Recently, Milstein and co-workers have used amino alcohols for CO₂ capture to

oxazolidinone [107]. Besides, Saito's work indicates that monoethanolamine is not a useful substrate and substituents at the α -position of the amine group can enhance the corresponding oxazolidinone product [108]. Hence, 2-amino-1-propanol has been considered as a CO₂ capturing agent for oxazolidinone formation. Milstein and co-workers have shown methanol formation from hydrogenation of the oxazolidinone using pincer-based Ru catalysts [107]. Alongside, Ding and co-workers have reported PNP based catalysts during oxazolidinone to methanol [109]. In this context, low-cost metal Mn can be a valuable alternative of expensive noble metal-based catalysts during oxazolidinone hydrogenation. Moreover, the PNP ligand moiety can interact with the oxazolidinone by following outer sphere mechanism with the N–H bond of the PNP pincer. Besides, the N–H functionalized of the ligand moiety can play crucial role in hydrogenation reactions. Therefore, we have explored the mechanisms of 2-amino-1-propanol participated CO₂ capture to oxazolidinone and oxazolidinone hydrogenation in the presence of Mn–PNP based catalysts (Figure 1.9).

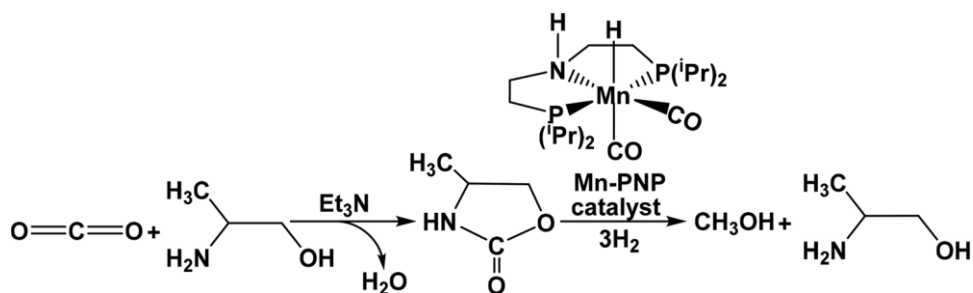


Figure 1.9: Amino alcohol participated CO₂ capture to oxazolidinone, and hydrogenation of CO₂ captured product to methanol.

1.3.2. Heterogeneous Catalysts

1.3.2.1. Cu Based Catalysts for C₁ Based Products

Among various transition metal-based heterogeneous catalysts Cu-based catalysts were recognized as active for CO₂ hydrogenation reaction [53-55]. Besides, industrially CH₃OH is generated using Cu/ZnO/Al₂O₃ catalyst,

under the pressure of 50–100 atm as well as 473–573 K temperature [110]. This catalyst also shows low product selectivity. Further to this, the encouraging usage of graphene has been inspired the scientific community for the development of monolayer (ML)-based efficient catalysts. However, few layers graphene with nitrogen-doped and metal-doped graphene oxide, as well as N, Fe-decorated nanosheets of carbon were investigated for CO₂ hydrogenation reaction [111-113]. The activity of the MLs with main group atom doped is improved due to the metal atom doping. Thus, we believe that MLs with pure metal atom can be more efficient. In this context, ultrathin nanosheet of Bi has been reported for the conversion of CO₂ to HCOO⁻ [114]. Encouraged by the previous investigations, we have designed a series of Cu MLs for CO₂ hydrogenation reaction (Figure 1.10).

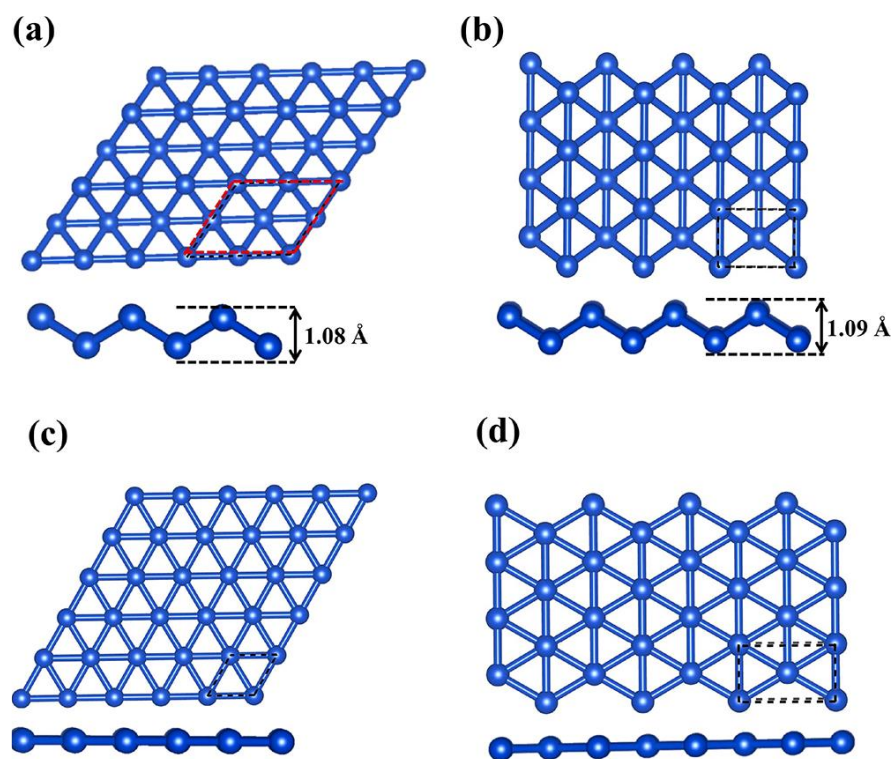


Figure 1.10: Modelled Cu-MLs for CO₂ hydrogenation reaction.

Liu et al. have investigated that Cu/ZnO catalyst for CO₂ hydrogenation to CH₃OH [115]. Chinchin et al. have investigated that the C-atom of CH₃OH

is achieved from the C of CO₂, i.e., CO₂ is the source for the CH₃OH formation [116]. After that, several other Cu/ZnO/Al₂O₃ based catalysts were identified for CO₂ hydrogenation [117-120]. In these cases, the synergistic effect is highly important and plays an essential role in advancing their activity. Side by side, Kattel et al. have reported that the Cu/ZnO assists CH₃OH formation in comparison with the Cu–Zn [120]. Therefore, it is very essential to investigate the impact of Cu as well as ZnO for CH₃OH formation. In recent times, single atom doping catalysts were recognized as encouraging for selective CH₃OH formation [121,122]. Most of these catalysts are highly useful because of their very low metal use which maximum their atom application efficiency. On the other hand, ZnO based nanostructures are very much abundant and non-toxic. In addition, several ZnO based nanostructures have been produced very easily [123,124]. Some of these nanostructures were found to be important for the various hydrogenation reactions [125,126]. In this context, Wu et al. have synthesized (ZnO)_n (n = 1–15) nanostructures and Dmytruk et al. have reported that (ZnO)₆₀, (ZnO)₃₄, and (ZnO)₇₀ nanostructures which are highly stable [127,128]. Based on the above structures, Tian and co-workers have explained that the nanocluster (ZnO)₆₀ is comprised of (ZnO)₁₂ where (ZnO)₁₂ is the basic unit [129]. Thus, we have considered Zn₁₂O₁₂ and Zn₂₄O₂₄ based NCs as well as Cu-doped SACs (Figure 1.11) for our study.

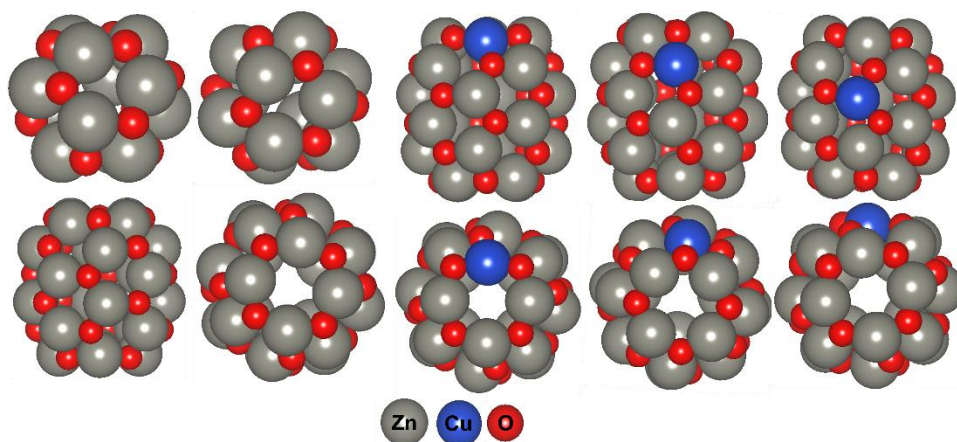


Figure 1.11: Modelled ZnO and Cu-doped ZnO based nanocages.

1.3.2.2. Cu Based Catalysts for C₂ Based Products

Early experiment by Hori and co-workers have investigated that C₁-based products are favourable on Cu(111) surface whereas C₂-based products are favourable on the Cu(100) facet [130-132]. In this context, several groups have investigated the C₂ based products formation on periodic Cu(100) surface [133-139]. All of these investigations shows the C–C bond formation favorability on the Cu(100) surface than Cu(111) surface. Moreover, nanoparticle-based catalysts show high catalytic activity that that of bulk structure [140-142]. Therefore, (100) facet exposed Cu nanoparticles can be highly efficient for C₂-based products (C₂H₄ and C₂H₅OH) formation. Recently, Nilsson and co-workers have examined that (100) facet exposed Cu nanocube is highly selectivity for C₂ based products [143]. Therefore, it is crucial to explore the full mechanistic pathways of CO₂ hydrogenation reaction on Cu nanocube. Henceforth, we have considered a Cu nanocube (Cu-NC) with Cu(100) facets (Figure 1.12).

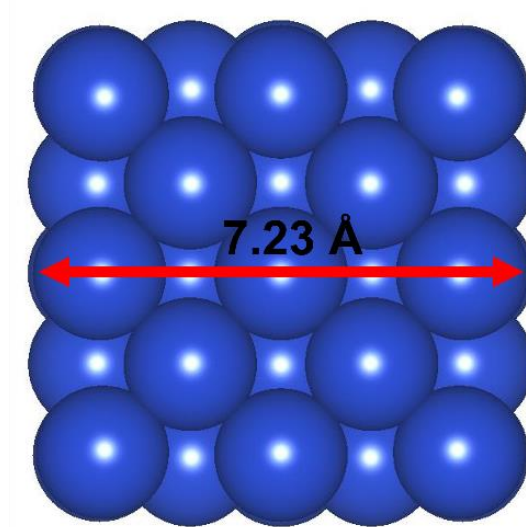


Figure 1.12: Modelled Cu(100) facets exposed Cu nanocube (Cu-NC) for CO₂ hydrogenation reaction.

1.4. Theoretical Methods

Application of electronic structure calculation methods have established as a reliable technique to study molecular and solid-state systems. Over past few decades, it has been used globally for better understanding of homogeneous and heterogeneous catalysis. In this section we will briefly discuss the techniques and methodologies of quantum mechanics those we have used throughout our work.

1.4.1. Schrödinger Equation

Utilizing quantum mechanics, all the properties of molecular and solid-state systems can be obtained by solving the Hamiltonian of a system. The time dependent form of the Schrödinger equation can be illustrated as shown in equation (1.1).

$$\hat{H} \Psi(r, t) = i\hbar \frac{\partial}{\partial t} \Psi(r, t) \quad (1.1)$$

$$\hat{H} = \hat{T} + \hat{V} = -\frac{\hbar^2}{2m} \nabla^2 + \hat{V} \quad (1.2)$$

In the above equation (1.2), \hat{H} is the Hamiltonian operation that contains kinetic (\hat{T}) as well as potential energy (\hat{V}) operators, Ψ is a function of position and time which contains all the possible information of the system, $i = \sqrt{-1}$ and \hbar is the reduced Planck's constant. Usually, we use time independent Schrödinger Equation to investigate the electronic structure as well as properties of the materials and molecules that can be represented by equation (1.3).

$$\hat{H} \Psi(r) = E \Psi(r) \quad (1.3)$$

The Hamiltonian operator \hat{H} for a many electrons system can be expressed as follows (1.4):

$$\hat{H} = -\frac{\hbar^2}{2m_e} \sum_i \nabla_i^2 - \sum_I \frac{\hbar^2}{2M_I} \nabla_I^2 + \frac{1}{2} \sum_{i \neq j} \frac{e^2}{|r_i - r_j|} + \frac{1}{2} \sum_{I \neq J} \frac{Z_I Z_J e^2}{|R_I - R_J|} - \sum_{i,I} \frac{Z_I e^2}{|r_i - R_I|} \quad (1.4)$$

Where m_e and r_i are the mass and position of the electron, whereas M_I , R_I and Z_I are the masses of the nuclei, it's position and nuclear charges, respectively. The first and second term in this equation represents the kinetic energy of the

electrons as well as nuclei, respectively. The following terms are corresponding to the electron-electron repulsion along with nuclei-nuclei repulsion and the electrons-nuclei attractive interaction, respectively.

Schrödinger equation is used to describe any problem, but it cannot be solved precisely for system which is containing more than one electron. To solve many-body systems quantum mechanically, we need to take help of several approximations those are discussed below.

1.4.2. The Born-Oppenheimer (BO) Approximation

The BO approximation states that the nucleus is too heavy in comparison to the electron and moves slowly in comparison to the electrons [144]. So, in the Hamiltonian of a many body system we keep the position of the nucleus fixed and can write the electronic and nuclear parts separately. By applying Born-Oppenheimer approximation reduced Hamiltonian can be described as shown in equation (1.5).

$$\hat{H} = -\frac{\hbar^2}{2m_e} \sum_i \nabla_i^2 + \frac{1}{2} \sum_{i \neq j} \frac{e^2}{|r_i - r_j|} - \frac{1}{2} \sum_{I \neq J} \frac{Z_I Z_J e^2}{|R_I - R_J|} - \sum_{i,I} \frac{Z_I e^2}{|r_i - R_I|} \quad (1.5)$$

The first term in the Hamiltonian relates to the electrons' kinetic energy, and the following next three terms signify the potential energy because of the electron-electron and electron-nuclei and nuclei-nuclei interactions. After applying the BO approximation also, the wave function is still complicated for many body systems. Therefore, there should be further modification of the above-mentioned equation to obtain the properties of many body systems. In this respect, Hartree-Fock Theory came into the picture.

1.4.3. Hartree-Fock Theory (HF Theory)

The HF theory calculates the single reference Slater determinant using self-consistent methods. According to HF theory, motion of a single electron is not dependent on the motions of other electrons and can be described as a one electron wave function. The beginning of Hartree-Fock method is the Hartree approximation that states that the multi-electron wavefunction can

be replaced by the product of the corresponding single-electron wavefunctions.

$$|\Psi(r_1, r_2, \dots, r_N)\rangle \approx \psi_1(r_1)\psi_2(r_2) \dots \psi_N(r_N) \quad (1.6)$$

But the straightforward Hartree wavefunction fails to satisfy antisymmetric condition for Fermions. For a two-electron system, the antisymmetry principle can be satisfied by the wave function like following type (1.7).

$$\Psi(x_1, x_2) = \frac{1}{\sqrt{2}} [\chi_1(x_1)\chi_2(x_2) - \chi_1(x_2)\chi_2(x_1)] \quad (1.7)$$

In case of N electron systems, it can be described by a determinant known as Slater determinant (1.8).

$$\Psi_{el} = \frac{1}{\sqrt{n!}} \begin{vmatrix} \varphi_1(1) & \varphi_2(1) & \dots & \varphi_n(1) \\ \varphi_1(2) & \varphi_2(2) & \dots & \varphi_n(2) \\ \dots & \dots & \dots & \dots \\ \varphi_1(n) & \varphi_2(n) & \dots & \varphi_n(n) \end{vmatrix} \quad (1.8)$$

Now we can simplify the Hamiltonian as,

$$\hat{H} = H^c + \frac{1}{2} \sum_{i \neq j} \frac{e^2}{|r_i - r_j|} \quad (1.9)$$

Where, the following core part of the Hamiltonian operator (\hat{H}^C) is exactly solvable.

$$\hat{H}^C = -\frac{\hbar^2}{2m_e} \sum_i \nabla_i^2 - \sum_{i,l} \frac{Z_l e^2}{|r_i - R_l|} \quad (1.10)$$

The second part that accounts the repulsion of electrons which cannot be solved exactly. Hartree-Fock (HF) theory considers the electron-electron repulsion in an average way, by considering independent motion of electrons. Therefore, by considering the Slater determinant one can obtain the state having lowest energy and optimization of the orbital using variation theorem leads to the lowest possible energy. The form of the HF equation is as follows (1.11):

$$f_i \chi_i = \epsilon_i \chi_i \quad (1.11)$$

In the above equation, χ_i is the eigen function and ϵ_i is the eigen value of the operator f_i , respectively. The energy eigen values are called as orbital energy of the system. The operator f_i is known as Fock operator which behaves like a one electron operator.

$$f_i = \hat{H}^C + V_{HF}(i) \quad (1.12)$$

where, V_{HF} is the second term in the Hamiltonian that describes the electron-electron repulsion in average.

$$V_{\text{HF}}(\mathbf{i}) = \sum_{i,l} \frac{z_i e^2}{|\mathbf{r}_i - \mathbf{r}_l|} \quad (1.13)$$

The HF potential can be expanded in terms of coulomb operator J_i and exchange operator K_i according to the following equation (1.14).

$$V_{\text{HF}}(\mathbf{i}) = \sum_i [J_i(\mathbf{x}_i) - K_i(\mathbf{x}_i)] \quad (1.14)$$

Where J_i signifies the classical repulsion among electrons and K_i denotes the exchange interaction which is generated from the anti-symmetric wave function nature. If one knows the eigen function χ_i then HF potential can be calculated using an iterative self-consistent field method starting with an arbitrary value of $V_{\text{HF}}(\mathbf{i})$. HF theory calculates the energy and other properties from the wave function of a system. For larger systems the wave function becomes too much complicated as it accounts three spatial as well as a spin coordinate for all the electrons. Hence, due to larger number of variables it is very difficult to apply HF theory on complex molecules.

1.4.4. Density Functional Theory (DFT)

DFT considers probability density $[\rho(x, y, z)]$ of electron to calculate the energy and properties of a system. The idea was first suggested by Thomas-Fermi in case of non-interacting gas molecules. Later, Hohenberg and Kohn proved this idea in their theorem known as Hohenberg-Kohn theorems [145,146].

1.4.4.1. The Hohenberg-Kohn theorems

(i) The first theorems says that for N electron system the energy of ground state is the electron density $\rho(\mathbf{r})$ functional of the interacting electrons moving under the external potential of $V_{\text{ext}}(\mathbf{r})$.

$$\text{Which signifies, } E = E_v[\rho] \quad (1.15)$$

In the above equation (1.15),

$$E_v[\rho] = T[\rho] + V_{\text{ee}}[\rho] + V_{\text{ext}}[\rho] \quad (1.16)$$

$T[\rho]$ and $V_{ee}[\rho]$ denotes kinetic energy and electron-electron interaction potential functional respectively. Whereas V_{ext} is the external potential given as,

$$V_{\text{ext}} = \int u(\mathbf{r})\rho(\mathbf{r})d\mathbf{r} = \sum_{A=1}^N \frac{Z_A}{r_{iA}} \quad (1.17)$$

(ii) The second theorem declares that the energy of ground state of the system can be obtained variationally and the electron density which minimizes the total energy is the correct ground-state density. Moreover, minimum energy can be achieved by considering the exact density of ground state.

The kinetic energy and interaction potential functionals can be established by decreasing the energy with respect to variation in $\rho(\mathbf{r})$.

$$E_v[\rho] \geq E_v[\rho_0] \quad (1.18)$$

But in these theorems, there was no proper way to calculate the density of ground state for a system. Later Kohn and Sham formulated the Kohn-Sham equation after which the actual application of Hohenberg-Kohn theorems begins to carry out density functional theory calculations.

1.4.4.2. Kohn-Sham Formulation

Kohn and Sham developed new ideas for the application of Hohenberg-Kohn theorems. According to this formalism, the difficulties in many-body problem can be reduced to non-interacting particle problem. Where, the single particles can be defined by an effective potential $V(\mathbf{r}_i)$, termed as Kohn-Sham potential. The total ground state energy can be described as:

$$E[\rho(\mathbf{r})] = T_0[\rho(\mathbf{r})] + \frac{1}{2} \iint \frac{\rho(\mathbf{r})\rho(\mathbf{r}')d\mathbf{r}d\mathbf{r}'}{|\mathbf{r}-\mathbf{r}'|} + \int V_{\text{ext}}(\mathbf{r})\rho(\mathbf{r})d\mathbf{r} + E_{\text{xc}}[\rho(\mathbf{r})] + E_{\text{II}} \quad (1.19)$$

Where, the first term denotes non-interacting electrons kinetic energy; the second term describes the classical electron-electron Coulomb interaction (Hartree energy); the third term is the interaction potential between valence and core electrons; the fourth term considers all non-classical many-body effects between electrons called exchange-correlation interaction. The last term describes the nuclei-nuclei interaction. Now, the above equation can

also be written as,

$$\left[-\frac{1}{2}\nabla^2 + V_{\text{eff}}(r)\right]\Psi_i(r) = E_i\Psi_i(r) \quad (1.20)$$

Where $\Psi_i(r)$ stands for the Kohn-Sham orbitals instead of wave function, whereas V_{eff} can be represented as

$$V_{\text{eff}} = V_{\text{Hartree}} + V_{\text{ext}} + V_{\text{xc}} \quad (1.21)$$

Hence, the effective potential can be described by external potential, Coulomb interaction and the exchange correlation interaction. That means, if one knows the exchange correlation potential then it is possible to solve many-body problem. However, the exchange correlation interaction is not easy to solve therefore different approximations are used to solve this problem. These approximations are broadly used for the simulation of molecular as well as solid state problems [147].

1.4.4.3. Exchange-correlation Functional

As the exchange correlation potential is not easy to solve, we need to take help of some approximate methods to carry out DFT calculations. We can divide the exchange-correlation functional $E_{xc}(\rho(r))$ into two parts namely exchange and correlation part, can be defined as:

$$E_{xc}(\rho(r)) = E_x(\rho(r)) + E_c(\rho(r)) \quad (1.22)$$

The exchange correlation energy functional $E_{xc}(\rho(r))$ can be approximated by some local functional based on the electron density.

1.4.4.4. Local Density Approximation (LDA)

LDA is the oldest exchange correlation functional proposed by Hohenberg and Kohn. Where they approximated the exchange correlation energy locally from homogeneous electron gas of identical density [148,149]. [5,6] Hence, LDA depends only on the local density i.e., the exchange correlation energy can be written as,

$$E_{xc}^{LDA} = \int \rho(r) \varepsilon_{xc}(\rho) dr \quad (1.23)$$

$$u_{xc} = \varepsilon_{xc}[\rho(r)] + \rho(r) \frac{\partial \varepsilon_{xc}[\rho]}{\partial \rho} \quad (1.24)$$

where $\varepsilon_{xc}(\rho)$ is the exchange-correlation energy density related to the homogeneous electron gas of density $\rho(r)$. Although, LDA produces quite good results for solids it is not a good approximation for molecules.

1.4.4.5. Generalized Gradient Approximation (GGA)

GGA is the mostly used exchange correlation functional in recent days. Along with electron density it accounts the gradient of electron density that leads the exchange correlation energy to,

$$E_x^{GGA}[\rho^\alpha, \rho^\beta] = \int f[\rho^\alpha(r), \rho^\beta(r), \nabla\rho^\alpha(r), \nabla\rho^\beta(r)]dr \quad (1.25)$$

These functional significantly reduces the over binding error in LDA.

Some commonly used important GGA functionals are Perdew, Burke and Ernzerhof (PBE), Perdew and Wang (PW91), PBEsol and revised PBE (RPBE) [150-152].

1.4.4.6. Hybrid Functionals

Hybrid functionals are a class of functional that combine HF exchange with GGA and produces significantly improved results compared to GGA. The exchange part can be fully estimated by HF method, as follows:

$$E_x^{Hybrid} = c_{HF}E_x^{HF} + c_{DFT}E_{xc}^{DFT} \quad (1.26)$$

Hybrid functionals are very commonly used for molecules in quantum chemistry. Among them B3LYP is most widely used one have the form

$$E_x^{B3LYP} = (1 - c_0 - c_x)E_x^{LSDA} + c_0E_x^{HF} + c_xE_x^{B88} + (1 - c_c)E_c^{VWN} + c_cE_c^{LYP} \quad (1.27)$$

where c's are constants ($c_0 = 0.20$, $c_x = 0.72$ and $c_c = 0.81$) to provide best fitting of the experimental atomization energies.

1.4.5. Basis Sets

Basis sets are a set of one particle functions those applied to define the molecular orbitals of any system. There is a set of basis functions for each and every atom in a molecule to guess its orbital. On the basis of the functional used to define, basis sets can be categorized as (i) Slater type (STO) (ii) Gaussian type (GTO) (iii) Effective core potential (ECP) (iv)

Plane wave and so on.

(i) Slater type orbitals (STO): Here Slater type orbitals are used to represent the atomic orbitals. [153]. The form of STO is like hydrogen atom orbitals.

$$\lambda_{\zeta,n,l,m}(r, \theta, \varphi) = Nr^{(n-1)}e^{-\zeta r}Y_l^m(\theta, \varphi) \quad (1.28)$$

where ζ is the orbital exponent mainly controls the width of the orbital, $\frac{Z-S}{a_0} = \frac{Z_{eff}}{a_0}$, S, N is the screening and normalization constant, respectively. The $Y_l^m(\theta, \varphi)$ is the wave function's angular part (spherical harmonics) and r, θ, φ are the three polar coordinates. The STO's are good for the calculation of small molecules but is difficult to afford for large molecules due to high computational cost.

(ii) Gaussian type orbitals (GTO): Gaussian type orbitals [154] were developed by Boys, can be represented as,

$$g_{\zeta,l_x,l_y,l_z}(x, y, z) = Nx^{l_x}y^{l_y}z^{l_z}e^{-\zeta r^2} \quad (1.29)$$

where ζ represents the orbital exponent that controls the width of the orbital and these are primitive Gaussians basis sets. Linear combinations of such primitive Gaussians leads to the contracted Gaussian functions χ_u such that,

$$\chi_u = \sum_p d_{up}g_p \quad (1.30)$$

Where, d_{up} is the contraction function and g_p is the primitive gaussian. But Gaussian functions do not look much like an atomic orbital. More specifically, they are flat in nature near the nucleus that is at $r=0$, and decreases more quickly for large values of r . To overcome this problem, a set of GTOs are used to mimic a STO. These types of orbitals are termed as STO-KG basis set. In STO-KG, K is the considered number of primitive Gaussian functions used to mimic an STO. These are established by Noble laureate John A. Pople and popularized by Gaussian programs. In a molecule the valence orbitals are engaged in the respective chemical bonding and each valence atomic orbital is illustrated in better way by

increment of the basis functions. In this case, split valence basis sets are those where valence and core electrons are treated separately. Based on the considered number of basis functions utilized for the valence atomic orbital it is called as double zeta (DZ), triplet zeta (TZ) etc. With the influence of other atom, the orbital shape can change which called polarization. To account these effects p- functions for H as well as d- functions for heavy atoms can be added. These are called polarized basis set. Diffuse functions are need to add for anions where electrons are far away from nucleus or high electronegative atoms with a large electron density. By considering all of these, the overall depiction of Pople basis set can be as follows:

$$k - nlm + +G(d, p) \text{ or } k - nlm + +G ** \quad (1.31)$$

Thom Dunning figured out that highly correlated systems need “correlation consistent” basis sets those optimized using correlated wavefunctions. Such examples are, cc-pVXZ type basis sets (X = D, T, Q).

Ahlrichs and co-workers has developed another variety of basis sets termed as Def2-basis [155]. Types of these basis stes are def2-SV(P), def2-TZV to def2-QZVPP.

(iii) Effective core potential (ECP): For the heavier elements the number of electrons is too high that demands huge computational cost. To reduce the computational time the core electrons in heavier elements can treated differently. As core orbital energies do not affect much by chemical bonding, they can be described by average potential [156]. The ECP is a pseudo potential which is shown in (1.32).

$$\text{ECP}(r) = \sum_{i=1}^M d_i r^{n_i} e^{-\zeta_i r^2} \quad (1.32)$$

Here d_i is the coefficient for every term, r is the distance of electrons from the nucleus and ζ_i is the exponent of the i^{th} term. The ECP's take less computational time because basis functions are considerably decreased due to the core potential and considers only valence electrons of the element. In general, ECPs are extensively applied to transition metals. There are several ECPs and among all Los Alamos National Laboratory double-zeta

(LANL2DZ) basis set is extensively used [157].

(iv) Plane wave: These are delocalized periodic basis functions where the quality is controlled by a single parameter cut-off energy. The functional form is shown in equation (1.33) [158].

$$\chi_i(r) = e^{ikr} \quad (1.33)$$

where k represents the momentum vector where r run through Bravais lattice. In all the cases, the perfect choice of basis set is highly essential during quantum mechanical methods. By considering this basis set one should be conscious about the basis set superposition error (BSSE). This is because of the extended larger basis functions explanation for the wave function of the system than that of the component. One of the important strategies to resolve this problem is the counterpoise correction scheme proposed by Boys and Bernardi [159].

1.4.6. Projector Augmented Wave (PAW) Method

The interaction between electron and nuclei are different for the electrons residing in core and valence orbital. This happens due to different distance of core and valence electrons with nuclei. As a result, the core electron wave functions oscillate rapidly but the valence electron wave functions are smooth. For the electrons outside the augmented region, we can consider the plane wave basis sets. But it is very difficult to describe the core electron wave functions with plane waves due to high computational cost. Hence, a partial wave expansion is used to describe the core electrons and it converts the rapidly oscillating wave functions to smoother one. This technique is based on the linear transformation operator (T) and termed as PAW method [160-163]. The all-electron wave function Ψ_n to be replaced by a pseudo wave function $\tilde{\Psi}_n$ such that

$$|\Psi_n\rangle = T|\tilde{\Psi}_n\rangle \quad (1.34)$$

Where, T is the transformation operator and both $|\Psi_n\rangle$ and $|\tilde{\Psi}_n\rangle$ can be described by a linear combination of partial waves for each augmentation regions.

$$|\Psi_n\rangle = \sum_i c_i |\phi_i\rangle \quad (1.35)$$

$$|\tilde{\Psi}_n\rangle = \sum_i c_i |\tilde{\phi}_i\rangle \quad (1.36)$$

The transformation operator, T is defined as

$$T = 1 + \sum_i (|\phi_n\rangle - |\tilde{\phi}_n\rangle) \langle \tilde{p}_i| \quad (1.37)$$

Here $\langle \tilde{p}_i|$ is called projection function. Hence, pseudopotential helps to get rid from the problem of core and valence electrons. However, PAW is combined with ultra-soft pseudopotentials and augmented-plane-wave.

1.4.7. Dispersion Corrected Density Functional Theory

Although, KS-DFT is extensively used from molecules to condensed phases it does not include the London part of the dispersion interaction which is a long ranged electron correlation effects. According to MP2 theory, coulombic interaction and exchange interactions are build up with the electron transition density of interacting fragments A and B.

$$E_{Disp}^{(2)} = \sum_{ia} \sum_{jb} \frac{(ia|jb)[(ia|jb)-(ja|ib)]}{\epsilon_a + \epsilon_b - \epsilon_i - \epsilon_j} \quad (1.38)$$

This is a sum of single particle hole excitations for orbitals $i \rightarrow a$ which is localized on A and $j \rightarrow b$ which is localized on B. Here, $(ia|jb)$ is a two-electron integral whereas, ϵ 's are the corresponding orbital energies. As the standard KS-DFT does not consider such pseudo excitations, they are unable to account the $-\frac{C_6}{R^6}$ dependence [164].

Most of the dispersion correction methods uses empirical corrections. The most widely used dispersion correction method is the one formulated by Stefan Grimme [165]. The general form of Grimme's DFT-D_n method where the dispersion energy (atom pair wise sum over $-\frac{C_6}{R^6}$ potentials) is add up to the Kohn-Sham energy is,

$$E_{Disp}^{DFT-D} = -\sum_{AB} \sum_{n=6,8,10,\dots} S_n \frac{C_n^{AB}}{R_{AB}^n} f_{damp}(R_{AB}) \quad (1.39)$$

where the sum denoted over all atom pairs in the considered system, C_n^{AB} is the dispersion coefficient in n^{th} order of atom pairs AB, whereas R_{AB} is their internuclear distances. Moreover, the S_n is the scaling factor which is generally utilized to alter the correction of repulsive actions of the chosen DFT [166]. The $f_{damp}(R_{AB})$ is the damping function.

In our thesis work we have mainly used Grimme's DFT-D3 dispersion correction which includes triplets of atoms to account for three body effects. Although dispersion correction does not influence much to the molecular properties, but it is sensitive for the geometry of the system. As dispersion correction significantly influence the forces acting on the atoms, the optimized geometries with and without dispersion differ significantly.

1.4.8. Other Computational Tools

In this thesis, I have used several other computational tools and techniques to understand the properties of the molecules and materials, e.g., Natural Bond Orbital (NBO), Noncovalent Interaction (NCI) Plots for molecules and Ab initio molecular dynamics (AIMD) simulation, Bader charge analysis, phonon dispersion, Nudged Elastic Band (NEB) Mechanical Properties etc. All of these have been discussed in the following sections in for more detail.

1.4.8.1. Natural Bond Orbital (NBO)

Natural bond orbital analysis shows the Lewis structure of the optimized geometry. From the Lewis structure one can understand the hybridisation nature and weight of each atom within the localized electron pair [167]. This type of analysis gives the stresses of intermolecular orbitals within the complex. All the possible interactions among occupied donor parts and vacant acceptor have been considered [168]. A second-order perturbation theory to predict the Natural bond orbitals and their energetic importance

[169]. For every donor and acceptor (i and j) NBO stabilisation energy (E) is associated with the delocalisation of the electrons between i and j. The equation for the stabilisation energy is as follow [170]:

$$E = q_i \frac{(F_{i,j})^2}{\varepsilon_j - \varepsilon_i} \quad (1.40)$$

1.4.8.2. Non-covalent Interaction (NCI) Plots

Noncovalent interactions are measured depending upon the electron density and its derivatives. The NCI study uses the relation between reduced density (s) and the electron density (ρ) [171].

$$s = \frac{1}{2(3\pi^2)^{1/3}} \frac{|\nabla\rho|}{\rho^{4/3}} \quad (1.41)$$

The plot of s versus ρ gives distinguishing peaks at low density values when there are noncovalent interactions because of the annihilation of density gradient at these considered points. For different values of ρ different kind of interactions are observed. Peaks corresponding to dispersion interactions comes at low density values ($\rho < 0.01$ a.u.), and stronger hydrogen bonds are observed at higher densities ($0.01 < \rho < 0.05$ a.u.) [172]. To understand the nature of the interaction as attractive or repulsive we need to account the accumulation and depletion of electron density in the plane which is directly perpendicular to the interaction i.e., mainly described by the second eigenvalue λ_2 . Here, the sign of λ_2 indicates the nature of interaction. Hence, the gradient is plotted with product of sign of λ_2 as well as electron density function. The value of $(\lambda_2)\rho$ is also used to show different types of noncovalent interactions by coloring the 3-D space of the molecule [173].

1.4.8.3. Nudged Elastic Band (NEB) Method

NEB method is implemented to illustrate the kinetic nature and diffusion pathways of a reaction. This method is broadly used in the field of

computational chemistry and condensed matter physics. This technique finds the saddle point of the minimum energy path (MEP) between the reactant and product of a reaction. Here, the harmonic approximation of transition state theory (hTST) [174] is used and the rate constant of the reaction for the transition around the saddle points is denoted as follows,

$$k^{hTST} = \frac{\prod_i^{3N} v_i^{init}}{\prod_i^{3N-1} v_i^\ddagger} e^{\left[-\frac{E^\ddagger - E^{init}}{k_B T}\right]} \quad (1.42)$$

Where, E^\ddagger and E^{init} are the energies of the saddle point as well as initial state (reactant), and v^\ddagger and v^{init} are the normal mode of frequencies for saddle point and the initial state, respectively. In general, NEB optimizes a number of intermediates within reactant and product. This intermediate optimization is done by adding spring forces along the band between images. In our calculations, we have used a code developed by Henkelmann for the formation of the images [175].

1.4.8.4. *Ab initio* Molecular Dynamics (AIMD)

AIMD is a useful computational tool to check the thermal stability of the studied materials. Where in classical molecular dynamics (CMD) atomic forces are generated from Newton's equation of motion, AIMD considers those calculated from DFT calculations [176]. As a consequence, AIMD calculations are extremely costly and are limited to a system having only few hundreds of atoms. In our thesis work, we have used canonical ensemble to carry out the AIMD simulations. System temperature was controlled by Nosé thermostat model [177].

1.4.8.5. Bader Charge Analysis

This method is used to calculate the electronic charge on each atom in a molecule or crystal. This technique uses the Bader partitioning scheme [178] to divide molecules into atoms and calculate individual charges. Here

the definition of an atom is completely based on the electronic charge density. In this study, zero-flux surfaces which refers to the two-dimensional surface where the charge density is minimum along the perpendicular to the surface determine the partitioning electronic density of the materials. The charge distribution can be utilized for the determination of multipole moments of interacting atoms and/or molecules. In this thesis work, we have used an algorithm developed by the Henkelman group [179]. The algorithm is offered for carrying out the decomposition of electronic charge density with in the atomic contributions.

1.4.8.6. Phonon Dispersion

Lattice vibrations in a crystal lattice behaves both as particles and as waves. This quantum particle is described as phonon. To understand the dynamical behavior of crystal lattice we need to calculate the phonon frequencies as a function of their wave vectors. The relationship between frequency of phonon and wave vectors is called phonon dispersion. However, we have used the Phonopy code for the calculation of the phonon modes through the density functional perturbation theory (DFPT) [180,181]. How the system responses to any form of perturbation, that determines the phonon frequency of the lattice. The external perturbations of the system may be calculated using DFT with the addition of some perturbing potential.

1.5. References

1. Gaikwad R., (2018) Carbon Dioxide to Methanol: Stoichiometric Catalytic Hydrogenation under High Pressure Conditions. PhD Dissertation, Institut Català d'Investigació Química
2. I. E. Agency, CO₂ emission from fuel combustion, IECD/IEA, France, (2016), pp. 166.
3. Lemay L. (2010) Environmental Product Declaration. National ready mixed concrete association. <https://www.nrmca.org/wp-content/uploads/2020/02/EPD10080.pdf>

4. (IEA) International Energy Agency, (2015) Key Trends in CO₂ emissions, Excerpt from: CO₂ emissions from fuel combustion Paris, France
5. Aresta M., Dibenedetto A. (2007), Utilisation of CO₂ as a chemical feedstock: opportunities and challenges. Dalton Trans., 2975-2992 (DOI: 10.1039/B700658F)
6. Wikimedia (2019) www. Wikimedia.org OR: CEC (2019), https://commons.wikimedia.org/wiki/File:Co2_by_fuel_pie_chart.svg
7. Xiaoding X., Moulijn, J.A. (1996), Mitigation of CO₂ by chemical conversion: Plausible chemical reactions and promising products, Energy and Fuels, 10, 305–325 (DOI: 10.1021/ef9501511)
8. Yang H. et al. (2008), Progress in carbon dioxide separation and capture: A review, J. Environ. Sci., 20, 14–27 (DOI: 10.1016/S1001-0742(08)60002-9)
9. Bertau, M., Offermanns, H., Plass, L., Schmidt, F., Wernicke, H.-J., (Eds.), (2013) Methanol: The Basic Chemical and Energy Feedstock of the Future, Springer
10. Babies H.G., Bahr A., Benitz U., Bremer J., Franke D., Meßner J., Rehder S., Rempel H., Schauer M., Schmidt S., Schwarz-Schampera U. (2010) Reserves, Resources and Availability of Energy Resources, Bundesanstalt für Geowissenschaften und Rohstoffe (BGR),
11. Balzani V., Armaroli N. (2011) Energy for a sustainable world: from the oil age to a sun-powered future; Wiley-VCH: Weinheim, Germany, (ISBN: 978-3-527-32540-5)
12. Banerjee R. et al. (2012) Global Energy Assessment: Toward a Sustainable Future; Cambridge University Press: Cambridge, U.K., (ISBN 9781 10700 5198).
13. Elam C.C., Padró C.E.G., Sandrock G., Luzzi A., Lindblad P., Hagen E.F. (2003), Realizing the hydrogen future: The

- International Energy Agency's efforts to advance hydrogen energy technologies, *Int. J. Hydrogen Energy*, 28, 601–607 (DOI: 10.1016/S0360-3199(02)00147-7)
14. Cammack R., Frey M., Robson R. (2002) *Hydrogen as a fuel: Learning from nature*; Taylor & Francis: London, (ISBN 0-415-24242-8)
 15. Armaroli N., Balzani V. (2011), The hydrogen Issue, *ChemSusChem*, 4, 21–36 (DOI: 10.1002/cssc.201000182)
 16. Ströbel R., Garche J., Moseley P.T., Jörissen L., Wolf, G. (2006), Hydrogen storage by carbon materials, *J. Power Sources*, 159, 781–801 (DOI: 10.1016/j.jpowsour.2006.03.047)
 17. Sculley J., Yuan D., Zhou H.-C., (2011), The current status of hydrogen storage in metal-organic frameworks-updated, *Energy Environ. Sci.*, 4, 2721–2735 (DOI: 10.1039/C1EE01240A)
 18. Dong J., Wang X., Xu H., Zhao Q., Li J. (2007), Hydrogen storage in several microporous zeolites, *Int. J. Hydrogen Energy*, 32, 4998–5004 (DOI: 10.1016/j.ijhydene.2007.08.009)
 19. Li H.-W., Yan Y., Orimo S., Züttel A., Jensen C.M. (2011), Recent Progress in Metal Borohydrides for Hydrogen Storage, *Energies*, 4, 185–214 (DOI: 10.3390/en4010185)
 20. Jensen C., Wang Y., Chou M.Y. (2008) *Alanes as Hydrogen Storage Materials*. In *Solid-State Hydrogen Storage: Materials and Chemistry*; Walker, G., Ed.; Woodhead Publishing Series in Electronic and Optical Materials; Woodhead Publishing: Cambridge, U.K., Chapter 14, pp 381–419, (ISBN 978-1-84569-270-4)
 21. Gregory D.H. (2008) *Imides and Amides as Hydrogen Storage Materials*. In *Solid-State Hydrogen Storage: Materials and Chemistry*; Walker, G., Ed.; Woodhead Publishing Series in Electronic and Optical Materials; Woodhead Publishing:

- Cambridge, U.K., Chapter 16, pp 450–477, (ISBN: 978-1-84569-270-4)
22. Peng B., Chen J. (2007), Ammonia borane as an efficient and lightweight hydrogen storage medium, *Energy Environ. Sci.*, 1, 479–483 (DOI: 10.1039/B809243P)
 23. VCI and DECHEMA, (2009) Position Paper: Utilisation and Storage of CO₂, Version 12
 24. Bertau M., Offermanns H., Plass L., Schmidt F., Wernicke H.-J., (Eds.), (2013) *Methanol: The Basic Chemical and Energy Feedstock of the Future*, Springer, (ISBN: 978-3-642-39709-7)
 25. Wei J., Ge Q., Yao R., Wen Z., Fang C., Guo L., Xu H., Sun J. Directly converting CO₂ into a gasoline fuel, *Nat. Commun.*, 8, 1–8. (DOI:10.1038/ncomms15174)
 26. Gao P., Li S., Bu X., Dang S., Liu Z., Wang H., Zhong L., Qiu M., Yang C., Cai J., Wei W., Sun Y. (2017), Direct conversion of CO₂ into liquid fuels with high selectivity over a bifunctional catalyst, *Nat. Chem.*, 9, 1019–1024 (DOI:10.1038/nchem.2794)
 27. Su J., Wang D., Wang Y., Zhou H., Liu C., Liu S., Wang C., Yang W., Xie Z., He M. (2018), Direct Conversion of Syngas into Light Olefins over Zirconium-Doped Indium(III) Oxide and SAPO-34 Bifunctional Catalysts: Design of Oxide Component and Construction of Reaction Network, *ChemCatChem.*, 10, 1536–1541. (DOI:10.1002/cctc.201702054)
 28. Gao P., Dang S., Li S., Bu X., Liu Z., Qiu M., Yang C., Wang H., Zhong L., Han Y., Liu Q., Wei W., Sun Y. (2018), Direct Production of Lower Olefins from CO₂ Conversion via Bifunctional Catalysis, *ACS Catal.*, 8, 571–578 (DOI:10.1021/acscatal.7b02649)
 29. Inui T., Takeguchi T., Kohama A., Tanida K. (1992), Effective conversion of carbon dioxide to gasoline, *Energy Convers. Manag.*, 33, 513–520. (DOI:10.1016/0196-8904(92)90050-7)

30. Jessop P.G., Ikariya T., Noyori R. (1995), Homogeneous Hydrogenation of Carbon Dioxide, *Chem. Rev.*, 95, 2, 259–272 (DOI: 10.1021/cr00034a001)
31. Muhich C.L., Ehrhart B.D., Al-Shankiti I., Ward B.J., Musgrave C.B., Weimer A.W. (2015), A review and perspective of efficient hydrogen generation via solar thermal water splitting, *WIREs Energy and Environment*, 5, 261–287 (DOI: 10.1002/wene.174)
32. McKone J.R., Lewis N.S., Gray H.B. (2013), Will Solar-Driven Water-Splitting Devices See the Light of Day?, *Chem. Mater.*, 26, 1, 407–414 (DOI: 10.1021/cm4021518)
33. Inoue Y., Izumida H., Sasaki Y., Hashimoto H., (1976), Catalytic Fixation of Carbon Dioxide to Formic Acid by Transition-Metal Complexes Under Mild Conditions, *Chem. Lett.*, 5, 863–864 (DOI: 10.1246/cl.1976.863)
34. Sasaki Y.Y., Hashimoto H. (1975), Synthesis of formates from alcohols, carbon dioxide, and hydrogen catalysed by a combination of group VIII transition-metal complexes and tertiary amines, *J. Chem. Soc., Chem. Commun.*, 718–719 (DOI: 10.1039/C39750000718)
35. Graf F., Leitner W. (1992), Direct formation of formic acid from carbon dioxide and dihydrogen using the $[\{\text{Rh}(\text{cod})\text{Cl}\}_2\text{-Ph}_2\text{P}(\text{CH}_2)_4\text{PPh}_2]$ catalyst system, *J. Chem. Soc., Chem. Commun.*, 623–624 (DOI: 10.1039/C39920000623)
36. Jessop P.G., Ikariya T., Noyori R. (1994), Homogeneous catalytic hydrogenation of supercritical carbon dioxide, *Nature*, 368, 231–233 (DOI: 10.1038/368231a0)
37. Munshi P., Main A.D., Linehan J.C., Tai C.C., Jessop P.G., (2002), Hydrogenation of Carbon Dioxide Catalyzed by Ruthenium Trimethylphosphine Complexes: The Accelerating Effect of Certain Alcohols and Amines, *J. Am. Chem. Soc.*, 124, 7963–7971 (DOI: 10.1021/ja0167856)

38. Tanaka R., Yamashita M., Nozaki K., (2009), Catalytic Hydrogenation of Carbon Dioxide Using Ir(III)–Pincer Complexes, *J. Am. Chem. Soc.*, 131, 14168–14169 (DOI: 10.1021/ja903574e)
39. Schmeier T.J., Dobereiner G.E., Crabtree R.H., Hazari N. (2011), Secondary Coordination Sphere Interactions Facilitate the Insertion Step in an Iridium(III) CO₂ Reduction Catalyst, *J. Am. Chem. Soc.*, 133, 9274–9277 (DOI: 10.1021/ja2035514)
40. Filonenko A. Smykowski G.D., Szyja B.M., Li G., Szczygieł J., Hensen E.J.M., Pidko E.A. (2015), Catalytic Hydrogenation of CO₂ to Formates by a Lutidine-Derived Ru–CNC Pincer Complex: Theoretical Insight into the Unrealized Potential, *ACS Catal.*, 5, 1145–1154 (DOI: 10.1021/cs501990c)
41. Filonenko G.A., Hensen E.J.M., Pidko E.A. (2014), Mechanism of CO₂ hydrogenation to formates by homogeneous Ru-PNP pincer catalyst: from a theoretical description to performance optimization, *Catal. Sci. Technol.*, 4, 3474–3485 (DOI: 10.1039/C4CY00568F)
42. Ohnishi Y., Matsunaga T., Nakao Y., Sato H., Sakaki S. (2005), Ruthenium(II)-Catalyzed Hydrogenation of Carbon Dioxide to Formic Acid. Theoretical Study of Real Catalyst, Ligand Effects, and Solvation Effects, *J. Am. Chem. Soc.*, 127, 4021–4032 (DOI: 10.1021/ja043697n)
43. Ohnishi Y., Nakao Y., Sato H., Sakaki S. (2006), Ruthenium(II)-Catalyzed Hydrogenation of Carbon Dioxide to Formic Acid. Theoretical Study of Significant Acceleration by Water Molecules, *Organometallics*, 25, 3352–3363 (DOI: 10.1021/om060307s)
44. Ogo S., Kabe R., Hayashi H., Harada R., Fukuzumi S. (2006), Mechanistic investigation of CO₂ hydrogenation by Ru(II) and Ir(III) aqua complexes under acidic conditions: two catalytic

- systems differing in the nature of the rate determining step, *Dalton Trans.*, 4657–4663 (DOI: 10.1039/B607993H)
45. Yang X. (2011), Hydrogenation of Carbon Dioxide Catalyzed by PNP Pincer Iridium, Iron, and Cobalt Complexes: A Computational Design of Base Metal Catalysts, *ACS Catal.*, 1, 849–854 (DOI: 10.1021/cs2000329)
 46. Tanaka R., Yamashita M., Chung L.W., Morokuma K., Nozaki K. (2011), Mechanistic Studies on the Reversible Hydrogenation of Carbon Dioxide Catalyzed by an Ir-PNP Complex, *Organometallics*, 30, 6742–6750 (DOI: 10.1021/om2010172)
 47. Osadchuk I., Tamm T., Ahlquist M.S.G. (2015), Theoretical Investigation of a Parallel Catalytic Cycle in CO₂ Hydrogenation by (PNP)IrH₃, *Organometallics*, 34, 4932–4940 (DOI: 10.1021/acs.organomet.5b00448)
 48. Hou C., Jiang J., Zhang S., Wang G., Zhang Z., Ke Z., Zhao C., Hydrogenation of Carbon Dioxide Using Half-Sandwich Cobalt, Rhodium, and Iridium Complexes: DFT Study on the Mechanism and Metal Effect, *ACS Catal.*, 4, 2990–2997 (DOI: 10.1021/cs500688q)
 49. Moret S., Dyson P.J., Laurency G. (2014), Direct synthesis of formic acid from carbon dioxide by hydrogenation in acidic media, *Nat. Commun.*, 5, 4017–4023 (DOI: 10.1038/ncomms5017)
 50. Huff C.A., Sanford M.S. (2013), Catalytic CO₂ Hydrogenation to Formate by a Ruthenium Pincer Complex, *ACS Catal.*, 3, 2412–2416 (DOI: 10.1021/cs400609u)
 51. Onishi N., Xu S., Manaka Y., Suna Y., Wang W., Muckerman J. T., Fujita E., Himeda Y. (2015), CO₂ Hydrogenation Catalyzed by Iridium Complexes with a Proton-Responsive Ligand, *Inorg. Chem.*, 54, 5114–5123 (DOI: 10.1021/ic502904q)
 52. Liu C., Xie J., Tian G., Li W., Zhou Q. (2015), Highly efficient hydrogenation of carbon dioxide to formate catalyzed by

- iridium(III) complexes of imine–diphosphine ligands, *Chem. Sci.*, 6, 2928–2931 (DOI: 10.1039/C5SC00248F)
53. Hori Y., Vayenas C.G., White R.E., Gamboa-Aldeco M.E. Eds., (2008) In *Modern Aspects of Electrochemistry*, Springer, New York, Vol. 42, pp 89–189.
54. Hori Y., Kikuchi K., Suzuki S. (1985), Production of CO and CH₄ in Electrochemical Reduction of CO₂ at Metal Electrodes in Aqueous Hydrogencarbonate Solution, *Chem. Lett.*, 14, 1695–1698 (DOI: 10.1246/cl.1985.1695)
55. Hori Y., Kikuchi K., Murata A., Suzuki S. (1986), Production of Methane and Ethylene in Electrochemical Reduction of Carbon Dioxide at Copper Electrode in Aqueous Hydrogencarbonate Solution, *Chem. Lett.*, 15, 897–898 (DOI: 10.1246/cl.1986.897)
56. Sutin N., Creutz C., Fujita E. (1997), Photo-induced generation of dihydrogen and reduction of carbon dioxide using transition metal complexes, *Comments Inorg. Chem.*, 19, 67-92 (DOI: 10.1080/02603599708032729)
57. Clark M.L., Grice K.A., Moore C.E., Rheingold A.L., Kubiak C.P. (2014), Electrocatalytic CO₂ reduction by M(bpy-R)(CO)₄ (M = Mo, W; R = H, tBu) complexes. Electrochemical, spectroscopic, and computational studies and comparison with group 7 catalysts, *Chem. Sci.*, 5, 1894–1900 (DOI: 10.1039/C3SC53470G)
58. Portenkirchner E., Kianfar E., Sariciftci N.S., Knör G. (2014), Two-electron carbon dioxide reduction catalyzed by rhenium(I) Bis(imino)acenaphthene carbonyl complexes, *ChemSusChem*, 7, 1347–1351 (DOI: 10.1002/cssc.201301116)
59. Agarwal J., Fujita E., Schaefer III H.F., Muckerman J.T. (2012), Mechanisms for CO production from CO₂ using reduced rhenium tricarbonyl catalysts, *J. Am. Chem. Soc.*, 134, 5180–5186 (10.1021/ja2105834)

60. Keith J.A., Grice K.A., Kubiak C.P., Carter E.A. (2013), Elucidation of the selectivity of proton-dependent electrocatalytic CO₂ reduction by fac-Re(bpy)(CO)₃Cl, *J. Am. Chem. Soc.*, 135, 15823–15829 (DOI: 10.1021/ja406456g)
61. Smieja J.M., Kubiak C.P. (2010), Re(bipy-tBu)(CO)₃Cl-improved catalytic activity for reduction of carbon dioxide: IR-spectroelectrochemical and mechanistic studies, *Inorg. Chem.*, 49, 9283–9289 (DOI: 10.1021/ic1008363)
62. Chabolla S.A., Machan C.W., Yin J., Dellamary E.A., Sahu S., Gianneschi N.C., Gilson M.K., Tezcan F.A., Kubiak C.P. (2017), Bio-inspired CO₂ reduction by a rhenium tricarbonyl bipyridine-based catalyst appended to amino acids and peptidic platforms: incorporating proton relays and hydrogen-bonding functional groups, *Faraday Discuss.*, 198, 279–300 (DOI: 10.1039/C7FD00003K)
63. Elgrishi N., Chambers M.B., Wang X., Fontecave M. (2017), Molecular polypyridine-based metal complexes as catalysts for the reduction of CO₂, *Chem. Soc. Rev.*, 46, 761–796 (DOI: 10.1039/C5CS00391A)
64. Hawecker J., Lehn J.M., Ziessel R. (1984), Electrocatalytic reduction of carbon dioxide mediated by Re(bipy)(CO)₃Cl (bipy = 2,2'-bipyridine), *J. Chem. Soc., Chem. Commun.*, 328–330 (DOI: 10.1039/C39840000328)
65. Hawecker J., Lehn J.M., Ziessel R. (1986), Photochemical and electrochemical reduction of carbon dioxide to carbon monoxide mediated by (2,2-Bipyridine)tricarbonylchlororhenium(I) and related complexes as homogeneous catalysts, *Helv. Chim. Acta*, 69, 1990–2012. (DOI: 10.1002/hlca.19860690824)
66. Benson E.E., Kubiak C.P., (2012), Structural investigations into the deactivation pathway of the CO₂ reduction electrocatalyst

- Re(bpy)(CO)₃Cl, *Chem. Commun.*, 48, 7374–7376 (DOI: 10.1039/C2CC32617E)
67. Machan C.W., Chabolla S.A., Yin J., Gilson M.K., Tezcan F.A., Kubiak C.P. (2014), Supramolecular assembly promotes the electrocatalytic reduction of carbon dioxide by Re(I) bipyridine catalysts at a lower overpotential, *J. Am. Chem. Soc.*, 136, 14598–14607 (DOI: 10.1021/ja5085282)
68. Grützmacher H. (2008), Cooperating ligands in catalysis, *Angew. Chem. Int. Ed.*, 47, 1814–1818 (DOI: 10.1002/anie.200704654)
69. Van der Vlugt J.I., Reek J.N.H., (2009), Neutral tridentate PNP ligands and their hybrid analogues: versatile non-innocent Scaffolds for homogeneous catalysis, *Angew. Chem. Int. Ed.*, 48, 8832–8846 (DOI: 10.1002/anie.200903193)
70. Dalle K.E., Warnan J., Leung J.J., Reuillard B., Karmel I.S., Reisner E. (2019), Electro- and Solar-Driven Fuel Synthesis with First Row Transition Metal Complexes, *Chem. Rev.*, 119 (4), 2752–2875 (DOI: 10.1021/acs.chemrev.8b00392)
71. Benson E.E., Kubiak C.P., Sathrum A.J., Smieja J.M. (2009), Electrocatalytic and Homogeneous Approaches to Conversion of CO₂ to Liquid Fuels, *Chem. Soc. Rev.*, 38, (1), 89–99 (DOI: 10.1039/B804323J)
72. Ahmed M.E., Rana A., Saha R., Dey S., Dey A. (2020), Homogeneous Electrochemical Reduction of CO₂ to CO by a Cobalt Pyridine Thiolate Complex, *Inorg. Chem.*, 59, 8, 5292–5302 (DOI: 10.1021/acs.inorgchem.9b03056)
73. Shvydkiy N.V., Vyhivskiy O., Nelyubina Y.V., Perekalin D.S. (2019), Design of man- ganese phenol Pi-complexes as Shvo-type catalysts for transfer hydrogenation of ketones, *ChemCatChem*, 11, 1602–1605 (DOI: 10.1002/cctc.201801797)
74. Graf F., Leitner W. (1992), Direct formation of formic acid from carbon dioxide and dihydrogen using the $[\{\text{Rh}(\text{cod})\text{Cl}\}_2]$ -

- Ph₂P(CH₂)₄PPh₂ catalyst system, *J. Chem. Soc., Chem. Commun.*, 623–624 (DOI: 10.1039/C39920000623)
75. Gassner F., Leitner, W. (1993), Hydrogenation of carbon dioxide to formic acid using water-soluble rhodium catalysts, *J. Chem. Soc., Chem. Commun.*, 1465–1466 (DOI: 10.1039/C39930001465).
76. Tanaka R., Yamashita M., Chung L.W., Morokuma K., Nozaki K. (2011), Mechanistic studies on the reversible hydrogenation of carbon dioxide catalyzed by an Ir-PNP complex, *Organometallics*, 30, 6742–6750 (DOI: 10.1021/om2010172)
77. Filonenko G.A., Van Putten R., Schulpen E.N., Hensen E.J.M., Pidko E.A. (2014), Highly efficient reversible hydrogenation of carbon dioxide to formates using a ruthenium PNP-pincer catalyst, *ChemCatChem*, 6, 1526–1530 (DOI: 10.1002/cctc.201402119)
78. Tai C.-C., Chang T., Roller B., Jessop P.G. (2003), High-pressure combinatorial screening of homogeneous catalysts: hydrogenation of carbon dioxide, *Inorg. Chem.*, 42, 7340–7341 (DOI: 10.1021/ic034881x)
79. Federsel C., Boddien A., Jackstell R., Jennerjahn R., Dyson P.J., Scopelliti R., Laurency G., Beller M. (2010), A well-defined iron catalyst for the reduction of bicarbonates and carbon dioxide to formates, alkyl formates, and formamides, *Angew. Chem. Int. Ed.*, 49, 9777–9780 (DOI: 10.1002/anie.201004263)
80. Federsel C., Ziebart C., Jackstell R., Baumann W., Beller M. (2012), Catalytic hydrogenation of carbon dioxide and bicarbonates with a well-defined cobalt dihydrogen complex, *Chem. – Eur. J.*, 18, 72–75 (DOI: 10.1002/chem.201101343)
81. Ziebart C., Federsel C., Anbarasan P., Jackstell R., Baumann W., Spannenberg A., Beller M. (2012), Well-defined iron catalyst for improved hydrogenation of carbon dioxide and bicarbonate, *J. Am. Chem. Soc.*, 134, 20701–20704 (DOI: 10.1021/ja307924a)

82. Langer R., Diskin-Posner Y., Leitus G., Shimon L.J.W., Ben-David Y., Milstein D. (2011), Low-pressure hydrogenation of carbon dioxide catalyzed by an iron pincer complex exhibiting noble metal activity, *Angew. Chem. Int. Ed.*, 50, 9948–9952 (DOI: 10.1002/anie.201104542)
83. Jeletic M.S., Mock M.T., Appel A.M., Linehan J.C. (2013), A cobalt-based catalyst for the hydrogenation of CO₂ under ambient conditions, *J. Am. Chem. Soc.*, 135, 11533–11536 (DOI: 10.1021/ja406601v)
84. Zhang Y., MacIntosh A.D., Wong J.L., Bielinski E.A., Williard P.G., Mercado B.Q., Hazari N., Bernskoetter W.H. (2015), Iron catalyzed CO₂ hydrogenation to formate enhanced by lewis acid co-catalysts, *Chem. Sci.*, 6, 4291–4299 (DOI: 10.1039/C5SC01467K)
85. Bertini F., Glatz M., Gorgas N., Stoöger B., Peruzzini M., Veiros L.F., Kirchner K., Gonsalvi L. (2017), Carbon dioxide hydrogenation catalysed by well-defined Mn(I) PNP pincerhydride complexes, *Chem. Sci.*, 8, 5024–5029 (DOI: 10.1039/C7SC00209B)
86. Bernskoetter W.H., Hazari N. (2013), A Computational Investigation of the Insertion of Carbon Dioxide into Four- and Five-Coordinate Iridium Hydrides, *Eur. J. Inorg. Chem.*, 4032–4041 (DOI: 10.1002/ejic.201300170)
87. Ohkuma T., Ooka H., Hashiguchi S., Ikariya T., Noyori R. (1995), Practical Enantioselective Hydrogenation of Aromatic Ketones, *J. Am. Chem. Soc.*, 117, 2675–2676 (DOI: 10.1021/ja00114a043)
88. Noyori R., Ohkuma T. (2001), Asymmetric Catalysis by Architectural and Functional Molecular Engineering: Practical Chemo- and Stereoselective Hydrogenation of Ketones, *Angew. Chem. Int. Ed.*, 40, 40–73 (DOI: 10.1002/1521-3773(20010105)40:1<40::aid-anie40>3.0.co;2-5)

89. Dub P.A., Henson N.J., Martin R.L., Gordon J.C. (2014), Unravelling the Mechanism of the Asymmetric Hydrogenation of Acetophenone by $[\text{RuX}_2(\text{diphosphine})(1,2\text{-diamine})]$ Catalysts, *J. Am. Chem. Soc.*, 136, 3505–3521 (DOI: 10.1021/ja411374j)
90. Dub P.A., Gordon J.C. (2017), The mechanism of enantioselective ketone reduction with Noyori and Noyori–Ikariya bifunctional catalysts, *Dalton Trans.*, 45, 6756–6781 (DOI: 10.1039/C6DT00476H)
91. Dub P.A., Gordon J.C. (2017), Metal–Ligand Bifunctional Catalysis: The “Accepted” Mechanism, the Issue of Concertedness, and the Function of the Ligand in Catalytic Cycles Involving Hydrogen Atoms, *ACS Catal.*, 7, 6635–6655 (DOI: 10.1021/acscatal.7b01791)
92. Dub P.A. Scott B.L. Gordon J.C. (2017), Why Does Alkylation of the N–H Functionality within M/NH Bifunctional Noyori-Type Catalysts Lead to Turnover?, *J. Am. Chem. Soc.*, 139, 1245–1260 (DOI: 10.1021/jacs.6b11666)
93. Dub P.A., Gordon J.C. (2018), The role of the metal-bound N–H functionality in Noyori-type molecular catalysts, *Nat. Rev. Chem.*, 2, 396–408 (10.1038/s41570-018-0049-z)
94. Bruneau-Voisine A., Wang D., Dorcet V., Roisnel T., Darcel C., Sortais J. (2017), Transfer Hydrogenation of Carbonyl Derivatives Catalyzed by an Inexpensive Phosphine-Free Manganese Precatalyst, *Org. Lett.*, 19, 3656–3659 (DOI: 10.1021/acs.orglett.7b01657)
95. Tominaga K., Sasaki Y., Watanabe T., Saito M. (1995), Homogeneous Hydrogenation of Carbon Dioxide to Methanol Catalyzed by Ruthenium Cluster Anions in the Presence of Halide Anions, *Bull. Chem. Soc. Jpn.*, 68, 2837–2842 (DOI: 10.1246/bcsj.68.2837)

96. Bai S-T., Smet G.D., Liao Y., Sun R., Zhou C., Beller M., Maes B.U.W., Sels B.F., (2021), Homogeneous and heterogeneous catalysts for hydrogenation of CO₂ to methanol under mild conditions, *Chem. Soc. Rev.*, 50, 4259-4298 (DOI: 10.1039/D0CS01331E)
97. Huff C.A., Sanford M.S. (2011), Cascade Catalysis for the Homogeneous Hydrogenation of CO₂ to Methanol, *J. Am. Chem. Soc.*, 133, 18122–18125 (DOI: 10.1021/ja208760j)
98. Balaraman E., Gunanathan C., Zhang J., Shimon L.J.W., Milstein D. (2011), Efficient hydrogenation of organic carbonates, carbamates and formates indicates alternative routes to methanol based on CO₂ and CO, *Nat. Chem.*, 3, 609–614 (DOI: 10.1038/nchem.1089)
99. Zhang L., Han Z., Zhao X., Wang Z., Ding K., (2015), Highly Efficient Ruthenium-Catalyzed N-Formylation of Amines with H₂ and CO₂, *Angew. Chem. Int. Ed.*, 54, 6186–6189 (DOI: 10.1002/ange.201500939)
100. Kar S., Sen R., Goeppert A., Prakash G.K.S. (2018), Integrative CO₂ Capture and Hydrogenation to Methanol with Reusable Catalyst and Amine: Toward a Carbon Neutral Methanol Economy, *J. Am. Chem. Soc.*, 140, 1580–1583 (DOI: 10.1021/jacs.7b12183)
101. Kothandaraman J., Goeppert A., Czaun M., Olah G., Prakash G.K.S. (2016), Conversion of CO₂ from Air into Methanol Using a Polyamine and a Homogeneous Ruthenium Catalyst, *J. Am. Chem. Soc.*, 138, 778–781 (DOI: 10.1021/jacs.5b12354)
102. Kar S., Goeppert A., Kothandaraman J., Prakash G.K.S. (2017), Manganese-Catalyzed Sequential Hydrogenation of CO₂ to Methanol via Formamide, *ACS Catal.*, 7, 6347–6351 (DOI: 10.1021/acscatal.7b02066)

103. Kar S., Kothandaraman J., Goeppert A., Prakash G.K.S. (2018), Advances in catalytic homogeneous hydrogenation of carbon dioxide to methanol, *J. CO₂ Util.*, 23, 212–218 (DOI: 10.1016/j.jcou.2017.10.023)
104. Arshadi S., Banaei A., Ebrahimiasl S., Monfared A., Vessally E. (2019), Solvent-free incorporation of CO₂ into 2-oxazolidinones: a review, *RSC Adv.*, 9, 19465–19482 (DOI: 10.1039/C9RA00551J)
105. Lin P. H., Wong D.S.H. (2014), Carbon dioxide capture and regeneration with amine/alcohol/water blends, *Int. J. Greenhouse Gas Control*, 26, 69–75 (DOI: 10.1016/j.ijggc.2014.04.020)
106. Sheng Z.Z., Huang M.M., Xue T., Xia F., Wu H.H. (2020), Alcohol amine-catalyzed CO₂ conversion for the synthesis of quinazoline-2,4-(1H,3H)-dione in water, *RSC Adv.*, 10, 34910–34915 (DOI: 10.1039/D0RA06439D)
107. Khusnutdinova J.R., Garg J.A., Milstein D. (2015), Combining Low-Pressure CO₂ Capture and Hydrogenation to Form Methanol, *ACS Catal.*, 5, 2416–2422 (DOI: 10.1021/acscatal.5b00194)
108. Foo S.W., Takada Y., Yamazaki Y., Saito S. (2013), Dehydrative synthesis of chiral oxazolidinones catalyzed by alkali metal carbonates under low pressure of CO₂, *Tetrahedron Lett.*, 54, 4717–4720 (DOI: 10.1016/j.tetlet.2013.06.100)
109. Han Z. Rong L., Wu J., Zhang L., Wang Z., Ding K. (2012), Catalytic Hydrogenation of Cyclic Carbonates: A Practical Approach from CO₂ and Epoxides to Methanol and Diols, *Angew. Chem. Int. Ed.*, 51, 13041–13045 (DOI: 10.1002/ange.201207781)
110. Waugh, K.C. (1992) Methanol Synthesis, *Catal. Today*, 15, 51–75 (DOI: 10.1016/0920-5861(92)80122-4)
111. Pan F., Zhao H., Deng W., Feng X., Li Y. (2018), A Novel N,Fe-Decorated Carbon Nanotube/Carbon Nanosheet Architecture for Efficient CO₂ Reduction, *Electrochim. Acta*, 273, 154–161 (DOI: 10.1016/j.electacta.2018.04.047)

112. Chai G.-L. Guo Z.-X. (2017), Highly Effective Sites and Selectivity of Nitrogen-Doped Graphene/CNT Catalysts for CO₂ Electrochemical Reduction, *Chem. Sci.*, 7, 1268–1275 (DOI: 10.1039/C5SC03695J)
113. Li P., Wang F., Wei S., Li X., Zhou Y. (2017), Mechanistic insights into CO₂ reduction on Cu/Mo-loaded two-dimensional g-C₃N₄(001), *Phys. Chem. Chem. Phys.*, 19, 4405–4410 (DOI: 10.1039/C6CP08409E)
114. Han N., Wang Y., Yang H., Deng J., Wu J., Li Y., Li Y. (2018) Ultrathin Bismuth Nanosheets from in Situ Topotactic Transformation for Selective Electrocatalytic CO₂ Reduction to Formate, *Nat. Commun.*, 9, 1320–1328 (DOI: 10.1038/s41467-018-03712-z)
115. Liu G., Willcox D., Garland M., Kung H.H. (1984), The rate of methanol production on a copper-zinc oxide catalyst: The dependence on the feed composition, *J. Catal.*, 1984, 90, 139–146 (DOI: 10.1016/0021-9517(84)90094-0)
116. Chinchin G.C., Denny P.J., Parker D.G., Spencer M.S., Whan D.A., (1987), Mechanism of methanol synthesis from CO₂/CO/H₂ mixtures over copper/zinc oxide/alumina catalysts: use of ¹⁴C-labelled reactants, *Appl. Catal.*, 30, 333–338 (DOI: 10.1016/S0166-9834(00)84123-8)
117. Lunkenbein T., Schumann J., Behrens M., Schlegel R., Willinger M.G., (2015), Formation of a ZnO Overlayer in Industrial Cu/ZnO/Al₂O₃ Catalysts Induced by Strong Metal–Support Interactions, *Angew. Chem., Int. Ed.*, 54, 4544–4548 (DOI: 10.1002/ange.201411581)
118. Behrens M., et al. (2012), The Active Site of Methanol Synthesis over Cu/ZnO/Al₂O₃ Industrial Catalysts, *Science*, 336, 893–897 (DOI: 10.1126/science.1219831)

119. Kuld S., Thorhauge M., Falsig H., Elkjær C.F., Helveg S., Chorkendorff I., Sehested J. (2016), Quantifying the promotion of Cu catalysts by ZnO for methanol synthesis, *Science*, 352, 969–974 (DOI: 10.1126/science.aaf0718)
120. Kattel S., Ramı́rez P.J., Chen J.G., Rodriguez J.A., Liu P. (2017), Active sites for CO₂ hydrogenation to methanol on Cu/ZnO catalysts, *Science*, 355, 1296–1299 (DOI: 10.1126/science.aal3573)
121. Back S., Lim J., Kim N.-Y., Kim Y.-H. Jung Y. (2017), Single-atom catalysts for CO₂ electroreduction with significant activity and selectivity improvements, *Chem. Sci.*, 8, 1090–1096 (DOI: 10.1039/C6SC03911A)
122. Zhao Z., Lu G. (2019), Cu-Based Single-Atom Catalysts Boost Electroreduction of CO₂ to CH₃OH: First-Principles Predictions, *J. Phys. Chem. C*, 123, 4380–4387 (DOI: 10.1021/acs.jpcc.8b12449)
123. Wang Z.L. (2004), Nanostructures of zinc oxide, *Mater. Today*, 7, 26–33 (DOI: 10.1016/S1369-7021(04)00286-X)
124. O'zgu'r U., Alivov Y.I., Liu C., Teke A., Reshchikov M.A., Dog'an S., Avrutin V., Cho S.-J., Morkoç H. (2005), A comprehensive review of ZnO materials and devices, *J. Appl. Phys.*, 98, 041301 (DOI: 10.1063/1.1992666)
125. Dent A.L., Kokes R.J. (1969), Hydrogenation of ethylene by zinc oxide. I. Role of slow hydrogen chemisorption, *J. Phys. Chem.*, 73, 3772–3780 (DOI: 10.1021/j100845a035)
126. Liu X., Ye L., Liu S., Li Y., Ji X. (2016), Photocatalytic Reduction of CO₂ by ZnO Micro/nanomaterials with Different Morphologies and Ratios of {0001} Facets, *Sci. Rep.*, 6, 38474 (DOI: 10.1038/srep38474)
127. Wu S., Yuan N., Xu H., Wang X., Schelly Z.A. (2006), Synthesis and bandgap oscillation of uncapped, ZnO clusters by

- electroporation of vesicles, *Nanotechnology*, 17, 4713–4718 (DOI: 10.1088/0957-4484/17/18/031)
128. Dmytruk A., Dmitruk I., Shynkarenko Y., Belosludovc R., Kasuyad A. (2017), ZnO nested shell magic clusters as tetrapod nuclei, *RSC Adv.*, 7, 21933–21942 (DOI: 10.1039/C7RA01610G)
129. Zhang S., Zhang Y., Huang S., Liu H., Wang P., Tian H. (2011), Theoretical investigation of growth, stability, and electronic properties of beaded ZnO nanoclusters, *J. Mater. Chem.*, 21, 16905–16910 (DOI: 10.1039/C1JM12061A)
130. Hori Y., Wakebe H., Tsukamoto T., Koga O. (1995), Adsorption of CO accompanied with simultaneous charge transfer on copper single crystal electrodes related with electrochemical reduction of CO₂ to hydrocarbons, *Surf. Sci.*, 335, 258–263 (DOI: 10.1016/0039-6028(95)00441-6)
131. Takahashi I., Koga O., Hoshi N., Hori Y. (2002), Electrochemical reduction of CO₂ at copper single crystal Cu(S)-[n(111)×(111)] and Cu(S)-[n(110)×(100)] electrodes, *J. Electroanal. Chem.*, 533, 135–143 (DOI: 10.1016/s0022-0728(02)01081-1)
132. Hori Y., Takahashi I., Koga O., Hoshi N. (2003), Electrochemical reduction of carbon dioxide at various series of copper single crystal electrodes, *J. Mol. Catal. A: Chem.*, 199, 39–47 (DOI: 10.1016/s1381-1169(03)00016-5)
133. Schouten K.J.P., Kwon Y., Van der Ham C.J.M., Qin Z., Koper M.T.M. (2011), A new mechanism for the selectivity to C₁ and C₂ species in the electrochemical reduction of carbon dioxide on copper electrodes, *Chem. Sci.*, 2, 1902–1909 (DOI: 10.1039/c1sc00277e)
134. Schouten K.J.P., Qin Z., Gallent E.P., Koper M.T.M. (2012), Two Pathways for the Formation of Ethylene in CO Reduction on Single-Crystal Copper Electrodes, *J. Am. Chem. Soc.*, 134, 9864–9867 (DOI: 10.1021/ja302668n)

135. Kortlever R., Shen J., Schouten K.J.P., Calle-Vallejo F., Koper M.T.M. (2015), Catalysts and Reaction Pathways for the Electrochemical Reduction of Carbon Dioxide, *J. Phys. Chem. Lett.*, 6, 4073– 4082 (DOI: 10.1021/acs.jpcllett.5b01559)
136. Calle-Vallejo F., Koper M.T.M. (2013), Theoretical Considerations on the Electroreduction of CO to C₂ Species on Cu(100) Electrodes, *Angew. Chem., Int. Ed.*, 125, 7423– 7426 (DOI: 10.1002/ange.201301470)
137. Montoya J.H., Shi C., Chan K., Nørskov J.K. (2015), Theoretical Insights into a CO Dimerization Mechanism in CO₂ Electroreduction, *J. Phys. Chem. Lett.*, 6, 2032–2037 (DOI: 10.1021/acs.jpcllett.5b00722)
138. Luo W., Nie X., Janik M. J., Asthagiri A. (2016), Facet Dependence of CO₂ Reduction Paths on Cu Electrodes, *ACS Catal.*, 6, 219– 229, (DOI: 10.1021/acscatal.5b01967)
139. Garza A.J., Bell A.T., Head-Gordon M. (2018), Mechanism of CO₂ Reduction at Copper Surfaces: Pathways to C₂ Products, *ACS Catal.*, 8, 1490– 1499 (DOI: 10.1021/acscatal.7b03477)
140. Mangione G., Huang J., Buonsanti R., Corminboeuf C. (2019), Dual-Facet Mechanism in Copper Nanocubes for Electrochemical CO₂ Reduction into Ethylene, *J. Phys. Chem. Lett.*, 10, 4259– 4265, (DOI: 10.1021/acs.jpcllett.9b01471)
141. De Gregorio G.L., Burdyny T., Loiudice A., Iyengar P., Smith W.A., Buonsanti R. (2020), Facet-Dependent Selectivity of Cu Catalysts in Electrochemical CO₂ Reduction at Commercially Viable Current Densities, *ACS Catal.*, 10, 4854– 4862 (DOI: 10.1021/acscatal.0c00297)
142. Todorova T.K., Schreiber M.W., Fontecave M. (2020), Mechanistic Understanding of CO₂ Reduction Reaction (CO₂RR) Toward Multicarbon Products by Heterogeneous Copper-Based

- Catalysts, ACS Catal., 10, 1754–1768 (DOI: 10.1021/acscatal.9b04746)
143. Roberts F.S., Kuhl K.P., Nilsson A. (2015), High Selectivity for Ethylene from Carbon Dioxide Reduction over Copper Nanocube Electrocatalysts, *Angew. Chem. Int. Ed.*, 54, 5179– 5182, (DOI: 10.1002/anie.201412214)
 144. Born M., Oppenheimer J. (1927), Zur quantentheorie der molekeln, *J. Ann. Physik*, 84, 457 (DOI: 10.1002/andp.19273892002)
 145. Hohenberg P., Kohn W. (1964), Inhomogeneous electron gas, *Phys. Rev. B*, 136, B864-B871 (DOI: 10.1103/PhysRev.136.B864)
 146. Kohn W., Sham L.J. (1965), Self-consistent equations including exchange and correlation effects, *Phys. Rev.*, 140, A1133-A1138 (DOI: 10.1103/PhysRev.140.A1133)
 147. Xia B. Y., Wu H.B., Wang X., Lou X.W. (2013), Index facets and enhanced electrocatalytic properties, *Angew. Chem. Int. Ed.*, 52, 12337-12340 (DOI: 10.1002/anie.201307518)
 148. Martin, R.M. (2004) *Electronic structure: basic theory and practical methods*, Cambridge University press.
 149. Ceperley D.M., Alder B. (1980), Ground State of the Electron Gas by a Stochastic Method, *J. Phys. Rev. Lett.* 45, 566 (DOI: 10.1103/PhysRevLett.45.566)
 150. Perdew J.P., Wang Y. (1992), Accurate and simple analytic representation of the electron-gas correlation energy, *Phys. Rev. B* 45: 13244-13249 (DOI: 10.1103/PhysRevB.45.13244)
 151. Perdew J.P., Burke K., Ernzerhof M. (1996), Generalized gradient approximation made simple, *Phys. Rev. Lett.*, 77, 3865-3868. (DOI: 10.1103/PhysRevLett.77.3865)
 152. Perdew J.P., Ruzsinszky A., Csonka G.I., Vydrov O.A., Scuseria G.E., Constantin L.A., Zhou X., Burke K. (2008), Restoring the density-gradient expansion for exchange in solids and surfaces,

- Phys. Rev. Lett., 100, 136406 (DOI: 10.1103/PhysRevLett.100.136406)
153. Slater J.C. (1930), Atomic shielding constants, Phys. Rev., 36, 57-64 (DOI: 10.1103/PhysRev.36.57)
154. Boys S.F. (1950), Electronic wave functions. I. A general method of calculation for the stationary states of any molecular system, 36, 542-554 (DOI: 10.1098/rspa.1950.0036)
155. Weigend F., Ahlrichs R. (2005), Balanced basis sets of split valence, triple zeta valence and quadruple zeta valence quality for H to Rn: Design and assessment of accuracy, Phys. Chem. Chem. Phys., 7, 3297-3305 (DOI: 10.1039/B508541A)
156. Russo T.V., Martin R.L., Hay P.J. (1995), Effective Core Potentials for DFT Calculations, J. Phys. Chem., 99, 17085-17087 (DOI: 10.1021/j100047a007)
157. Hay P.J., Wadt W.R. (1985), Ab initio effective core potentials for molecular calculations. Potentials for the transition metal atoms Sc to Hg, J. Chem. Phys., 82, 270–283 (DOI: 10.1063/1.448799)
158. Ihm J., Zunger A., Cohen M.L. (1979), Momentum-space formalism for the total energy of solids, J. Phys. C: Solid State Physics, 12, 4409 (DOI: 10.1088/0022-3719/12/21/009)
159. Boys S.F., Bernardi F. (1970), The calculation of small molecular interactions by the differences of separate total energies. Some procedures with reduced errors, Mol. Phys., 19, 553-566 (DOI: 10.1080/00268977000101561)
160. Vanderbilt D. (1990), Soft self-consistent pseudopotentials in a generalized eigenvalue formalism, Phys. Rev. B, 41, 7892-7895 (DOI: 10.1103/PhysRevB.41.7892)
161. Andersen, O.K. (1975), Linear methods in band theory, Phys. Rev. B., 12, 3060-3083 (DOI: 10.1103/PhysRevB.12.3060)
162. Blochl P.E. (1994), Projector augmented-wave method, Phy. Rev. B, 50, 17953 (DOI: 10.1103/PhysRevB.50.17953)

163. Hamann D.R., Schlüter M., Chiang C. (1979), Norm-conserving pseudopotentials, *Phys. Rev. Lett.*, 43, 1494-1497 (DOI: 10.1103/PhysRevLett.43.1494)
164. Grimme S. (2011), Density functional theory with London dispersion corrections, *WIREs Comput. Mol. Sci.*, 1, 211-228 (DOI: 10.1002/wcms.30)
165. Grimme S., Antony J., Ehrlich S., Krieg H. (2010), A consistent and accurate ab initio parametrization of density functional dispersion correction (DFT-D) for the 94 elements H-Pu, *J. Chem. Phys.*, 132, 154104 (DOI: 10.1063/1.3382344)
166. Chai J.D., Head-Gordon M. (2008), Long-range corrected hybrid density functionals with damped atom-atom dispersion corrections, *Phys. Chem. Chem. Phys.*, 10, 6615-6620 (DOI: 10.1039/B810189B)
167. Bochicchio, R.C., Miranda-Quintana, R.A., Rial D. (2013), Communication: Reduced density matrices in molecular systems: Grand-canonical electron states, *J. Chem. Phys.*, 139, 191101-191104 (DOI: 10.1063/1.4832495)
168. Reed A.E., Curtiss L.A., Weinhold F. (1988), Intermolecular interactions from a natural bond orbital, donor-acceptor viewpoint, *Chem. Rev.*, 88, 899–926 (DOI: 10.1021/cr00088a005)
169. Carlson B.C., Keller J.M. (1957), Orthogonalization Procedures and the Localization of Wannier Functions, *Phys. Rev.*, 105, 102-103 (DOI: 10.1103/PhysRev.105.102)
170. Rubarani P., Gangadharan S., Krishnan S. (2014), Natural Bond Orbital (NBO) Population Analysis of 1-Azanaphthalene-8-ol, *Acta Phys. Pol. A*, 125, 18-22, (DOI: 10.12693/APhysPolA.125.18)
171. Johnson E.R., Keinan S., Mori-Sánchez P., Contreras-García J., Cohen A.J., Yang, W. (2010), Revealing Noncovalent Interactions, *J. Am. Chem. Soc.*, 132, 6498-6506 (DOI: 10.1021/ja100936w)

172. Contreras-García J., Johnson E.R., Keinan S., Chaudret R., Piquemal J.P., Beratan D.N., Yang W. (2011), NCIPLLOT: A Program for Plotting Noncovalent Interaction Regions, *J. Chem. Theory Comput.*, 7, 625-632 (DOI: 10.1021/ct100641a)
173. Alonso M., Woller T., Martín-Martínez F.J., Contreras-García J., Geerlings P., De P. F. (2014), Understanding the Fundamental Role of π/π , σ/σ , and σ/π Dispersion Interactions in Shaping Carbon-Based Materials, *Chem. Eur. J.*, 20, 4931-4941 (DOI: 10.1002/chem.201400107)
174. Mills G., Jónsson H. (1994), Quantum and thermal effects in H₂ dissociative adsorption: Evaluation of free energy barriers in multidimensional quantum systems, *Phys. Rev. Lett.*, 72, 1124. (DOI: 10.1103/PhysRevLett.72.1124)
175. Henkelman G., Jonsson H. (2000), A climbing image nudged elastic band method for finding saddle points and minimum energy paths, *J. Chem. Phys.*, 113, 9978-9985. (DOI: 10.1063/1.1329672)
176. Paquet E., Viktor H.L. (2018), Computational Methods for Ab Initio Molecular Dynamics, *Advances in Chemistry*, 9839641, 14 pages (DOI: 10.1155/2018/9839641)
177. Nosé S. (1984), A unified formulation of the constant temperature molecular dynamics methods, *J. Chem. Phys.*, 81, 511-519 (DOI: 10.1063/1.447334)
178. Bader, R.F.W. (1994) *Atoms in Molecules: A Quantum Theory*; Oxford University Press: USA.
179. Henkelman G., Arnaldsson A., Jonsson H. (2006), A fast and robust algorithm for Bader decomposition of charge density, *Comput. Mater. Sci.*, 36, 354-360. (DOI: 10.1016/j.commatsci.2005.04.010)
180. Togo A., Oba F., Tanaka I. (2008), First-principles calculations of the ferroelastic transition between rutile-type and CaCl₂-type SiO₂

at high pressures, Phys. Rev. B: Condens. Matter., 78, 134106.
(DOI: 10.1103/PhysRevB.78.134106)

181. Baroni S., Giannozzi P., Testa A. (1987), Green's-function approach to linear response in solids, Phys. Rev. Lett., 58, 1861.
(DOI: 10.1103/PhysRevLett.58.1861)

Chapter 2

*Electrocatalytic CO₂ Reduction by Mn(I)
Half Sandwich Based Catalysts: Role of
Substitution and Solvent*

2.1. Introduction

Electrochemical CO₂ reduction to CO is one of the promising ways to convert electrical energy into chemical energy [1,2]. The product CO can be further utilized for the formation of HCOOH, CH₃OH, and other liquid-based fuels [3-8]. However, selective and efficient conversion of CO₂ to CO remains a longstanding challenge. Several homogeneous catalysts have been found to be active for electrochemical CO₂ reduction as it requires less energy due to proton-coupled reduction pathways [1,2,9-24]. However, most of these reported catalysts are noble metal-based catalysts. Therefore, the role of metal is very important. However, the ligand sphere also plays a significant role to improve the catalytic activity [25,26]. So, it is possible to develop a highly active catalyst with a proper combination of metal and ligand. In this regard, computational studies play a very important role towards the designing of such active catalysts [11,13,14]. For example, Carter et al. have computationally studied the mechanistic pathways of [Re(bpy)Cl(CO)₃] based electrochemical CO₂ reduction reaction to understand the reason behind the excellent catalytic activity [15]. Similarly, several other noble metal-based active catalysts have been studied to understand the reasons behind their excellent catalytic activities [11,12,14-22]. However, there are only few reports available for non-noble metal based active catalysts [9,10,13,23]. For example, Bourrez et al. have shown the catalytic activity of fac-Mn(bpy-R)(CO)₃Br (R = H and CH₃) catalysts as an alternative of [Re(bpy)Cl(CO)₃] for the formation of CO from CO₂ [27,28]. Kubiak and his co-workers have also shown that the tBu substitution on the ligand sphere of Mn(I)-bpy based catalyst is an active catalyst for selective CO formation [16]. Recently, our group has also demonstrated through computational studies that [MnBr(NHC-pyridine)(CO)₃] and Mn(bpy-R)(CO)₃Br catalysts can be active for selective CO₂ reduction (over proton reduction) and the activity of the catalysts can be tuned through ligand modifications [29,30]. Though some of these earth abundant metal-based catalysts have been reported to be

active, however the activities of these catalysts are far from the noble metal-based catalysts. Therefore, industrialization of non-noble metal-based catalysts is yet to be realized. Hence, the designing of non-noble metal based highly selective and efficient catalysts are very important. Generally, redox ligand-based catalysts are highly active for the electrochemical CO₂ reduction to CO due to the reversible electron transfer process between the metal center and ligand sphere [14,31]. Inspired by all these, we have modelled Mn(I) redox ligand-based catalysts for the electrochemical CO₂ reduction to CO. Recently, Perekalin and coworkers have reported a series of Mn(I) half sandwich-based catalysts for the ketone hydrogenation reaction where benzene ring of the half sandwich ligand can act as a redox ligand owing to the π electron delocalization [32]. Such π -delocalization can certainly stabilize the formation of the active catalyst. Agarwal et al. have shown that the axial ligand of the complex is highly important for product selectivity (CO₂ vs. proton reduction) [33]. They have demonstrated that ligands, such as NCS and CN favor proton reduction, whereas Br substitution favors CO₂ reduction reaction. Interestingly, Br is present as an axial ligand in the Mn(I) half sandwich-based complexes (Figure 2.1). Therefore, such complexes can be promising for CO₂ reduction reaction. To understand the role of electronic properties of the ligands, different electron-donating (CH₃ and CMe₃) and electron withdrawing (OH, NH₂, COOH) substituents at the phenyl group of the Mn(I) half sandwich-based complex are studied.

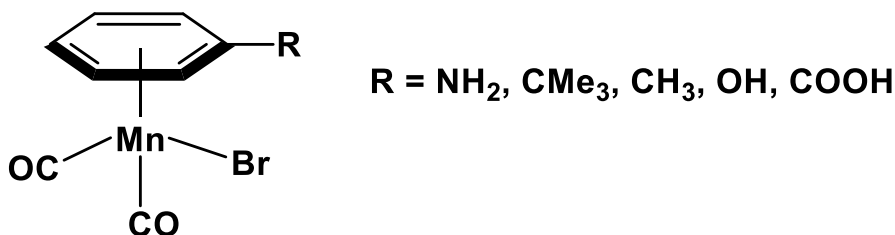


Figure 2.1: Modelled Mn(I) half sandwich-based complexes for the electrochemical CO₂ reduction reaction.

Hydroxy and amine substitutions (R= -OH and -NH₂) on the phenyl group of the Mn(I) half sandwich-based complexes have been experimentally reported for ketone hydrogenation [32]. Interestingly, substituents such as CH₃, CMe₃, COOH have been earlier reported to be promising for CO₂ reduction for the Mn-bpy based complexes [30]. On the other hand, solvent plays an important role to improve the catalytic activity of the complexes. Most of the CO₂ reduction reactions are reported in the organic solvents like acetonitrile, N, N-dimethylformamide, tetrahydrofuran, dimethyl sulfoxide (DMSO) and so on [10-12,14-19]. There are some reports where the electrochemical CO₂ reduction reaction occurs in the aqueous solution also [9,13,34,35]. Hence, it is highly important to find out the effect of different kinds of solvent during the CO₂ reduction reaction. Henceforth, we have considered acetonitrile, water and DMSO solvents during the electrochemical CO₂ reduction reaction to understand the importance of solvents. Moreover, earlier reports have shown that the Mn(I)-based catalysts are active for CO₂ reduction reaction in the presence of weak Brønsted acids (H₂O, CH₃OH, CH₃COOH, PhOH, and 2,2,2-trifluoroethanol) which can be used as a proton source during the reaction [36,37]. In this context, Kubiak and his coworkers have demonstrated that the PhOH can produce more amount of CO compared to other Brønsted acids, such as CH₃COOH and 2,2,2-trifluoroethanol [37]. Thus, we have considered PhOH as a proton source in our study.

2.2. Computational Details

All the calculations have been carried out using the density functional theory (DFT) as implemented in the Gaussian 09 D.01 package [38]. The unrestricted Becke's three-parameter exchange and Lee-Yang-Parr exchange-correlation (UB3LYP) functional [39-41] is used for all the calculations. 6-31+G** diffuse basis sets for C, H, N and O atoms and LANL2DZ basis sets for Mn and Br atoms are used [42-45]. The considered

functional and basis sets have been used in earlier studies and showed that the functional and basis set can reproduce the experimental trends for electrochemical CO₂ reduction reaction by Mn(I) based catalysts [29,30]. Therefore, we have considered the UB3LYP functional with the combination of 6-31+G** and LANL2DZ basis sets for further study. We have also used Grimme's dispersion correction (DFT-D3) for the description of noncovalent interactions [46]. Furthermore, the geometry optimizations and frequency calculations are performed in three different solvents: acetonitrile ($\epsilon = 35.688$), water ($\epsilon = 78.3553$) and DMSO ($\epsilon = 46.826$) using the conductor-like polarizable continuum model [47,48]. These solvents are mainly used in experiments for the electrochemical CO₂ reduction reaction. Besides, we have considered higher basis sets and different solvation model for the NH₂ and COOH based half sandwich catalysts to verify the results. The Pople basis set 6-311++G** has been considered for C, H, N and O atoms whereas SDD basis set has been considered for the Mn and Br atoms [42-44, 49,50]. We have also compared the results of these two catalysts calculated using two different sets of basis sets in three different solvents (acetonitrile, water and DMSO). The solvation model based on density (SMD) has also been considered for these two systems calculated using higher basis sets [51]. All the intermediates are characterized to be minimum energy structures due to the absence of any imaginary frequencies and similarly all the transition states are characterized through one imaginary frequency which connect the corresponding reactant and product structures in the reaction pathway. Further to this, all the transition states are confirmed through intrinsic reaction coordinate calculations. In all the cases, we have included zero-point vibrational energy (ZPVE) and thermal energy corrections. In this study, all the calculations have been performed at a temperature of 298.15 K and 1 atm pressure. The reaction free energies (ΔG) of the reaction are calculated from the free energy difference between the reactant and the product, whereas activation barriers (ΔG^\ddagger) are calculated from the free

energy difference between the transition state and the reactant, respectively. Besides, all the reaction reduction potentials (E) have been calculated using the following equation (2.1) [52]:

$$E = \left(\frac{-\Delta G_{\text{soln}}}{nF} \right) - E_{\text{ref}}^0 \quad (2.1)$$

In the above equation ΔG_{soln} is the calculated reaction free energy of the considered step in solution, n is the number of electrons involved in the reaction, F is the Faraday's constant and E_{ref}^0 is the absolute reduction potential of the reference electrode. In this study, we have calculated all the reduction potential values with respect to the saturated calomel electrode (SCE). Thus, the reference electrode's absolute reduction potentials are considered as 4.801, 4.481 and 4.319 V in acetonitrile, water and DMSO solvent, respectively [53,54]. All these values have been considered from the earlier reports where they have considered these values with respect to the standard hydrogen electrode (SHE). Additionally, we have considered the proton free energies in different solvents and the free energies of proton are found to be -260.2, -265.9 and -273.3 kcal/mol [55,56] in acetonitrile, water and DMSO solvent, respectively. These values are obtained by the combination of experimental gas-phase free energies of formation and solution-phase reduction potentials, solubility products, and acid dissociation constants where solvation free energies have been calculated from ions in these solvents. Though, these free energy values are calculated using different level of theory (B97-1/MG3S and SM6/MPW25), the calculated free energy of proton in water is in good agreement with the experimental value reported earlier [57]. Moreover, the proton free energy in acetonitrile solvent has also been considered in earlier report for electrochemical CO₂ reduction reaction [30]. Therefore, we assumed that the computed absolute free energy obtained for proton in acetonitrile and DMSO solvent using the B97-1/MG3S and SM6/MPW25 level of theory can be good enough for our investigation as they reproduced the experimental absolute free energy value of proton in water solvent. Hence, we have considered these values for our reaction free energy calculations.

We have also performed Natural bond orbital (NBO) analysis [58] using the UB3LYP/6-311++G** + SDD with SMD solvation model and UB3LYP/6-31+G** + LANL2DZ with CPCM solvation model for the investigation of natural charges of atoms on some of the important intermediates of CO₂ reduction reaction. In the presence of strong acid, protonation step become a barrierless process. Therefore, protonation step is thermodynamically and kinetically more favourable compared to the CO₂ reduction step in the presence of strong acid [29]. Moreover, Cowan and his co-workers have reported homogeneous CO₂ reduction at pH 7 [59]. Based on these previous findings, the reaction free energies have been calculated to the non-standard condition of pH 7 instead of pH 0 by using the following equation (2.2):

$$\Delta G = RT \ln \left(\frac{Q}{K_{eq}} \right) \quad (2.2)$$

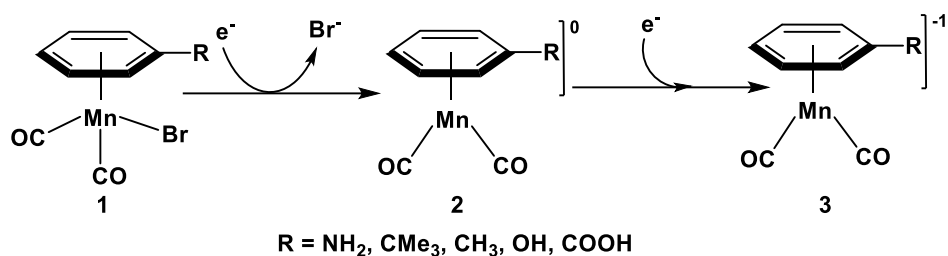
In the above equation R is the universal gas constant (0.00198588 kcal K⁻¹ mol⁻¹), T is the temperature (298.15 K), Q is the reaction quotient and K_{eq} is the equilibrium constant.

2.3. Results and Discussion

2.3.1. Formation of Active Catalysts

We begin our analysis by considering the reduction of the considered precatalysts. The Mn(I) half sandwich-based complex can be reduced to form an active catalyst as shown in Scheme 2.1 (**1** → **2** → **3**). In the very first step, precatalyst **1** can be reduced, which may lead to the dissociation of Br⁻ ion for the formation of **2** (**1** + e⁻ → **2** + Br⁻). In the next step, intermediate **2** can be reduced further for the formation of **3** (**2** + e⁻ → **3**), which is the active catalyst. Our calculated reduction potential values are listed in Table 2.1. These calculated reduction potential values show a significant difference when we use different kind of solvents. In all the cases, the reduction potential values are high in acetonitrile solvent compared to that in water and DMSO as the absolute reduction potential

value of SCE is different in different solvents. The absolute reduction potential values of SHE is dependent on the gas-phase free energy of proton formation and the absolute solvation free energy of proton [56].



Scheme 2.1: Proposed reduction pathways for the active catalyst formation for half sandwich Mn(I) catalysts.

In this context, absolute solvation free energy of proton changes with respect to the solvent. Therefore, the absolute reduction potential values of SHE is different in different solvents. As the reduction potential values of SCE are with respect to the SHE, absolute reduction potential of SCE is also different in different solvents [56]. From Table 2.1 it is clear that the reduction potential values in DMSO solvent are 0.45–0.50 V less compared to that in acetonitrile solvent and 0.10–0.15 V less compared to that in water solvent. Therefore, DMSO can be a very promising solvent for the formation of the active catalyst as absolute solvation free energy of proton is maximum in DMSO compared to the acetonitrile and water solvent. The calculated reduction potential values in three different solvents for all the catalysts show that the first reduction potential values ($\mathbf{1} + e^- \rightarrow \mathbf{2} + \text{Br}^-$) are less compared to the second reduction potential values ($\mathbf{2} + e^- \rightarrow \mathbf{3}$). The trend is very much in agreement with the previous reports [29,30]. Further to this, we have calculated the reduction potential values of NH₂ and COOH based Mn(I) half sandwich complexes using the UB3LYP/6-311++G** + SDD with SMD solvation model and the calculated values are listed in Table 2.1. The calculated reduction potential values show similar trends with the values calculated at UB3LYP/6-31+G** + LANL2DZ and CPCM

solvation model. Therefore, the UB3LYP/6-31+G** + LANL2DZ with CPCM solvation model is good enough for the investigation of the active catalyst formation pathway of CMe₃, CH₃ and OH based Mn(I) half sandwich complexes in three different solvents.

Table 2.1: Calculated two separate one-electron reduction potentials (E in V) in three different solvents (acetonitrile, water and DMSO) for all the considered half sandwich Mn(I) complexes calculated at UB3LYP/6-31+G** + LANL2DZ with CPCM solvation model. The calculated values with UB3LYP/6-311++G** + SDD and SMD solvation model are shown in parenthesis.

Substituents	Solvents	$\mathbf{1} + e^- \rightarrow \mathbf{2} + \text{Br}^-$	$\mathbf{2} + e^- \rightarrow \mathbf{3}$
NH ₂	Acetonitrile	-1.57 (-1.54)	-2.06 (-2.17)
	Water	-1.21 (-1.17)	-1.71 (-1.71)
	DMSO	-1.07 (-1.07)	-1.57 (-1.68)
CMe ₃	Acetonitrile	-1.42	-1.92
	Water	-1.05	-1.57
	DMSO	-0.92	-1.43
CH ₃	Acetonitrile	-1.47	-1.88
	Water	-1.11	-1.58
	DMSO	-0.97	-1.44
OH	Acetonitrile	-1.49	-1.85
	Water	-1.12	-1.50
	DMSO	-0.99	-1.36
COOH	Acetonitrile	-1.45 (-1.48)	-1.49 (-1.69)
	Water	-1.02 (-1.11)	-1.21 (-1.19)
	DMSO	-0.95 (-0.86)	-1.00 (-1.31)

Besides, substitutions on the phenyl group also affect the reduction potential values. The calculated first reduction potential value decreases in the

following order: $\text{NH}_2 > \text{OH} > \text{CH}_3 > \text{COOH} > \text{CMe}_3$. So, the first reduction potential value is maximum for NH_2 substitution (-1.57 V in acetonitrile), whereas minimum for CMe_3 (-1.42 V in acetonitrile) substitution. The calculated second reduction potential values follow the following order: $\text{NH}_2 > \text{CMe}_3 > \text{CH}_3 > \text{OH} > \text{COOH}$. Our calculated first reduction potential values indicate the independency of the reduction step on the basis of electronic nature of different types of ligand modification. The differences between highest and lowest first reduction potential values for different catalysts are 0.15 V for acetonitrile and 0.15 V for DMSO, whereas 0.19 V for water solvent. Therefore, the first reduction potential values are almost comparable for different type of catalysts. Besides, the differences between highest and lowest second reduction potential values for different catalysts are 0.57 V for acetonitrile/DMSO, whereas 0.50 V for water solvent. Therefore, the second reduction potential values are quite different for different types of ligand modification. The calculated second reduction potential values are lower for electron withdrawing substituents (OH and COOH) compared to the electron-donating substituents (NH_2 , CMe_3 , CH_3). This may be due to the delocalization of charges in the presence of electron withdrawing substituents. To understand further, we have calculated the NBO charges of Mn atom and half sandwich ligand part of the catalysts using the UB3LYP/6-311++G** + SDD with SMD solvation model and UB3LYP/6-31+G** + LANL2DZ with CPCM solvation model, and the calculated values are listed in Table 2.2 for the intermediates **1**, **2** and **3** in acetonitrile solvent. Acetonitrile solvent is only considered, as water and DMSO also show similar trend. Our calculated NBO charges of the Mn atom and half sandwich part of all the substituted complexes vary for intermediate **1**, **2** and **3**, which indicate that the ligand part of the complex behaves as a redox ligand which is important for the electrochemical CO_2 reduction reaction. The calculated NBO charges show that the Mn center of the catalyst accumulated more negative charges compared to the half sandwich part of the ligand for all the intermediates. The negative charge

on the Mn center for intermediate **2** follow: $\text{NH}_2 > \text{CMe}_3 > \text{COOH} > \text{CH}_3 > \text{OH}$ whereas Ph-R of intermediate **2** follow: $\text{NH}_2 < \text{CMe}_3 < \text{CH}_3 = \text{OH} < \text{COOH}$ order. If the negative charge on the Mn atom is more than the reduction potential value will be high. Similarly, more positive charge on the half sandwich part means high reduction potential.

Table 2.2: The calculated NBO charges of the Mn atom and the ligand part of the intermediates **1**, **2** and **3** for different substitutions in acetonitrile solvent by UB3LYP/6-31+G** + LANL2DZ with CPCM solvation model. The calculated NBO using UB3LYP/6-311++G** + SDD with SMD solvation model values are shown in parenthesis.

Subs.	Mn			Ph-R		
	1	2	3	1	2	3
NH ₂	-0.95 (-0.99)	-0.70 (-0.74)	-1.29 (-1.38)	0.70 (0.69)	0.43 (0.43)	0.21 (0.23)
CMe ₃	-0.95 (0.99)	-0.70 (-0.73)	-1.27 (-1.36)	0.64 (0.64)	0.39 (0.40)	0.16 (0.17)
CH ₃	-0.95 (-0.99)	-0.69 (-0.70)	-1.28 (-1.36)	0.65 (0.64)	0.38 (0.38)	0.16 (0.17)
OH	-0.95 (-1.00)	-0.67 (-0.69)	-1.27 (-1.37)	0.65 (0.65)	0.38 (0.38)	0.15 (0.17)
COOH	-0.96 (-1.00)	-0.69 (-0.71)	-1.20 (-1.28)	0.58 (0.58)	0.31 (0.30)	-0.01 (0.01)

Here charges of the half sandwich ligand part dominate the charges of the Mn atom. Hence, the second reduction potential follow the following order: $\text{NH}_2 > \text{CMe}_3 > \text{CH}_3 > \text{OH} > \text{COOH}$. So, CMe₃ substitution in the Mn(I) based half sandwich-based complex is best for first reduction potential, whereas COOH substitution is best for second reduction potential. Now, considering the solvent and ligand effects, we find that CMe₃ substitution in DMSO is best for first reduction potential (-0.92 V in DMSO solvent)

and COOH substitution in DMSO is best for second reduction potential (-1.00 V in DMSO solvent). To understand the electronic effect of the ligand substitution on second reduction potential, we have calculated the LUMO energies of **2** in acetonitrile solvent (Figure 2.2). Our calculated LUMO energies show that the LUMO value is maximum for NH₂ substitution and minimum for COOH substitution with the following order: NH₂ > CMe₃ = CH₃ > OH > COOH. Therefore, the second reduction potential value is maximum for NH₂ substitution-based catalyst and minimum for COOH substitution-based catalyst. Most of our calculated reduction potential values in acetonitrile and water are comparable with our earlier theoretical reports on the Mn-bpy and Mn-NHC based catalyst whereas the active catalysts formation in DMSO solvent is found to be highly favourable compared to that on the bpy and NHC based Mn(I) catalysts [29,30].

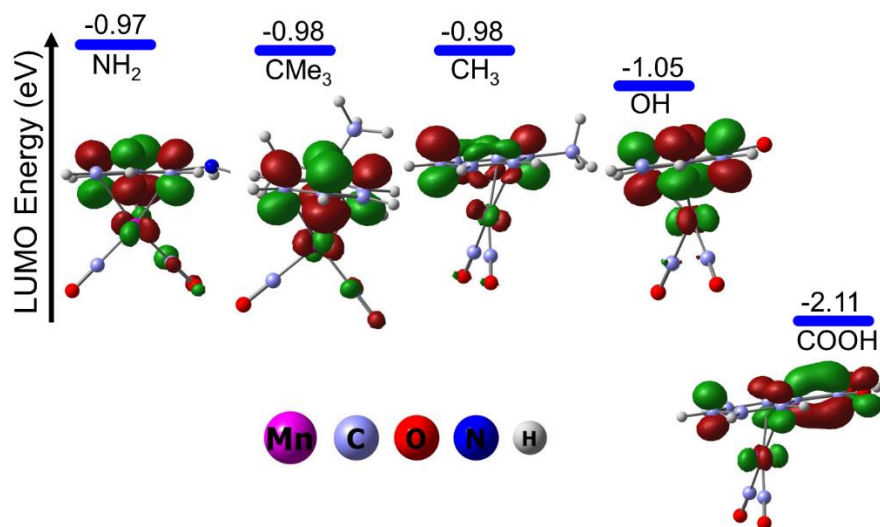
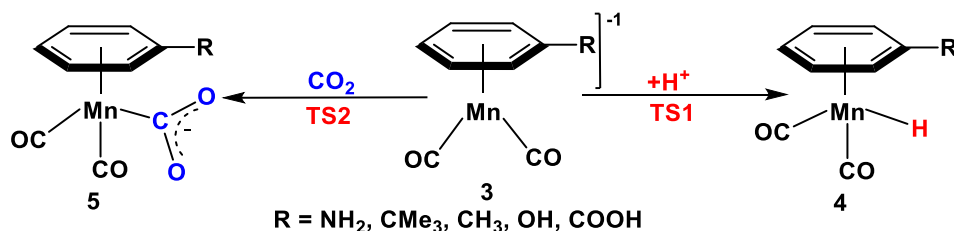


Figure 2.2: Calculated LUMO energies of intermediate **2**. All the LUMO energies are in eV.

2.3.2. CO₂ vs. Proton Binding

The presence of weak Brønsted acid is highly important for the electrochemical CO₂ reduction reaction. However, there is a competition between CO₂ vs. proton reduction in the presence of the active catalyst. In

this section, the possible reaction pathways for the binding of proton and CO₂ molecule (Scheme 2.2) have been investigated. The active catalyst [(C₆H₅R)Mn(CO)₂]⁻¹ has a vacant site where proton or CO₂ can bind for the reduction reaction. Therefore, this is a highly important step for reaction selectivity, that is CO₂ vs. proton reduction selectivity. Earlier reports have shown that in case of the *bpy* based Mn and Re complexes, proton reduction reaction is thermodynamically favourable compared to the CO₂ reduction reaction, whereas CO₂ reduction reaction is kinetically more favourable compared to the proton reduction reaction [1,15,29,30]. In our earlier studies, we have demonstrated that the CO₂ reduction reaction is favored in the presence of weak Brønsted acid and proton reduction reaction is favored in the presence of strong Brønsted acid [29]. Thus, we have considered the reaction in the presence of a weak Brønsted acid (PhOH).



Scheme 2.2: Possible CO₂ vs. proton reduction pathways using the Mn(I) half sandwich-based active catalyst.

Our calculated reaction free energies and activation barriers for CO₂ vs. proton reduction reaction by Mn(I) half sandwich-based catalysts are given in Table 2.3. The calculated reaction free energy values show that the proton reduction reaction is thermodynamically much more favourable compared to the CO₂ reduction reaction for all the considered catalysts in three different solvents. The proton reduction is most favourable in acetonitrile followed by that in water and DMSO. This is due to the different absolute free energy of the proton in three different solvents.

Table 2.3: The calculated reaction free energies (ΔG in kcal/mol) and activation barriers (ΔG^\ddagger in kcal/mol) of proton and CO₂ reduction reaction by half sandwich Mn(I) based complexes using UB3LYP/6-31+G** + LANL2DZ with CPCM solvation model. The calculated UB3LYP/6-311++G** + SDD with SMD solvation model values are shown in parenthesis.

Substituents	Solvents	Proton Reduction		CO ₂ reduction	
		3 \rightarrow 4	3 \rightarrow TS1	3 \rightarrow 5	3 \rightarrow TS2
NH ₂	Acetonitrile	-48.6 (-47.9)	8.7 (8.9)	-4.8 (-0.4)	8.2 (7.8)
	Water	-40.4 (-37.9)	8.9 (6.9)	-5.1 (-15.7)	8.3 (4.6)
	DMSO	-35.1 (-34.8)	8.8 (8.9)	-4.9 (3.2)	8.2 (8.4)
CMe ₃	Acetonitrile	-45.2	11.6	-1.3	9.1
	Water	-38.8	10.6	-0.2	9.5
	DMSO	-31.8	10.6	-0.1	9.5
CH ₃	Acetonitrile	-45.3	11.0	-1.1	9.7
	Water	-40.0	10.7	-2.4	8.7
	DMSO	-33.0	10.4	-2.3	8.6
OH	Acetonitrile	-43.5	12.5	-0.7	10.0
	Water	-37.1	12.7	-1.0	10.0
	DMSO	-30.1	12.6	-0.8	9.9
COOH	Acetonitrile	-37.2 (-40.8)	14.3 (12.1)	4.5 (6.5)	10.3 (9.6)
	Water	-30.8 (-30.3)	14.4 (11.3)	4.2 (-5.2)	10.4 (7.4)
	DMSO	-23.8 (-27.6)	14.3 (13.3)	4.4 (9.1)	10.4 (9.2)

The absolute free energy of the proton depends on the gas-phase free

energies of formation, solution-phase potentials and acid dissociation constants, and gas-phase clustering free energies [54]. As the solution phase potentials and acid dissociation constants are different for different solvent, the absolute free energy of proton is also different in different solvents. The CO₂ reduction reaction free energies are very much comparable (within 1.3 kcal/mol) for same substituents in three different solvents. The calculated reaction free energy values show that the proton reduction reaction is more favourable for NH₂ substituent (-48.6 kcal/mol) and less favourable for COOH substituents (-37.2 kcal/mol) in acetonitrile solvent. Similarly, CO₂ reduction reaction is also more favourable for NH₂ functional-based complex (-4.8 kcal/mol) and less favourable for COOH functional-based complex (4.5 kcal/mol) in acetonitrile solvent. However, our calculated activation barrier values show that the CO₂ reduction reaction is kinetically more favourable compared to the proton reduction reaction for all the considered catalysts in three different solvents though the differences are within 0.5-4.0 kcal/mol. This is very much similar with the trend previous reported on the noble metal-based complexes [1,15,29,30]. Additionally, we have calculated the reaction free energies (ΔG) and activation barriers (ΔG^\ddagger) of proton vs. CO₂ binding steps of NH₂ and COOH based Mn(I) half sandwich catalysts using the UB3LYP/6-311++G** + SDD with SMD solvation model and the calculated results are listed in Table 2.3. The calculated reaction free energies (ΔG) and activation barriers (ΔG^\ddagger) using higher basis sets also show that the proton reduction step thermodynamically more favourable whereas CO₂ reduction step is kinetically favorable. Hence, the UB3LYP/6-31+G** + LANL2DZ with CPCM solvation model is good enough to investigate the CO₂ vs. proton binding pathways of CMe₃, CH₃ and OH based Mn(I) half sandwich catalysts in different solvents. Interestingly, the calculated activation barriers are almost same irrespective of the solvent though different for different ligand substitutions. In this context, the calculated values show that the activation barriers for CO₂ reduction step are less for NH₂ based

catalyst (8.2 kcal/mol in acetonitrile) and more for COOH based catalyst (10.3 kcal/mol in acetonitrile). Similarly, the activation barriers for proton reduction step are less for NH₂ based catalyst (8.7 kcal/mol in acetonitrile) and more for COOH based catalyst (14.3 kcal/mol in acetonitrile). To understand the reason behind the different activation barrier of CO₂ reduction step for different ligand modification in the catalyst, we have calculated the HOMO of the catalyst and LUMO of the CO₂ molecule in acetonitrile solvent. Most of the cases, we have observed that the d orbital electron density is mainly in the HOMO–1 level of the active catalyst (Figure 2.3). Therefore, the electron transfer will be easy if the energy gap between the HOMO/HOMO–1 of active catalyst and LUMO of the CO₂ molecule is less. Our calculated HOMO/HOMO–1 and LUMO gap shows minimum for NH₂ based ligand followed by for CMe₃, CH₃, OH and maximum for COOH substituents (Figure 2.3).

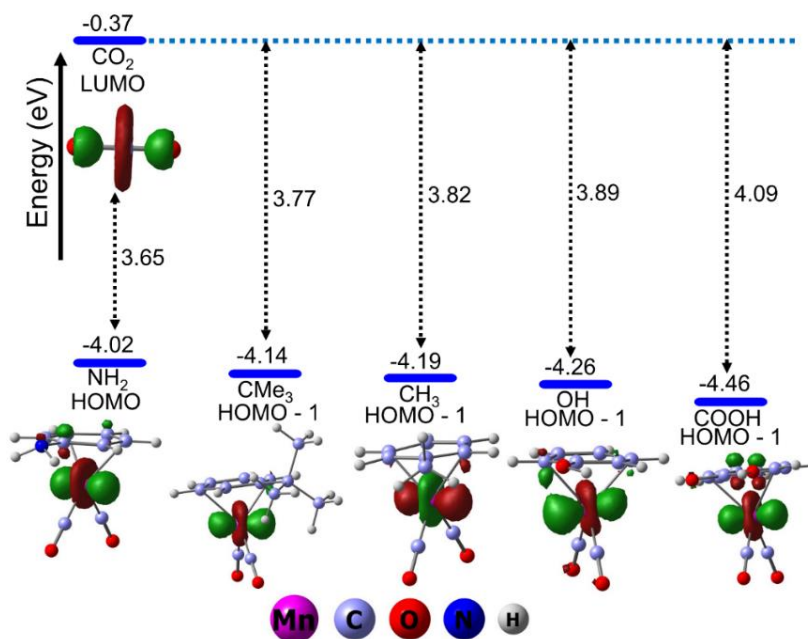


Figure 2.3: Occupied d-orbital energies and shapes (HOMO or HOMO-1) of intermediate **3** with antibonding orbital energy and shape (LUMO) of the CO₂ molecule.

Therefore, the activation barrier is maximum for COOH and minimum for NH₂ substituents for the CO₂ reduction reaction. Now, combining both the solvent and ligand modification effect, we get that NH₂ based ligand modification is the best for the CO₂ reduction step. However, NH₂ based ligand modification in acetonitrile solvent is the best for proton reduction reaction among all the Mn(I) sandwich-based catalysts. Furthermore, we have checked the possibility of NH₂ group protonation of [(C₆H₅NH₂)Mn(CO)₂]⁻ in the presence of PhOH. Our calculated reaction free energy values show that the NH₂ protonation is 8 kcal/mol more endergonic compared to the CO₂ binding. Therefore, the catalyst will favour CO₂ reduction over protonation of the NH₂ group. Moreover, Truhlar and his co-workers have reported that the presence of one explicit solvent molecule with implicit solvent model gives quite accurate results [60]. So, we have considered one water molecule as an explicit solvent and calculated the reaction free energies for proton and CO₂ binding steps. The intermediates **3**, **4** and **5** with one explicit water molecule for all the considered catalysts are shown in Figure 2.4. Our calculated results (Table 2.4) also show that the proton reduction step is thermodynamically more favourable compared to the CO₂ reduction step as found without the explicit model. Moreover, we have considered NH₂ based Mn(I) half sandwich intermediate **3** and **4** for the understanding of the reaction free energy at pH 7 in water solvent. The calculated activation free energy barrier for the protonation step of NH₂ based Mn(I) half sandwich intermediate **3** to **4** is 8.9 kcal/mol (Scheme 2.3). At pH 7 the reaction free energy is -0.64 kcal/mol.

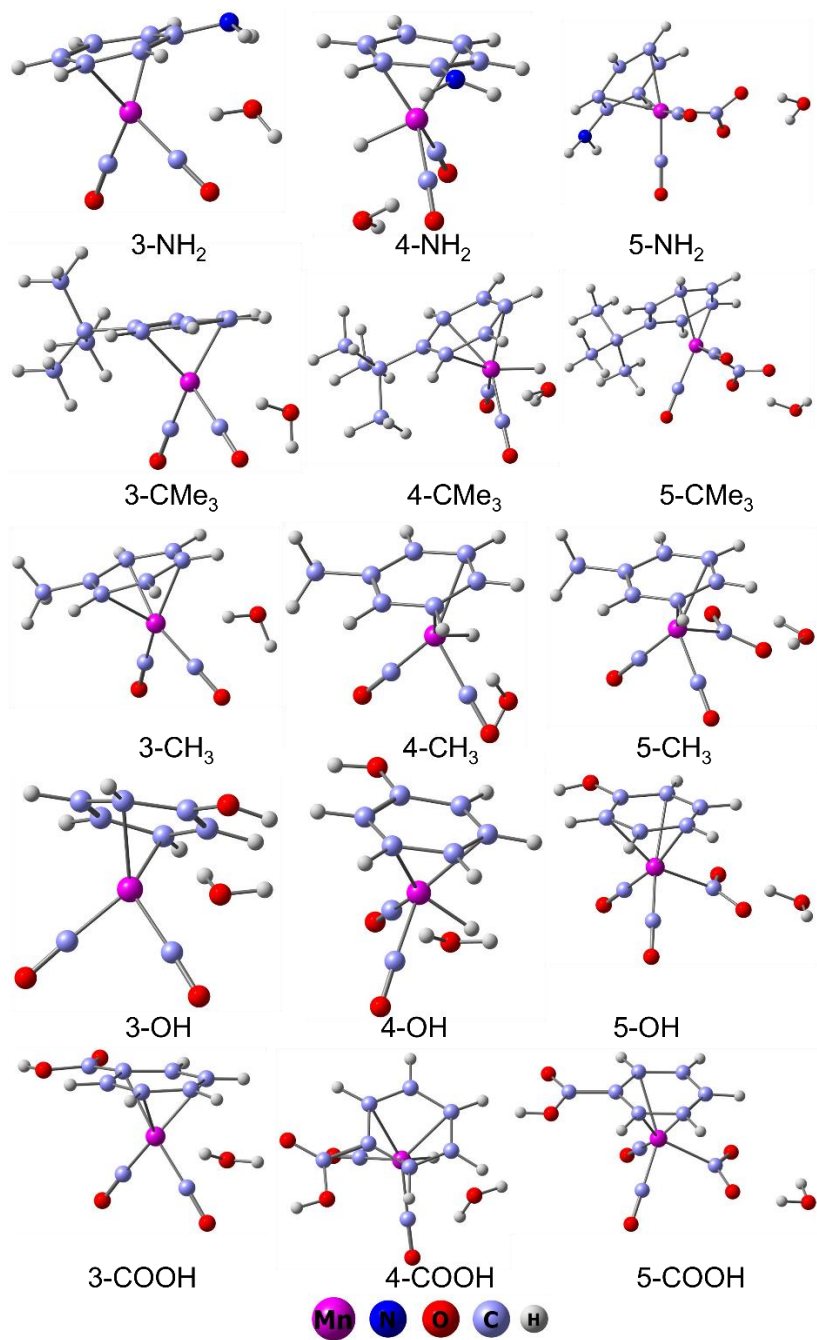
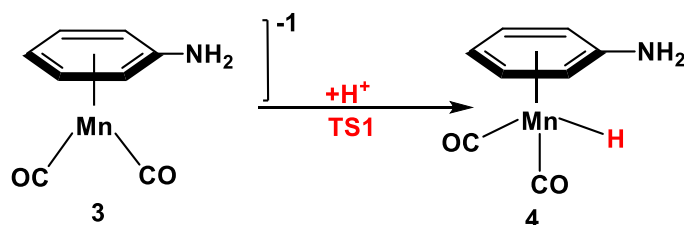


Figure 2.4: Structures of intermediates **3**, **4** and **5** with one explicit water molecule for all the modelled catalysts.

Table 2.4: Calculated reaction free energies (ΔG) and activation barriers (ΔG^\ddagger) of proton and CO₂ reduction reaction of all considered Mn(I) half sandwich-based complexes with one explicit solvent molecule. The

calculated reaction free energies (ΔG) and activation barriers (ΔG^\ddagger) of proton and CO₂ reduction reaction without explicit solvent molecule are shown in parenthesis. All these calculated reaction free energies and barriers are in kcal/mol.

Substituents	Solvents	Proton Reduction	CO ₂ reduction
		3 → 4	3 → 5
NH ₂	Water	-37.9 (-40.4)	-4.5 (-5.1)
CMe ₃	Water	-34.2 (-38.8)	-1.8 (-0.2)
CH ₃	Water	-34.9 (-40.0)	-2.4 (-2.4)
OH	Water	-37.8 (-37.1)	-6.1 (-1.0)
COOH	Water	-25.0 (-30.8)	3.8 (4.2)

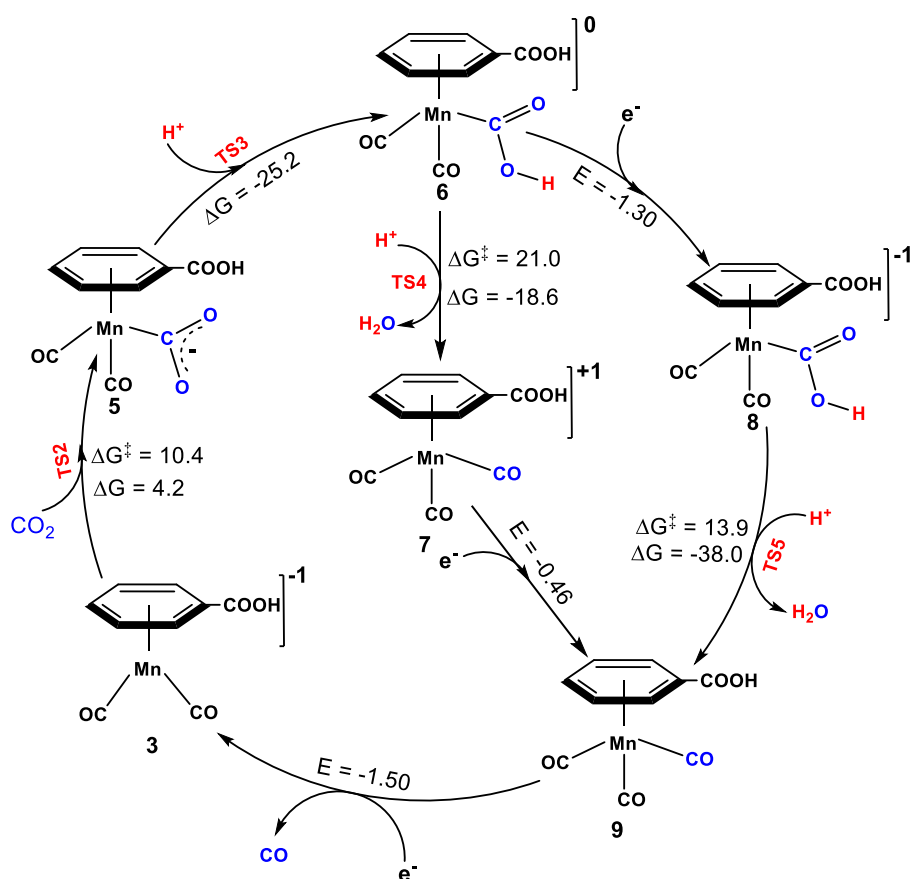


Scheme 2.3: Proton reduction pathways using the NH₂ based Mn(I) half sandwich based active catalyst.

2.3.3. Formation and Breaking of C–OH Bond

The CO₂ reduced intermediate, **5**, does not have any proton source for further reduction. Here, we have considered PhOH as a proton source for this step also. Therefore, intermediate **5** can be protonated in the presence of PhOH, which may lead to C–OH bond cleavage for the formation of CO. Scheme 2.4 shows all possible steps of protonation and C–OH bond cleavage of COOH based Mn(I) half sandwich-based catalyst and the corresponding reaction free energy (ΔG), activation barrier (ΔG^\ddagger) and reduction potential values (E vs. SCE) are given in Table 2.5. There are two reduction mechanism pathways: (i) protonation followed by reduction (**6** → **7** → **9**) and (ii) reduction followed by protonation (**6** → **8** → **9**). Our

calculated reaction free energy values show that the first protonation step (**5** + H⁺ → **6**) is highly exergonic in nature. The calculated activation barriers in the presence of PhOH also show that this is a barrierless process. Even though the protonation step is highly exergonic for all the complexes, NH₂ substitution in the ligand framework of the complex in acetonitrile solvent (-36.1 kcal/mol) is most favourable and COOH substitution in DMSO solvent (-18.3 kcal/mol) is least favourable. Earlier, reports have also shown that the protonation step is highly exergonic [29,30].



Scheme 2.4: Proposed catalytic pathway for the CO₂ reduction reaction to CO catalyzed by the COOH based Mn(I) half sandwich active catalysts **3**. The calculated reaction free energies (ΔG), activation barriers (ΔG^\ddagger) and reduction potential values (E vs. SCE) of COOH substituted Mn(I) half sandwich catalyst in water solvent.

Table 2.5: Calculated reaction free energies (ΔG in kcal/mol), activation barriers (ΔG^\ddagger in kcal/mol) and reduction potentials (E vs. SCE) of CO₂ reduction reaction to CO by Mn(I) half sandwich-based complexes by considering UB3LYP/6-31+G** + LANL2DZ with CPCM solvation model. The calculated UB3LYP/6-311++G** + SDD with SMD solvation model values are shown in parenthesis.

Subs.	Solvents	5→6	6→7	8→9	5→T S3	6→T S4	8→ TS5	6→8	7→9	9→3
NH ₂	Acetonitrile	-36.1 (-42.7)	-33.2 (-39.6)	-56.3 (-59.9)	-1.4 (-1.7)	17.4 (13.7)	6.3 (2.2)	-2.22 (-2.41)	-1.22 (-1.53)	-2.38 (-2.52)
	Water	-29.5 (-24.3)	-28.1 (-31.5)	-49.9 (-47.3)	-1.2 (-) ()	17.3 (15.7)	6.5 (3.5)	-1.87 (-1.86)	-0.93 (-1.17)	-2.03 (-2.10)
	DMSO	-22.6 (-33.5)	-20.3 (-25.8)	-43.0 (-47.1)	-1.3 (-3.8)	17.4 (13.3)	5.6 (3.3)	-1.73 (-1.95)	-0.75 (-1.03)	-1.89 (-2.08)
CMe ₃	Acetonitrile	-32.6	-31.3	-55.4	-0.2	16.2	10.5	-2.13	-1.08	-2.13
	Water	-27.4	-26.1	-49.1	-1.2	16.3	10.6	-1.79	-0.79	-1.78
	DMSO	-20.5	-18.4	-42.0	-1.3	16.2	10.5	-1.64	-0.61	-1.63
CH ₃	Acetonitrile	-34.3	-30.0	-55.1	0.3	19.1	10.7	-2.21	-1.12	-2.11
	Water	-27.7	-24.9	-48.7	0.3	19.1	10.8	-1.86	-0.83	-1.80
	DMSO	-20.8	-17.2	-41.8	0.4	19.1	10.7	-1.71	-0.65	-1.66
OH	Acetonitrile	-34.2	-29.7	-55.6	-1.7	18.9	10.8	-2.19	-1.07	-2.13
	Water	-27.6	-24.6	-49.2	-1.4	18.9	10.9	-1.84	-0.78	-1.77
	DMSO	-20.7	-16.8	-42.2	-1.6	18.8	10.5	-1.70	-0.60	-1.63
COOH	Acetonitrile	-31.8 (-37.1)	-23.6 (-32.6)	-44.3 (-52.8)	- (7.8)	21.0 (15.3)	13.8 (6.2)	-1.64 (-1.99)	-0.75 (-1.11)	-1.85 (-2.09)
	Water	-25.2 (-21.3)	-18.6 (-26.0)	-38.0 (-41.7)	- (6.7)	21.0 (17.8)	13.9 (-)	-1.30 (-1.49)	-0.46 (-0.81)	-1.50 (-1.64)
	DMSO	-18.3 (-26.1)	-10.8 (-19.2)	-33.7 (-40.1)	- (-) 1.7)	21.0 (-)	11.0 (4.9)	-1.27 (-1.54)	-0.28 (-0.63)	-1.35 (-1.62)

In the next step, **6** either can be protonated or reduced for the formation of **7** ($6 + H^+ \rightarrow 7 + H_2O$) or **8** ($6 + e^- \rightarrow 8$), respectively. The calculated reaction

free energies for the formation of **7** in different solvents indicate that acetonitrile is the best solvent. Among all the considered substituents, NH₂ ligand is best in acetonitrile solvent, whereas COOH substituents is bad in DMSO solvent. However, the calculated activation barrier values indicate that the following ordering of substituents, CMe₃ < NH₂ < OH < CH₃ < COOH, is best for the formation of **7**. The calculated reaction free energy and activation barrier values indicate that the step is highly favorable while catalyzed by the Mn(I) half sandwich-based complexes compared to the previously reported some of the highly active catalysts [15,29,30]. Besides, the calculated reduction potential values for **6** + e⁻ → **8** indicate that the formation of intermediate **8** in DMSO is highly favourable compared to that in water and acetonitrile solvents. The reduction potential value (**6** + e⁻ → **8**) of the NH₂ substituted complex in acetonitrile solvent is maximum (-2.22 V), whereas minimum (-1.27 V) for COOH substituted complex in DMSO solvent. These reduction potential values are comparable with the earlier reports, which certainly indicate the considered complexes can be promising for such CO₂ reduction [29,30,37]. However, the calculated reaction free energy values indicate that formation of **7** is more favourable compared to the formation of intermediate **8**. In the next step, intermediate **7** can be reduced (**7** + e⁻ → **9**), whereas intermediate **8** can be protonated (**8** + H⁺ → **9** + H₂O) for the formation of **9**. The calculated reaction free energies for the formation of **9** through protonation (**8** + H⁺ → **9** + H₂O) is highly favourable. Again, NH₂ substituent favors formation of **9** (-56.3 kcal/mol) in the acetonitrile solvent, whereas COOH substitution is not good for the formation of **9** in DMSO solvent (-33.7 kcal/mol). Even, the calculated activation barrier value suggests that the formation of **9** is kinetically more favourable in case of NH₂ substitution (6.3 kcal/mol in acetonitrile), whereas less favourable in case of COOH substitution (13.8 kcal/mol in acetonitrile). Besides, the calculated reduction potential values of **7** + e⁻ → **9** step show that the formation of intermediate **9** in DMSO is favourable compared to that in acetonitrile and water solvents. The

reduction potential of NH₂ substituent in acetonitrile is maximum (-1.22 V) whereas minimum (-0.28 V) for COOH substituent in DMSO solvent. These reduction potential values show that the step is also highly favourable. Hence, formation of **9** via protonation followed by reduction (**6** → **7** → **9**) is more favourable compared to the reduction followed by protonation (**6** → **8** → **9**) pathway. In the next step intermediate **9** can be reduced through one electron reduction for the completion of the catalytic cycle as it would release back the active catalyst **3** along with CO. This step is calculated to be favourable in DMSO solvent compared to that in water and acetonitrile solvents. Our calculated results, earlier absolute reduction potential values of SCE and absolute reaction free energy of proton show that the protonation step is highly favourable in acetonitrile compared to that in water and DMSO solvent. Besides, the reduction step is highly favourable in DMSO solvent compared to that in water and acetonitrile solvents. Therefore, water is the best solvent for the electrochemical CO₂ reduction to CO by Mn(I) half sandwich-based catalysts as electrochemical CO₂ reduction reaction proceeds via both protonation and reduction steps. Alongside, our calculated results show that COOH substitution is the best in Mn(I) half sandwich-based catalysts for the electrochemical CO₂ reduction reaction to CO. Moreover, the possibilities for hydrogen bond formation between the substituent and adsorbed *CO₂ in 3D geometric shape in structure **5** of COOH based Mn(I) half sandwich complexes has been checked. Figure 2.5 shows that there is a little possibility of hydrogen bond formation between the substituent and the adsorbed *CO₂ in 3D geometric shape. We have also calculated the reaction free energies (ΔG), activation barriers (ΔG^\ddagger) and reduction potentials of CO₂ reduction steps for NH₂ and COOH based Mn(I) half sandwich complexes using the UB3LYP/6-311++G** + SDD with SMD solvation model and the calculated values are listed in Table 2.5. The calculated reaction free energies (ΔG), activation barriers (ΔG^\ddagger) and reduction potential values are comparable with the UB3LYP/6-31+G** + LANL2DZ and CPCM

solvation model. Therefore, UB3LYP/6-31+G** + LANL2DZ and CPCM is good enough for CO₂ reduction reactions using Mn(I) half sandwich-based catalysts.

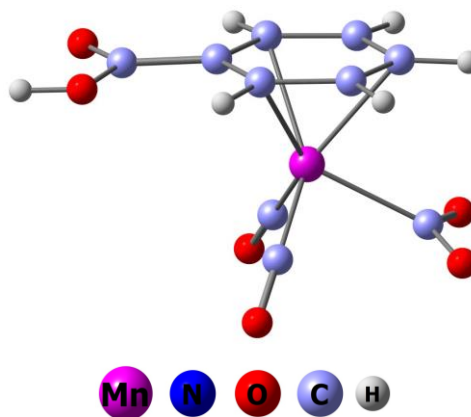


Figure 2.5: Intermediate 5 for COOH based Mn(I) half sandwich complex.

2.4. Conclusions

In this study, a series of Mn(I) half sandwich-based complexes have been explored in acetonitrile, water and DMSO solvents for the electrochemical CO₂ reduction to CO. Interestingly, for active site formation, substitution effect is found to be very significant for second reduction potential value compared to the first reduction potential value. The redox property of the half sandwich ligand moiety changes with substitution. Therefore, the ligand of the catalyst behaves as a redox ligand and found to be very effective due to substitution. Besides, our calculated results show that the active catalyst formation is more favourable in DMSO solvent whereas protonation is more favourable in acetonitrile solvent compared to other. Therefore, water is the best solvent as the electrochemical CO₂ reduction reaction proceeds through both the steps. The selectivity of CO₂ vs proton reduction reaction has also been explored and we have found out that proton reduction is thermodynamically favourable whereas CO₂ reduction is kinetically favourable. The substitution effects further show that the ligand substitution such as COOH is the best for electrochemical CO₂ reduction

reaction (CO₂ to CO) as it improves one of the rate-determining steps (C-OH bond cleavage step) significantly. Therefore, all these results indicate that substitution and solvent effects can play major roles towards the designing of efficient electrocatalysts for CO₂ reduction reactions.

2.5. References

1. Riplinger C., Sampson M.D., Ritzmann A.M., Kubiak C.P., Carter E.A. (2014), Mechanistic Contrasts between Manganese and Rhenium Bipyridine Electrocatalysts for the Reduction of Carbon Dioxide, *J. Am. Chem. Soc.*, 136, 16285–16298 (DOI: 10.1021/ja508192y)
2. Zhang W., Hu Y., Ma L., Zhu G., Wang Y., Xue X., Chen R., Yang S., Jin Z. (2018), Progress and Perspective of Electrocatalytic CO₂ Reduction for Renewable Carbonaceous, *Adv. Sci.*, 5, 1700275 (DOI:10.1002/advs.201700275).
3. Schmidt F., Swiderek P., Bredehöf J.H. (2019), Formation of Formic Acid, Formaldehyde, and Carbon Dioxide by Electron-Induced Chemistry in Ices of Water and Carbon Monoxide, *ACS Earth Space Chem.*, 3, 1974–1986 (DOI: 10.1021/acsearthspacechem.9b00168).
4. Lange J.P. (2001), Methanol synthesis: a short review of technology improvements, *Catal. Today*, 64, 3–8 (DOI:10.1016/S0920-5861(00)00503-4).
5. Martin O., Perez-Ramirez J. (2013), New and revisited insights into the promotion of methanol synthesis catalysts by CO₂, *Catal. Sci. Technol.*, 3, 3343–3352 (DOI: 10.1039/c3cy00573a).
6. Wiedner E.S., Appel A.M. (2014), Thermochemical Insight into the Reduction of CO to CH₃OH with [Re(CO)]⁺ and [Mn(CO)]⁺ Complexes, *J. Am. Chem. Soc.*, 136, 8661–8668 (DOI: 10.1021/ja502316e).
7. Mandal S.C., Rawat K.S., Garg P., Pathak B. (2019), Hexagonal Cu(111) Monolayers for Selective CO₂ Hydrogenation to CH₃OH:

- Insights from Density Functional Theory, *ACS Appl. Nano Mater.*, **2**, 7686–7695 (DOI: 10.1021/acsanm.9b01751).
8. Franke R., Selent D., Borner E. (2012), *Applied Hydroformylation*, *Chem. Rev.*, **112**, 5675–5732 (DOI: 10.1021/cr3001803).
 9. Beley M., Collin J., Ruppert R., Sauvage J.-P. (1986), *Electrocatalytic Reduction of CO₂ by Ni Cyclam²⁺ in Water: Study of the Factors Affecting the Efficiency and the Selectivity of the Process*, *J. Am. Chem. Soc.*, **108**, 7461–7467 (DOI: 10.1021/ja00284a003).
 10. Fujita E., Haff J., Sanzenbacher R., Elias H. (1994), *High Electrocatalytic Activity of RRSS-[Ni^{II}DMC](ClO₄)₂ and [Ni^{II}DMC](ClO₄)₂ for Carbon Dioxide Reduction (HTIM = 2,3,9,10-Tetramethyl-1,4,8,11-tetraazacyclotetradecane, DMC = C-meso-5,12-Dimethyl-1,4,8,11-tetraazacyclotetradecane*, *Inorg. Chem.*, **33**, 4627–4628 (DOI: 10.1021/ic00099a011).
 11. Clark M.L., Grice K.A., Moore C.E., Rheingold A.L., Kubiak C.P. (2014), *Electrocatalytic CO₂ reduction by M(bpy-R)(CO)₄ (M = Mo, W; R = H, tBu) complexes. Electrochemical, spectroscopic, and computational studies and comparison with group 7 catalysts*, *Chem. Sci.*, **5**, 1894–1900 (DOI: 10.1039/C3SC53470G).
 12. Portenkirchner E., Kianfar E., Sariciftci N.S., Knör G. (2014), *Two-Electron Carbon Dioxide Reduction Catalyzed by Rhenium(I) Bis(imino)acenaphthene Carbonyl Complexes*, *ChemSusChem*, **7**, 1347–1351 (DOI: 10.1002/cssc.201301116).
 13. Song J., Klein K.L., Neese F., Ye S. (2014), *The Mechanism of Homogeneous CO₂ Reduction by Ni(cyclam): Product Selectivity, Concerted Proton–Electron Transfer and C–O Bond Cleavage*, *Inorg. Chem.*, **53**, 7500–7507 (DOI: 10.1021/ic500829p).
 14. Agarwal J., Fujita E., Schaefer H.F., III, Muckerman J.T. (2012), *Mechanisms for CO Production from CO₂ Using Reduced Rhenium Tricarbonyl Catalysts*, *J. Am. Chem. Soc.*, **134**, 5180–5186 (DOI: 10.1021/ja2105834).

15. Keith J.A., Grice K.A., Kubiak C.P., Carter E.A. (2013), Elucidation of the Selectivity of Proton-Dependent Electrocatalytic CO₂ Reduction by fac-Re(bpy)(CO)₃Cl, *J. Am. Chem. Soc.*, 135, 15823–15829 (DOI: 10.1021/ja406456g).
16. Smieja J.M., Kubiak C.P. (2010), Re(bipy-tBu)(CO)₃Cl-improved Catalytic Activity for Reduction of Carbon Dioxide: IR-Spectroelectrochemical and Mechanistic Studies, *Inorg. Chem.*, 49, 9283–9289 (DOI: 10.1021/ic1008363).
17. Chen Z., Concepcion J.J., Brennaman M.K., Kang P., Norris M.R., Hoertz P.G., Meyer T.J. (2012), Splitting CO₂ into CO and O₂ by a single catalyst, *PNAS*, 109, 15606–15611 (DOI: 10.1073/pnas.1203122109).
18. Chabolla S.A., Machan C.W., Yin J., Dellamary E.A., Sahu S., Gianneschi N.C., Gilson M.K., Tezcan F.A., Kubiak C.P. (2017), Bio-inspired CO₂ reduction by a rhenium tricarbonyl bipyridine-based catalyst appended to amino acids and peptidic platforms: incorporating proton relays and hydrogen-bonding functional groups, *Faraday Discuss.*, 198, 279–300 (DOI: 10.1039/C7FD00003K).
19. Elgrishi N., Chambers M.B., Wang X. (2017), Fontecave M., Molecular polypyridine-based metal complexes as catalysts for the reduction of CO₂, *Chem. Soc. Rev.*, 46, 761–796 (DOI: 10.1039/C5CS00391A).
20. Hawecker J., Lehn J.M., Ziessel R. (1984), Electrocatalytic Reduction of Carbon Dioxide Mediated by Re(bipy)(CO)₃Cl (bipy = 2,2'-bipyridine), *J. Chem. Soc., Chem. Commun.*, 328 – 330 (DOI: 10.1039/C39840000328).
21. Hawecker J., Lehn J.M., Ziessel R. (1986), Photochemical and Electrochemical Reduction of Carbon Dioxide to Carbon Monoxide Mediated by (2,2'-Bipyridine)tricarbonylchlororhenium(I) and Related Complexes as Homogeneous Catalysts, *Helv. Chim. Acta* 69, 1990 – 2012 (DOI: 10.1002/hlca.19860690824).

22. Benson E.E., Kubiak C.P. (2012), Structural investigations into the deactivation pathway of the CO₂ reduction electrocatalyst Re(bpy)(CO)₃Cl, *Chem. Commun.*, 48, 7374 – 7376 (DOI: 10.1039/C2CC32617E).
23. Machan C.W., Sampson M.D., Chabolla S.A., Dang T., Kubiak C.P. (2014), Developing a Mechanistic Understanding of Molecular Electrocatalysts for CO₂ Reduction using Infrared Spectroelectrochemistry, *Organometallics*, 33, 4550 – 4559 (DOI: 10.1021/om500044a).
24. Machan C.W., Chabolla S.A., Yin J., Gilson M.K., Tezcan F.A., Kubiak C.P. (2014), Supramolecular Assembly Promotes the Electrocatalytic Reduction of Carbon Dioxide by Re(I) Bipyridine Catalysts at a Lower Overpotential, *J. Am. Chem. Soc.*, 136, 14598 – 14607 (DOI: 10.1021/ja5085282).
25. Grützmacher H. (2008), Cooperating Ligands in Catalysis, *Angew. Chem. Int. Ed.*, 47, 1814-1818 (DOI: 10.1002/anie.200704654).
26. Van der Vlugt J.I., Reek J.N.H. (2009), Neutral Tridentate PNP Ligands and Their Hybrid Analogues: Versatile Non-Innocent Scaffolds for Homogeneous Catalysis, *Angew. Chem. Int. Ed.*, 48, 8832 – 8846 (DOI: 10.1002/anie.200903193).
27. Bourrez M., Molton F., Chardon-Noblat S., Deronzier A. (2011), [Mn(bipyridyl)(CO)₃Br]: An Abundant Metal Carbonyl Complex as Efficient Electrocatalyst for CO₂ Reduction, *Angew. Chem. Int. Ed.*, 50, 9903 – 9906 (DOI: 10.1002/anie.201103616).
28. Bourrez M., Orio M., Molton F., Vezin H., Duboc C., Deronzier A., Chardon-Noblat S. (2014), Pulsed-EPR Evidence of a Manganese(II) Hydroxycarbonyl Intermediate in the Electrocatalytic Reduction of Carbon Dioxide by a Manganese Bipyridyl Derivative, *Angew. Chem. Int. Ed.*, 53, 240 – 243 (DOI: 10.1002/anie.201306750).
29. Rawat K.S., Mahata A., Choudhuri I., Pathak B. (2016), N-Heterocyclic Carbene-Based Mn Electrocatalyst for Two-Electron

- CO₂ Reduction over Proton Reduction, *J. Phys. Chem. C*, 120, 8821–8831 (DOI: 10.1021/acs.jpcc.6b02209).
30. Rawat K.S., Mandal S.C., Pathak B. (2019), A computational study of electrocatalytic CO₂ reduction by Mn(I) complexes: Role of bipyridine substituents, *Electrochim. Acta*, 297, 606–612, (DOI: 10.1016/J.ELECTACTA.2018.11.210).
 31. Zeng Q., Tory J., Hartl F. (2014), Electrocatalytic Reduction of Carbon Dioxide with a Manganese(I) Tricarbonyl Complex Containing a Nonaromatic α -Diimine Ligand, *Organometallics*, 33, 5002–5008 (DOI: 10.1021/om500389y).
 32. Shvydkiy N.V., Vyhivskiy O., Nelyubina Y.V., Perekalin D.S. (2019), Design of Manganese Phenol Pi-complexes as Shvo-type Catalysts for Transfer Hydrogenation of Ketones, *ChemCatChem* 11, 1602–1605 (DOI: 10.1002/cctc.201801797).
 33. Agarwal J., Stanton III C.J., Shaw T.W., Vandezande J.E., Majetich G.F., Bocarsly A.B., Schaefer H.F., III (2015), Exploring the effect of axial ligand substitution (X = Br, NCS, CN) on the photodecomposition and electrochemical activity of [MnX(N–C)(CO)₃] complexes, *Dalton Trans.*, 44, 2122–2131 (DOI: 10.1039/C4DT03079F).
 34. Walsh J.J., Neri G., Smith C.L., Cowan A.J. (2019), Water-Soluble Manganese Complex for Selective Electrocatalytic CO₂ Reduction to CO, *Organometallics*, 38, 1224–1229 (DOI: 10.1021/acs.organomet.8b00336).
 35. Costentin C., Robert M., Savéant J.-M., Tatin A. (2015), Efficient and selective molecular catalyst for the CO₂-to-CO electrochemical conversion in water, *PNAS*, 112, 6882–6886 (DOI: 10.1073/pnas.1507063112).
 36. Smieja J.M., Sampson M.D., Grice K.A., Benson E.E., Froehlich J.D., Kubiak C.P. (2013), Manganese as a Substitute for Rhenium in CO₂

- Reduction Catalysts: The Importance of Acids, *Inorg. Chem.*, 52, 2484–2491 (DOI: 10.1021/ic302391u).
37. Clark M.L., Cheung P.L., Lessio M., Carter E.A., Kubiak C. P. (2018), Kinetic and Mechanistic Effects of Bipyridine (bpy) Substituent, Labile Ligand, and Brønsted Acid on Electrocatalytic CO₂ Reduction by Re(bpy) Complexes, *ACS Catal.*, 8, 2021–2029 (DOI: 10.1021/ACSCATAL.7B03971).
 38. Frisch M.J. et al. (2013), Gaussian Revision D.01, Gaussian, Inc., Wallingford CT.
 39. Becke A.D. (1993), Density-Functional Thermochemistry. III. The Role of Exact Exchange, *J. Chem. Phys.*, 98, 5648-5652 (DOI: 10.1063/1.464913).
 40. Becke A.D. (1996), Density-functional Thermochemistry. IV. A New Dynamical Correlation Functional and Implications for Exact-Exchange Mixing, *J. Chem. Phys.*, 104, 1040-1046 (DOI: 10.1063/1.470829).
 41. Lee C.T., Yang W.T., Parr R.G. (1988), Development of the Colle-Salvetti Correlation-Energy Formula into a Functional of the Electron Density, *Phys. Rev. B Condens. Matter*, 37, 785-789 (DOI: 10.1103/physrevb.37.785).
 42. Clark T., Chandrasekhar J., Spitznagel G.W., Schleyer P.V.R. (1983), Efficient Diffuse Function-Augmented Basis Sets for Anion Calculations. III. The 3-21+G Basis Set for First-Row Elements, Li–F, *J. Comput. Chem.*, 4, 294 – 301 (DOI:10.1002/JCC.540040303).
 43. Hariharan P.C., Pople J.A. (1973), The Influence of Polarization Functions on Molecular Orbital Hydrogenation Energies, *Theor. Chim. Acta*, 28, 213 – 222 (DOI: 10.1007/BF00533485).
 44. Krishnan R., Binkley J.S., Seeger R., Pople J.A. (1980), Self-consistent molecular orbital methods. XX. A basis set for correlated

- wave functions, *J. Chem. Phys.*, 72, 650–654 (DOI: 10.1063/1.438955).
45. Hay P.J., Wadt W.R. (1985), Ab initio effective core potentials for molecular calculations. Potentials for the transition metal atoms Sc to Hg, *J. Chem. Phys.*, 82, 270 – 283 (DOI: 10.1063/1.448799).
 46. Grimme S., Antony J., Ehrlich S., Krieg H. (2010), A consistent and accurate ab initio parametrization of density functional dispersion correction (DFT-D) for the 94 elements H-Pu, *J. Chem. Phys.*, 132, 154104–154123 (DOI: 10.1063/1.3382344).
 47. Cossi M., Rega N., Scalmani G., Barone V. (2003), Energies, structures, and electronic properties of molecules in solution with the C-PCM solvation model, *J. Comput. Chem.*, 24, 669–681 (DOI: 10.1002/jcc.10189).
 48. Barone V., Cossi M. (1998), Quantum Calculation of Molecular Energies and Energy Gradients in Solution by a Conductor Solvent Model, *J. Phys. Chem. A*, 102, 1995–2001 (DOI: 10.1021/jp9716997).
 49. Oolg M., Wedig U., Stoll H., Preuss H. (1987), Energy-adjusted ab initio pseudopotentials for the first row transition elements, *J. Chem. Phys.*, 86, 866–872 (DOI: 10.1063/1.452288).
 50. Boulbazine M., Boudjahem A.-G. (2019), Stability, Electronic and Magnetic Properties of Mn-Doped Copper Clusters: A Meta-GGA Functional Investigation, *J. Clust. Sci.*, 30, 31–44 (DOI: 10.1007/s10876-018-1456-5).
 51. Marenich A.V., Cramer C.J., Truhlar D. G. (2009), Universal Solvation Model Based on Solute Electron Density and on a Continuum Model of the Solvent Defined by the Bulk Dielectric Constant and Atomic Surface Tensions, *J. Phys. Chem. B*, 113, 6378–6396 (DOI: 10.1021/jp810292n).
 52. Marenich A. V., Ho J., Coote M., Cramer C.J. (2014), Truhlar D.G., Computational electrochemistry: prediction of liquid-phase reduction

- potentials, *Phys. Chem. Chem. Phys.*, 16, 15068–15106 (DOI: 10.1039/C4CP01572J).
53. Fawcett W.R. (2008), The Ionic Work Function and its Role in Estimating Absolute Electrode Potentials, *Langmuir*, 24, 9868-9875 (DOI: 10.1021/la7038976).
54. Isse A.A., Gennaro A. (2010), Absolute Potential of the Standard Hydrogen Electrode and the Problem of Interconversion of Potentials in Different Solvents, *J. Phys. Chem. B*, 114, 7894–7899 (DOI: 10.1021/jp100402x).
55. Kelly C.P., Cramer C.J., Truhlar D.G. (2007), Single-Ion Solvation Free Energies and the Normal Hydrogen Electrode Potential in Methanol, Acetonitrile, and Dimethyl Sulfoxide, *J. Phys. Chem. B*, 111, 408-422 (DOI: 10.1021/jp065403l).
56. Kelly C.P., Cramer C.J., Truhlar D.G. (2006), Aqueous Solvation Free Energies of Ions and Ion–Water Clusters Based on an Accurate Value for the Absolute Aqueous Solvation Free Energy of the Proton, *J. Phys. Chem. B*, 110, 16066-16081 (DOI: 10.1021/jp063552y).
57. Palascak M. W., Shields G. C. (2004), Accurate Experimental Values for the Free Energies of Hydration of H^+ , OH^- , and H_3O^+ , *J. Phys. Chem. A*, 108, 3692-3694 (DOI: 10.1021/jp049914o).
58. Glendening E.D., Reed A.E., Carpenter J.E., Weinhold F., NBO, Version 3.1.
59. Walsh J.J., Neri G., Smith C.L., Cowan A.J. (2014), Electrocatalytic CO_2 reduction with a membrane supported manganese catalyst in aqueous solution, *Chem. Commun.*, 50, 12698-12701 (DOI: 10.1039/C4CC06404F).
60. Kelly C.P., Cramer C.J., Truhlar D.G. (2006), Adding Explicit Solvent Molecules to Continuum Solvent Calculations for the Calculation of Aqueous Acid Dissociation Constants, *J Phys Chem A*, 110, 2493–2499 (DOI: 10.1021/jp055336f).

Chapter 3

*CO₂ Hydrogenation to HCOOH Using
Earth Abundant Homogenous Based Mn-
Catalysts*

3.1. Introduction

Catalytic conversion of CO₂ to liquid fuels (formic acid, methanol, dimethyl ether, higher alcohols) using molecular hydrogen is one of the promising ways to store hydrogen [1,2]. Formic acid is an important liquid-based hydrogen storage compound that contains 4.38 wt.% of hydrogen. Therefore, the development of a molecular catalyst for this has attracted considerable attention from the scientific community. In last three decades, several highly active and selective molecular catalysts have been reported for CO₂ hydrogenation reaction for the formation of formic acid/formate anion (a hydrogen storage material) [3-25]. Inoue *et al.*, have reported one of the first homogeneous catalysts RhCl(PPh₃)₃ for CO₂ hydrogenation [4]. After that, several noble metals (Ir, Ru, Rh etc.) based catalysts have been reported experimentally as well as computationally for homogeneous CO₂ hydrogenation to formic acid/formate anion [3-23]. Initially, noble metal-based catalysts have been primarily studied for catalytic CO₂ hydrogenation reaction. Though noble metal-based catalysts show high catalytic activity, but their industrial use is restricted due to low abundance and the high cost of the metal. So, it is very important to design a cheap catalyst with earth abundant (Mn, Fe, Co, Ni etc.) metal based complexes [24-43]. Generally, the catalytic activity of the non-noble metal-based catalyst is far from the noble metal-based catalysts. Therefore, it is very important to understand the mechanistic pathway of the catalytic reaction to improve their activity. In this context, several studies suggest that heterolytic H₂ cleavage and hydride transfer are the rate-determining steps for CO₂ hydrogenation reaction [8-51]. Therefore, modifications have been done in the ligand site to improve the rate-determining steps *via* involvement of the ligand in the reaction. For this, Hazari and co-workers have reported a series of aromatic PNP [PNP = 2,6-bis(dialkylphosphinomethyl)pyridine] ligand based Ir(III) complexes, where the PNP ligand behaves as a non-innocent ligand and favors the heterolytic H₂ cleavage *via* a metal-ligand cooperation mechanism [50]. Several other groups have reported PNP based metal

complexes (Ir, Fe, Co etc.) for CO₂ hydrogenation reaction, where the heterolytic H₂ cleavage is done using an external base [15,16]. Gonsalvi and co-workers have reported a series of highly active Mn-PNP based complexes with a maximum TON of 30,000 for CO₂ hydrogenation to formate in the presence of LiOTf Lewis acid co-catalyst [33]. Their Mn(I) hydrido PNP complex reported to be one of the most active Mn(I) based catalysts for CO₂ hydrogenation reaction. However, their computational study shows that the N–H bond may or may not participate in the reaction mechanism as the calculated total barriers are very much comparable (within 2 kcal/mol). However, Yang and Ahlquist have also found that the external base assisted heterolytic H₂ cleavage is more favorable compared to the ligand assisted heterolytic H₂ cleavage [15,52]. Further to this, pendant ligand containing oxyanion acts as a base and helps in heterolytic H₂ cleavage. Our group has also reported a series of pendant amine-based Fe complexes, where pendant amine initiates the heterolytic H₂ cleavage [26]. All these previous studies suggest that the active participation of ligand is very important for CO₂ hydrogenation reaction. Interestingly, there have been reports that catalysts with N–H functionality (present in the primary coordination sphere) play a crucial role in hydride/proton transfer in the hydrogenation reaction. Such N–H functionality actively participates in the catalytic reaction *via* formation/cleavage of the N–H bond through metal-ligand cooperation as stated by Noyori, Ikariya, and co-workers in the classical asymmetric ketone hydrogenation reaction [53,54]. They suggest that the N–H functionality is very important for the heterolytic H₂ cleavage and proton transfer reaction. However, Dub *et al.*, have proposed a revised Noyori mechanism and suggest that N–H functionality does not participate actively in the reaction. However, N–H functionality stabilizes the oxy-anion intermediate *via* formation of strong N–H···O hydrogen-bonding interactions [55-59]. This anionic intermediate further initiates the heterolytic H₂ cleavage. Inspired by these studies, we have tried to understand the role of N–H functionality in CO₂ hydrogenation. For CO₂

hydrogenation, we predict formate anion can be a promising oxy-anion intermediate, which can also be stabilized through N–H···O hydrogen-bonding interactions and may favour the heterolytic H₂ cleavage. Recently Bruneau–Voisine *et al.*, have demonstrated that Mn(I)-2-(aminomethyl)pyridine and Mn(I)-2-(methylaminomethyl)pyridine complexes are promising for aldehyde and ketone hydrogenation [60]. Furthermore, manganese catalyzed CO₂ hydrogenation and transfer hydrogenation with aminomethylpyridine type ligands have been known [61,62]. Therefore, we believe that Mn(I)-aminomethyl type of bifunctional catalysts may be promising for CO₂ hydrogenation reaction. Therefore, to investigate the role of N–H functionality in the CO₂ hydrogenation reaction, we have modelled a series of phosphine free 2-aminomethylpyridine ligand-based manganese (I) complexes (Figure 3.1). Furthermore, we have modified the pyridine moiety with other moieties to understand the role of the ligand for CO₂ hydrogenation reaction.

3.2. Computational Details

We have used density functional theory (DFT) as implemented in Gaussian 09 D.01 for electronic structure and energy calculations [63]. For this, Becke's three-parameter exchange and Lee-Yang-Parr's correlation functional (B3LYP) have been used for all the calculations [64-67]. Pople's 6-31++G(d, p) and LANL2DZ–ECP (effective core potential) basis sets have been used for non-metals (C, H, O, and N) and Mn, respectively [68-72]. DFT–D3 version of Grimme's dispersion correction has been extended with B3LYP functional to describe the non-covalent interactions effectively [73]. The accuracy of the B3LYP hybrid density functional is well demonstrated by previous studies on CO₂ reduction and hydrogenation reaction by Mn(I) catalyst [26,43,74]. In experiments, THF is one of most used solvents for CO₂ hydrogenation reaction [9,11,13]. Therefore, conductor-like polarizable continuum model (CPCM) has been used to account the solvent effect ($\epsilon=7.4257$ for THF) in our calculations [75,76].

Vibrational frequency analysis has been performed to ensure the stationary points with no imaginary frequencies for intermediates. On the other hand, transition states have been characterized by the single imaginary frequency along the reaction coordinate and further confirmed by the intrinsic reaction coordinate (IRC) calculation. The reaction free energies have been calculated at 298.15 K and 1 atmospheric pressure. Zero-point energy and thermal corrections have been incorporated into the electronic energies to obtain the reaction free energy. The reaction free energies (ΔG) have been calculated from the energy difference between final and initial states and the energy barriers (ΔG^\ddagger) have been calculated from the free energy change between the transition state and reactant. The bond affinity of the metal complexes has been studied through the non-covalent interaction using the NCI package, which has been further visualized by VMD program [77-79]. The atomic electron contribution in bonding orbitals have been investigated using natural bond orbital (NBO) as implemented in Gaussian 09 [80].

3.3. Results and Discussion

For ketone and aldehyde hydrogenation reactions, the Mn(I)-2-(aminomethyl)pyridine based complexes show promising catalytic activity [60]. Inspired by these findings, we have modelled a series of aminomethylpyridine based Mn complexes (Figure 3.1) for CO₂ hydrogenation reaction. Besides, some of these complexes are modelled by changing the pyridine moiety with imidazole, imidazoline, and N-heterocyclic carbene (NHC) moieties to understand the role of the ligand. For simplicity, the Mn(I)-2-(aminomethyl)pyridine and Mn(I)-2-(methylaminomethyl)pyridine complexes are designated as **Mn-AMP** and **Mn-MAMP**, respectively. In case of **Mn-MAMP**, a methyl group substitutes one of the protic hydrogens. Similarly, imidazole, imidazoline and NHC substituted moieties are referred as **Mn-AMI** [Mn(I)-2-(aminomethyl)imidazole], **Mn-AMIM** [Mn(I)-2-(aminomethyl)imidazoline], and **Mn-AMNHC** [Mn(I)-2-(aminomethyl)N-heterocycliccarbene], respectively, whereas methyl

substituted imidazole, imidazoline and NHC named as **Mn-MAMI** [Mn(I)-2-(methylaminomethyl)imidazole], **Mn-MAMIM** [Mn(I)-2-(methylaminomethyl)imidazoline], and **Mn-MAMNHC** [Mn(I)-2-(methylaminomethyl)N-heterocycliccarbene], respectively.

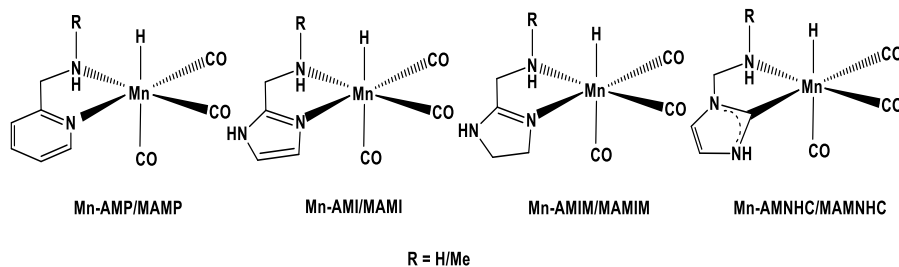


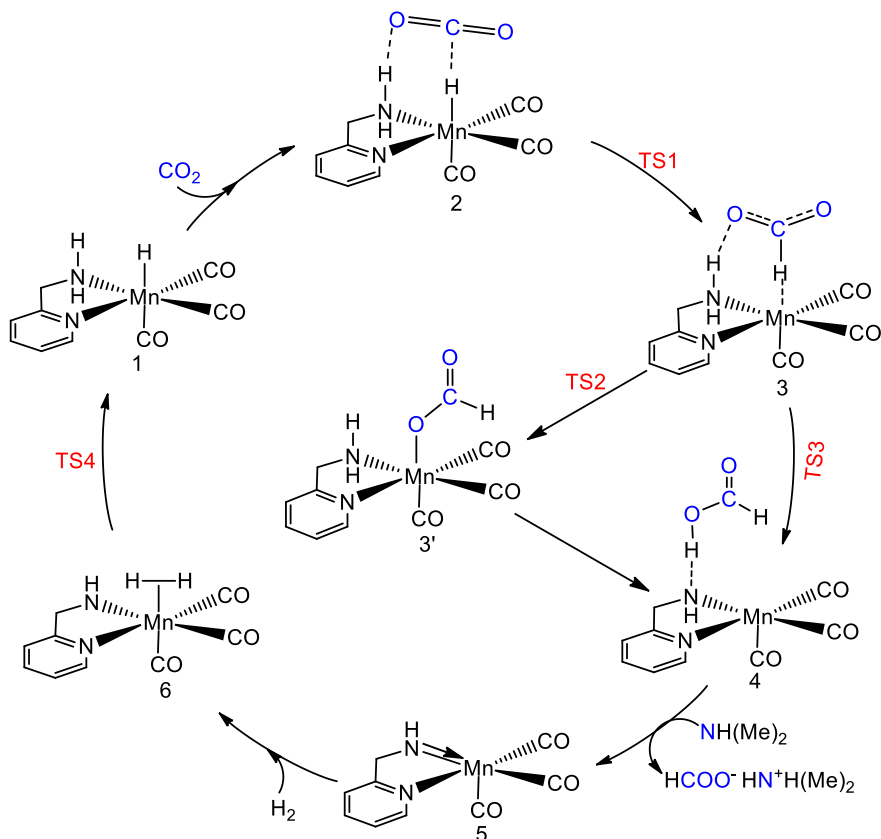
Figure 3.1: Structure of modelled Mn(I) complexes for CO₂ hydrogenation reaction.

Several possible mechanistic pathways have been investigated to understand the exact mechanistic pathway for CO₂ hydrogenation. In the classical Noyori mechanism for ketone hydrogenation, N–H bond actively participates in the reaction *via* cleavage/formation of N–H bond [53,54]. Alternatively, we predict that N–H bond may not like to actively participate in the reaction mechanism but may play a crucial role in stabilizing the oxy-anionic intermediate [55-59]. Based on these two possibilities, our study has been divided into two parts (i) ligand participated mechanism and (ii) ligand assisted mechanism.

3.3.1. Ligand Participated Mechanism

Here, Scheme 3.1 shows the ligand involved mechanism for CO₂ hydrogenation by the **Mn-AMP** catalyst. **Mn-AMP** has a hydridic (Mn–H) and protic (N–H) hydrogen atoms and both of these hydrogen atoms can actively participate in the reaction mechanism. This is analogous to the mechanism proposed by Noyori for ketone hydrogenation, where proton-transfer from N–H and hydride-transfer from M–H occur simultaneously [53,54]. Therefore, we predict that reaction can start with CO₂ binding to **1**

for the formation of **2** ($1 + \text{CO}_2 \rightarrow 2$).



Scheme 3.1: Proposed ligand participated CO₂ hydrogenation reaction mechanism for **Mn-AMP** complex.

Here, carbon/oxygen atom of CO₂ may simultaneously interact (Figure 3.2) with the hydridic/protic hydrogen atom of **1** for the formation of **2**. Then the intermediate **2** may proceed further for hydride transfer for the formation of **3** via transition state **TS1** (Figure 3.3). Figure 3.4 presents reaction free energy profile for Scheme 3.1. The calculated free energy barrier for hydride transfer is 3.3 kcal/mol for the **Mn-AMP** complex. This indicates that such complex requires a low free energy barrier for hydride transfer, which is an important step for CO₂ hydrogenation reaction. Furthermore, intermediate **3** can isomerize into a more stable intermediate **3'** via transition state **TS2**. The free energy barrier for this step (**3** → **3'**) is 5.1 kcal/mol and intermediate **3'** is 13.6 kcal/mol more stable than **3**. All these indicate that

Mn–O bond formation is favored due to the more electronegative nature of the oxygen atom over hydrogen atom.

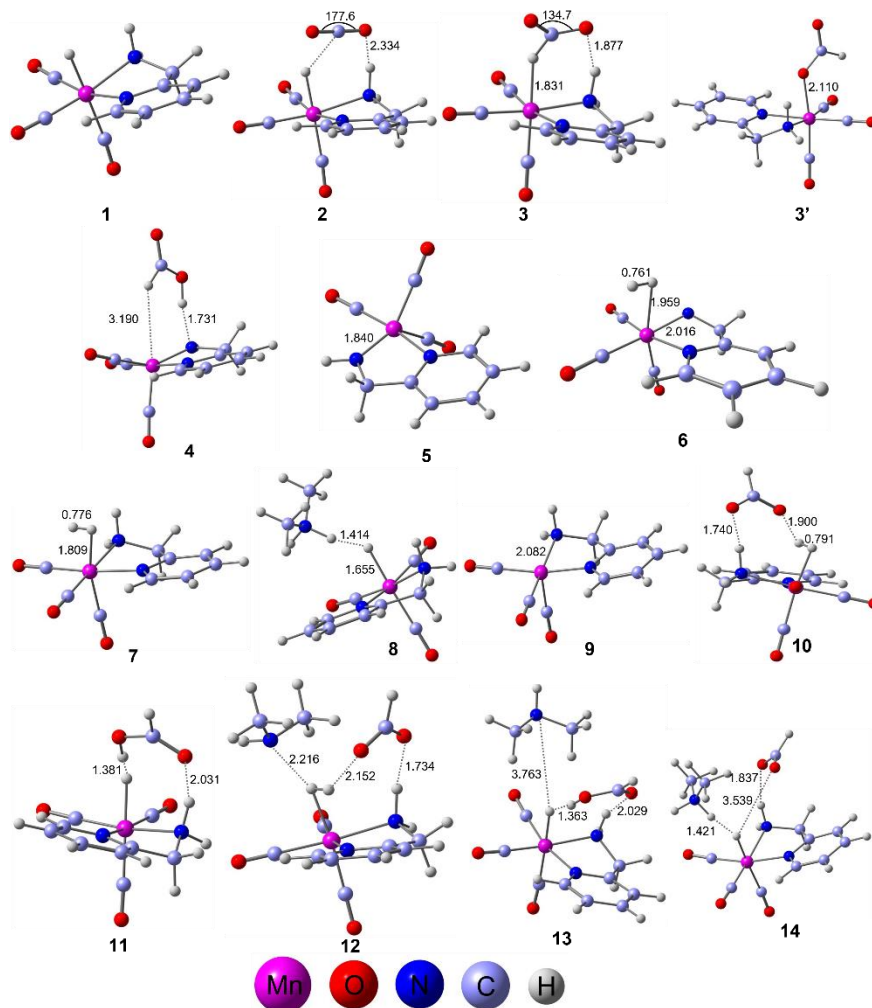


Figure 3.2: Optimized geometries of intermediates for CO₂ hydrogenation catalyzed by **Mn-AMP** complex. Bond lengths and bond angles are in Å and °, respectively.

However, such highly stabilized intermediate **3'** could be a resting state for this reaction, which may affect the catalytic activity of the complex. Alternatively, **3** may abstract proton from the N–H bond for the formation of **4** via transition state (**TS3**). Here geometry of the transition state is more closely resembles to the product. Therefore, intermediate **4** would release

$[\text{H}2\text{N}(\text{CH}_3)_2]^+[\text{HCO}_2]^-$ in the presence of $\text{NH}(\text{CH}_3)_2$ base for the formation of **5**. Intermediate **5** has a vacant site where H_2 can coordinate for the formation of Mn- H_2 intermediate (**6**).

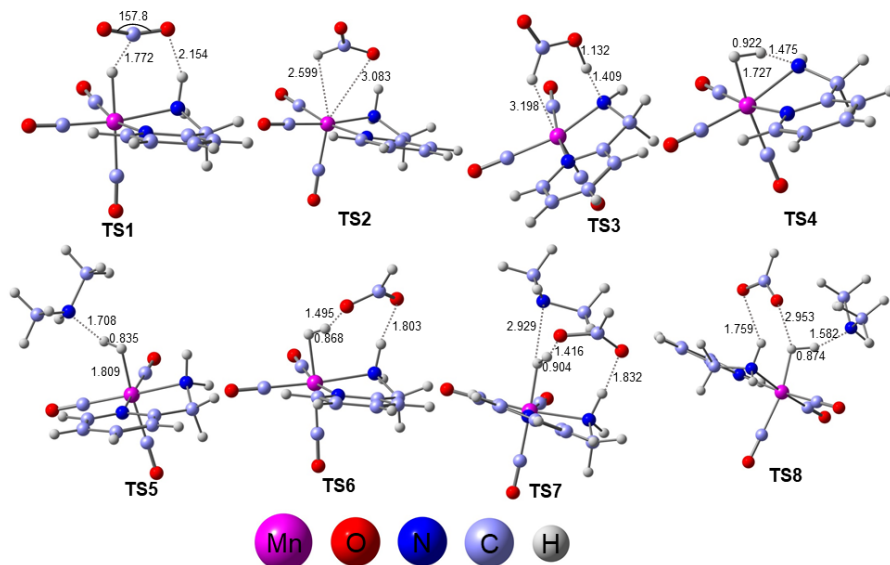


Figure 3.3: Optimized geometries of transition states for CO₂ hydrogenation catalyzed by **Mn-AMP** complex. Bond lengths and bond angles are in Å and °, respectively.

However, the calculated reaction free energy associated with this step is 18.9 kcal/mol, which suggests that the formation of **6** is very much unfavorable. Furthermore, the lone pair on nitrogen atom can initiate the heterolytic H₂ cleavage (**6**→**1**) via **TS4** for the regeneration of catalyst **1**. We have calculated the total reaction free energy barrier ($\Delta\Delta G^{\ddagger R}$) using the energetic span model (δE) [81] and the calculated total reaction free energy barrier is 38.9 kcal/mol when catalysed by **Mn-AMP**. Furthermore, we have calculated total free energy barriers (*via* ligand participated mechanism) for all the other modelled Mn (I)-complexes. The calculated barriers (Table 3.1) show that the barrier is highest for **Mn-AMP** complex (38.9 kcal/mol) and lowest for **Mn-MAMNHC** (35.3 kcal/mol). This suggests that the ligand participated mechanism requires a high-energy

barrier for CO₂ hydrogenation reaction.

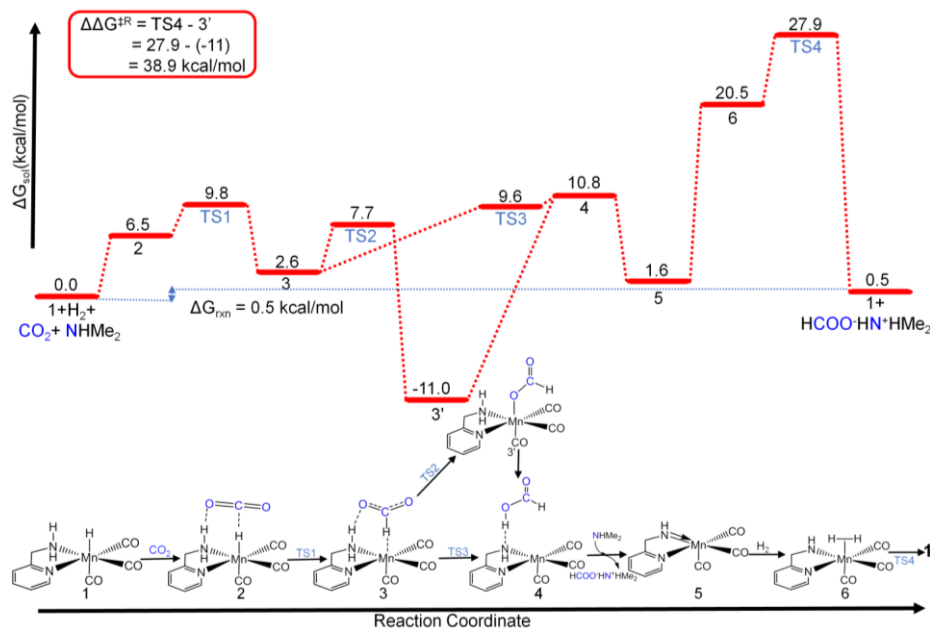
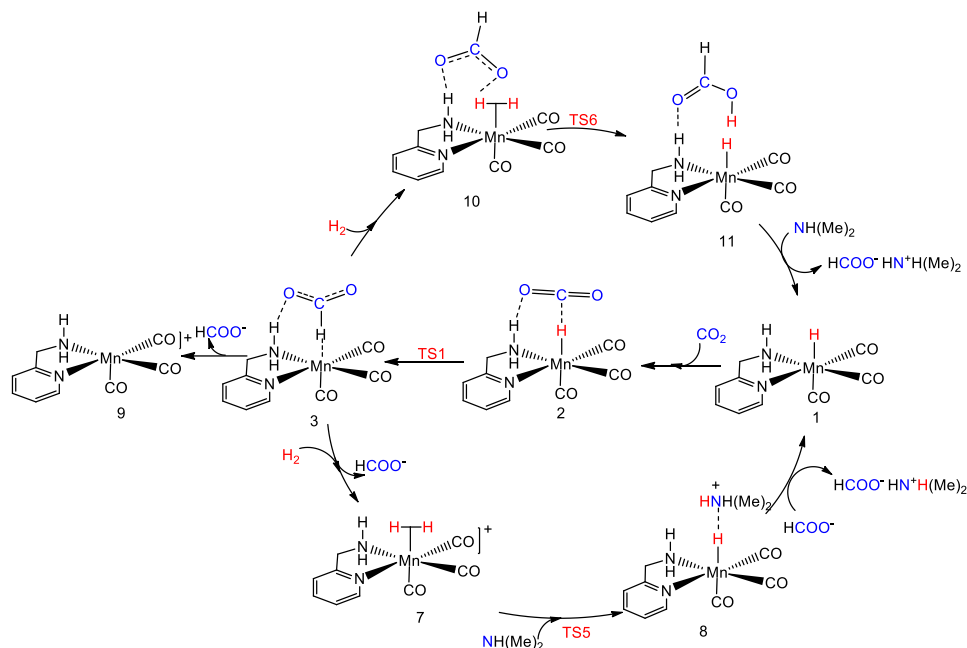


Figure 3.4: Reaction free energy profile diagram of CO₂ hydrogenation *via* ligand involvement mechanism catalyzed by **Mn-AMP** complex. $\Delta \Delta G^{\ddagger R}$ and ΔG_{rxn} denote the total free energy barrier and total reaction free energy of the overall catalytic cycle, respectively.

3.3.2. Ligand Assisted Mechanism

Furthermore, we have considered the possibility of ligand assisted CO₂ hydrogenation mechanism as shown in Scheme 3.2 [55-59]. Here, we have proposed two pathways for the ligand assisted mechanism. In one case, we have considered that formate anion would release from the Mn center, which in turn would allow H₂ to bind the vacant Mn site for the formation of the η^2 -coordinated Mn-H₂ complex (**3**→**7**). The calculated reaction free energy of this step is 18.5 kcal/mol (Figure 3.5), which is highly endergonic. After that, heterolytic H₂ cleavage may be initiated in the presence of external base NHMe₂ via transition state **TS5**. The calculated free energy barrier for this step (**7**→**8**) is 6.3 kcal/mol. Furthermore, [HNH(CH₃)₂]⁺[HCO₂]⁻ may be released from **8** for the regeneration of the

catalyst **1** and the associated reaction free energy with this step is -20.4 kcal/mol. However, the total reaction free energy barrier for external base initiated H₂ cleavage pathway is 38.4 kcal/mol which is as high as we found for the ligand participated mechanism (38.9 kcal/mol).



Scheme 3.2: Proposed ligand assisted CO₂ hydrogenation mechanisms by **Mn-AMP** complex.

The calculated total reaction free energy barriers for all the other modelled complexes are given in Table 3.1. Our calculated barriers indicate that **Mn-MAMP** has lowest (32.3 kcal/mol) total free energy barrier and **Mn-AMP** has highest (38.4 kcal/mol) total free energy. This suggests that both the ligand participated, and ligand assisted (in the presence of external base) mechanisms are not favorable for CO₂ hydrogenation reaction. Alternatively, we have considered another pathway in the ligand-assisted mechanism, where H₂ can react with intermediate **3** for the formation of **10**. Further to this, the formate anion may interact with N–H/Mn–H₂ through hydrogen bonding interactions as shown in Scheme 3.2. Interestingly, we find that such interaction is possible, and the reaction free energy associated

with this step is 5.8 kcal/mol (**3**→**10**). Moreover, the formate anion could initiate the heterolytic H₂ cleavage *via* transition state **TS6** and this calculated to be a barrierless process.

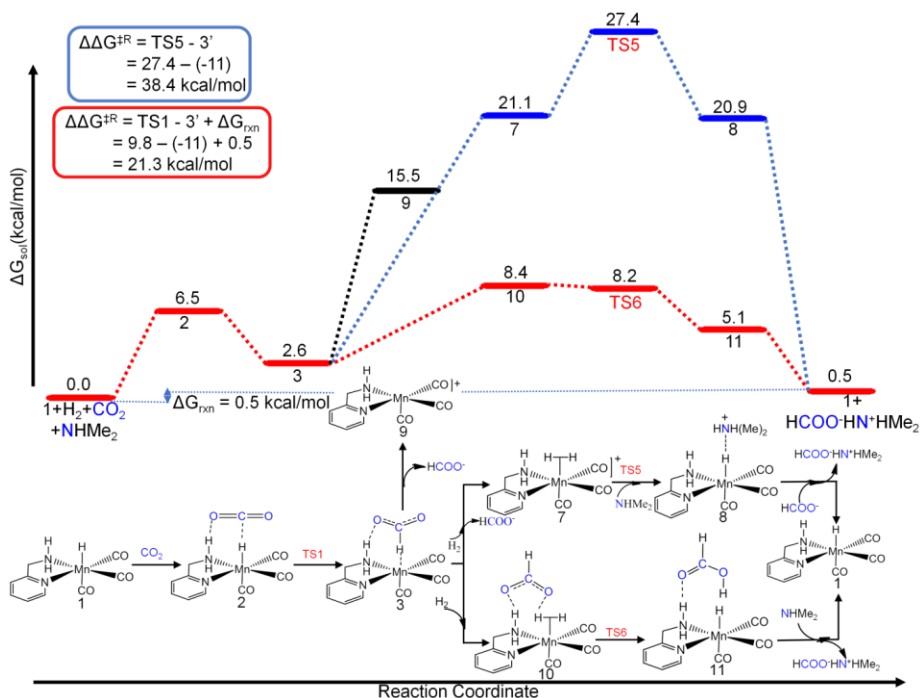


Figure 3.5: Reaction free energy profile diagram of CO₂ hydrogenation catalyzed by **Mn-AMP** complex *via* ligand assisted mechanism. $\Delta\Delta G^{\ddagger R}$ and ΔG_{rxn} denote the total free energy barrier and total reaction free energy of the overall catalytic cycle, respectively.

Here, the geometry of the transition state is more closely resembles with the reactant. This agrees well with previous computational and experimental reports that formate anion can act as a base in the CO₂ hydrogenation reaction, which promotes heterolytic H₂ cleavage [11,33,45,46]. After this, **11** can react with the external base for the regeneration of catalyst **1**. The total reaction free energy barrier for formate anion assisted heterolytic H₂ cleavage is 21.3 kcal/mol, which is 17.6 kcal/mol and 17.1 kcal/mol lower compared to the ligand participated and ligand+external base assisted heterolytic H₂ cleavage pathway, respectively. Our modelled complexes show a different trend compared to the report of Gonsalvi and coworkers

(for **Mn-PNP** catalyst), where they have reported that the total reaction free energy barriers are very much comparable (within 2 kcal/mol) for N–H ligand assisted and N-H participated mechanisms [33].

Table 3.1: The calculated total reaction free energy barriers (in kcal/mol) for CO₂ hydrogenation via Ligand assisted (presence of external base) and ligand participated mechanisms.

Complexes	Ligand Participated Mechanism	Ligand Assisted Mechanism (Presence of external base)
Mn-AMP	38.9	38.4
Mn-MAMP	38.4	32.3
Mn-AMI	38.4	36.4
Mn-MAMI	37.8	-
Mn-AMIM	37.0	37.7
Mn-MAMIM	37.8	-
Mn-AMNHC	35.8	35.8
Mn-MAMNHC	35.3	36.0

This suggests that the N–H···O hydrogen-bonding interactions between N–H and formate anion may be very important for ligand assisted reaction mechanism which is absent in the **Mn-PNP** catalyst of Gonsalvi and coworkers [33]. Therefore, our results suggest that the role of N–H bond is very important for the stabilization of formate anion *via* N–H···O hydrogen-bonding interactions, which in turn triggers the heterolytic H₂ cleavage. To understand the importance of such hydrogen bonding interactions, we have investigated the role of N–H moiety by substituting the –H with a –Me group. However, there can be two isomers (Figure 3.6) for this. In one case, methyl can be positioned towards the formate anion (**Mn-MAMP**) and in the other case it could be positioned quite far from the

formate anion (**Mn-MAMP'**). The total free energy barrier for **Mn-MAMP** is 21.3 kcal/mol, which is same as in **Mn-AMP**. This suggests that presence of methyl group far from the formate anion does not affect the catalytic reaction. On the other hand, the total free energy barrier for **Mn-MAMP'** is 25.4 kcal/mole, which is 4.1 kcal/mole higher than that of **Mn-AMP** and **Mn-MAMP** (Figure 3.7 and Figure 3.8).

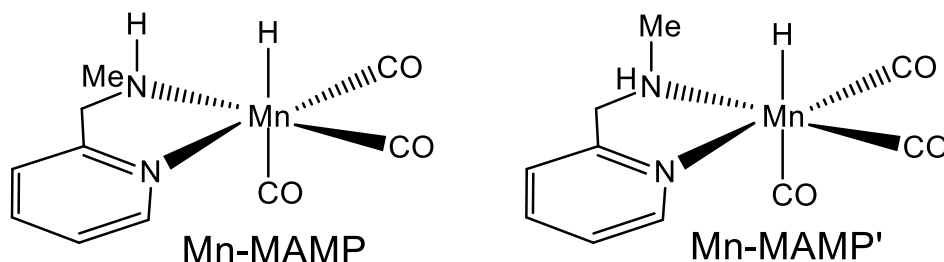


Figure 3.6: Structure of **Mn-MAMP** and **Mn-MAMP'** (Isomer of each other)

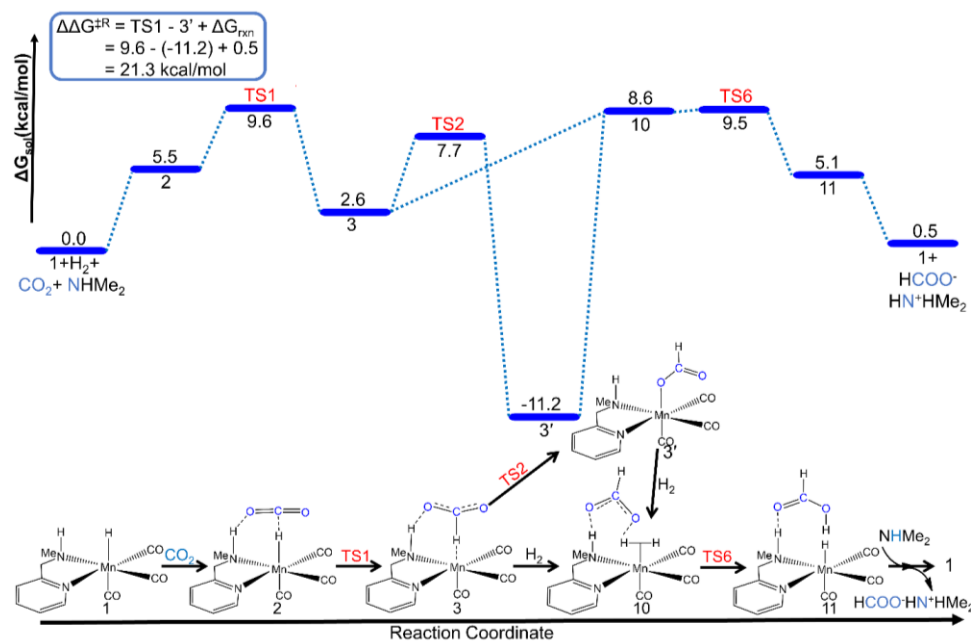


Figure 3.7: Reaction free energy profile diagram of CO₂ hydrogenation via ligand assisted mechanism catalyzed by **Mn-MAMP** complex. $\Delta\Delta G^{\ddagger R}$ and $\Delta G_{\text{rxn}}^{\ddagger}$ denote the total free energy barrier and total reaction free energy,

respectively.

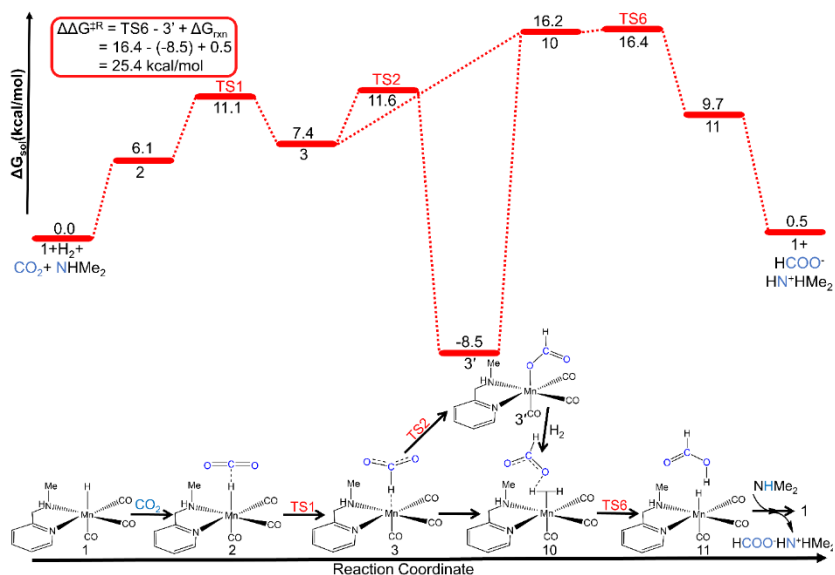


Figure 3.8: Reaction free energy profile diagram of CO₂ hydrogenation via ligand assisted mechanism catalyzed by **Mn-MAMP'** complex. $\Delta\Delta G^{\ddagger R}$ and ΔG_{rxn} denote the total free energy barrier and total reaction free energy, respectively.

This could be due to the absence of N–H···O hydrogen-bonding interactions in case of **Mn-MAMP'**. Furthermore, ligand assisted *via* formate anion initiated heterolytic H₂ cleavage mechanism has been studied for all the other Mn(I) catalysts and their respective free energy values are given in Table 3.2. Our results show that the total reaction free energy barrier is lowest for **Mn-AMNHC** (20.7 kcal/mol) and highest for **Mn-AMIM** (23.5 kcal/mol). However, the total barriers are very much comparable for all the Mn(I) complexes and we can say that all the modelled Mn(I)-catalysts are promising for CO₂ hydrogenation reaction.

Table 3.2: Ligand assisted reaction free energy for CO₂ hydrogenation reaction catalyzed by Mn(I) modelled complexes of amply ligands. $\Delta\Delta G^{\ddagger}$ represents the total reaction free energy barriers for reaction. All free

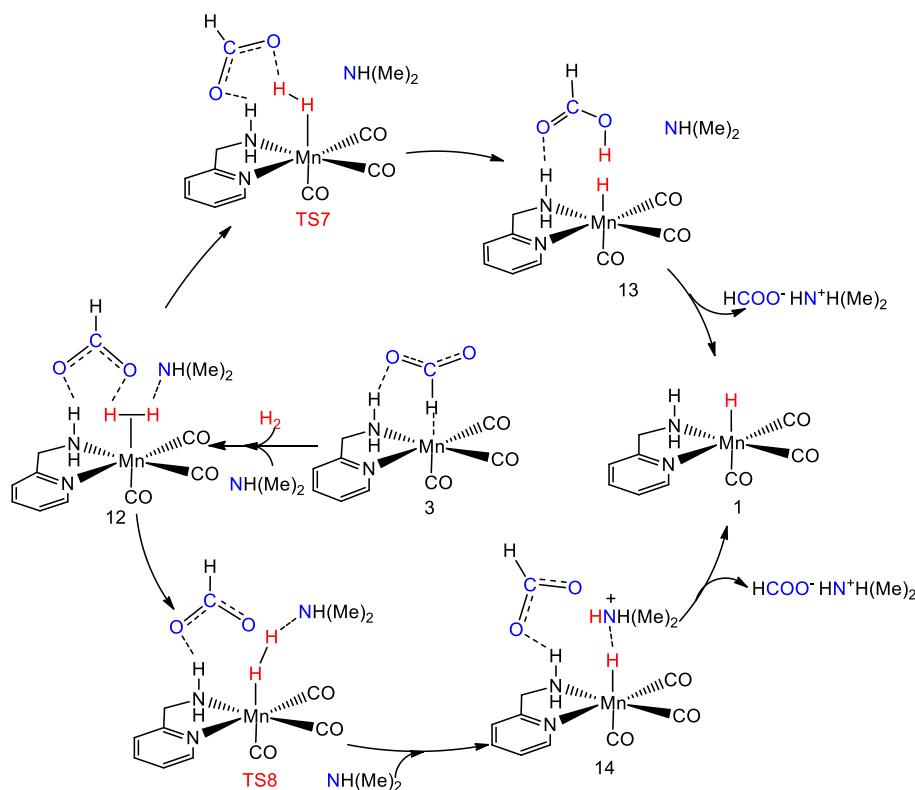
energies are in kcal/mol.

Complexes	Relative Free Energies (kcal/mol)										$\Delta\Delta G$ ‡
	1+H ₂ + CO ₂ + NHMe ₂	2	TS1	3	TS2	3'	10	TS6	11	1+ [HNH(CH ₃) ₂] ⁺ [HCO ₂] ⁻	
Mn-AMP	0.0	6.5	9.8	2.6	7.7	-11.0	8.4	8.2	5.1	0.5	21.3
Mn-MAMP	0.0	5.5	9.6	2.6	7.7	-11.2	9.4	9.5	5.1	0.5	21.3
Mn-AMI	0.0	5.3	10.1	0.1	3.1	-12.2	6.1	6.8	4.0	0.5	22.8
Mn-MAMI	0.0	5.3	10.2	0.0	3.9	-12.3	6.7	8.7	4.6	0.5	23.0
Mn-AMIM	0.0	6.0	9.9	-1.6	-1.7	-13.1	4.1	7.2	4.3	0.5	23.5
Mn-MAMIM	0.0	5.5	9.6	-1.6	-1.5	-13.2	4.2	5.2	4.6	0.5	23.3
Mn-AMNHC	0.0	5.5	11.1	1.8	7.6	-9.1	6.8	10.5	6.4	0.5	20.7
Mn-MAMNHC	0.0	5.2	11.2	1.9	6.8	-9.3	7.5	8.6	6.1	0.5	21.0

3.3.3. Formate Anion vs External Base

Furthermore, we have proposed two different mechanistic pathways of the catalytic cycles where heterolytic H₂ cleavage is initiated by formate and external base in the presence of each other (Scheme 3.3). The external base and H₂ can attack on **3** for the formation of **12**, where formate anion and external base both can simultaneously interact with the Mn-H₂. The calculated reaction free energy for the formation of **12** is 12.4 kcal/mol (Figure 3.9). However, in this case, formate anion and external base both are competing with each other to initiate the heterolytic H₂ cleavage. One possibility is that heterolytic H₂ cleavage can be initiated by the formate anion in the presence of an external base for the formation of **13** via transition state (TS7). The calculated reaction free energy barrier for this process is 0.9 kcal/mol. In another possibility, the external base in the presence of formate can initiate heterolytic H₂ cleavage. This requires a free

energy barrier of 1.4 kcal/mol via **TS8** for the formation of **14**. In the next step, intermediate **13/14** will release $[\text{HNH}(\text{CH}_3)_2]^+[\text{HCO}_2]^-$ to complete the catalytic cycle. The calculated total barriers are 26.9 and 27.4 kcal/mol via **TS7** and **TS8**, respectively.



Scheme 3.3: Formate anion vs external base assisted CO₂ hydrogenation catalyzed by the **Mn-AMP** complex.

These calculated barriers are ~7.0 kcal/mol higher than the formate assisted heterolytic H₂ cleavage pathway (Figure 3.5). This suggests that the active participation of the external base in heterolytic H₂ cleavage increases the overall barrier. Therefore, among all the possible mechanistic pathways, ligand participated *via* formate anion assisted heterolytic H₂ cleavage mechanism is highly favorable. Furthermore, we have studied the effect of temperature on different possible reaction pathways (Table 3.3 and 3.4). It suggests that the hydride transfer is more than 10⁵ times slower compared to the formate anion assisted heterolytic H₂ cleavage, which is the most

favorable pathway for CO₂ hydrogenation reaction.

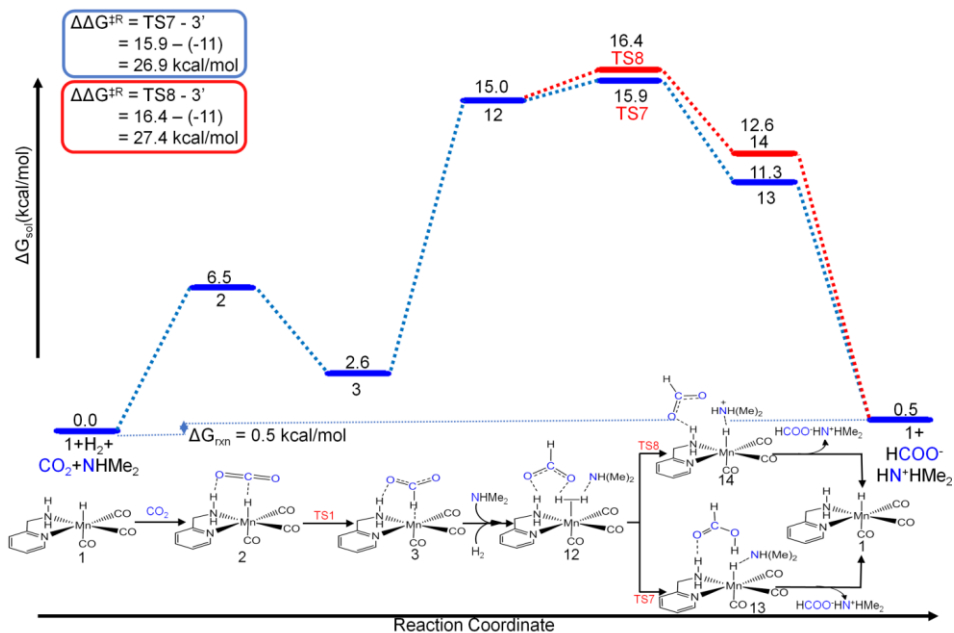


Figure 3.9: Reaction energy profile diagram of CO₂ hydrogenation of formate anion vs external base catalyzed by **Mn-AMP** complex. $\Delta\Delta G^{\ddagger R}$ and ΔG_{rxn} denote the total free energy barrier and total reaction free energy of the overall catalytic cycle, respectively.

Table 3.3: Stepwise reaction kinetic model for all barriers at different temperatures. All the temperatures are in Kelvin (K) and all the rate constants are in $\text{M}^{-1}\text{S}^{-1}$.

Temp (K)	TS1 (Hydride transfer step)	TS2 (Isomerisation step)	TS3 (N–H bond breaking)	TS4 (Heterolytic H ₂ cleavage)	TS5 (Base assisted H ₂ cleavage)	TS6 (Formate assisted H ₂ cleavage)	TS7 (Formate assisted H ₂ cleavage presence of external base)	TS8 (Base assisted H ₂ cleavage presence of formate)
298.15	4.52×10^5	1.20×10^9	4.95×10^7	2.53×10^7	1.60×10^8	barrierless	1.28×10^3	5.52×10^2
323.15	1.75×10^6	2.52×10^9	1.33×10^8	7.17×10^7	3.93×10^8	barrierless	7.78×10^3	3.59×10^3
398.15	5.60×10^6	4.78×10^9	3.12×10^8	1.76×10^8	8.53×10^8	barrierless	3.67×10^4	1.79×10^4
423.15	1.53×10^7	8.35×10^9	6.54×10^8	3.82×10^8	1.67×10^9	barrierless	1.41×10^5	7.19×10^4

Table 3.4: Overall reaction kinetic model for all possible pathways at different temperatures. All the temperatures are in Kelvin (K) and all the rate constants are in $M^{-1}S^{-1}$.

Temp(K)	Ligand Participated	Ligand assisted (H ₂ cleavage by base)	Ligand assisted (Formate anion assisted H ₂ cleavage)	Formate vs base (formate assisted H ₂ cleavage)	Formate vs base (base assisted H ₂ cleavage)
298.15	1.25×10^{-16}	2.89×10^{-16}	1.91×10^{-3}	6.87×10^{-8}	2.97×10^{-8}
323.15	2.25×10^{-14}	4.88×10^{-14}	3.27×10^{-2}	2.61×10^{-6}	1.20×10^{-6}
398.15	1.93×10^{-12}	3.96×10^{-12}	3.76×10^{-1}	5.90×10^{-5}	2.88×10^{-5}
423.15	8.98×10^{-11}	1.76×10^{-10}	3.09	8.69×10^{-4}	4.45×10^{-4}

3.4. Effect of N–H Functionality

We have investigated the role (participated/assisted) of N–H bond during CO₂ hydrogenation as the calculated total barrier for ligand participated mechanism is highly endothermic (39.4 kcal/mol). Therefore, to understand the reason behind such high barrier, we have studied the structural parameters (Figure 3.2) and natural bond orbitals (NBO). This is because the chemical nature of Mn–N bond is different in **5** and **6**. Our NBO data shows that **5** has a Mn–N double bond (1.840 Å) and the Mn–N π -bond is formed due to overlap between N p-orbitals (~20%) and Mn d-orbitals (~80%). However, **6** does not have a Mn–N π -bond (2.016 Å). This could be the reason that **6** lies in higher energy in the reaction free energy profile. Furthermore, we predict that weak interaction plays a significant role in the ligand assisted mechanism (*via* formate anion initiated heterolytic H₂ cleavage) as N–H functionality lowers the total energy barrier compared to N–Me functionality. Here, N–H functionality stabilizes the intermediates *via* N–H \cdots O hydrogen-bonding interactions in **3** and **10**. Therefore, we have investigated the non-covalent interaction (NCI) for intermediates **3** and **10** for **Mn-MAMP** and **Mn-MAMP'** (Figure 3.10) complexes to understand the importance of such covalent interactions in the CO₂

hydrogenation reaction. Figure 3.10 shows that N–H···O (1.848 Å) interaction and C–H···O (2.722 Å) interaction are present in **3-Mn-MAMP** and **3-Mn-MAMP'** respectively and the N–H···O (1.848 Å) interaction is stronger (as shown in Figure 3.10) than C–H···O (2.722 Å) interaction. This is very much in consistent with our reaction free energy values. Similarly, N–H···O (1.735 Å) and H–H···O (1.901 Å) interactions are present in **10-Mn-MAMP**, whereas C–H···O (2.456 Å) and H–H···O (1.775 Å) interactions are present in **10-Mn-MAMP'**. However, **10-Mn-MAMP** is 7.6 kcal/mol more stable than **10-Mn-MAMP'** and this could be due to the stronger N–H···O interaction over C–H···O. So, hydrogen bonding interaction plays a crucial role in stabilization of formate anion which in turn favors heterolytic H₂ cleavage and thus lowers the total reaction free energy barrier.

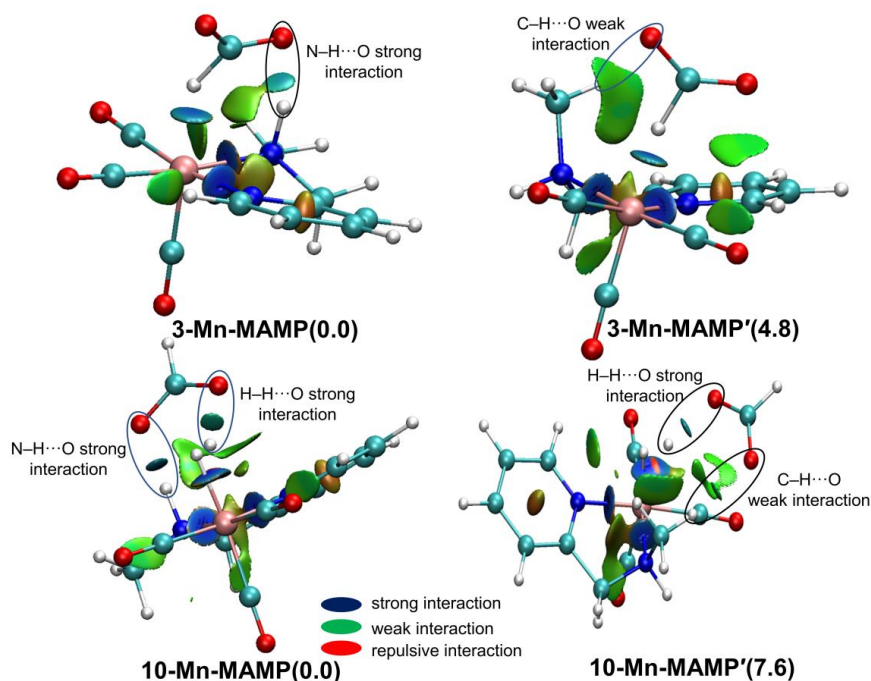


Figure 3.10: Non-covalent interaction of intermediate **3** and intermediate **10** of **Mn-MAMP** and **Mn-MAMP'**. The relative energy (in kcal/mol) values are given in parentheses for **Mn-MAMP** and **Mn-MAMP'**. The colours of NCI regions represent the type of interaction present in the

intermediate (blue=strong, green=weak, and red=repulsive interaction).

3.5. Conclusions

We have investigated a series of aminomethyl based bifunctional Mn(I) catalysts for CO₂ hydrogenation reaction. For this, we have proposed two different mechanisms: Ligand participated, and Ligand assisted mechanisms. Furthermore, we have checked whether CO₂ hydrogenation mechanism follows the classical ketone hydrogenation mechanism as proposed by Noyori or not. In the case of classical ketone hydrogenation mechanism, the role of N–H functionality is very important. Therefore, we have studied the role of N–H functionality in the ligand participated *vs.* ligand assisted mechanism. We find that the N–H functionality of the ligand can show a molecular M/NH bifunctional nature via metal-ligand cooperation (MLC) mechanism. The total reaction free energy barrier for N–H functionality participated mechanism is 39.4 kcal/mol when catalysed by the **Mn-AMP** complex and here, the cleavage and formation of N–H bond occur during the course of the reaction. On the other hand, the calculated total reaction free energy barrier for the ligand assisted mechanism is 21.3 kcal/mol, where the ligand does not actively participate in the reaction mechanism. Thus, our total energy barrier calculations suggest that the cleavage/formation of N–H bond may not occur in the CO₂ hydrogenation mechanism (via ligand assisted mechanism). In such case, the formed formate anion interacts with the N–H functionality via N–H···O hydrogen bonding interaction. Such interaction stabilizes the formate anion, which in turn brings the formate anion and H₂ closer and favours the heterolytic H₂ cleavage. This process lowers the total reaction free energy barrier significantly. Therefore, our study shows that the ligand assisted mechanism is favourable over ligand participated mechanism, which is quite opposite to the classical Noyori mechanism for ketone hydrogenation. Furthermore, we show that the substitution of N–H (**Mn-AMP**) by N–Me group (**Mn-MAMP'**) increases (by 4.1 kcal/mol) the total reaction free

energy barrier. This suggests that the role of N–H···O hydrogen bonding interaction for the formate anion stabilization is very important for CO₂ hydrogenation interaction. Therefore, our detailed mechanistic study shows that bifunctional ligand-based metal catalysts are very promising for CO₂ hydrogenation reaction.

3.6. References

1. Olah G.A., Goepfert A., Surya Prakash G.K. (2009), Chemical Recycling of Carbon Dioxide to Methanol and Dimethyl Ether: From Greenhouse Gas to Renewable, Environmentally Carbon Neutral Fuels and Synthetic Hydrocarbons, *J. Org. Chem.*, 74, 487–498 (DOI: 10.1021/jo801260f)
2. Porosoff M.D., Yan B. and Chen J. G. (2016), Catalytic reduction of CO₂ by H₂ for synthesis of CO, methanol and hydrocarbons: challenges and opportunities, *Energy Environ. Sci.*, 9, 62–73 (DOI: 10.1039/c5ee02657a)
3. Inoue Y., Sasaki Y., Hashimoto H. (1975), Synthesis of Formates from Alcohols, Carbon Dioxide, and Hydrogen Catalysed by a Combination of Group VIII Transition-metal Complexes and Tertiary Amines *J. Chem. Soc., Chem. Commun.*, 718–719 (DOI not found)
4. Inoue Y., Izumida H., Sasaki Y., Hashimoto H. (1976), Catalytic Fixation Of Carbon Dioxide To Formic Acid By Transition-Metal Complexes Under Mild Conditions, *Chem. Lett.*, 5, 863–864. (DOI: 10.1246/cl.1976.863)
5. Graf F., and Leitner W. (1992), Direct Formation of Formic Acid from Carbon Dioxide and Dihydrogen using the [Rh(cod)Cl]₂–Ph₂P(CH₂)₄PPh₂ catalyst system, *J. Chem. Soc. Chem. Commun.*, 623–624. (DOI: 10.1039/C39920000623)
6. Jessop P.G., Ikariya T., Noyori R. (1994), Homogeneous Catalytic-Hydrogenation of Supercritical Carbon-Dioxide, *Nature*, 368, 231–233. (DOI: 10.1038/368231a0)

7. Munshi P., Main A.D., Linehan J.C., Tai C.C., Jessop P.G. (2002), Hydrogenation of Carbon Dioxide Catalyzed by Ruthenium Trimethylphosphine Complexes: The Accelerating Effect of Certain Alcohols and Amines, *J. Am. Chem. Soc.*, 124, 7963–7971. (DOI: 10.1021/ja0167856)
8. Tanaka R., Yamashita M., Nozaki K. (2009), Catalytic Hydrogenation of Carbon Dioxide Using Ir(III)-Pincer Complexes, *J. Am. Chem. Soc.*, , 131, 14168–14169. (DOI: 10.1021/ja903574e)
9. Schmeier T.J., Dobereiner G.E., Crabtree R.H., Hazari N. (2011), Secondary Coordination Sphere Interactions Facilitate the Insertion Step in an Iridium(III) CO₂ Reduction Catalyst, *J. Am. Chem. Soc.*, , **133**, 9274–9277. (DOI: 10.1021/ja2035514)
10. Filonenko A., Smykowski G.D., Szyja B.M., Li G., Szczygieł J., Hensen E.J.M., Pidko E.A. (2015), Catalytic Hydrogenation of CO₂ to Formates by a Lutidine-Derived Ru–CNC Pincer Complex: Theoretical Insight into the Unrealized Potential, *ACS Catal.*, 5, 1145–1154. (DOI: 10.1021/cs501990c)
11. Filonenko G.A., Hensen E.J.M., Pidko E.A. (2014), Mechanism of CO₂ hydrogenation to formates by homogeneous Ru-PNP pincer catalyst: from a theoretical description to performance optimization, *Catal. Sci. Technol.*, 4, 3474–3485. (DOI: 10.1039/C4CY00568F)
12. Ohnishi Y., Matsunaga T., Nakao Y., Sato H., Sakaki S. (2005), Ruthenium(II)-Catalyzed Hydrogenation of Carbon Dioxide to Formic Acid. Theoretical Study of Real Catalyst, Ligand Effects, and Solvation Effects, *J. Am. Chem. Soc.*, 127, 4021–4032. (DOI: 10.1021/ja043697n)
13. Ohnishi Y., Nakao Y., Sato H., Sakaki S. (2006), Ruthenium(II)-Catalyzed Hydrogenation of Carbon Dioxide to Formic Acid. Theoretical Study of Significant Acceleration by Water Molecules, *Organometallics*, 25, 3352–3363. (DOI: 10.1021/om060307s)

14. Ogo S., Kabe R., Hayashi H., Harada R., Fukuzumi S. (2006), Mechanistic investigation of CO₂ hydrogenation by Ru(II) and Ir(III) aqua complexes under acidic conditions: two catalytic systems differing in the nature of the rate determining step, *Dalton Trans.*, 4657–4663. (DOI: 10.1039/b607993h)
15. Yang X. (2011), Hydrogenation of Carbon Dioxide Catalyzed by PNP Pincer Iridium, Iron, and Cobalt Complexes: A Computational Design of Base Metal Catalysts, *ACS Catal.*, 1, 849–854. (DOI: 10.1021/cs2000329)
16. Tanaka R., Yamashita M., Chung L.W., Morokuma K., Nozaki K. (2011), Mechanistic Studies on the Reversible Hydrogenation of Carbon Dioxide Catalyzed by an Ir-PNP Complex, *Organometallics*, 30, 6742–6750. (DOI: 10.1021/om2010172)
17. Osadchuk I., Tamm T., Ahlquist M.S.G. (2015), Theoretical Investigation of a Parallel Catalytic Cycle in CO₂ Hydrogenation by (PNP)IrH₃, *Organometallics*, 34, 4932–4940. (DOI: 10.1021/acs.organomet.5b00448)
18. Hou C., Jiang J., Zhang S., Wang G., Zhang Z., Ke Z., Zhao C. (2014), Hydrogenation of Carbon Dioxide Using Half-Sandwich Cobalt, Rhodium, and Iridium Complexes: DFT Study on the Mechanism and Metal Effect, *ACS Catal.*, 4, 2990–2997. (DOI: 10.1021/cs500688q)
19. Moret S., Dyson P.J., Laurency G. (2014), Direct synthesis of formic acid from carbon dioxide by hydrogenation in acidic media, *Nat. Commun.*, 5, 4017. DOI: 10.1038/ncomms5017.
20. Huff C.A., Sanford M.S. (2013), Catalytic CO₂ Hydrogenation to Formate by a Ruthenium Pincer Complex, *ACS Catal.*, 3, 2412–2416. (DOI: 10.1021/cs400609u)
21. Onishi N., Xu S., Manaka Y., Suna Y., Wang W., Muckerman J.T., Fujita E., Himeda Y. (2015), CO₂ Hydrogenation Catalyzed by Iridium Complexes with a Proton Responsive Ligand, *Inorg. Chem.*, 54, 5114–5123. (DOI:10.1021/ic502904q)

22. Liu C., Xie J., Tian G., Li W., Zhou Q. (2015), Highly efficient hydrogenation of carbon dioxide to formate catalyzed by iridium(III) complexes of imine–diphosphine ligands, *Chem. Sci.*, 6, 2928–2931. (DOI: 10.1039/c5sc00248f)
23. Zou F., Cole J.M., Jones T.G.J., Jiang L. (2012) Rhodium nitrosyl catalysts for CO₂ hydrogenation to formic acid under mild conditions, *Appl. Organometal. Chem.*, 26, 546–549 (DOI: 10.1002/aoc.2898)
24. Federsel C., Boddien A., Jackstell R., Jennerjahn R., Dyson P.J., Scopelliti R., Laurency G., Beller M. (2010) A Well-Defined Iron Catalyst for the Reduction of Bicarbonates and Carbon Dioxide to Formates, Alkyl Formates, and Formamides, *Angew. Chem., Int. Ed.*, 49, 9777–9780 (DOI: 10.1002/anie.201004263)
25. Bernskoetter W.H., Hazari N. (2017), Reversible Hydrogenation of Carbon Dioxide to Formic Acid and Methanol: Lewis Acid Enhancement of Base Metal Catalysts, *Acc. Chem. Res.* 50, 1049–1058 (DOI: 10.1021/acs.accounts.7b00039)
26. Rawat K.S., Mahata A., Pathak B. (2016), Catalytic Hydrogenation of CO₂ by Fe Complexes Containing Pendant Amines: Role of Water and Base, *J. Phys. Chem. C*, 120, 26652–26662 (DOI: 10.1021/acs.jpcc.6b09333)
27. Fong H., Peters J.C. (2015), Hydricity of an Fe–H Species and Catalytic CO₂ Hydrogenation, *Inorg. Chem.*, 54, 5124–5135 (DOI: 10.1021/ic502508p)
28. Zhang Y., MacIntosh A.D., Wong J.L., Bielinski E.A., Williard P.G., Mercado B.Q., Hazari N., Bernskoetter W.H. (2015), Iron catalyzed CO₂ hydrogenation to formate enhanced by Lewis acid co-catalysts, *Chem. Sci.*, 6, 4291–4299 (DOI: 10.1039/C5SC01467K)
29. Yang X. (2015), Bio-inspired computational design of iron catalysts for the hydrogenation of carbon dioxide, *Chem. Commun.*, 51, 13098–13101 (DOI: 10.1039/C5CC03372A)

30. Langer R., Diskin-Posner Y., Leitus G., Shimon L.J.W., Ben-David Y., Milstein D. (2011), Low-Pressure Hydrogenation of Carbon Dioxide Catalyzed by an Iron Pincer Complex Exhibiting Noble Metal Activity, *Angew. Chem. Int. Ed.*, 50, 9948–9952 (DOI: 10.1002/anie.201104542)
31. Rivada-Wheelaghan O., Dauth A., Leitus G., Diskin-Posner Y., Milstein D. (2015), Synthesis and Reactivity of Iron Complexes with a New Pyrazine-Based Pincer Ligand, and Application in Catalytic Low-Pressure Hydrogenation of Carbon Dioxide, *Inorg. Chem.*, 54, 4526–4538 (DOI: 10.1021/acs.inorgchem.5b00366)
32. Rawat K.S., Pathak B. (2017), Aliphatic Mn–PNP complexes for the CO₂ hydrogenation reaction: a base free mechanism, *Catal. Sci. Technol.*, 7, 3234–3242 (DOI: 10.1039/C7CY00737J)
33. Bertini F., Glatz M., Gorgas N., Stoger B., Peruzzini M., Veiros L.F., Kirchner K., Gonsalvi L. (2017), Carbon dioxide hydrogenation catalysed by well-defined Mn(I) PNP pincer hydride complexes, *Chem. Sci.*, 8, 5024–5029 (DOI: 10.1039/C7SC00209B)
34. Dubey A., Nencini L., Fayzullin R.R., Nervi C., Khusnutdinova J.R. (2017), Bio-Inspired Mn(I) Complexes for the Hydrogenation of CO₂ to Formate and Formamide, *ACS Catal.*, 7, 3864–3868 (DOI: 10.1021/acscatal.7b00943)
35. Jeletic M.S., Mock M.T., Appel A.M., Linehan J.C. (2013), A Cobalt-Based Catalyst for the Hydrogenation of CO₂ under Ambient Conditions, *J. Am. Chem. Soc.*, 135, 11533–11536 (DOI: 10.1021/ja406601v)
36. Schneidewind J., Adam R., Baumann W., Jackstell R., Beller M. (2017), Low-Temperature Hydrogenation of Carbon Dioxide to Methanol with a Homogeneous Cobalt Catalyst, (2017), *Angew. Chem. Int. Ed.*, 56, 1890–1893 (DOI: 10.1002/anie.201609077)

37. Zall C.M., Linehan J.C., Appel A.M. (2015), A Molecular Copper Catalyst for Hydrogenation of CO₂ to Formate, (2015), ACS Catal., 5, 5301–5305 (DOI: 10.1021/acscatal.5b01646)
38. Watari R., Kayaki Y., Hirano S., Matsumoto N., Ikariya T. (2015), Hydrogenation of Carbon Dioxide to Formate Catalyzed by a Copper/1,8-Diazabicyclo[5.4.0]undec-7-ene System, Adv. Synth. Catal., 357, 1369–1373 (DOI: 10.1002/adsc.201500043)
39. Burgess S.A., Kendall A.J., Tyler D.R., Linehan J.C., Appel A.M. (2017), Hydrogenation of CO₂ in Water Using a Bis(diphosphine) Ni–H Complex, ACS Catal., 7, 3089–3096 (DOI: 10.1021/acscatal.7b00350)
40. Song J., Klein E.L., Neese F., Ye S. (2014), The Mechanism of Homogeneous CO₂ Reduction by Ni(cyclam): Product Selectivity, Concerted Proton–Electron Transfer and C–O Bond Cleavage, Inorg. Chem., 53, 7500–7507 (DOI: 10.1021/ic500829p)
41. Jeletic M.S., Helm M.L., Hulley E.B., Mock M.T., Appel A.M., Linehan J.C. (2014), A Cobalt Hydride Catalyst for the Hydrogenation of CO₂: Pathways for Catalysis and Deactivation, ACS Catal., 4, 3755–3762 (DOI: 10.1021/cs5009927)
42. Spentzos A.Z., Barnes C.L., Bernskoetter W.H. (2016), Effective Pincer Cobalt Precatalysts for Lewis Acid Assisted CO₂ Hydrogenation, Inorg. Chem., 55, 8225–8233 (DOI: 10.1021/acs.inorgchem.6b01454)
43. Rawat K.S., Mahata A., Choudhuri I., Pathak B. (2016), Catalytic Hydrogenation of CO₂ by Manganese Complexes: Role of π -Acceptor Ligands, J. Phys. Chem. C, 120, 16478–16488 (DOI: 10.1021/acs.jpcc.6b05065)
44. Mondal B., Neese F., Ye S. (2015), Control in the Rate-Determining Step Provides a Promising Strategy To Develop New Catalysts for CO₂ Hydrogenation: A Local Pair Natural Orbital Coupled Cluster Theory Study, Inorg. Chem., 54, 7192–7198 (DOI: 10.1021/acs.inorgchem.5b00469)

45. Bertini F., Gorgas N., Stöger B., Peruzzini M., Veiros L.F., Kirchner K., Gonsalvi L. (2016), Efficient and Mild Carbon Dioxide Hydrogenation to Formate Catalyzed by Fe(II) Hydrido Carbonyl Complexes Bearing 2,6-(Diaminopyridyl)diphosphine Pincer Ligands, *ACS Catal.*, 6, 2889–2893 (DOI: 10.1021/acscatal.6b00416)
46. Zhang Z., Li Y., Hou C., Zhao C., Ke Z. (2018), DFT study of CO₂ hydrogenation catalyzed by a cobalt-based system: an unexpected formate anion-assisted deprotonation mechanism, *Catal. Sci. Technol.*, 8, 656-666 (DOI: 10.1039/C7CY02012K)
47. Rawat K.S., Pathak B. (2018), Flexible proton-responsive ligand-based Mn(i) complexes for CO₂ hydrogenation: a DFT study, *Phys. Chem. Chem. Phys.*, 20, 12535–12542 (DOI: 10.1039/C7CP08637G)
48. Hull J.F., Himeda Y., Wang W., Hashiguchi B., Periana R., Szalda D.J., Muckerman J.T., Fujita E. (2012), Reversible hydrogen storage using CO₂ and a proton-switchable iridium catalyst in aqueous media under mild temperatures and pressures, *Nat. Chem.*, 4, 383–388 (DOI: 10.1038/nchem.1295)
49. Wang W., Hull J.F., Muckerman J.T., Fujita E., Himeda Y. (2012), Second-coordination-sphere and electronic effects enhance iridium(iii)-catalyzed homogeneous hydrogenation of carbon dioxide in water near ambient temperature and pressure, *Energy Environ. Sci.*, 5, 7923–7926 (DOI: 10.1039/C2EE21888G)
50. Bernskoetter W.H., Hazari N. (2013), A Computational Investigation of the Insertion of Carbon Dioxide into Four- and Five-Coordinate Iridium Hydrides, *Eur. J. Inorg. Chem.*, 4032–4041 (DOI: 10.1002/ejic.201300170)
51. Rawat K.S., Pathak B. (2018), The significance of acid-base properties in the key ligand for CO₂ hydrogenation: role of amido ligand, *J Chem Sci.*, 130: 65 (DOI: 10.1007/s12039-018-1477-5)

52. Ahlquist M.S.G. (2010), Iridium catalyzed hydrogenation of CO₂ under basic conditions—Mechanistic insight from theory, *J. Mol. Catal. A: Chem.*, 324, 3–8 (DOI: 10.1016/j.molcata.2010.02.018)
53. Ohkuma T., Ooka H., Hashiguchi S., Ikariya T., Noyori R. (1995), Practical Enantioselective Hydrogenation of Aromatic Ketones, *J. Am. Chem. Soc.*, 117, 2675–2676 (DOI: 10.1021/ja00114a043)
54. Noyori R., Ohkuma T. (2001), Asymmetric Catalysis by Architectural and Functional Molecular Engineering: Practical Chemo- and Stereoselective Hydrogenation of Ketones, *Angew. Chem., Int. Ed.*, 40, 40–73 (DOI: 10.1002/1521-3773(20010105)40:1<40::AID-ANIE40>3.0.CO;2-5)
55. Dub P.A., Henson N.J., Martin R.L., Gordon J.C. (2014), Unravelling the Mechanism of the Asymmetric Hydrogenation of Acetophenone by [RuX₂(diphosphine)(1,2-diamine)] Catalysts, *J. Am. Chem. Soc.*, 136, 3505–3521 (DOI: 10.1021/ja411374j)
56. Dub P.A., Gordon J.C. (2016), The mechanism of enantioselective ketone reduction with Noyori and Noyori–Ikariya bifunctional catalysts *Dalton Trans.*, 45, 6756–6781 (DOI: 10.1039/C6DT00476H)
57. Dub P.A., Gordon J.C. (2017), Metal–Ligand Bifunctional Catalysis: The “Accepted” Mechanism, the Issue of Concertedness, and the Function of the Ligand in Catalytic Cycles Involving Hydrogen Atoms, *ACS Catal.*, 7, 6635–6655 (DOI: 10.1021/acscatal.7b01791)
58. Dub P.A., Scott B.L., Gordon J.C. (2017), Why Does Alkylation of the N–H Functionality within M/NH Bifunctional Noyori-Type Catalysts Lead to Turnover? *J. Am. Chem. Soc.*, 139, 1245–1260 (DOI: 10.1021/jacs.6b11666)
59. Dub P.A., Gordon J.C. (2018), The role of the metal-bound N–H functionality in Noyori-type molecular catalysts, *Nature Reviews Chemistry*, 2, 396–408 (DOI: 10.1038/s41570-018-0049-z)
60. Bruneau-Voisine A., Wang D., Dorcet V., Roisnel T., Darcel C., Sortais J. (2017), Transfer Hydrogenation of Carbonyl Derivatives Catalyzed

- by an Inexpensive Phosphine-Free Manganese Precatalyst, *Org. Lett.*, 19, 3656–3659 (DOI: 10.1021/acs.orglett.7b01657)
61. Das S., Pati S.K. (2018), Mechanistic insights into catalytic CO₂ hydrogenation using Mn(i)-complexes with pendant oxygen ligands, *Catal. Sci. Technol.*, 8, 3034–3043 (DOI: 10.1039/C8CY00183A)
 62. Wang D., Bruneau-Voisine A., Sortais J. (2018), Practical (asymmetric) transfer hydrogenation of ketones catalyzed by manganese with (chiral) diamines ligands, *Catal. Commun.*, 105, 31–36 (DOI: 10.1016/j.catcom.2017.10.028)
 63. Frisch M.J. et al. (2013), Gaussian Revision D.01, Gaussian, Inc., Wallingford CT
 64. Lee C., Yang W., Parr R.G. (1988), Development of the Colle-Salvetti correlation-energy formula into a functional of the electron density, *Phys. Rev. B*, 37, 785–789 (DOI: 10.1103/PhysRevB.37.785)
 65. Becke A.D. (1993), Density-functional thermochemistry. III. The role of exact exchange, *J. Chem. Phys.*, 98, 5648–5652 (DOI: 10.1063/1.464913)
 66. Becke A.D. (1988), Density-functional exchange-energy approximation with correct asymptotic behavior, *Phys. Rev. A*, 38, 3098–3100 (DOI: 10.1103/PhysRevA.38.3098)
 67. Becke A.D. (1993), A new mixing of Hartree–Fock and local density-functional theories, *J. Chem. Phys.*, 98, 1372 (DOI: 10.1063/1.464304)
 68. Hay P.J., Wadt W.R. (1985), Ab initio effective core potentials for molecular calculations. Potentials for the transition metal atoms Sc to Hg, *J. Chem. Phys.*, 82, 270–283 (DOI: 10.1063/1.448799)
 69. Hay P.J., Wadt W.R. (1985), Ab initio effective core potentials for molecular calculations. Potentials for K to Au including the outermost core orbitals, *J. Chem. Phys.*, 82, 299–310 (DOI: 10.1063/1.448975)
 70. Hehre W.J., Ditchfield R., Pople J.A. (1972), Self—Consistent Molecular Orbital Methods. XII. Further Extensions of Gaussian—

- Type Basis Sets for Use in Molecular Orbital Studies of Organic Molecules, *J. Chem. Phys.*, 56, 2257-2261 (DOI: 10.1063/1.1677527)
71. Hariharan P.C., Pople J.A. (1973), The influence of polarization functions on molecular orbital hydrogenation energies, *Theor. Chim Acta*, 28, 213-222 (DOI: 10.1007/BF00533485)
72. Krishnan R., Binkley J.S., Seeger R., Pople J.A. (1980), Self-consistent molecular orbital methods. XX. A basis set for correlated wave functions, *J. Chem. Phys.*, 72, 650–654 (DOI: 10.1063/1.438955)
73. Grimme S., Antony J., Ehrlich S., Krieg H. (2010), A consistent and accurate ab initio parametrization of density functional dispersion correction (DFT-D) for the 94 elements H-Pu, *J. Chem. Phys.*, 132, 154104 (DOI: 10.1063/1.3382344)
74. Rawat K.S., Mahata A., Choudhuri I., Pathak B. (2016), N-Heterocyclic Carbene-Based Mn Electrocatalyst for Two-Electron CO₂ Reduction over Proton Reduction, *J. Phys. Chem. C*, 120, 8821–8831 (DOI: 10.1021/acs.jpcc.6b02209)
75. Barone V., Cossi M. (1998), Quantum Calculation of Molecular Energies and Energy Gradients in Solution by a Conductor Solvent Model, *J. Phys. Chem. A*, 102, 1995 –2001 (DOI: 10.1021/jp9716997)
76. Cossi M., N Rega., Scalmani G., Barone V. (2003), Energies, structures, and electronic properties of molecules in solution with the C-PCM solvation model, *J. Comput. Chem.*, 24, 669 –681 (DOI: 10.1002/jcc.10189)
77. Johnson E.R., Keinan S., Mori-Sanchez P., Contreras-García J., Cohen A.J., Yang W. (2010), Revealing Noncovalent Interactions, *J. Am. Chem. Soc.*, 132, 6498–6506 (DOI: 10.1021/ja100936w)
78. Contreras-García J., Johnson E.R., Keinan S., Chaudret R., Piquemal J., Beratan D.N., Yang W. (2011), NCIPLOT: A Program for Plotting Noncovalent Interaction Regions, *J. Chem. Theory Comput.*, 7, 625–632 (DOI: 10.1021/ct100641a)

79. Humphrey W., Dalke A., Schulten K. (1996), VMD: Visual molecular dynamics, *J. Mol. Graphics*, 14, 33–38 (DOI: 10.1016/0263-7855(96)00018-5)
80. Glendening E.D., Reed A.E., Carpenter J.E., Weinhold F. NBO Version 3.1.
81. Kozuch S., Shaik S. (2011), How to Conceptualize Catalytic Cycles? The Energetic Span Model, *Acc. Chem. Res.*, 44, 101–110 (DOI: 10.1021/ar1000956)

Chapter 4

*CO₂ Hydrogenation to Methanol Using
Earth Abundant Homogenous Based Mn
Catalysts*

4.1. Introduction

The global energy demand has been increasing tremendously due to the rapid growth of the world's population. On the other hand, the combustion of non-renewable fossil fuel based conventional energy sources leads to the emission of greenhouse gases which brings out harmful repercussions on the environment [1]. Therefore, CO₂ remediation *via* capturing and/or hydrogenation is one of the most attractive ways to address the energy and global warming related problems [2-8]. This process has been termed as the “carbon capture and storage” (CCS) [2-4]. The valuable CCS products (*via* CO₂ hydrogenation) are HCOOH, CH₃OH, HCHO, CH₄ and so on. Among all the CO₂ hydrogenated products, methanol is a very important product due to its uses in direct methanol fuel cells and in internal combustion engines. Besides, methanol is widely used as a precursor for various chemicals and fuels and can be a sustainable energy carrier for “methanol economy” [5-8]. In the past few decades, Cu/ZnO and many other heterogeneous based catalysts have been developed for CO₂ hydrogenation to CH₃OH [9-12]. Obtaining good selectivity is an obstacle for heterogeneous catalysts. Homogeneous catalysts operate at lower temperatures and pressures compared to heterogeneous catalysts [13-17]. Thus, the development of a homogeneous catalyst along with heterogeneous catalysts for CO₂ hydrogenation has attracted considerable attention among the researchers. Tominaga et al. have reported the first homogeneous catalyst for CO₂ hydrogenation to methanol in 1993, where they have used Ru₃(CO)₁₂ complex and N-methyl-2-pyrrolidone under 240 °C and 9 MPa pressure [17]. They have shown that CO₂ first reduces to CO, which is further hydrogenated to methanol. Later, several other noble metal-based homogeneous catalysts have been reported for CO₂ hydrogenation to methanol [13-16]. Side by side, several other groups have also reported indirect ways of CO₂ hydrogenation to methanol [18-23]. In this context, Sanford and co-workers have investigated an alternative tandem catalytic three-step CO₂ hydrogenation approach for methanol formation. In the first

step, CO₂ and H₂ converted into HCOOH acid in the presence of Ru(II) and Fe(II) catalysts. After that, HCOOH is esterified in the presence of a Lewis acid. Then the formate ester is hydrogenated to methanol in the presence of Ru pincer catalyst [15]. Alongside, Milstein and co-workers have developed an alternative approach for methanol synthesis using the [(PNN)Ru-(CO)(H)] complex. Firstly, they have synthesized a CO₂ derived product (such as carbonates, carbamates, formate, and urea), which then hydrogenated to CH₃OH [18]. After that, Miller et al., have reported the formation of methanol by transfer hydrogenation of formaldehyde using formic acid solution when catalyzed by the [Cp*Ir(2,2'-bipyridine)(H₂O)][OTf]₂ complex [23]. Wesselbaum et al., have also reported CO₂ hydrogenation to methanol catalyzed by the (triphos)Ru(TMM) [TMM: trimethylenemethane] catalyst [16]. However, all these indirect hydrogenation methods to methanol suffer from the low TON. Hence, indirect CO₂ hydrogenation is not an efficient approach for methanol production. Recently, Sanford and co-workers have reported high TON for co-catalyst-based CO₂ hydrogenation to methanol using the Ru pincer catalyst via formamide intermediate in the presence of dimethylamine [24]. Similarly, Zhang et al., have shown sequential CO₂ hydrogenation to methanol using the Ru-PNP and Mn-PNP catalysts in the presence of morpholine co-catalyst [25]. They have demonstrated that morpholine produces N-formylmorpholine and H₂O with CO₂ and H₂. This N-formylmorpholine undergoes further hydrogenation reaction and leads to the formation of methanol as a final product. However, all these active homogeneous catalysts are based on noble-metals, which restricts their large-scale industrial application. This opens the door for non-noble metal (Mn, Fe, Ni, Co, Cu etc.) based catalysts. Very recently, Prakash and co-workers have made significant contributions in this area and reported non-noble metal-based Mn, Fe-catalysts (in the presence of co-catalyst) for CO₂ hydrogenation to methanol with considerable activity [26-29]. Earlier studies have shown that non-noble metal based bifunctional catalysts can

also be promising for CO₂ hydrogenation to methanol in the presence of co-catalyst though Zheng and co-workers have shown that Ru-PNP is the most active catalyst compared to the Mn-PNP complex [25-29]. However, there is a lack of theoretical studies compared to the experimental reports to gain further insights into the reaction mechanisms of these type of reactions and why noble metal based catalysts are active over non-noble metal based catalysts. Inspired by all these findings, we have considered N-H functionalized (non-innocent) PNP-based Mn(I), Fe(II) and Ru(II) catalysts (Figure 4.1) and morpholine co-catalyst for our CO₂ hydrogenation to methanol study [28,29]. Hence, the detailed mechanistic pathways for the CO₂ hydrogenation reaction to methanol in the presence of co-catalyst and noble and non-noble metal based catalyst are very much important for the comprehensive understanding of the whole reaction mechanisms. Furthermore, it is highly important to identify the most favourable reaction pathway of this reaction and why such pathway is favourable over other possible reaction pathways. We have compared the catalytic activity of the Mn-PNP and Fe-PNP catalysts over the most active Ru-PNP complex to understand why Ru-PNP is the most active catalyst amongst all the three. We have also investigated the importance of the morpholine co-catalyst in such sequential CO₂ hydrogenation reaction.

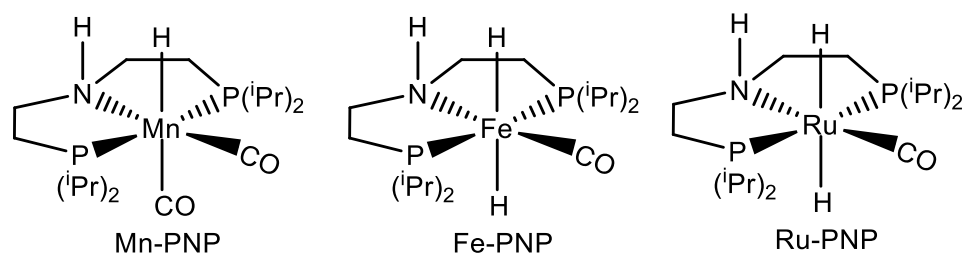
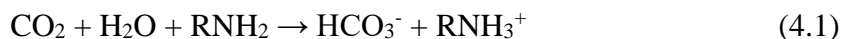


Figure 4.1: Considered metal catalysts for indirect CO₂ hydrogenation reaction to methanol [25,28,29].

Side by side, CO₂ capture and then conversion of captured product to methanol is of particular interest as methanol can be used as an energy

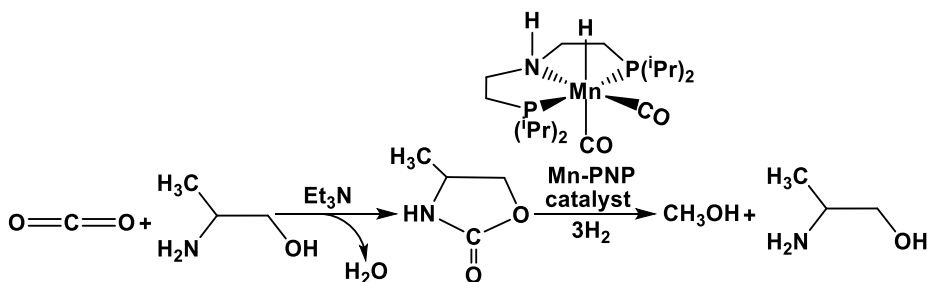
carrier in the direct methanol fuel cell, internal combustion engines and so on [1,30-32]. Other than these, there are several ways in which CO₂ can be hydrogenated to methanol. Some reports have shown that the CO₂ capture via functionalizations through the formation of C–N, C–O, C–C bonds are highly important for the formation of functional molecules, such as carbonates, carbamates, or urethanes, which can then be hydrogenated to various products [33-36]. In this study, we have considered CO₂ capture followed by hydrogenation to methanol to understand the process. Even for CO₂ capture part, there are several steps involved, such as the production of hydrocarbonate and carbamate in the presence of amines (equation 4.1 and 4.2) [37,38].



In the following steps, CO₂ can be released through heating, which then can be compressed and transported to a storage site with the removal of amine solution. So, the major drawbacks of these processes are the thermal degradation of the amines during the thermal treatment of the hydrocarbonate and carbamate. Recently, Bellona Foundation has reported 300-3000 tons of amine waste annually for a million ton of CO₂ capture [39]. Therefore, the economic viability of such a process is less. Besides, earlier reports have suggested that the oxazolidinone is an important CO₂ captured product [40-43]. Hence, instead of storing the CO₂ captured products, conversion of oxazolidinone to other valuable products is highly beneficial. In this context, amines and amino alcohols are the most common CO₂ capturing agents [41,44,45]. In this regard, amino alcohols are highly useful for the capturing of CO₂ to oxazolidinone. Milstein and co-workers have made significant progress in this field by reporting a series of amino alcohols for the formation of oxazolidinone based products [40]. Their study shows that the presence of the electron-donating group in amino alcohol enhances the formation of methanol. Besides, Saito's study shows that the monoethanolamine is not a good substrate for the formation

oxazolidinone due to the unfavourable thermodynamics of the reaction [46]. Side by side, they have shown that the substituents in the α -position of the amine group show a higher tendency toward cyclization and form the higher corresponding oxazolidinone product. Therefore, we have considered 2-amino-1-propanol as a CO₂ capturing agent, which has an electron-donating group in the α -position of the amine group. Amino alcohols are also used in industries as a CO₂ capturing agent [47]. In the next step, CO₂ captured product will be hydrogenated for the formation of value-added products. Thus, finding an efficient catalyst for the hydrogenation of CO₂ captured product (oxazolidinone) is highly beneficial. Milstein and co-workers have represented a novel approach for the hydrogenation of oxazolidinone to methanol using the Ru based pincer catalysts [40]. Besides, Ding and co-workers have shown PNP based catalysts for the hydrogenation of oxazolidinone to methanol [48]. Several other catalysts have also been reported for the hydrogenation of oxazolidinone to alcohol [49]. However, most of these active catalysts are based on noble metals. Therefore, a large-scale application of these catalysts is not feasible, which opens the door for non-noble metal (Mn, Fe, Ni, Co, etc.) based catalysts. Besides, to the best of knowledge, the mechanistic details for such reactions are yet to be reported. Moreover, there is a lack of detailed computational study as compared to the experimental reports to gain further insight into the reaction mechanism of CO₂ to methanol via oxazolidinone. Thus, it is very essential to gain computational insights into CO₂ capture followed by hydrogenation to methanol. In order to address these, we have considered 2-amino-1-propanol as a CO₂ capturing agent for the formation of oxazolidinone. In the next step, oxazolidinone should be hydrogenated to methanol. For industrial scale applications, the earth abundant 3d metal-based catalysts are very important and therefore replacements of the noble metal-based pincer catalysts are important. In this context, biocompatible and inexpensive 3d metal Mn can be an important alternate of noble metal-based catalysts for oxazolidinone hydrogenation to

methanol. The PNP ligand can facilitate rigidity of the Mn-metal complexes due to its tridentate PNP coordination with the Mn atom. Besides, the PNP ligand moiety of the catalyst can interact with the considered molecule by outer sphere mechanism via N–H bond of the central N-donor of the PNP pincer. Moreover, the N–H functionalized ligand moiety of the Mn-PNP based catalyst can play an important role for such reaction due to their non-innocent nature. Prakash and co-workers have shown that the activity of non-noble metal-based PNP complexes (Mn-PNP and Fe-PNP) can be promising for the methanol formation [28]. Hence, it is of great interest to study the oxazolidinone hydrogenation to methanol reaction mechanism over the Mn-PNP based catalyst. Moreover, hydride transfer and heterolytic H₂ cleavage are two important steps for hydrogenation reactions, which are also important steps for oxazolidinone hydrogenation to methanol [50]. Beller and co-workers have revealed that the Mn-PNP catalyst can be used for hydride transfer and heterolytic H₂ cleavage step during hydrogenation reaction [51]. Therefore, we believe that the Mn-PNP catalyst can be a promising catalyst for oxazolidinone hydrogenation reaction. Inspired by all these, we have investigated the reaction mechanisms for CO₂ capture (using 2-amino-1-propanol) to oxazolidinone followed by oxazolidinone hydrogenation to methanol using the Mn-PNP based catalysts (Scheme 4.1).



Scheme 4.1: The overall reaction mechanisms of CO₂ capture using 2-amino-1-propanol followed by hydrogenation to methanol in the presence of Mn-PNP catalyst.

4.2. Computational Details

All the calculations have been carried out with Gaussian 09 D.01 [52] package using Pople diffuse basis set 6-31++G(d,p) for non-metals (C, H, O, N and P) [53-55] and LANL2DZ effective core potentials (ECP) for metals (Mn, Fe, and Ru) [56,57]. The density functional theory (DFT) calculations have been carried out with Becke's three-parameter hybrid exchange and Lee-Yang-Parr's correlation functional (B3LYP) [58-62]. We have used the B3LYP functional based on our earlier reports (on CO₂ reduction/hydrogenation), where we have found out that they could reproduce the experimental number/trend [63-65]. In the case of Mn(I)-PNP based catalysts, Beller and co-workers have reported the reversibility of the active catalyst formation step in the presence of H₂ gas [51]. Therefore, we have calculated the reaction free energies for the reversible step of the active catalyst formation for Mn-PNP based catalyst in the presence of H₂ using different functional, basis sets and solvent models. For non-metals 6-31++G(d,p)/6-311++G(d,p) basis sets have been considered along with LANL2DZ-ECP and SDD for Mn atom. The conductor-like polarizable continuum (CPCM) solvent model and solvation model based on density (SMD) have been used for THF solvent as Milstein and co-workers have experimentally used THF for their reactions [40,66-68]. The Grimme's DFT-D3 interactions have been included in our all calculations to account the non-covalent interactions [69]. Experimentally, THF is the mostly used solvent for CO₂ hydrogenation reactions [24,25,27-29]. Our calculated reaction free energies (Table 4.1) show that the activate catalyst formation step is more or less agreement with the reversibility when we use the 6-31++G(d,p) basis set for non-metals and LANL2DZ ECP for Mn atom with DFT-D3 functional and CPCM solvent model. Furthermore, the calculated results show that CPCM solvation model is more appropriate as the calculated reaction free energy of the reversible active catalyst formation step in the presence of H₂ gas is close to zero whereas SMD solvation model gives a far greater exergonicity in this case. Therefore, all

the structures have been fully optimized in the presence of THF solvent ($\epsilon = 7.4257$) using the conductor-like polarizable continuum solvation model (CPCM) [66,67]. Harmonic vibrational frequency calculations have been carried out to characterize the nature of stationary points. All the transition states (TS) have been confirmed based on the presence of one imaginary frequency along the expected reaction coordinate. Furthermore, intrinsic reaction coordinate (IRC) calculations have been used to confirm the transition states (TS). Zero-point vibrational energy (ZPVE) and thermal corrections have been included in our total electronic energy to get the reaction free energy at 298.15 K temperature and 1 atm pressure. The reaction free energy changes (ΔG) and barriers (ΔG^\ddagger) have been obtained from the reaction free energy difference between final and initial intermediates, and the reaction free energy difference between the transition state and the reactant, respectively. Natural bond orbital (NBO) calculations have also been performed on some of the intermediates to investigate natural charges of atoms and atomic electron contribution in bonding orbitals [70]. The progress of the reactions has been simulated by first, calculating the rate constants using the transition state theory (TST), and then building microkinetic models of the all-over reaction paths [71]. For each of the catalytic cycles, simplified schemes were used to calculate the change in concentration of the substrates and intermediates in course of the reactions. The Livermore Solver for Ordinary Differential Equations (LSODA) algorithm implemented in Complex Pathway Simulator (COPASI) software (version 4.22) has been used for the time-course simulation of the microkinetic model [72,73]. Moreover, we have calculated the rate constant (k) value of the rate determining step (RDS) for oxazolidinone hydrogenation to methanol over 273–600 K using highly accurate Kisthelp kinetic programme as follows [74]:

$$k_{(T)}^{\text{TST}} = \sigma \frac{k_B T}{h} \left(\frac{RT}{p^0} \right)^{\Delta n} e^{\frac{-\Delta G^\ddagger}{k_B T}}$$

Here, σ , k_B , T , h , R , p^0 , Δn and ΔG^\ddagger are the reaction path degeneracy,

Boltzmann constant, system's temperature, Planck constant, ideal gas constant, system's standard pressure, change in moles of gaseous molecule and Gibbs free energy of activation for the considered step, respectively.

Table 4.1: Evaluation of functional, basis sets and solvation model for Mn(I)-PNP based catalyst.

Functional	Basis set for nonmetals	Basis set for Mn atom	Solvent model for THF	Reaction free energy (kcal/mol)
B3LYP+D3	6-31++G(d,p)	LANL2DZ	CPCM	-1.1
B3LYP+D3	6-31++G(d,p)	LANL2DZ	SMD	-9.7
B3LYP+D3	6-311++G(d,p)	LANL2DZ	CPCM	-1.4
B3LYP+D3	6-311++G(d,p)	LANL2DZ	SMD	-9.4
B3LYP+D3	6-31++G(d,p)	SDD	CPCM	-0.8
B3LYP+D3	6-31++G(d,p)	SDD	SMD	-9.2
B3LYP+D3	6-311++G(d,p)	SDD	CPCM	-0.7
B3LYP+D3	6-311++G(d,p)	SDD	SMD	-8.8
B3LYP	6-31++G(d,p)	LANL2DZ	CPCM	1.2

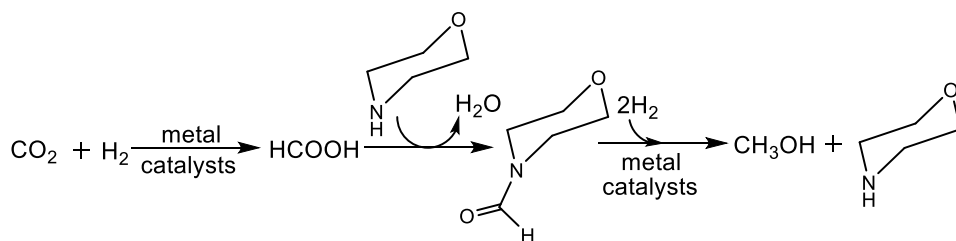
4.3. Results and Discussion

In this section we have discussed the morpholine and amino alcohol assisted CO₂ hydrogenation to methanol using PNP based catalysts.

4.3.1. Morpholine Assisted CO₂ Hydrogenation to Methanol

The chemically non-innocent N-H functionally pincer ligand-based metal catalysts have been widely used for various hydrogenation reaction [25-29,75,76]. This N-H functional shows a classical Noyori type metal-ligand co-operation mechanism. Besides, this N-H functional shows promising catalytic activity for CO₂ hydrogenation to methanol reaction too. Previous studies show that in the presence of morpholine co-catalyst, the rate of the

reaction increases for CO₂ hydrogenation to methanol when catalyzed by the Mn(I), Fe(II), and Ru(II) PNP based catalysts [25,28,29]. For mechanistic insights, we have investigated all the three Mn-PNP, Fe-PNP and Ru-PNP complexes (Figure 4.1) for CO₂ hydrogenation to methanol in the presence of morpholine co-catalyst. To this extent, the whole mechanistic pathway (Scheme 4.2) of CO₂ hydrogenation to methanol has been divided into three parts: (i) CO₂ hydrogenation to HCOOH, (ii) HCOOH to N-formylmorpholine and (iii) N-formylmorpholine hydrogenation to methanol.

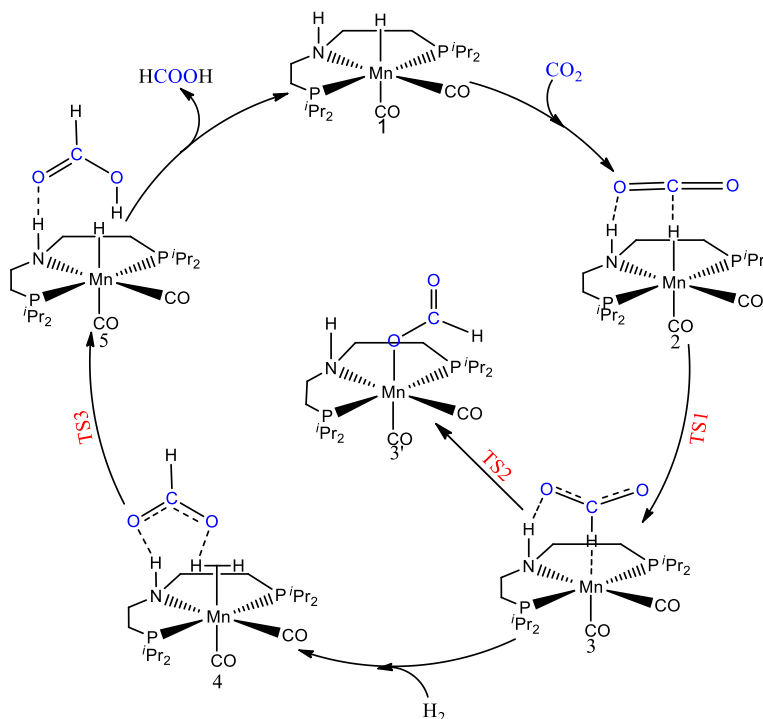


Scheme 4.2: The reaction mechanisms of CO₂ hydrogenation to methanol in the presence of morpholine.

4.3.1.1. CO₂ Hydrogenation to HCOOH

Intriguingly, Dub *et al.*, have proposed that the revised Noyori type mechanism is more favorable than the classical Noyori type mechanism for ketone hydrogenation when catalysed by the pincer ligand based Ir and Ru catalysts [77-79]. Similarly, we have also investigated that revised Noyori type mechanism, which is a highly favourable mechanism for CO₂ hydrogenation to formate in the presence of aminomethyl based Mn(I) complexes [80]. The modelled Mn-PNP, Fe-PNP and Ru-PNP catalysts are also similar kind of catalyst as reported by Dub and co-workers. Hence, we have studied the revised Noyori type (Ligand assisted, Scheme 4.3) as well as the classical Noyori type mechanism (Ligand participated, Scheme 4.4) for CO₂ hydrogenation reaction to HCOOH. In the revised Noyori type mechanism, Intermediate **1** with hydridic and protic hydrogens can interact

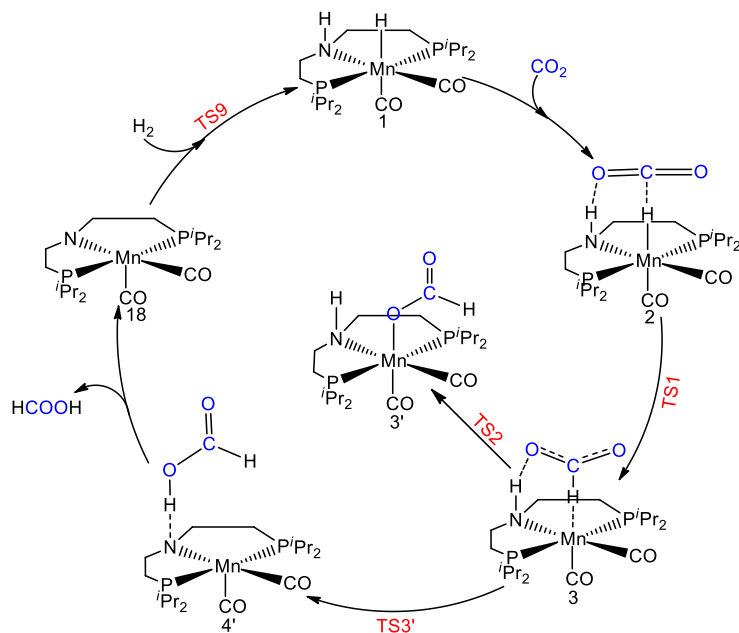
with carbon and oxygen atoms of CO₂ molecule, respectively. So, the reaction may start with CO₂ interacting with **1** for the formation of **2** (**1** + CO₂ → **2**). After that, hydride may transfer to CO₂ for the formation of intermediate **3** (via transition state **TS1**). Figure 4.2 shows our calculated reaction free energy profile for CO₂ hydrogenation to HCOOH by the Mn-PNP catalyst for ligand assisted, whereas Figure 4.3 shows the reaction free energy profile for ligand participated mechanism. More often than not, hydride transfer step is the rates determining step for such reaction [63-65]. The calculated reaction free energy barrier for hydride transfer is 1.8 kcal/mol for the Mn-PNP catalyst.



Scheme 4.3: Ligand assisted CO₂ hydrogenation to HCOOH catalyzed by Mn-PNP catalyst.

Therefore, Mn-PNP requires a very low free energy barrier for hydride transfer, which suggests that Mn-PNP can be a promising catalyst for CO₂ hydrogenation reaction. Furthermore, intermediate **3** may isomerize into a more stable intermediate **3'** (via transition state **TS2**) and the **3**→**3'**

isomerization process calculated to be a barrier-less process. However, intermediate **3'** is 18.3 kcal/mol more stable than **3**, which could be due to the formation of a strong Mn–O bond. This is even consistent with the experimental reports as **3'** can be isolated for such reaction [81,82]. Nevertheless, such kind of highly stabilized intermediate state within the catalytic cycle can be a resting state, which may decrease the catalytic activity of the catalyst. On the other hand, intermediate **3** can react with H₂ for the formation of intermediate **4**, where formate anion may interact with metal complex *via* Mn–H₂···O (2.51 Å) and N–H···O (1.79 Å) hydrogen bonding interactions (Figure 4.4).



Scheme 4.4: Ligand participated CO₂ hydrogenation to HCOOH catalyzed by Mn-PNP.

We find that formate anion can initiate the heterolytic H₂ cleavage *via* transition state **TS3** with N–H···O 1.88Å and H–H···O 1.26Å for the formation of intermediate **5** (Figure 4.5). The calculated reaction free energy barrier is 4.3 kcal/mol for the formate anion assisted heterolytic H₂ cleavage, which is significantly low as heterolytic H₂ cleavage is another

important reaction step for CO₂ hydrogenation reaction. Such a low barrier could be due to the presence of N–H bond functionality as such N-H bond functionality interacts with formate through hydrogen bonding interactions, which in turn facilitate the heterolytic H₂ cleavage. Furthermore, intermediate **5** may release formate anion for the regeneration of the catalyst (**1**). The energetic span model has been used for the calculation of total reaction free energy barrier [83] and the calculated total reaction free energy barrier ($\Delta\Delta G^{\ddagger R}$) for CO₂ hydrogenation to HCOOH is 30.2 kcal/mol for the ligand-assisted mechanism for **Mn-PNP** catalyst.

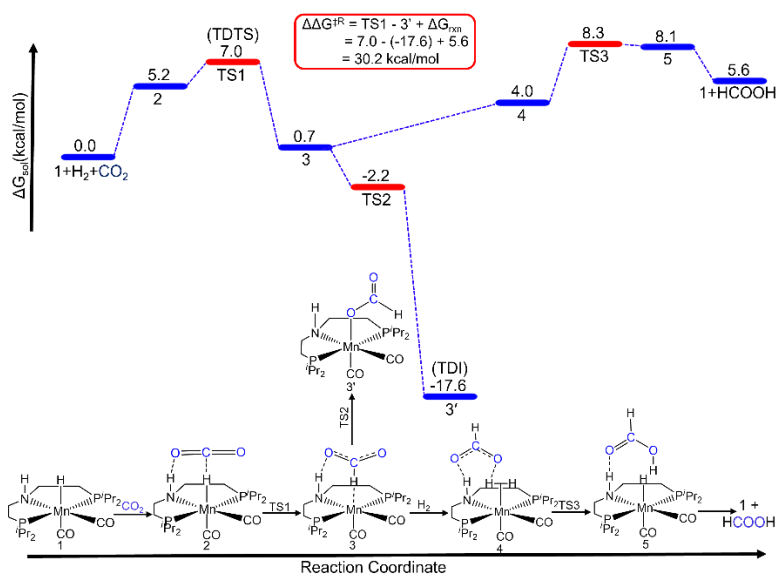


Figure 4.2: Reaction free energy profile diagram of CO₂ hydrogenation to HCOOH *via* ligand assisted mechanism catalyzed by Mn-PNP complex. $\Delta\Delta G^{\ddagger R}$ and ΔG_{rxn} denote the total free energy barrier and total reaction free energy of the catalytic cycle, respectively.

We find that the ligand-assisted pathway is 18.1 kcal/mol more favorable compared to the ligand participate mechanistic. As ligand assisted pathway is calculated to be the most favorable pathway for CO₂ hydrogenation to methanol, same mechanism has been considered for Fe-PNP and Ru-PNP complexes too. The calculated total reaction free energy barriers for CO₂ to

HCOOH are 30.2 kcal/mol, 28.5 kcal/mol and 24.5 kcal/mol for the Mn-PNP, Fe-PNP and Ru-PNP complexes, respectively (Table 4.2).

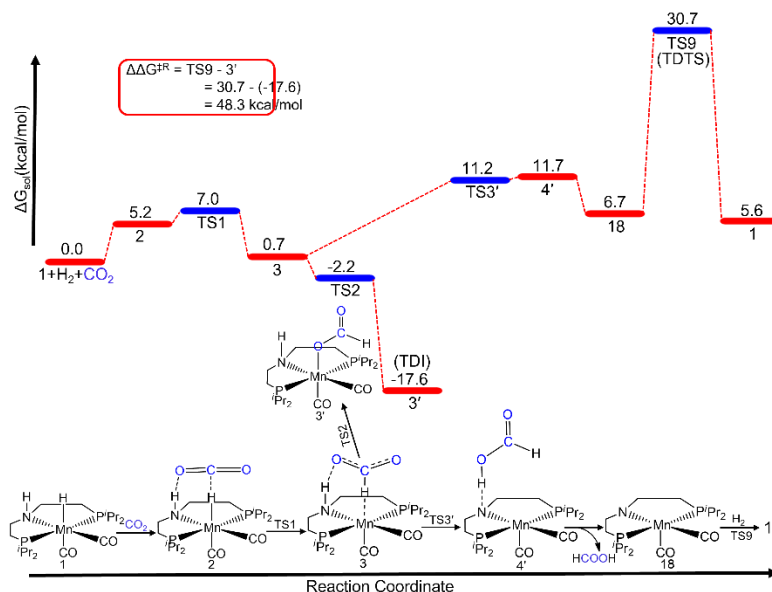


Figure 4.3: Reaction free energy profile diagram of CO₂ hydrogenation to HCOOH *via* ligand participated mechanism catalysed by Mn-PNP complex. $\Delta\Delta G^{\ddagger R}$ and ΔG_{rxn} denote the total free energy barrier and total reaction free energy of the catalytic cycle, respectively.

Therefore, the Mn-PNP complex requires higher barrier (by 5.7 kcal/mol) compared to the most active Ru-PNP complex. Similarly, the barrier for the hydride transfer step (one of the rate determining steps) is also favourable for the Ru-PNP (4.5 kcal/mol) complex compared to the Mn-PNP (7.0 kcal/mol) and Fe-PNP (5.3 kcal/mol) complexes. Our calculated NBO charges show that the negative charge on the H-atom of M-H bond is more on Ru-PNP (-0.07) compared to that on the Mn-PNP (-0.01), which is consistent with our calculated barriers for hydride transfer. Likewise, in our reaction free energy profile too, we find that the resting state (intermediate **3'**) of the Mn-PNP complex is highly stabilized (-17.6 kcal/mol) compared to the resting state of Ru-PNP complex (-14.4 kcal/mol).

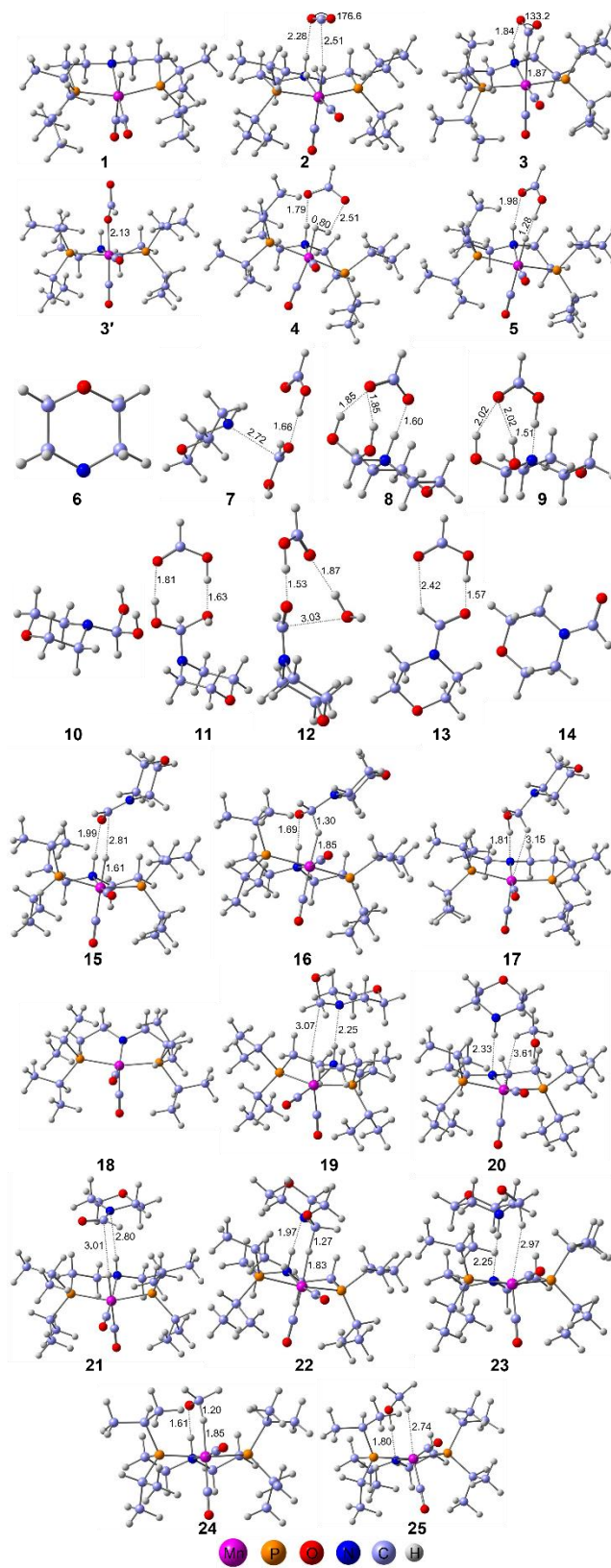


Figure 4.4: Optimized geometries of intermediates for CO₂ hydrogenation

to methanol catalyzed by Mn-PNP complex. Bond lengths and bond angles are in Å and °, respectively.

All these results indicate that Ru-PNP complex is the most active complex over Fe-PNP and Mn-PNP complexes, which is in agreement with the experimental findings [25]. However, the total reaction free energy barriers for the non-noble catalysts (Fe and Mn based PNP catalysts) are not very high compared to the noble metal-based Ru-PNP complex.

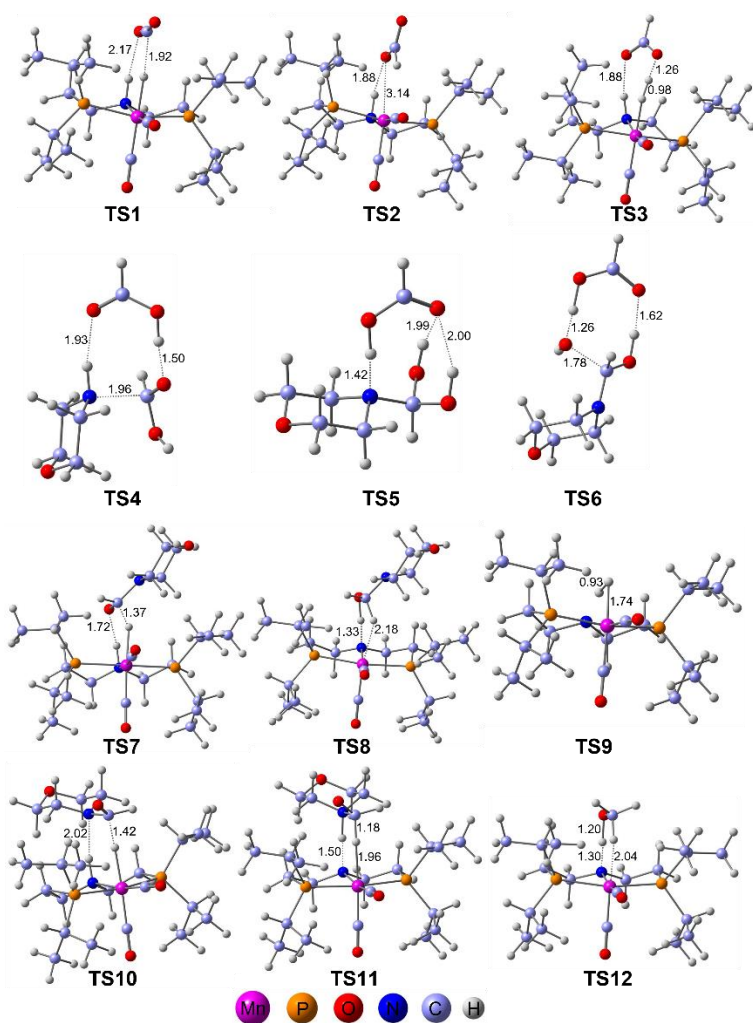


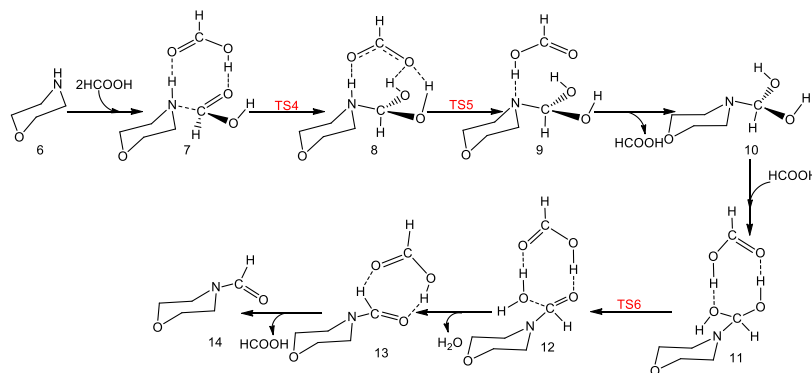
Figure 4.5: Optimized geometries of transition states for CO₂ hydrogenation to methanol catalyzed by Mn-PNP complex. Bond lengths and bond angles are in Å and °, respectively.

Table 4.2: Ligand assisted reaction free energy for CO₂ hydrogenation reaction to HCOOH by PNP based Mn(I), Fe(II) and Ru(II) complexes. $\Delta\Delta G^\ddagger$ represents the total reaction free energy barriers for reaction. All free energies are in kcal/mol.

Complexes	Relative Free Energies (kcal/mol)										$\Delta\Delta G^\ddagger$
	1+H ₂ + CO ₂	2	TS1	3	TS2	3'	4	TS3	5	1+ HCOOH	
Mn-PNP	0.0	5.2	7.0	0.7	-2.2	-	4.0	8.3	8.1	5.6	30.2
Fe-PNP	0.0	3.8	5.3	-9.5	-5.1	-	2.3	4.7	4.9	5.6	28.5
Ru-PNP	0.0	4.1	4.5	-9.3	-6.8	-	-1.5	5.6	5.6	5.6	24.5

4.3.1.2. HCOOH to N-formylmorpholine

In the presence of morpholine base, HCOOH may react to morpholine for the formation of N-formylmorpholine (Scheme 4.5). Lu et al., have reported mechanism for the conversion of amine (morpholine) to an amide (N-formylmorpholine), [84] where two molecules of HCOOH can interact with morpholine for the formation of **7**.



Scheme 4.5: HCOOH to N-formylmorpholine (amidation).

In the next step, **7** may isomerize into **8** via **TS4**. Figure 4.6 presents the reaction free energy profile for the amidation reaction. The calculated reaction free energy barrier (**7**→**TS4**) is 5.0 kcal/mol for the isomerization step. This suggests that isomerization requires a low free energy barrier, which could be due to the formation of a C-N bond. Furthermore, intermediate **8** may isomerize into **9** via transition state **TS5**. The calculated free energy barrier is very low (1.5 kcal/mol) for such isomerization too. In the following step, **9** may release HCOOH for the formation of the methylene glycol functional group based intermediate **10**.

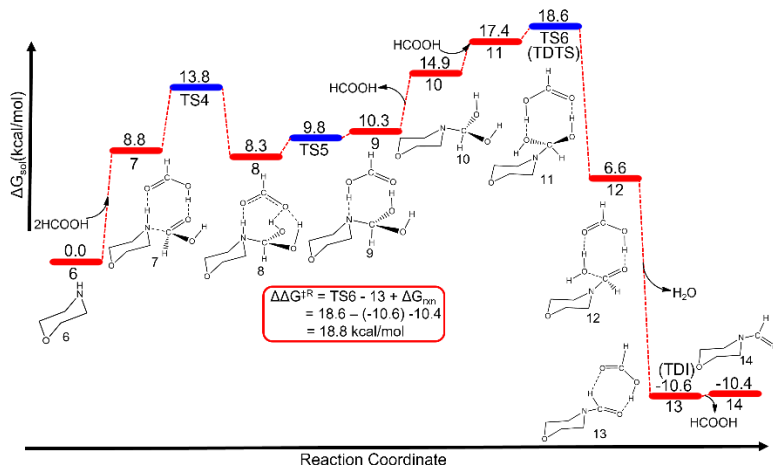
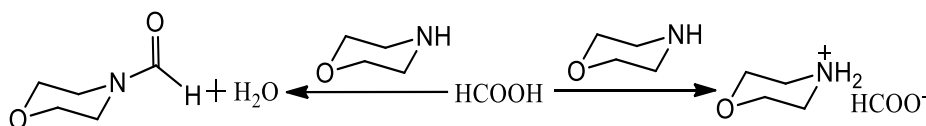


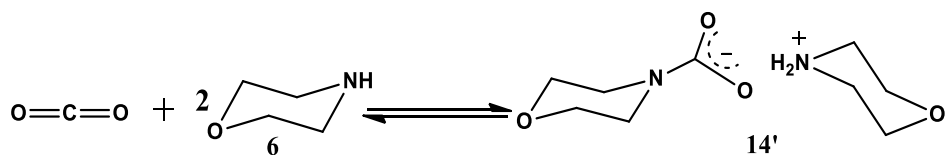
Figure 4.6: Reaction free energy profile diagram of HCOOH to N-formylmorpholine (amidation).

Besides, HCOOH may again interact with intermediate **10** for the formation of intermediate **11**, where HCOOH can interact with the methylene glycol part of intermediate **10**. Further to this, **11** can rearrange to **12** via transition state **TS6** and the proton from HCOOH/glycol can be transferred to glycol/HCOOH. Such rearrangement calculated to be possible as the calculated reaction free energy barrier is only 1.2 kcal/mol. Subsequently, **12** may release H₂O for the formation of **13**, which may further release HCOOH for the formation of **14** (N-formylmorpholine). The calculated total reaction free energy value shows that the formation of N-

formylmorpholine is very much favorable. Hence, amidation reaction is calculated to be thermodynamically favorable. More importantly, the total reaction free energy barrier (18.8 kcal/mol) for amidation is also low, which suggests that the reaction may be kinetically favorable too. Such highly favorable amidation reaction suggests that the overall catalytic activity of the CO₂ hydrogenation to methanol reaction may be highly favorable via amidation. The CO₂ hydrogenation to HCOOH is calculated to be endergonic by 5.6 kcal/mol. Subsequently, the formic acid can react with morpholine (Scheme 4.6) for the formation of formate anion (deprotonation of formic acid) or amide (amidation). The calculated reaction free energy values suggest that amidation step is highly exergonic (10.4 kcal/mol) compared to the deprotonation step (4.4 kcal/mol). Therefore, the reaction will proceed via amidation intermediate as the overall reaction free energy is exergonic compared to the deprotonation step. Prior to CO₂ hydrogenation, there can be an uncatalyzed reaction (Scheme 4.7) between two equivalents of amine (base) and CO₂ to form the carbamate salt CO₂ [24].



Scheme 4.6: Formation of formate and amide intermediates in the presence of morpholine base.



Scheme 4.7: Uncatalyzed reaction between two equivalents of morpholine and CO₂ for the formation of carbamate salt.

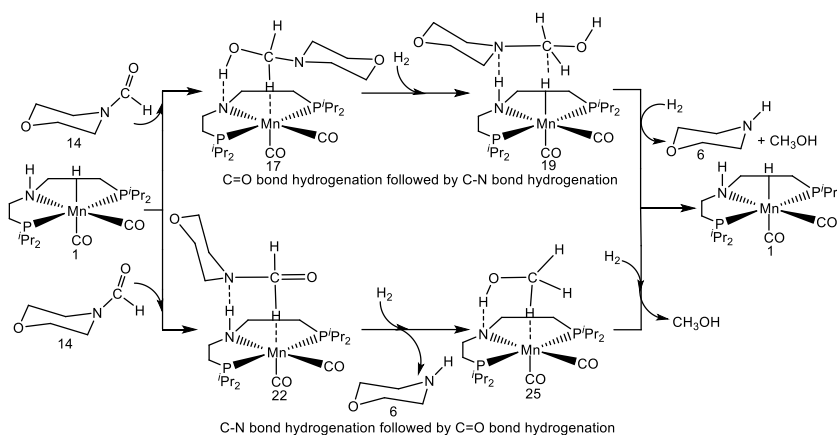
We have calculated the reaction free energy for such reaction and the

calculated low reaction free energy value (1.2 kcal/mol) suggests that the reaction can be very much reversible. However, the overall reaction free energy for CO₂ to amide formation is exergonic (4.8 kcal/mol) in nature. Hence, the exergonic nature of the reaction (CO₂ to amide formation) will be the driving force for the subsequent steps for CO₂ hydrogenation to methanol. There can be several possible mechanisms for CO₂ hydrogenation to methanol, such as single pot process, sequential approach and so on [24,28,29,85]. Our calculated results suggest that the morpholine co-catalyst based amidation step that is HCOOH to amide is highly exergonic. Furthermore, such amide-based intermediate has been characterised in the co-catalyst-based CO₂ hydrogenation reaction to methanol [24,28,29]. Inspired by the experimental findings, we have considered the sequential approach for CO₂ hydrogenation to methanol for our study.

4.3.1.3. N-formylmorpholine Hydrogenation to Methanol

Furthermore, N-formylmorpholine can undergo hydrogenation for the formation of methanol in the presence of the catalyst. Such hydrogenation of amide is very important for various industrial applications such as amine formation, sustainable pharmaceutical production, alcohol production and so on. However, amide hydrogenation to methanol is a challenging reaction in terms of selective hydrogenation as there are two functional groups (C=O and C–N) to be hydrogenated. In this regard, pincer bifunctional types of catalysts have been extensively studied [13-29]. Therefore, it's very important to find out the exact mechanistic pathways for the reaction. Milstein and co-workers have reported about the selective hydrogenation of the ketonic part of the amide group while catalysed by the manganese pincer based complex. However, these catalysts are different from our modelled complexes as they have used aromatic pincer ligand based catalysts [86]. Here, two different hydrogenation possibilities have been considered for N-formylmorpholine hydrogenation to methanol: (i) C=O bond hydrogenation

followed by C–N bond hydrogenation and (ii) C–N bond hydrogenation followed by C=O bond hydrogenation (Scheme 4.8).

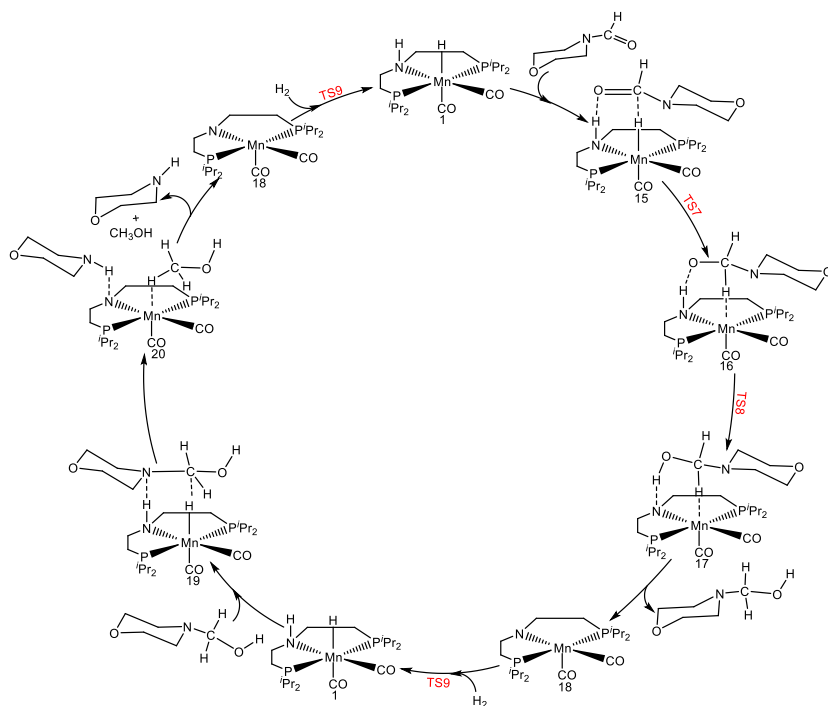


Scheme 4.8: Expected two different possibilities for N-formylmorpholine hydrogenation to methanol by Mn-PNP catalyst.

4.3.1.3.1. C=O Bond Hydrogenation Followed by C–N Bond Hydrogenation

Here we have considered N-formylmorpholine hydrogenation to methanol catalyzed by the Mn-PNP catalyst where the reaction proceeds via C=O bond hydrogenation followed by C–N bond hydrogenation (Scheme 4.9). Furthermore, we show that the hydridic and protonic hydrogen atoms of Mn-PNP can simultaneously interact with the N-formylmorpholine for the formation of **15**. Subsequently, hydride of Mn-PNP can transfer for the formation of **16** via the transition state (**TS7**). Figure 4.7 presents the reaction free energy profile for N-formylmorpholine hydrogenation. The calculated reaction free energy barrier for the hydride transfer step (**15**→**16**) is 15.3 kcal/mol, which is quite high for the amide hydrogenation reaction. Furthermore, **16** can rearrange to **17** via transition state **TS8**, with a barrier of 2.0 kcal/mol, where proton transfer occurs from the nitrogen atom to oxygen atom. Nova and co-workers have also reported amide hydrogenation reaction to alcohol via hemiaminal intermediate in the presence of aliphatic pincer based Fe-complexes [87]. We have also

considered such mechanism in our amide hydrogenation to methanol (C=O bond hydrogenation followed by C–N bond hydrogenation) study and we find that the formation of such hemiaminal is favourable.



Scheme 4.9: N-formylmorpholine hydrogenation reaction to methanol via C=O bond hydrogenation followed by C–N bond hydrogenation catalyzed by Mn-PNP complex.

Successively, **17** may release the hydrogenated (C=O bond) N-formylmorpholine for the formation of a 5-coordinated intermediate **18**, which is calculated to be a highly favorable process. Then the unsaturated intermediate **18** can facilitate the heterolytic H₂ cleavage via transition state **TS9**. The calculated reaction free energy barrier (**18**→**TS9**) is 24.0 kcal/mol, which could be a rate-determining step for the N-formylmorpholine hydrogenation to methanol reaction. Earlier reports also suggest that the heterolytic hydrogen cleavage step is highly unfavourable [88,89]. The calculated reaction free energy difference between intermediate **18** and **1** is 1.1 kcal/mol, which agrees well with the earlier

report suggested by Beller and co-workers [90]. Subsequently, C=O bond hydrogenated morpholine can interact with intermediate **1** for the formation of **19**.

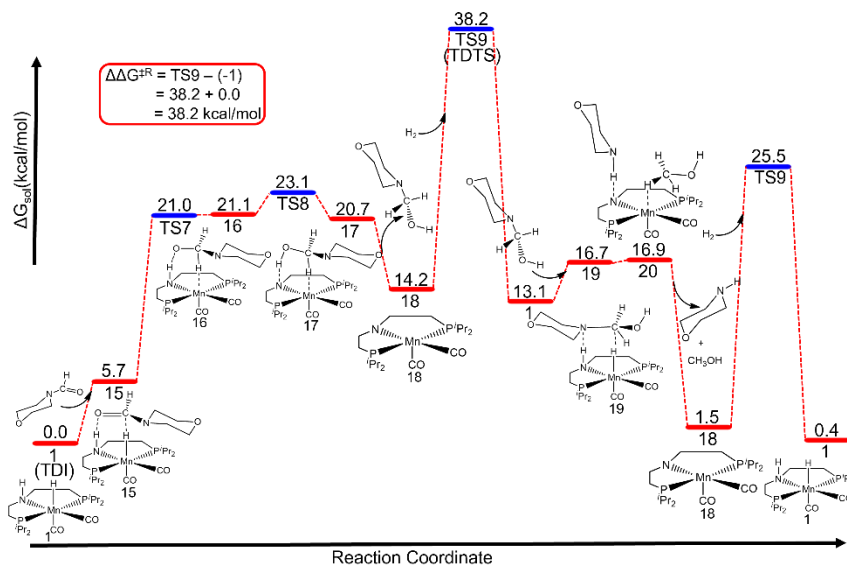


Figure 4.7: Reaction free energy profile diagram of N-formylmorpholine hydrogenation to methanol *via* C=O bond hydrogenation followed by C–N bond hydrogenation catalyzed by Mn-PNP complex. $\Delta\Delta G^{\ddagger R}$ and ΔG_{rxn} denote the total free energy barrier and total reaction free energy of the catalytic cycle, respectively.

Further, hydride and proton may transfer to the carbon and nitrogen atoms of the C=O hydrogenated morpholine, respectively. Intermediate **20** may release methanol and morpholine for the regeneration of **18**, which is calculated to be a highly favorable process (15.4 kcal/mol) *i.e.*, the release of morpholine and CH_3OH . Intermediate **18** can further react with H_2 for the regeneration of **1** to initiate the next catalytic cycle. The calculated total reaction free energy barrier for the N-formylmorpholine hydrogenation to methanol *via* C=O hydrogenation followed by C–N hydrogenation is 38.2 kcal/mol, which is considerably high. The calculated total reaction free energy barriers for Fe-PNP and Ru-PNP are 37.6 and 38.8 kcal/mol respectively. This indicates that the Mn-PNP and Fe-PNP catalysts require

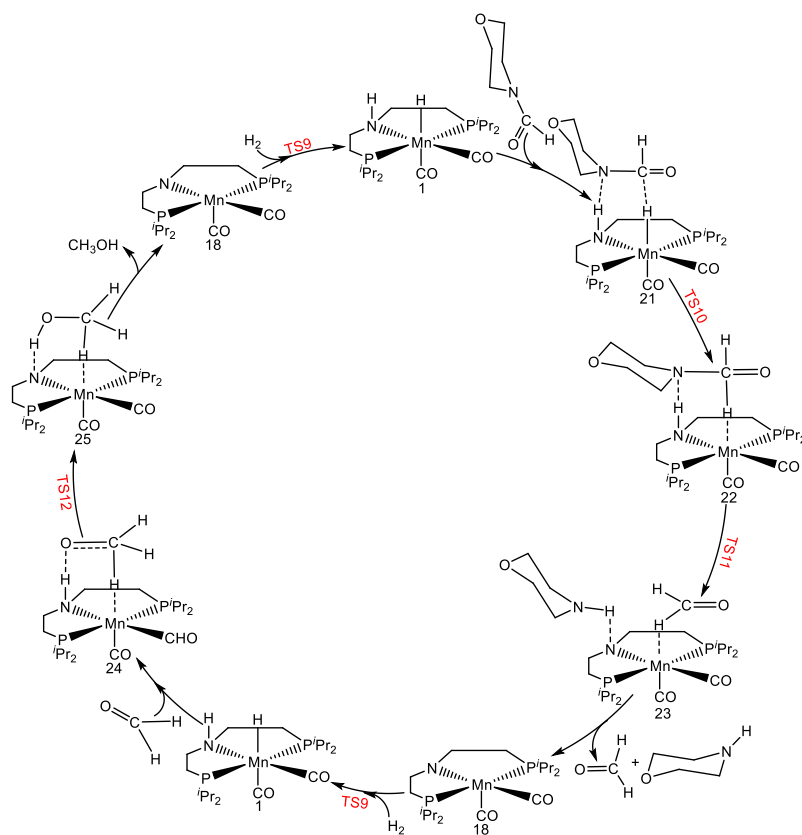
an almost equivalent amount of free energy barrier compared to the noble metal-based Ru-PNP catalysts (Table 4.3). The reaction free energies show that hydride transfer is one of the important steps in the amide hydrogenation to methanol too. The calculated reaction free energy barriers of hydride transfer step for Mn-PNP and Ru-PNP complexes are 21.0 and 16.4 kcal/mol (Table 4.3), respectively. This again indicates that Ru-PNP is the most active catalyst for amide hydrogenation to methanol [25].

Table 4.3: N-formylmorpholine hydrogenation to methanol via C=O bond hydrogenation followed by C–N bond hydrogenation reaction by PNP based Mn(I), Fe(II) and Ru(II) complexes. $\Delta\Delta G^{\ddagger R}$ represents the total reaction free energy barriers for reaction. All free energies are in kcal/mol.

Complexes	Relative Free Energies (kcal/mol)														$\Delta\Delta G^{\ddagger R}$
	1	15	TS7	16	TS8	17	18	TS9	1	19	20	18	TS9	1	
Mn-PNP	0.0	5.7	21.0	21.1	23.1	20.7	14.2	38.2	13.1	16.7	16.9	1.5	25.5	0.4	38.2
Fe-PNP	0.0	5.0	17.4	17.9	17.5	17.7	18.4	37.6	13.0	16.1	14.5	5.8	25.0	0.4	37.6
Ru-PNP	0.0	4.3	16.4	17.3	22.9	18.5	18.4	38.8	13.0	16.1	15.0	5.8	26.2	0.4	38.8

4.3.1.3.2. C–N Bond Hydrogenation Followed by C=O Bond Hydrogenation

Similarly, we have studied another possible pathway (Scheme 4.10) for N-formylmorpholine hydrogenation to methanol. Here we have considered N-formyl hydrogenation to methanol can occur *via* C–N bond hydrogenation followed by C=O bond hydrogenation. Sanford and co-workers have shown C–N bond cleavage in the amide hydrogenation reaction for the formation of amine and alcohol [91]. We have also considered same mechanism for our study. Herein, we predict that N-formylmorpholine can interact with **1** for the formation of **21**. Consequently, intermediate **21** can rearrange to intermediate **22** *via* transition state **TS10**. Figure 4.8 represents the reaction free energy profile diagram for N-formylmorpholine hydrogenation to methanol catalyzed by the Mn-PNP catalyst.



Scheme 4.10: N-formylmorpholine hydrogenation to methanol *via* C–N bond hydrogenation followed by C=O bond hydrogenation catalysed by Mn-PNP complex.

The calculated reaction free energy barrier of hydride transfer step is 17.4 kcal/mol, which is 2.1 kcal/mol higher than the hydride transfer step in C=O bond hydrogenation followed by C–N bond hydrogenation reaction mechanism. After that, N-formylmorpholine can abstract the proton from N–H of the ligand sphere for the formation of **23** *via* transition state **TS11**. In intermediate **23**, morpholine and HCHO can interact with the ligand sphere of Mn-PNP. Subsequently, intermediate **23** may release morpholine and HCHO for the formation of unsaturated intermediate **18**. The formation of **18** is calculated to be highly exergonic (14.9 kcal/mol) from intermediate **23**. Consequently, **18** can facilitate the heterolytic H₂ cleavage and further converted to **24**. Further to this, metal hydride (Mn–H) and N–H proton of

the catalyst would transfer to the carbon and oxygen of HCHO respectively for the formation of **25** via transition state **TS12**. This step is calculated to be a barrier-less process.

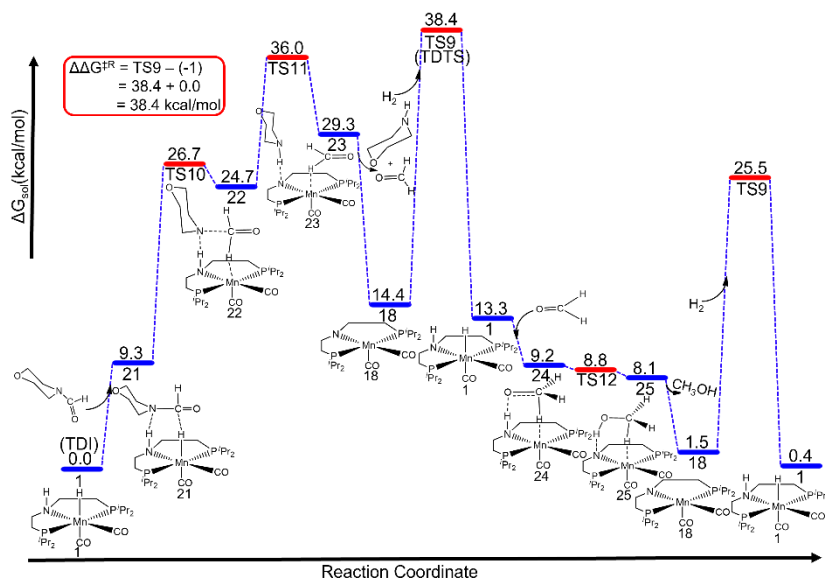


Figure 4.8: Reaction free energy profile diagram of N-formylmorpholine hydrogenation to methanol via C–N bond hydrogenation followed by C=O bond hydrogenation catalyzed by Mn-PNP complex. $\Delta\Delta G^{\ddagger R}$ and ΔG_{rxn} denote the total free energy barrier and total reaction free energy of the catalytic cycle, respectively.

Afterward, **26** would release methanol and form intermediate **18**, followed by regeneration of catalyst **1** in the presence of molecular H_2 . The calculated total reaction free energy barrier is 38.4 kcal/mol for N-formylmorpholine hydrogenation to methanol via the C–N bond hydrogenation followed by C=O bond hydrogenation mechanism. Similar reaction mechanisms have been studied for the Fe-PNP and Ru-PNP catalysts too and the calculated total reaction free energy barriers are 37.9 and 39.0 kcal/mol for Fe-PNP and Ru-PNP catalysts respectively (Table 4.4). Therefore, the non-noble metal-based catalysts (Mn-PNP) require almost the same amount of free energy barrier as required for the noble metal-based catalyst. Our calculated

results show that both the proposed mechanisms for N-formylmorpholine hydrogenation to methanol are very much competitive for all the three catalysts. So, our detailed study shows that Mn and Fe-based metal-based complexes have strong affinity for H and O-atoms, which in turn reduces their catalytic activity for CO₂ hydrogenation compared to the Ru-PNP complex [25].

Table 4.4: N-formylmorpholine hydrogenation to methanol via C–N bond hydrogenation followed by C=O bond hydrogenation reaction by PNP based Mn(I), Fe(II) and Ru(II) complexes. $\Delta\Delta G^{\ddagger R}$ represents the total reaction free energy barriers for reaction. All free energies are in kcal/mol.

Complexes	Relative Free Energies (kcal/mol)														$\Delta\Delta G^{\ddagger R}$
	1	21	TS1 0	22	TS11	23	18	TS9	1	24	TS12	25	18	TS9	
Mn-PNP	0.0	9.3	26.7	24.7	36.0	29.3	14.4	38.4	13.3	9.2	8.8	8.1	1.5	25.0	38.4
Fe-PNP	0.0	7.9	21.1	23.1	31.1	26.1	18.7	37.9	13.3	7.1	-	2.5	5.8	25.0	37.9
Ru-PNP	0.0	8.7	23.7	23.5	30.5	29.0	18.7	39.0	13.3	6.3	12.1	3.9	5.8	26.2	39.0

4.3.1.4. Hydride Transfer Step

Two competitive reaction mechanisms have been studied for N-formylmorpholine hydrogenation to methanol and it is obvious that rate-determining steps (i.e., the heterolytic H₂ cleavage) in both these reaction mechanisms require comparable energy to overcome the total reaction free energy barrier for all the considered catalysts. In general, hydride transfer and heterolytic H₂ cleavage are found to be the two important steps for hydrogenation of N-formylmorpholine to methanol. However, the reaction free energy profile diagrams of the two considered mechanisms show that hydride transfer steps (metal hydride to N-formylmorpholine) are quite different from one to other. Furthermore, we have observed that the very first hydride transfer step is highly unfavorable compared to the second in both the mechanisms. Molecular orbital analysis has been performed (Figure 4.9) for some important intermediates to understand the difference

in hydride transfer steps. The HOMO-LUMO energy gap is used as a modest indicator of stability. A small HOMO-LUMO gap suggests low stability and high reactivity, because of its favorable electron transition to low lying LUMO. The molecular orbital diagram shows that the HOMO-LUMO gap is higher for intermediate **15** (4.85 eV) compared to that in intermediate **16** (4.55 eV).

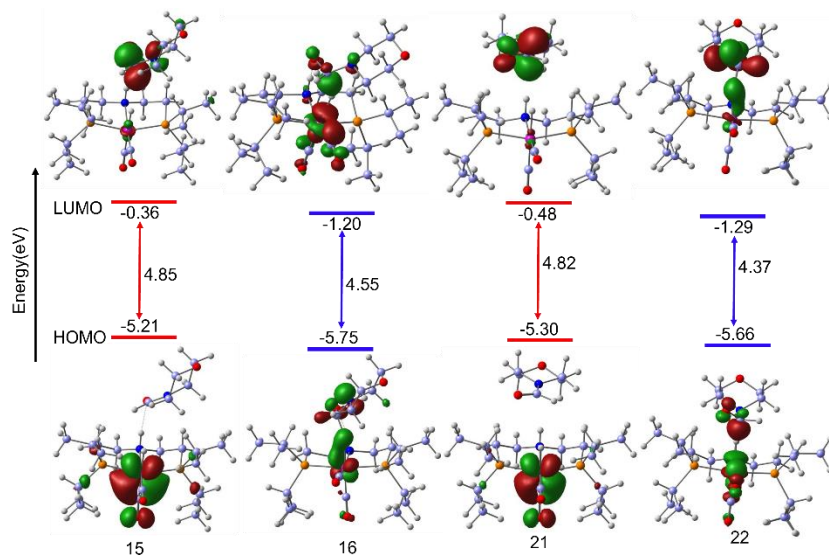


Figure 4.9: Frontier molecular orbitals of intermediates **15**, **16**, **21**, and **22** for Mn-PNP complex.

Similarly, HOMO-LUMO energy gap is higher in **21** (4.82 eV) as compared to **22** (4.37 eV). Therefore, these values (reaction free energy and HOMO-LUMO gap) suggest that the formation of intermediates **16** (**15**→**16**) and **22** (**21**→**22**) are unfavorable. Natural Bond Orbital (NBO) method has been used to analyze the nature of bonding in hydride transfer steps. This NBO data shows that natural charges of the hydrogen atom in Mn-H for intermediate **15** and **21** are 0.00 and -0.01 whereas in the next immediate (**16** and **22**) after the transfer of the hydride from metal to carbon, natural charges increase to 0.08 and 0.08, respectively. The greater natural charges observed for hydrogen bonded to carbon as compared to metal implies that the transformation of hydrogen from Mn-H to the carbon atom is

unfavorable and hence requires high energy.

4.3.1.5. Microkinetic Modelling

The overall mechanism proposed for CO₂ hydrogenation to methanol involves some organic intermediates. This conversion follows one general catalytic pathway; at first CO₂ to N-formylmorpholine *via* formic acid followed by hydrogenation of N-formylmorpholine to methanol. In this context, PNP based Mn and Fe catalysts are considered for hydrogenation reaction. However, the activation process of H₂ in the hydrogenation process remains unclear. Whereas, the overall catalytic activity is enhanced due to the presence of morpholine co-catalyst [14,28]. Here, the total reaction free energy barrier is high. This suggests that the reaction may be favorable at high pressure and temperature. Nonetheless, the heterolytic hydrogen cleavage step involves maximum energy barriers for all the considered catalysts. Furthermore, we have studied microkinetic modelling to correlate the theoretical results with the experimental observations of chemical reactions under various conditions. We have used Complex Pathway Simulator (COPASI) software (version 4.22) for Microkinetic modeling with Livermore Solver for Ordinary Differential Equations (LSODA) algorithm [72,73]. However, the microkinetic modelling part has been simplified. Here, we have just considered the main important steps of the overall reaction. In case of dimerization reactions which are proceeding without barrier, the rate constants have been calculated by diffusion-controlled method [92]. Therefore, rate constant is given by $k=8k_B T/3\eta$, where k_B is the Boltzmann constant, T is the temperature, and η is the solvent's viscosity [93]. Diffusion controlled rate constant has been found out at 298.15 K whereas all the other rate constants have been found out at 383.15 K. Here all the factors have been considered as described in the experiment [28]. The initial concentration of morpholine has been considered 1.0 M, whereas Mn-PNP catalyst is 0.005 M and concentration of gaseous molecules have been varied to understand the gaseous

concentration effect towards product formation. The concentrations of the gaseous molecules (H_2 and CO_2) have been considered to remain fixed during the reaction. Furthermore, we have followed reaction time effect towards product formation. For first step, CO_2 hydrogenation to methanol followed by amide formation in the presence of amine simulations have been carried out up to 24 hours (86400 Sec) and for second step amide hydrogenation to methanol and amine simulations were carried out for a total time 36 hour (129600 Sec). The elementary steps of the reaction mechanisms which are considered in the microkinetic model are given in Table 4.5 with reaction free energy and rate constant. This model facilitates the interpretation of reaction conversion with respect to time and concentration of gaseous reactants (Figure 4.10). At first, H_2 and CO_2 react and form $HCOOH$ followed by amide formation. Interestingly, this model can easily explain the dependence of amide formation with the concentration of H_2 and CO_2 (Figure 4.10a). Our study discloses that conversion increase with increasing the gaseous concentration and it is maximum by considering the 1 M concentration of both H_2 and CO_2 . Therefore, considering 1 M concentration of H_2 and CO_2 effect of time on the product formation has been studied (Figure 4.10b) and it clearly shows that increasing time also increase the product formation, and product formation is maximum after 24 h (86400 sec) [28]. In the next part, we have considered amide hydrogenation part by C–N bond hydrogenation followed by C=O bond hydrogenation. In this case, also varied H_2 concentration product formation varied and shows high conversion at high concentration (Figure 4.10c). Interestingly, at 0.3 M of hydrogen concentration product formation certainly increase. This is due to the sudden decrease of the intermediate $HCHO$ concentration (Figure 4.11) which is one of the important intermediates in the reaction. Initially, amount of $HCHO$ increase which decrease the amount of product formation.

Table 4.5: Reaction mechanisms elementary step's gibbs free energy and

rate constant. $\Delta\Delta G^{\ddagger R}$ represents the total reaction free energy barriers for reaction. All free energies are in kcal/mol and rate constants are in $M^{-1}S^{-1}$.

Steps	Reaction free energy barrier ($\Delta\Delta G^{\ddagger R}$) in kcal/mol	Rate constant (At 383.15 K) (k) in $M^{-1}S^{-1}$
$1 + CO_2 = 3'$	7.0	8.11E+08
$3' = 1 + CO_2$	24.6	7.40E-02
$3' + H_2 = 1 + HCOOH$	25.9	1.34E-02
$1 + HCOOH = 3' + H_2$	2.7	2.30E+11
$6 + 2HCOOH = 9$	13.8	1.07E+05
$9 = 6 + 2HCOOH$	3.5	8.05E+10
$9 = 14 + HCOOH + H_2O$	8.3	1.47E+08
$14 + HCOOH + H_2O = 9$	29	2.29E-04
$1 + 14 \rightarrow 21$		1.65E+10
$21 = 22$	17.4	9.47E+02
$22 = 21$	2.0	5.77E+11
$22 = 18 + HCHO + 6$	11.3	2.86E+06
$18 + HCHO + 6 = 22$	21.6	3.81E+00
$18 + H_2 = 1$	24.0	1.63E-01
$1 = 18 + H_2$	25.1	3.84E-02
$1 + HCHO = 18 + CH_3OH$	2.9	1.77E+11
$18 + CH_3OH = 1 + HCHO$	14.7	3.29E+04
$18 + H_2 = 1$	24.0	1.63E-01
$1 = 18 + H_2$	25.1	3.84E-02

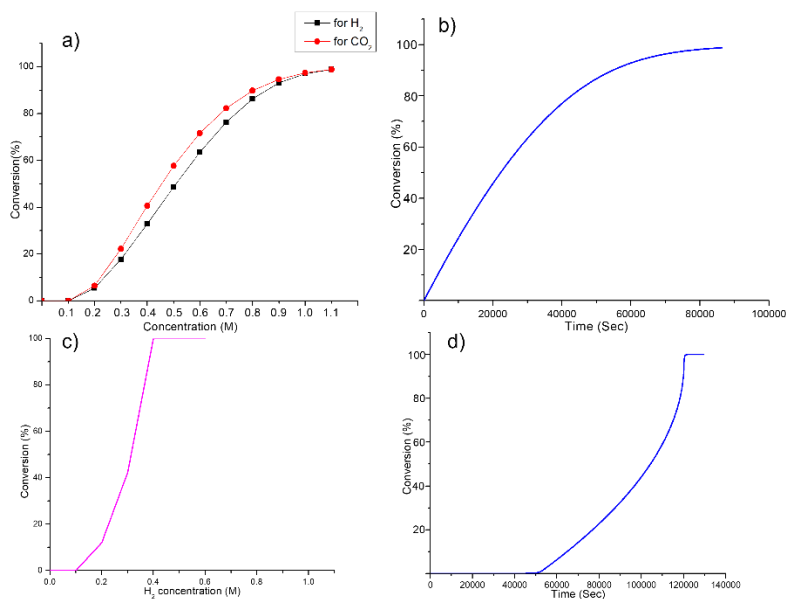


Figure 4.10: **(a)** Amine conversion over H₂ and CO₂ concentration for the amide formation. Simulations based-on Scheme 4.3 and 4.5. **(b)** Amine conversion over time for the amide formation. Simulations based-on Scheme 4.3 and 4.5. **(c)** Amide conversion to methanol over H₂ concentration. Simulations based-on Scheme 4.10. **(d)** Amide conversion to methanol over time. Simulations based-on Scheme 4.10. Here reaction time, initial conditions, pressure, and temperature were similar as used in the experiments.

Furthermore, increasing temperature of the reaction can easily overcome this problem and form product. However, our detail study of product formation relation with time shows that proportional with time (Figure 4.10d) up to the maximum conversion. Our results are exactly similar to the experimental results for Mn(I)-PNP catalyst [28]. Therefore, we can predict that the CO₂ hydrogenation reaction to methanol follows the above mechanism (amide formation followed by hydrogenation to methanol) in the presence of co-catalyst.

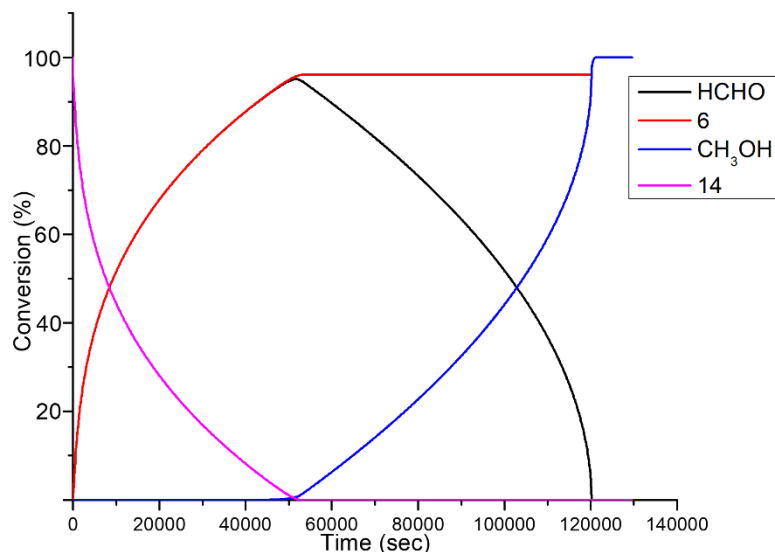


Figure 4.11: Amide conversion to methanol over time. Simulations on the based-on scheme S5. Change of concentration of reactant amide (14), intermediate (HCHO) and products CH₃OH and amine (6).

4.3.1.6. Conclusions

In conclusion, this computational study shows the underlying reaction mechanism of CO₂ hydrogenation to methanol by PNP based Mn(I), Fe(II) and Ru(II) metal complexes in the presence of morpholine co-catalyst. The DFT calculations show that the overall reaction follows three different steps: CO₂ hydrogenation to HCOOH, HCOOH to N-formylmorpholine, and N-formylmorpholine hydrogenation to methanol. In this sequential hydrogenation at first CO₂ is hydrogenated to HCOOH by the PNP based metal complexes. After that, amidation starts in the presence of morpholine co-catalyst and HCOOH is transformed to N-formylmorpholine. This step is highly exergonic (-10.4 kcal/mol), which increases the overall rate of the reaction. Lastly, N-formylmorpholine is hydrogenated to methanol in the presence of the PNP based metal complexes. This is found to be the most important step for CO₂ hydrogenation to methanol and can follow two competing routes based on the sequential hydrogenation of C=O and C–N groups that is C=O bond hydrogenation followed by C–N bond hydrogenation or C–N bond hydrogenation followed by C=O bond

hydrogenation. The total reaction free energies of N-formylmorpholine hydrogenation to methanol by Mn-PNP catalyst are 38.2 kcal/mol, and 38.4 kcal/mol for the former and the latter, respectively. The reaction free energy profile diagrams show that the catalytic activities of Mn-PNP and Fe-PNP catalysts are very much comparable to the noble metal-based Ru-PNP catalyst. Furthermore, we have correlated our results with experimental studies by microkinetic modelling. This model shows that for CO₂ to amide conversion increases by increasing the concentration of gaseous molecules and time. It is maximum at 24h where CO₂ and H₂ concentration is 1 M. Similarly, time and concentration of H₂ increase conversion for amide hydrogenation to methanol. In this case at ~0.3 M of H₂ concentration, conversion increases suddenly due to the decrease of HCHO concentration. Therefore, our detailed mechanistic study shows that earth-abundant metal-based catalysts may be promising for CO₂ hydrogenation reaction to methanol and our theoretical insights will be very much useful for experimentalists for the development of highly active earth abundant metal-based catalysts for CO₂ hydrogenation to methanol.

4.3.2. CO₂ Hydrogenation to Methanol via Capturing

In this section, we have discussed the CO₂ capture using amino alcohol to oxazolidinone followed by hydrogenation of the captured product oxazolidinone to methanol in the presence of Mn-PNP catalyst.

4.3.2.1. CO₂ Capture to Oxazolidinone

CCS is a very important strategy for the conversion of CO₂ into valuable products. Several reports have shown CO₂ capture using amino alcohols can proceed through hydrocarbonate and carbamate salts [37,38]. However, the final CO₂ captured product is oxazolidinone in the presence of amino alcohol. In this study, we have considered 2-amino-1-propanol as an amino alcohol for CO₂ capture in the presence of triethylamine (Et₃N) base. In this context, Vessally and co-workers have shown the mechanistic pathway for

CO₂ capturing to oxazolidinone [41]. Here, we have also considered mechanistic pathway of CO₂ capturing to oxazolidinone in the presence of 2-amino-1-propanol and base. Et₃N is a very commonly used base for catalyst-free CO₂ capturing reaction [28]. Figure 4.12 shows that the gaseous CO₂ molecule reacts with 2-amino-1-propanol (intermediate **1**) for the formation of intermediate **2** in the presence of Et₃N base (**1** + CO₂ + Et₃N → **2**).

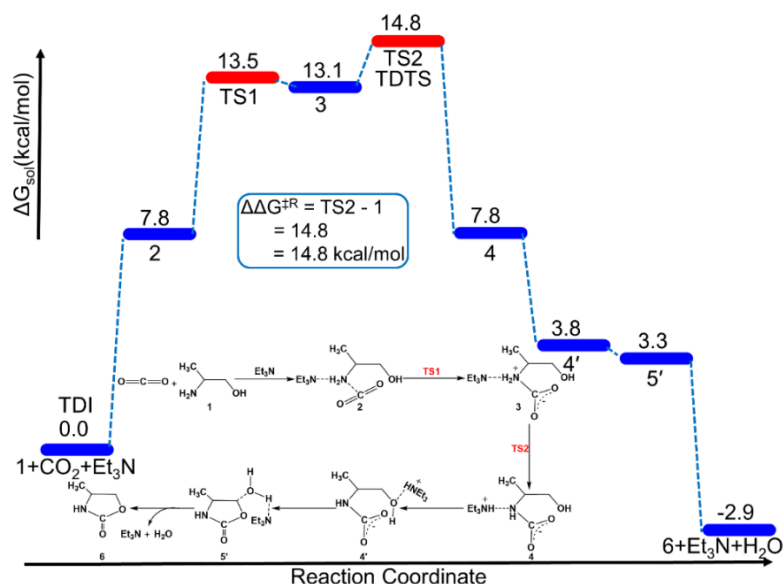


Figure 4.12: Possible reaction mechanism and corresponding reaction free energy profile diagram of CO₂ capturing to oxazolidinone using 2-amino-1-propanol amino alcohol in the presence of Et₃N base.

In the following step, intermediate **2** may proceed for the formation of **3** via transition state (TS1). More often than not, the addition of CO₂ is a very important step for such reaction. The calculated reaction free energy barrier for this step is 5.7 kcal/mol. Hence, the C–N bond formation, between CO₂ and 2-amino-1-propanol amino alcohol, requires a low reaction free energy barrier, which suggests that the CO₂ molecule may interact with the 2-amino-1-propanol amino alcohol in the presence of Et₃N base. Et₃N is a weak base having aliphatic tertiary amine which can abstract proton from

intermediate **3** and can form intermediate **4**. Hence, we have considered Et₃N can abstract a proton from the amine part of the amino alcohol for the formation of carbamate intermediate (**4**). This step can proceed via a transition state (TS2) with a reaction free energy barrier of 1.7 kcal/mol. The calculated reaction free energy shows that the step is 5.3 kcal/mol exergonic that is Et₃N can be used for the proton extraction in case of CO₂ capture to oxazolidinone. In the subsequent step, cyclisation may occur for the formation of intermediate **5** (Figure 4.13).

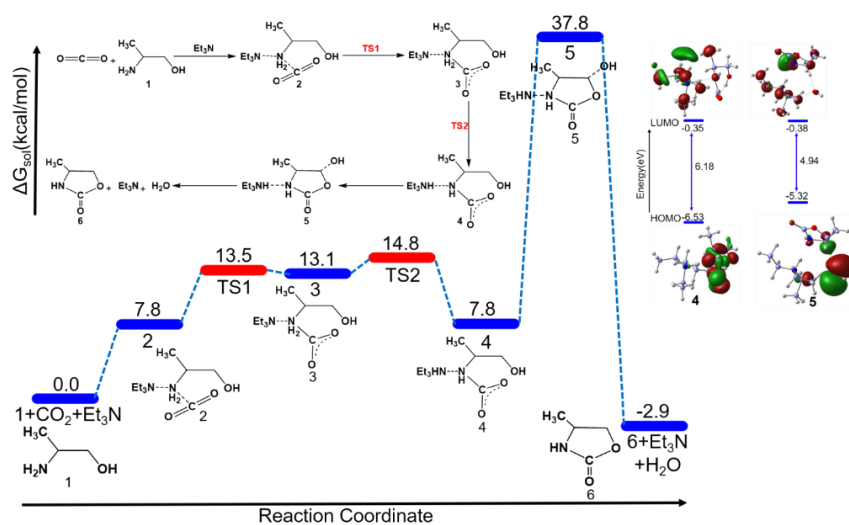


Figure 4.13: Possible reaction mechanism and corresponding reaction free energy profile diagram of CO₂ capturing to oxazolidinone using 2-amino-1-propanol amino alcohol in the presence of Et₃N base and frontier molecular orbitals of intermediates **4** and **5**.

However, the cyclisation step (**4**→**5**) is calculated to be highly endergonic (30.0 kcal/mol), which could be due to the structural rearrangement of intermediate **4** during the formation of intermediate **5**. Besides, Intermediate **4** can isomerise into **4'**, followed by cyclisation to **5'**. In case of **4**→**4'**, Et₃NH⁺ has been used for the stabilisation of OH⁻ functional of intermediate **4'**. This step is 4.0 kcal/mol exergonic. In the next step, **4'** cyclization to **5'** which is also 0.5 kcal/mol exergonic due to the presence of Et₃N base. In

the following step, intermediate **5/5'** favours the formation of oxazolidinone (4-methyl-2-oxazolidinone, **6**), which is calculated to be an exergonic reaction (40.7 kcal/mol from **5** and 6.2 kcal/mol from **5'**). Therefore, the calculated reaction free energy value shows that CO₂ can be captured for the formation of 4-methyl-2-oxazolidinone using 2-amino-1-propanol in the presence of Et₃N base. Hence, CO₂ capture to oxazolidinone reaction requires a free energy barrier of 14.8 kcal/mol, where TS2 is the turnover frequency (TOF)-determining transition state (TDTS) and **1** is the TOF-determining intermediate (TDI).

4.3.2.2. Oxazolidinone Hydrogenation to Methanol

In this section, we have considered the oxazolidinone hydrogenation reaction to methanol. Overall, the oxazolidinone hydrogenation reaction to methanol can happen via three consecutive hydrogenations steps. Therefore, we have considered all the possible pathways for first step of oxazolidinone hydrogenation which has also been divided into three parts. Figure 4.14a shows all the possible pathways for the first step of oxazolidinone hydrogenation to various products. The possibilities of C–N bond cleavage (Pathway I), C–O bond cleavage (Pathway II) and C=O bond hydrogenation (Pathway III) steps have been considered for oxazolidinone hydrogenation. The detailed reaction mechanisms for these steps in the presence of Mn-PNP catalyst have been shown in the Scheme 4.11-4.13 and their corresponding reaction free energy profile diagrams are shown in Figure 4.14b-4.14d. In the very first step of Pathway I (Figure 4.14b), Mn(I)-PNP catalyst can react with oxazolidinone towards the cleavage of C–N bond for the formation of intermediate **8**. Subsequently, hydride (Mn–H) transfer may occur for the formation of **9** via transition state (TS3). Consequently, the N–H proton can be transferred to the nucleophilic part of the oxazolidinone via TS4 for the formation of oxazolidinone hydrogenated product 2-aminopropyl formate (**11**). The calculated reaction free energy barrier for this step (**9**→**TS4**) is 5.7 kcal/mol.

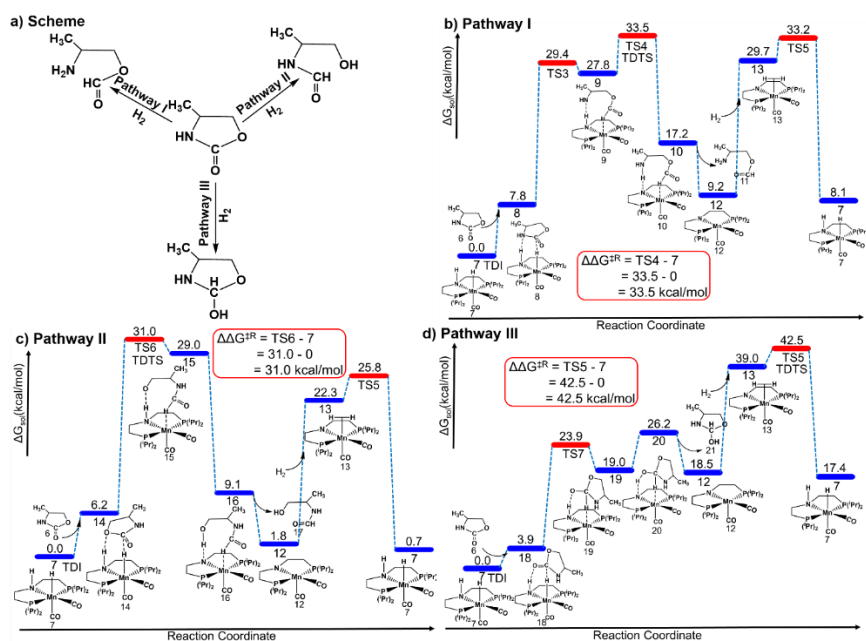
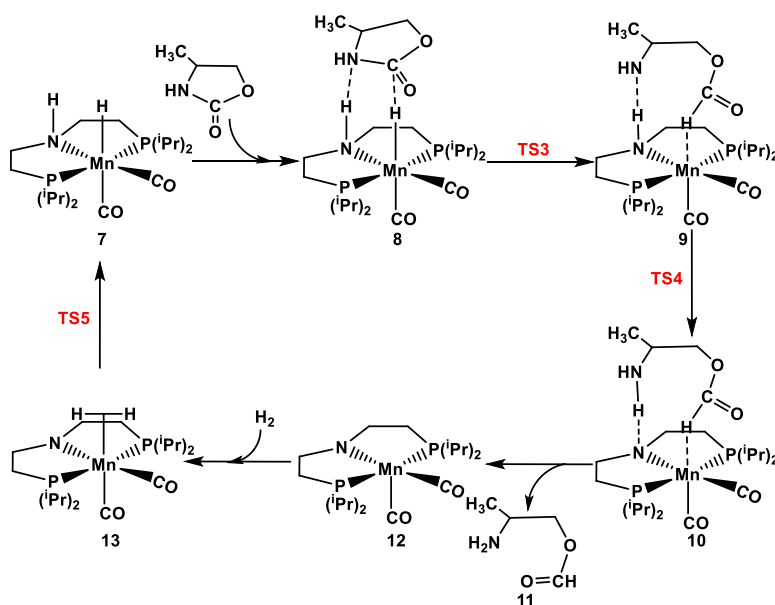
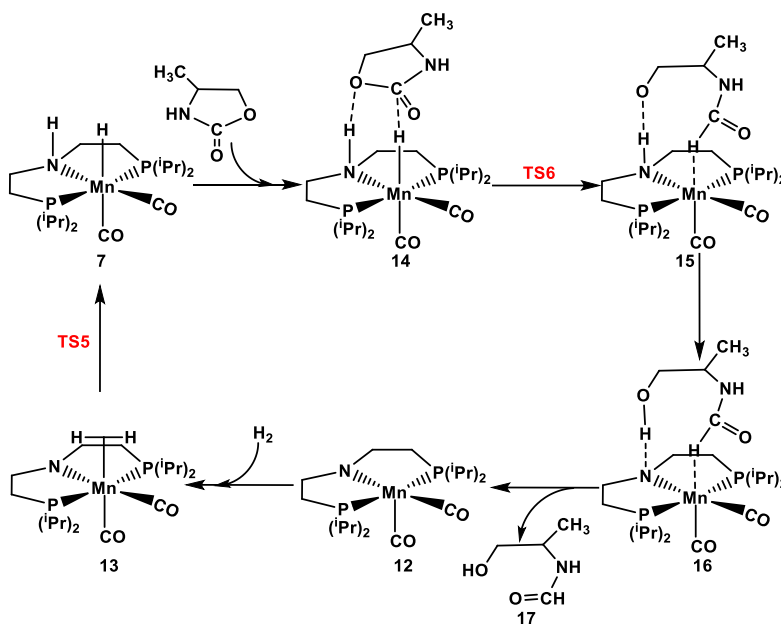


Figure 4.14: Reaction scheme (a) and corresponding reaction free energy profile diagrams of oxazolidinone hydrogenation to various products in the presence of Mn-PNP catalyst through various pathways: (b) Pathway I (via C–N bond cleavage), (c) Pathway II (via C–O bond cleavage), and (d) Pathway III (via C=O bond cleavage). Here $\Delta\Delta G^{\ddagger R}$ denotes the total reaction free energy barrier of the catalytic cycle.



Scheme 4.11: Proposed mechanistic pathway of Pathway I for C–N bond cleavage of oxazolidinone by Mn-PNP catalyst.

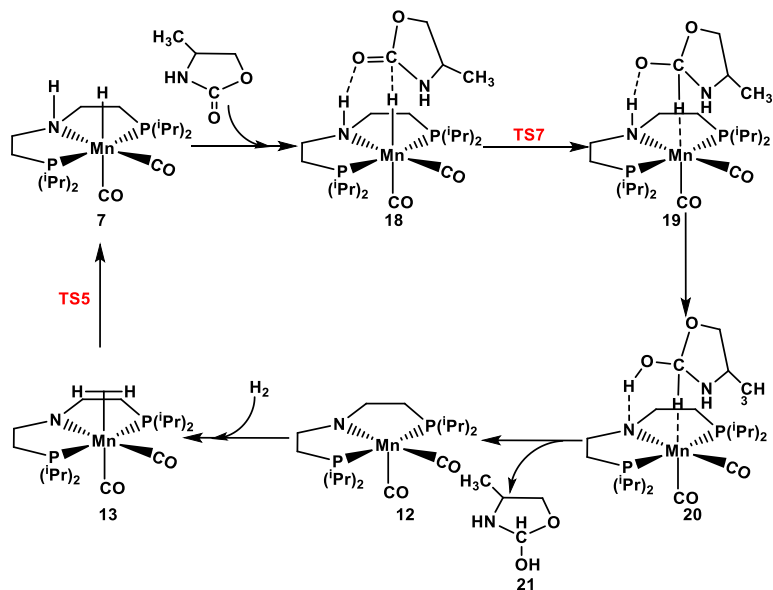
The subsequent step is common for all the pathways, where intermediate **12** binds with molecular H₂ for the formation of intermediate **13** (**1** + H₂ → **13**), which further undergoes heterolytic H₂ cleavage for the regeneration of the catalyst (**7**). In the case of Pathway I, TS4 is the TDTS and intermediate **7** with oxazolidinone is the TDI. Therefore, the calculated total reaction free energy barrier for Pathway I is 33.5 kcal/mol.



Scheme 4.12: Proposed mechanistic pathway of Pathway II for C–O bond cleavage of oxazolidinone by Mn-PNP catalyst.

Moreover, we have investigated the spin state of Mn(I) in Mn complexes of Pathway I, using singlet and triplet multiplicity for all the intermediates. Our calculated results shows that the singlet state of Mn(I) is more stable compared to triplet state of the intermediates (Table 4.6). Eisenstein and co-workers have also reported that singlet state of Mn-based catalysts is more stable than that of triplet state of the complexes [94]. This may be due to

the presence of two strong field ligand CO in the metal complexes of the intermediates which stabilize the low spin state of the Mn atom.



Scheme 4.13: Proposed mechanistic pathway of Pathway III for C=O bond hydrogenation of oxazolidinone by Mn-PNP catalyst.

Hence, it is expected that singlet state of Mn(I) in the complexes would be more favourable. In the case of Pathway II, we have proposed C–O bond cleavage followed by hydride transfer and protonation for the oxazolidinone hydrogenation. Figure 4.14c shows that the transition state for the hydride transfer (TS6) step is highest energy step in the reaction free energy profile. Hence, the hydride transfer transition state (TS6) is the TDTS for Pathway II. Thus, the calculated total reaction free energy barrier for Pathway II is 31.0 kcal/mol. Similarly, for the Pathway III, we have considered C=O bond hydrogenation by hydride and proton transfer reactions. Figure 4.14d shows that the transition state for heterolytic H₂ cleavage step is the highest energy step in the reaction energy profile. Hence, the transition state for heterolytic H₂ cleavage step (TS5) is the TDTS for Pathway III and the Pathway III requires a total reaction free energy barrier of 42.5 kcal/mol. The calculated reaction free energy barriers for the hydride transfer step show that the

hydride transfer is easier for the C=O bond hydrogenation compared to that for C–N and C–O bond hydrogenation reactions.

Table 4.6: The total energies (in Hartree) of the singlet and triplet states of Mn(I) based intermediates associated in Pathway I and the energy difference (kcal/mol) between the singlet and triplet states of the Mn(I) based intermediates.

Intermediates	Singlet	Triplet	Energy difference (kcal/mol)
7	-1700.378366	-1700.338063	25.3
8	-2062.186089	-2062.144316	26.2
9	-2062.154250	-2062.140130	8.9
10	-2062.171121	-2062.137400	21.2
12	-1699.196572	-1699.161504	22.0

To understand further, we have checked the NBO charge distribution in oxazolidinone (**6**) along with charge of the hydride of Mn-H. The NBO charges of hydride atom for intermediate **8**, **14** and **18** are -0.00, -0.01 and -0.02, respectively. Though, hydride is the same every time, the slight charge differs because of the non-covalently bound adducts formed prior to hydride transfer. Our calculated NBO results show that the charge on N, and O atom of C–N (Pathway I), C–O (Pathway II) and C=O (Pathway III) bonds are -0.69, -0.57 and -0.68, respectively in oxazolidinone (**6**) (Figure 4.15a). Hence, it is expected that hydride transfer step will require similar energy barrier in case of Pathway I and III whereas pathway II will require higher barrier. But the hydride transfer step of Pathway III requires lowest energy. This may be due to the presence of antibonding π^* orbital associated with C=O bond which is formed by the side-on overlap of C and O p-orbitals (Figure 4.15b). This π^* orbital acts as receptor of electrons from the hydride of Mn-H and facilitate the hydride transfer. On the other hand, C–

N bond cleavage is easier compared to the C–O bond cleavage as the charge on N is more negative compared to that of charge on O in oxazolidinone (6).

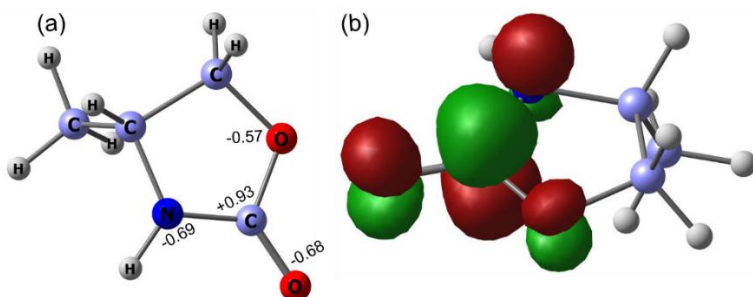


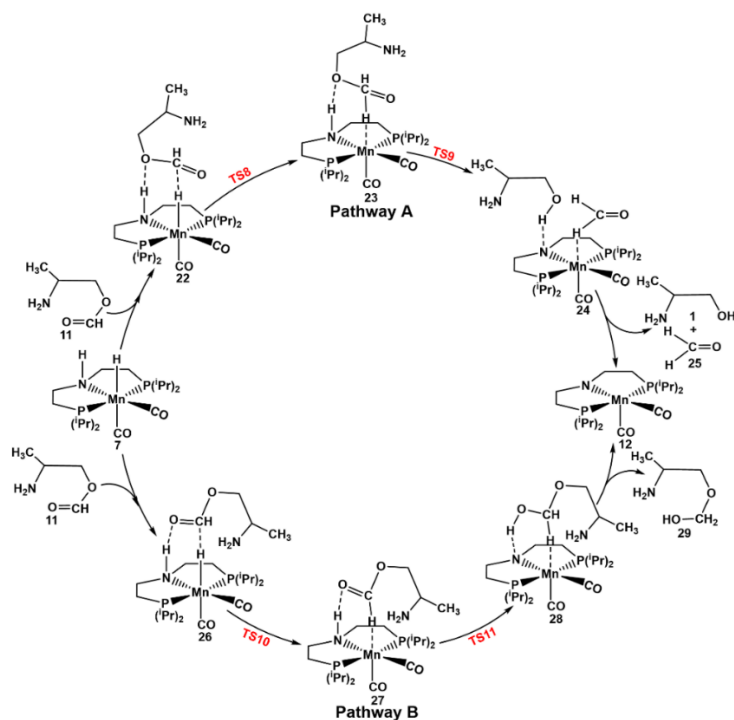
Figure 4.15: (a) Figure of oxazolidinone with NBO charge distribution on C, N, and O atom of C–N, C–O and C=O bonds, (b) electron density diagram of LUMO+4 of oxazolidinone.

In case of C–N and C–O bond hydrogenation of oxazolidinone (Pathway I and II) the reaction free energy barriers are 33.5 and 31.0 kcal/mol with 8.1 and 0.7 kcal/mol endergonic in nature, respectively. The equilibrium of the reaction can be moved to the product side and proceed the reaction in the forward direction by applying high temperature, high H₂ and CO₂ pressure in the reaction mixture. The detailed mechanistic pathways show that the hydride and proton transfer steps are very important steps for oxazolidinone hydrogenation, whereas heterolytic H₂ cleavage is the most important step for the regeneration of the catalyst. The calculated total reaction free energy barriers show that the Mn(I)-PNP complex requires very high barrier via Pathway III compared to that in the Pathway I and II. So, we have considered the subsequent hydrogenations of Pathway I and II hydrogenated products (**11** and **17**) only in the following sections. On the other hand, the partial hydrogenated oxazolidinone products are 2-aminopropyl formate (**11**) and (1-hydroxypropan-2-yl)formamide (**17**) for Pathway I and II, respectively. Moreover, Ding and co-workers have successfully isolated a lactol intermediate during hydrogenation of ethylene

carbonate which is equivalent to the 4-methyloxazolidin-2-ol (**21**) which can be obtained through partial oxazolidinone hydrogenation (via Pathway III) [19]. Besides, they have shown the reversibility of lactol to 2-hydroxyethylformate in the reaction mixture. Similarly, we have also considered (1-hydroxypropan-2-yl)formamide (**17**) as oxazolidinone hydrogenated product via Pathway II which is equivalent to the 2-hydroxyethylformate. Likewise, He and co-workers have reported 2-oxazolidinol and 2-aminoethylformic ether are the two important intermediates during oxazolidinone hydrogenation reaction [95]. In this perspective, 4-methyloxazolidin-2-ol (**21**) and 2-aminopropyl formate (**11**) are similar to 2-oxazolidinol and 2-aminoethylformic ether obtained from our investigation. Therefore, the considered mechanistic pathways are very much feasible via partial oxazolidinone hydrogenation reaction.

Furthermore, the first oxazolidinone hydrogenated products can be hydrogenated in the presence of Mn-PNP based catalyst. However, the second hydrogenation step can proceed via four different possibilities (Pathway A–D) as shown in Scheme 4.14 and 4.15. Here, we are interested to find out the most favourable pathways among all the possible pathways. In the case of Pathway A–B, we have shown that 2-aminopropyl formate (**11**) reacts with H₂ in the presence of Mn-PNP catalyst (**7**). As shown in Scheme 4.14, there are two bonds (C–O and C=O) which can be hydrogenated for the formation of methanol. In Pathway A, we have considered C–O bond cleavage followed by C=O bond hydrogenation whereas in the Pathway B, C=O bond hydrogenation followed by C–O bond cleavage. In Pathway A, 2-aminopropyl formate (**11**) interacts with the Mn-PNP catalyst and forms **22**. In the subsequent step, hydride transfer takes place for the formation of intermediate **23** via TS8. Our calculated reaction free energy barrier for hydride transfer is 14.3 kcal/mol (Figure 4.16). In the following step, proton transfer takes place for the formation of **24** via TS9. The calculated reaction free energy barrier for the proton transfer step is 6.4 kcal/mol. Afterwards, the hydrogenated product, formaldehyde (**25**), along

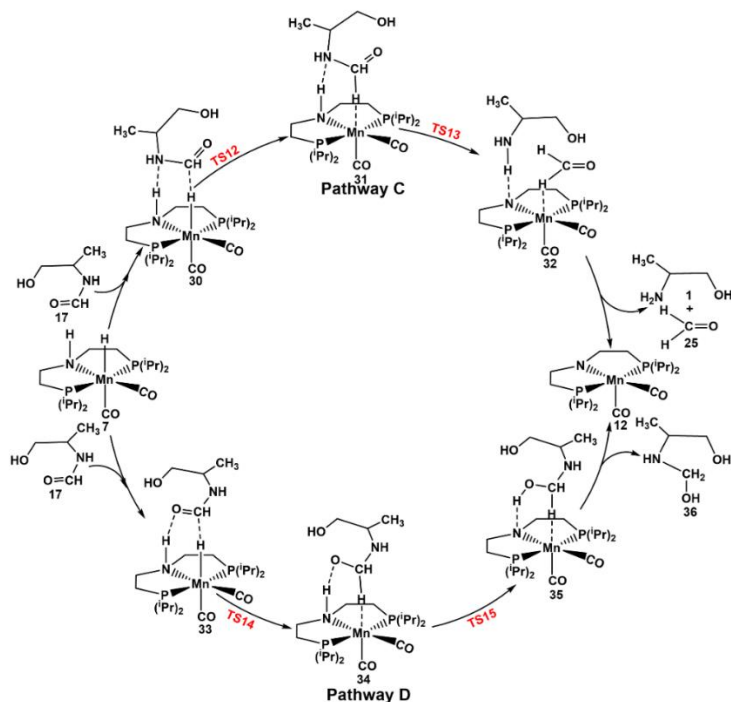
with the amino alcohol (**1**) can be released for the formation of intermediate **12**.



Scheme 4.14: The reaction mechanisms of C–O bond cleavage (Pathway A) and C=O bond hydrogenation (Pathway B) of 2-aminopropyl formate (**11**) to formaldehyde (**25**) and (2-aminopropoxy)methanol (**29**) in the presence of Mn-PNP catalyst.

Intermediate **12** can then react with H_2 for the heterolytic H_2 cleavage for the regeneration of the catalyst **7**. The calculated reaction free energy value shows that the transition state for heterolytic H_2 cleavage (TS5) is the TDTS for Pathway A with a total reaction free energy barrier of 28.8 kcal/mol. Likewise, Pathway B also proceeds through hydride transfer followed by proton transfer mechanisms for the formation of the hydrogenated product (2-aminopropoxy)methanol (**29**) and the calculated respective free energies are 9.8 kcal/mol (via TS10) and 4.6 kcal/mol (via TS11). In the case of Pathway B too, the heterolytic H_2 cleavage (TS5) step is the TDTS with a total reaction free energy barrier of 30.5 kcal/mol. Therefore, Pathway A is

favourable over Pathway B, which could be due to the release of the hydrogenated products favourable in Pathway A over that in Pathway B.



Scheme 4.15: The reaction mechanisms of C–N bond cleavage (Pathway C) and C=O bond hydrogenation (Pathway D) of (1-hydroxypropan-2-yl)formamide (**17**) to formaldehyde (**25**) and 2-((hydroxymethyl)amino)propan-1-ol (**36**) in the presence of Mn-PNP catalyst.

Interestingly, Ding and co-workers have also demonstrated that the CO₂ capture followed by hydrogenation steps proceed via formaldehyde intermediate [19]. So, our considered mechanistic pathways are very much likely pathways for oxazolidinone hydrogenation to methanol. Further to this, the product (1-hydroxypropan-2-yl)formamide (**17**) from pathway II can interact with the Mn-PNP catalyst for further hydrogenation (Scheme 4.15). Similarly, the C–N bond and C=O bond of **17** can be hydrogenated further. The calculated total reaction free energy barrier is 36.2 kcal/mol for Pathway C and 40.4 kcal/mol for pathway D (Figure 4.17).

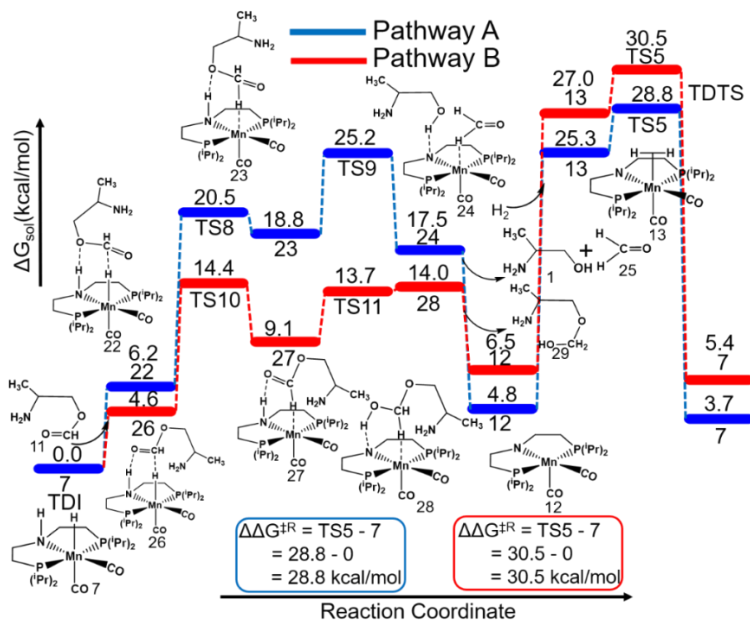


Figure 4.16: Reaction free energy profile diagram for C–O bond cleavage (Pathway A) and C=O bond hydrogenation (Pathway B) of 2-aminopropyl formate (**11**) to formaldehyde (**25**) and (2-aminopropoxy)methanol (**29**) using the Mn-PNP catalyst. Here, $\Delta\Delta G^{\ddagger R}$ denotes the total free energy barrier of the catalytic cycle.

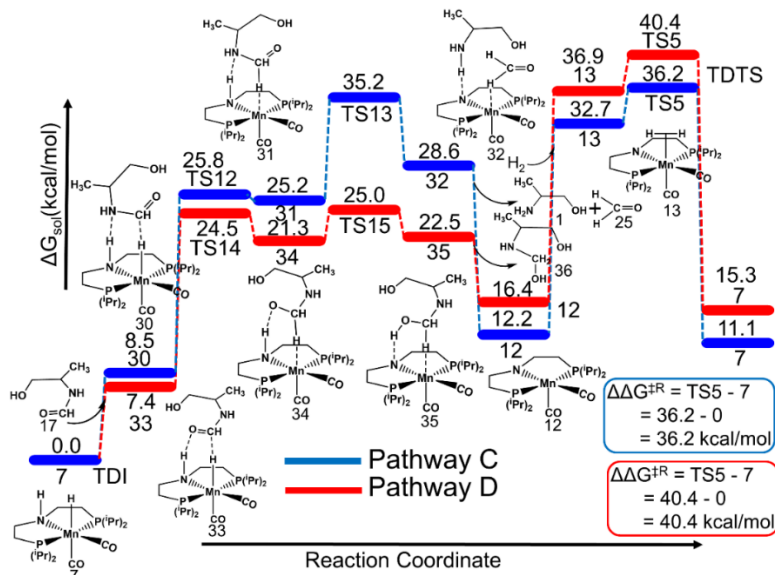
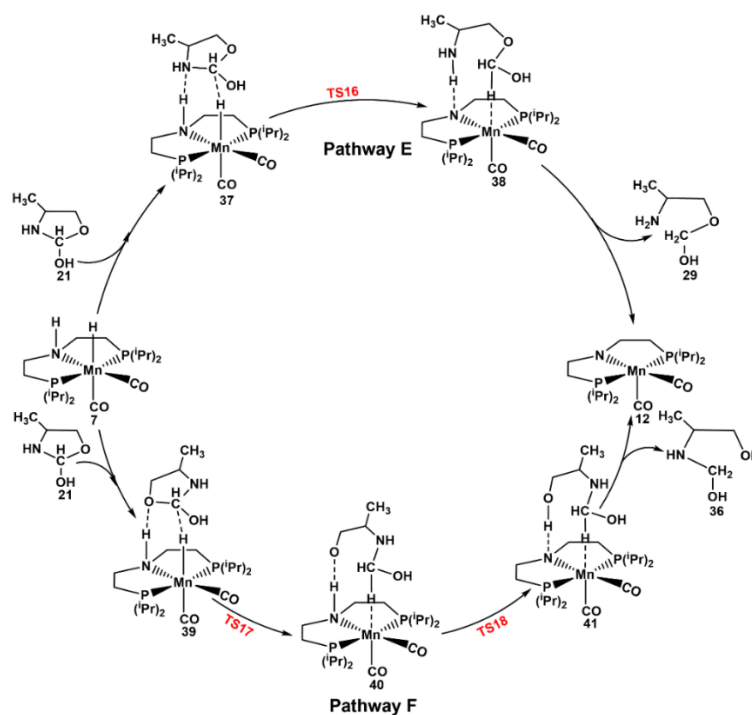


Figure 4.17: Reaction free energy profile diagram for C–N bond cleavage

(Pathway C) and C=O bond hydrogenation (Pathway D) of (1-hydroxypropan-2-yl)formamide (**17**) to formaldehyde (**25**) and 2-((hydroxymethyl)amino)propan-1-ol (**36**) using the Mn-PNP catalyst. Here, $\Delta\Delta G^{\ddagger R}$ denotes the total free energy barrier of the catalytic cycle.

Therefore, the C–N bond cleavage is 4.2 kcal/mol (pathway C) more favourable compared to the C=O bond hydrogenation step (pathway D). However, the scheme and reaction free energy profile diagram for subsequent hydrogenation of the product 4-methyloxazolidin-2-ol (**21**) obtained from Pathway III can be found in the Scheme 4.16 and Figure 4.18. Among the possible pathways (Pathway A–D), it is clear that the Pathway A is most favourable and Pathway D is least favourable.



Scheme 4.16: Reaction scheme for C–N bond cleavage (Pathway E) and C–O bond hydrogenation (Pathway F) of 4-methyloxazolidin-2-ol (**21**) to (2-aminoproxy)methanol (**29**) and 2-((hydroxymethyl)amino)propan-1-ol (**36**) in the presence of Mn-PNP catalyst.

Besides, three different hydrogenated products [formaldehyde (**25**), (2-aminopropoxy)methanol (**29**), and 2-((hydroxymethyl)amino)propan-1-ol (**36**)] can be formed even though the reactions can proceed through different possible hydrogenation pathways. As formaldehyde (**25**) and (2-aminopropoxy)methanol (**29**) formation require less reaction free energy barrier compared to 2-((hydroxymethyl)amino)propan-1-ol (**36**) formation, at first we have considered only hydrogenation of formaldehyde (**25**), and (2-aminopropoxy)methanol (**29**) for methanol formation. The detailed scheme and reaction free energy profile diagrams of formaldehyde (**25**) and (2-aminopropoxy)methanol (**29**) hydrogenations are shown in Figure 4.19 and Figure 4.20.

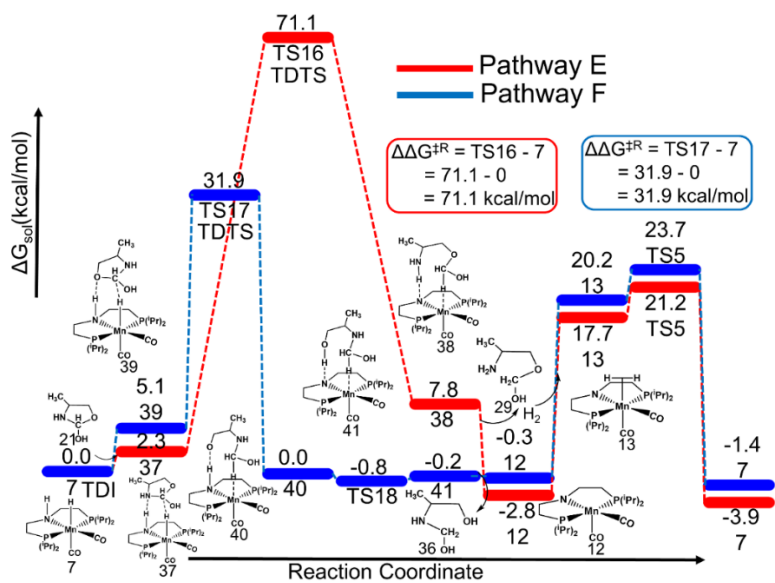


Figure 4.18: Reaction scheme and corresponding reaction free energy profile diagram for C–N bond cleavage (Pathway E) and C–O bond hydrogenation (Pathway F) of 4-methyloxazolidin-2-ol (**21**) to (2-aminopropoxy)methanol (**29**) and 2-((hydroxymethyl)amino)propan-1-ol (**36**) using the Mn-PNP catalyst. Here, $\Delta\Delta G^{\ddagger R}$ denotes the total free energy barrier of the catalytic cycle.

We have also shown the scheme and reaction free energy profile diagram

of 2-((hydroxymethyl)amino)propan-1-ol (**36**) hydrogenation to methanol in the supporting information (Figure 4.21). In case of formaldehyde (**25**) hydrogenation, formaldehyde can interact with the catalyst Mn-PNP for the hydride and proton transfer reactions as shown in Figure 4.19. In this pathway, transition state of heterolytic H₂ cleavage (TS5) is the TDTS whereas hydride and proton transfer steps are barrierless. Our calculated total reaction free energy barrier of formaldehyde hydrogenation to methanol is 24.0 kcal/mol, that is formaldehyde hydrogenation to methanol is highly favourable.

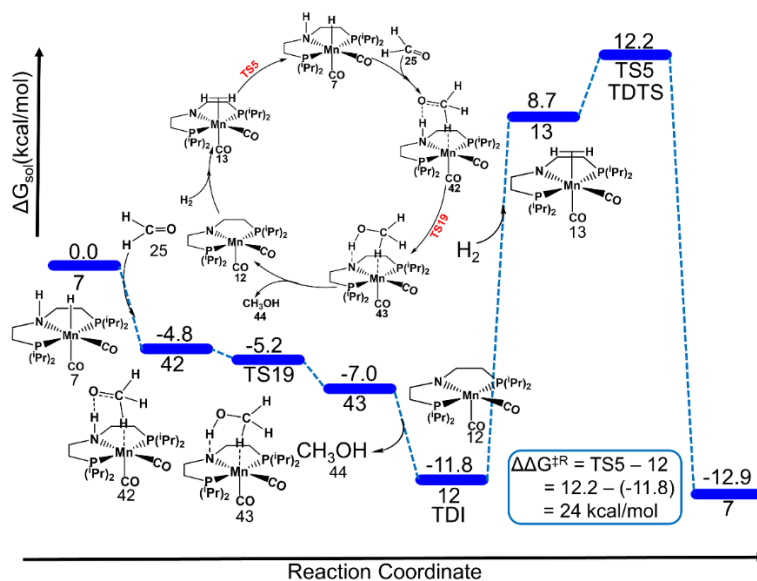


Figure 4.19: Reaction schemes and corresponding reaction free energy profile diagrams of formaldehyde (**25**) hydrogenation to methanol using the Mn-PNP catalyst. Here, $\Delta\Delta G^{\ddagger R}$ denotes the total free energy barrier of the catalytic cycle.

Several other groups have also reported that formaldehyde hydrogenation to methanol is favourable in the presence of pincer-based catalysts [95,96]. In this perspective, Prakash and co-workers have demonstrated that methanol can be produced very quickly from formaldehyde in the presence of PNP based catalysts [96]. Similarly, Zhou et al. have reported that the

formaldehyde hydrogenation to methanol is an exergonic and barrierless process [95]. Besides, we have considered the (2-aminopropoxy)methanol (**29**) hydrogenation reaction to methanol (Figure 4.20). In this case hydride and proton transfer step proceeds through TS20 with a reaction free energy barrier of 46.3 kcal/mol. In the subsequent steps, methanol (**44**) and 2-amino-1-propanol (**1**) can be separated with the formation of intermediate **12**. The transition state (TS20) of the hydride and proton transfer is the TDTS with a total reaction free energy barrier of 51.8 kcal/mol for methanol formation. Our calculated results demonstrate that the cleavage of formaldehyde (**25**) hydrogenation is more favourable compared to the (2-aminopropoxy)methanol (**29**) hydrogenation.

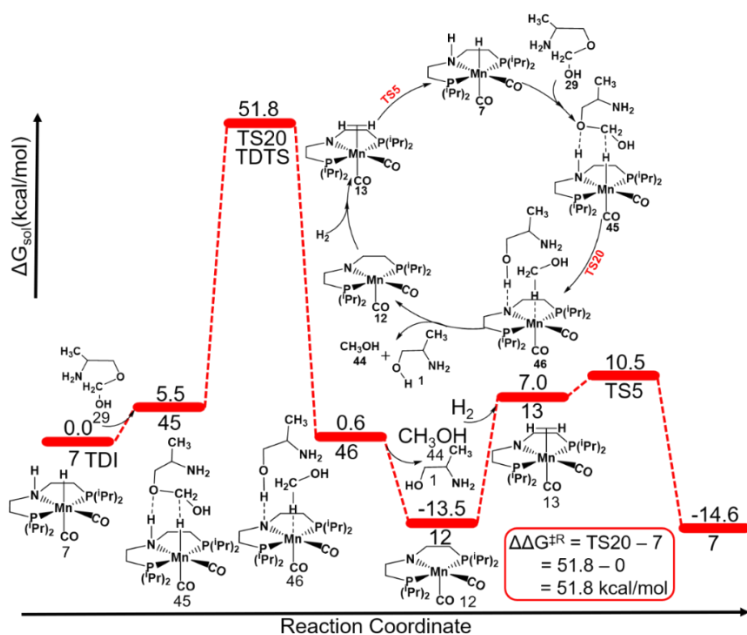


Figure 4.20: Reaction schemes and corresponding reaction free energy profile diagrams of (2-aminopropoxy)methanol (**29**) hydrogenation to methanol using the Mn-PNP catalyst. Here, $\Delta\Delta G^{\ddagger R}$ denotes the total free energy barrier of the catalytic cycle.

Therefore, our study indicates that CO_2 can be captured to oxazolidinone in the presence of Et_3N base and amino alcohol. Moreover, CO_2 captured

product (oxazolidinone) can undergo three subsequent hydrogenations for the formation of methanol in the presence of Mn-PNP based catalyst. Among all the possible mechanistic pathways, C–O bond hydrogenation followed by C–N and C=O bond hydrogenations and C–N bond hydrogenation followed by C–O and C=O bond hydrogenation using the Mn-PNP catalyst is the favourable pathways with a total reaction free energy barrier of 36.9 kcal/mol (Figure 4.22 and Figure 4.23).

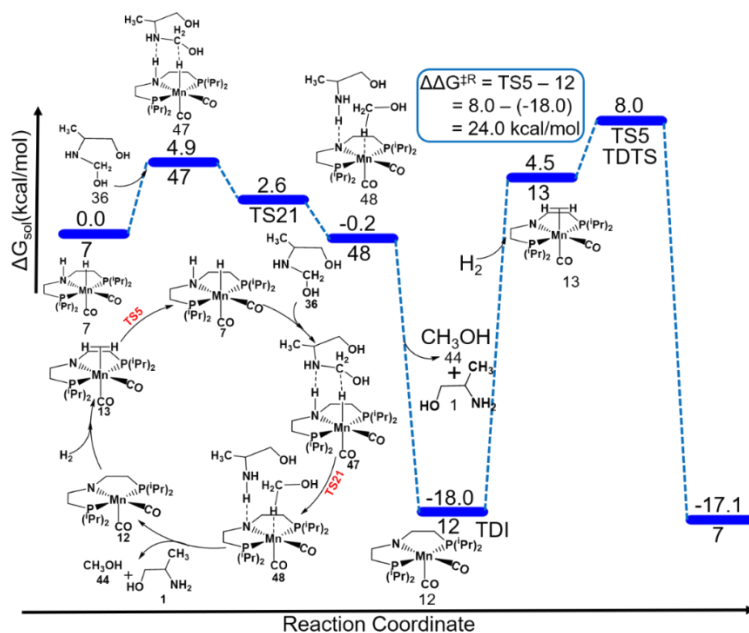


Figure 4.21: Reaction schemes and corresponding reaction free energy profile diagrams of 2-((hydroxymethyl)amino)propan-1-ol (36) hydrogenation to methanol using the Mn(I)-PNP catalyst. Here, $\Delta\Delta G^{\ddagger R}$ denotes the total free energy barrier of the catalytic cycle.

These overall reaction free energy barriers are comparable with cocatalyst based indirect (~38 kcal/mol) CO₂ hydrogenation to methanol using the Mn(I) based catalysts. Hence, Mn-PNP based catalyst can be promising for oxazolidinone hydrogenation to methanol. However, C=O bond hydrogenation followed by C–N/C–O and C–O/C–N, C–N bond hydrogenation followed by C=O and C–O bond hydrogenations, and C–O

bond hydrogenation followed C=O and C–N bond hydrogenations are very unlikely pathways for oxazolidinone hydrogenation to methanol (Figure 4.23–4.24). In all the possible pathways, heterolytic H₂ cleavage is calculated to be the rate determining step whereas hydride transfer is also a very important step for the hydrogenation initiation reaction.

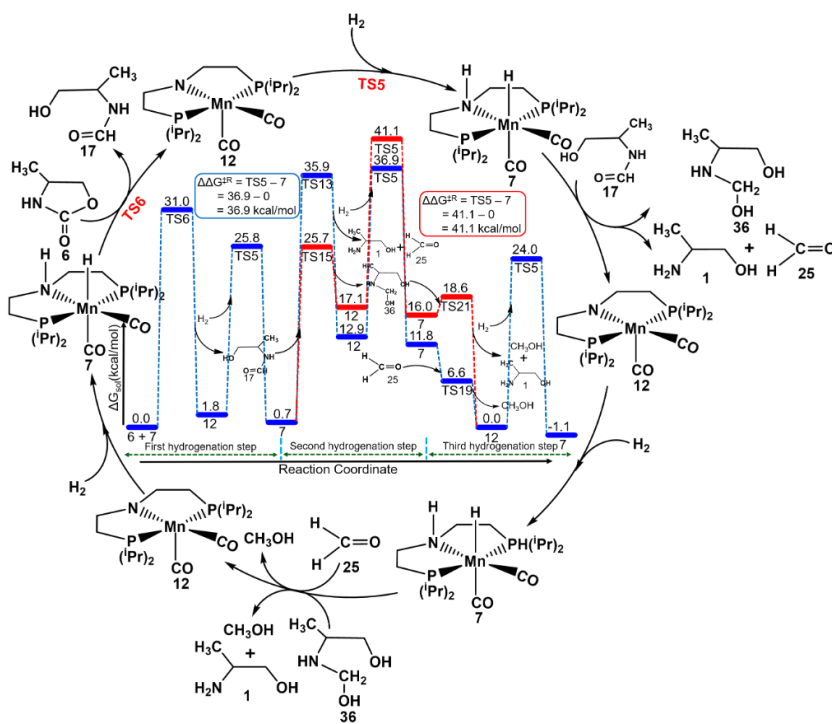


Figure 4.22: Overall reaction free energy profile diagram for oxazolidinone hydrogenation to methanol via C–O bond hydrogenation followed by C–N/C=O and C=O/C–N bond hydrogenation using the Mn-PNP catalyst. Here, $\Delta\Delta G^{\ddagger R}$ denotes the total free energy barrier of the catalytic cycle.

Moreover, to relate the overall reaction free energy barrier over ~36.0 kcal/mol for most plausible oxazolidinone hydrogenation reaction with experimental conditions, we have calculated the rate constant (*k*) value of the heterolytic hydrogen cleavage (RDS) over 273–600 K using the Kisthelp kinetic programme [74]. Our calculated rate constant values in the range of 273–600 K shows that rate increases exponentially above 400 K (Figure 4.25). Milstein and co-workers have also reported oxazolidinone

hydrogenation to methanol at 408.15 K and 60 bars of H₂ pressure using Ru-PNN based catalysts [40].

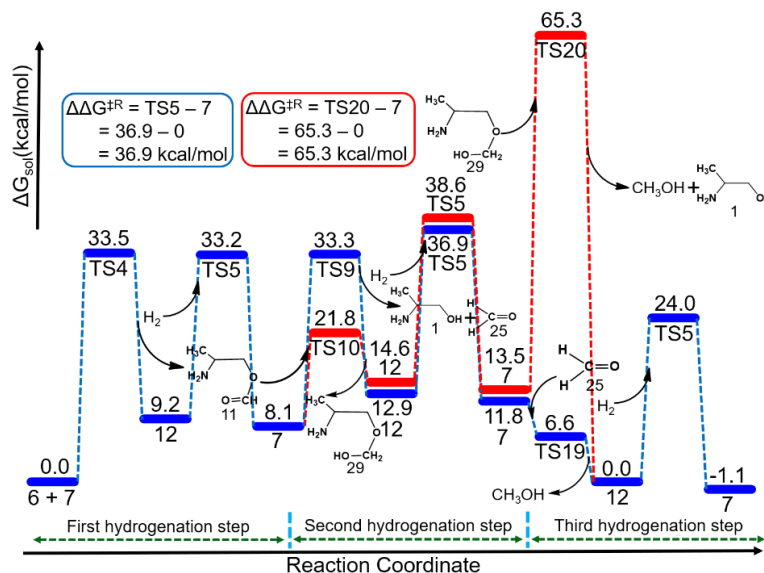


Figure 4.23: Overall reaction free energy profile diagram for oxazolidinone hydrogenation to methanol via C–N bond hydrogenation followed by C–O/C=O and C=O/C–O using Mn-PNP catalyst. Here, $\Delta\Delta G^{\ddagger R}$ denotes the total free energy barrier of the catalytic cycle.

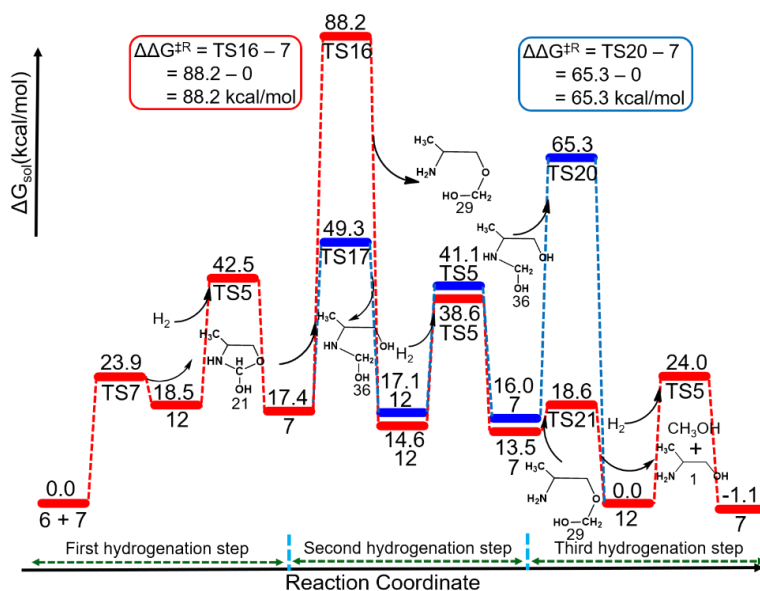


Figure 4.24: Overall reaction free energy profile diagram for oxazolidinone

hydrogenation to methanol via C=O bond hydrogenation followed by C–N/C–O and C–O/C–N using Mn(I)-PNP catalyst. Here, $\Delta\Delta G^{\ddagger R}$ denotes the total free energy barrier of the catalytic cycle.

Moreover, the similar barrier (35-38 kcal/mol) has been reported in cocatalyst based CO₂ hydrogenation to methanol. Therefore, in this study oxazolidinone can be hydrogenated to methanol experimentally above ~400 K using the Mn-PNP based catalysts.

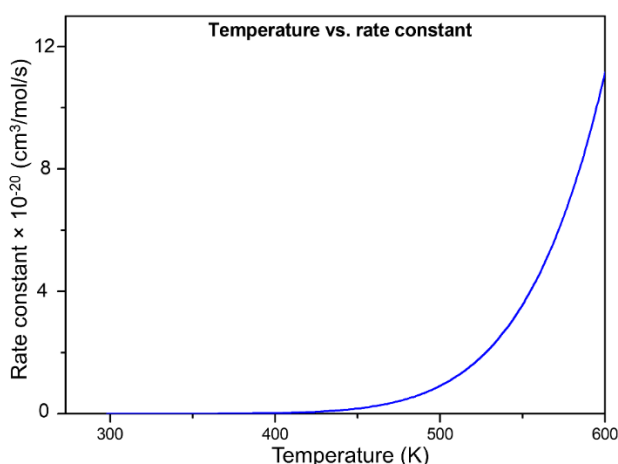


Figure 4.25: Plot of rate constant (k) of the heterolytic hydrogen cleavage (RDS) for oxazolidinone hydrogenation to methanol at 273–600 K.

4.3.2.3. Conclusions

In conclusion, the present DFT study guides us to investigate the underlying reaction mechanism of CO₂ to methanol. The overall CO₂ hydrogenation to methanol reaction involves two steps: (i) CO₂ capture to oxazolidinone and (ii) oxazolidinone hydrogenation to methanol. The CO₂ can be captured to oxazolidinone in the presence of 2-amino-1-propanol. In the next step, oxazolidinone catalysed plausible mechanistic pathways have been investigated in the presence of Mn-PNP based catalyst. During investigation of all the possible pathways of oxazolidinone hydrogenation, hydride and proton transfers steps are found to be the most important steps of the

reaction. Besides, heterolytic H₂ cleavage is found to be the most important step for the regeneration of the catalyst. The oxazolidinone hydrogenation total reaction free energy profile diagrams show that C–O bond cleavage followed by C–N/C=O and C=O/C–N bond hydrogenation are the most favourable pathways compared other which are comparable with our direct and cocatalyst based CO₂ hydrogenation to methanol. These mechanistic pathways reveal that methanol can be formed via CO₂ capture followed by hydrogenation of the captured product in the presence of Mn-PNP catalyst. Thus, we believe that our study can be very much helpful not only for the designing of new catalysts but also for the development of a bifunctional earth-abundant metal-based catalyst for oxazolidinone hydrogenation to methanol.

4.4. References

1. Annual Energy Review (2009), U.S. Energy Information Administration: Washington, DC, 2010; Tables 12.2-12.4, 349-353.
2. Figueroa J.D., Fout T., Plasynski S., McIlvried H., Srivastava R.D. (2008), Advances in CO₂ capture technology—The U.S. Department of Energy's Carbon Sequestration Program, *Int. J. Greenhouse Gas Control*, 2, 9-20 (DOI: 10.1016/S1750-5836(07)00094-1)
3. MacDowell N., Florin N., Buchard A., Hallett J., Galindo A., Jackson G., Adjiman C. S., Williams C. K., Shah N., Fennell P. (2010), An overview of CO₂ capture technologies, *Energy Environ. Sci.*, 3, 1645-1669 (DOI: 10.1039/C004106H)
4. Goeppert A., Czaun M., Prakash G. K. S., Olah G. A. (2012), Air as the renewable carbon source of the future: an overview of CO₂ capture from the atmosphere, *Energy Environ. Sci.*, 5, 7833-7853 (DOI: 10.1039/C2EE21586A)
5. Olah G.A., Goeppert A., Prakash G.K.S., (2005), Beyond Oil and Gas: The Methanol Economy, *Angew. Chem. Int. Ed.*, 44, 2636-2639 (DOI: 10.1002/anie.200462121)

6. Goeppert A., Czaun M., Jones J. P., Prakash G. K. S., Olah G. A. (2014), Recycling of carbon dioxide to methanol and derived products – closing the loop, *Chem. Soc. Rev.*, 43, 7995–8048 (DOI: 10.1039/C4CS00122B)
7. Olah G. A., Goeppert A., Prakash G. K. S. (2009), Chemical Recycling of Carbon Dioxide to Methanol and Dimethyl Ether: From Greenhouse Gas to Renewable, Environmentally Carbon Neutral Fuels and Synthetic Hydrocarbons, *J. Org. Chem.*, 74, 487–498 (DOI: 10.1021/jo801260f)
8. Centi G., Perathoner S. (2010), Towards solar fuels from water and CO₂, *ChemSusChem.*, 3, 195-208 (DOI: 10.1002/cssc.200900289)
9. Gesmanee S., Wanida K. (2017), Catalytic hydrogenation of CO₂ for methanol production in fixed-bed reactor using Cu-Zn supported on gamma-Al₂O₃, *Energy Procedia*, 138, 739–744 (DOI: 10.1016/j.egypro.2017.10.211)
10. Behrens M., Studt F., Kasatkin I., Kühl S., Hävecker M., Abildpedersen F., Zander S., Girgsdies F., Kurr P., Kniep B., Tovar M., Fischer R. W., Nørskov J. K., Schlögl R. (2012), The active site of methanol synthesis over Cu/ZnO/Al₂O₃ industrial catalysts, *Science*, 336, 893–898 (DOI: 10.1126/science.1219831)
11. Liu C., Yang B., Tjo E.C., Seifert S., DeBartolo J., Issendorff B.V., Zapol P., Vajda S., Curtiss L. A. (2015), Carbon Dioxide Conversion to Methanol over Size-Selected Cu₄ Clusters at Low Pressures, *J. Am. Chem. Soc.*, 137, 8676–8679 (DOI: 10.1021/jacs.5b03668)
12. Graciani J., Mudiyansele K., Xu F., Baber A.E., Evans J., Senanayake S. D., Stacchiola D.J., Liu P., Hrbek J., Sanz J.F., Rodriguez J.A. (2014), Catalysis. Highly active copper-ceria and copper-ceria-titania catalysts for methanol synthesis from CO₂, *Science*, 345, 546–550 (DOI: 10.1126/science.1253057)

13. Li Y.N., Ma R., He L.N., Diao Z.F., (2014), Homogeneous hydrogenation of carbon dioxide to methanol, *Catal. Sci. Technol.*, 4, 1498-1512 (DOI: 10.1039/C3CY00564J)
14. Wesselbaum S., VomStein T., Klankermayer J., Leitner W. (2012), Hydrogenation of Carbon Dioxide to Methanol by Using a Homogeneous Ruthenium–Phosphine Catalyst, *Angew. Chem. Int. Ed.*, 51, 7499–7502 (DOI: 10.1002/anie.201202320)
15. Huff C.A., Sanford M.S. (2011), Cascade Catalysis for the Homogeneous Hydrogenation of CO₂ to Methanol, *J. Am. Chem. Soc.*, 133, 18122–18125 (DOI: 10.1021/ja208760j)
16. Wesselbaum S., Moha V., Meuresch M., Brosinski S., Thenert K. M., Kothe J., Stein T., Englert U., Hölscher M., Klankermayer J., Leitner W. (2015), Hydrogenation of carbon dioxide to methanol using a homogeneous ruthenium–Triphos catalyst: from mechanistic investigations to multiphase catalysis, *Chem. Sci.*, 6, 693–704 (DOI: 10.1039/C4SC02087A)
17. Tominaga K., Sasaki Y., Watanabe T., Saito M. (1995), Homogeneous Hydrogenation of Carbon Dioxide to Methanol Catalyzed by Ruthenium Cluster Anions in the Presence of Halide Anions, *Bull. Chem. Soc. Jpn.*, 68, 2837–2842 (DOI: 10.1246/bcsj.68.2837)
18. Balaraman E., Gunanathan C., Zhang J., L. Shimon J.W., Milstein D. (2011), Efficient hydrogenation of organic carbonates, carbamates and formates indicates alternative routes to methanol based on CO₂ and CO, *Nat. Chem.*, 3, 609–614 (DOI: 10.1038/nchem.1089)
19. Han Z., Rong L., Wu J., Zhang L., Wang Z., Ding K. (2012), Catalytic Hydrogenation of Cyclic Carbonates: A Practical Approach from CO₂ and Epoxides to Methanol and Diols, *Angew. Chem. Int. Ed.*, 51, 13041–13045 (DOI: 10.1002/anie.201207781)
20. Schneidewind J., Adam R., Baumann W., Jackstell R., Beller M. (2017), Low-Temperature Hydrogenation of Carbon Dioxide to

- Methanol with a Homogeneous Cobalt Catalyst, *Angew. Chem. Int. Ed.*, 56, 1890–1893 (DOI: 10.1002/anie.201609077)
21. Alberico E., Nielsen M. (2015), Towards a methanol economy based on homogeneous catalysis: methanol to H₂ and CO₂ to methanol, *Chem. Commun.*, 51, 6714–6725 (DOI: 10.1039/C4CC09471A)
 22. Sordakis K., Tsurusaki A., Iguchi M., Kawanami H., Himeda Y., Laurenczy G. (2016), Carbon Dioxide to Methanol: The Aqueous Catalytic Way at Room Temperature, *Chem. - Eur. J.*, 22, 15605–15608 (DOI: 10.1002/chem.201603407)
 23. Miller A.J.M., Heinekey D.M., Mayer J.M., Goldberg K.I. (2013), Catalytic Disproportionation of Formic Acid to Generate Methanol, *Angew. Chem. Int. Ed.*, 52, 3981–3984 (DOI: 10.1002/anie.201208470)
 24. Rezayee N.M., Huff C.A., Sanford M.S. (2015), Tandem Amine and Ruthenium-Catalyzed Hydrogenation of CO₂ to Methanol *J. Am. Chem. Soc.*, 137, 1028–1031 (DOI: 10.1021/ja511329m)
 25. Zhang L., Han Z., Zhao X., Wang Z., Ding K. (2015), Highly Efficient Ruthenium-Catalyzed N-Formylation of Amines with H₂ and CO₂, *Angew. Chem. Int. Ed.*, 54, 6186–6189 (DOI: 10.1002/anie.201500939)
 26. Kar S., Sen R., Goepfert A., Prakash G.K.S. (2018), Integrative CO₂ Capture and Hydrogenation to Methanol with Reusable Catalyst and Amine: Toward a Carbon Neutral Methanol Economy, *J. Am. Chem. Soc.*, 140, 1580–1583 (DOI: 10.1021/jacs.7b12183)
 27. Kothandaraman J., Goepfert A., Czaun M., Olah G.A., Prakash G.K.S. (2016), Conversion of CO₂ from Air into Methanol Using a Polyamine and a Homogeneous Ruthenium Catalyst, *J. Am. Chem. Soc.*, 138, 778–781 (DOI: 10.1021/jacs.5b12354)
 28. Kar S., Goepfert A., Kothandaraman J., Prakash G.K.S. (2017), Manganese-Catalyzed Sequential Hydrogenation of CO₂ to Methanol

- via Formamide, *ACS Catal.*, **7**, 6347–6351 (DOI: 10.1021/acscatal.7b02066)
29. Kar S., Kothandaraman J., Goeppert A., Prakash G.K.S. (2018), Advances in catalytic homogeneous hydrogenation of carbon dioxide to methanol, *Journal of CO₂ Utilization*, **23**, 212–218 (DOI: 10.1016/j.jcou.2017.10.023)
 30. Olah G.A., Goeppert A., Prakash G.K.S. (2009), Chemical Recycling of Carbon Dioxide to Methanol and Dimethyl Ether: From Greenhouse Gas to Renewable, Environmentally Carbon Neutral Fuels and Synthetic Hydrocarbons, *J. Org. Chem.*, **74**, 487–498, (DOI: 10.1021/jo801260f)
 31. Goeppert A., Prakash G.K.S., Olah G.A., Czaun M., Jones J.-P. (2014), Recycling of carbon dioxide to methanol and derived products – closing the loop, *Chem. Soc. Rev.*, **43**, 7995–8048 (DOI: 10.1039/C4CS00122B)
 32. Centi G., Perathoner S. (2010), Towards Solar Fuels from Water and CO₂, *ChemSusChem*, **3**, 195–208 (DOI: 10.1002/cssc.200900289)
 33. Balaraman E., Gunanathan C., Zhang J., Shimon L.J.W., Milstein D. (2011), Efficient hydrogenation of organic carbonates, carbamates and formates indicates alternative routes to methanol based on CO₂ and CO, *Nat. Chem.*, **3**, 609–614 (DOI: 10.1038/nchem.1089)
 34. Blondiaux E., Pouessel J., Cantat T. (2014), Carbon Dioxide Reduction to Methylamines under Metal-Free Conditions, *Angew. Chem. Int. Ed.*, **53**, 12186–12190 (DOI: 10.1002/anie.201407357)
 35. Tlili A., Blondiaux E., Frogneux X., Cantat T. (2015), Reductive functionalization of CO₂ with amines: an entry to formamide, formamidine and methylamine derivatives, *Green Chem.*, **17**, 157–168 (DOI: doi.org/10.1039/C4GC01614A)
 36. Jin G., Werncke C.G., Escudie Y., Sabo-Etienne S., Bontemps S. (2015), Iron-Catalyzed Reduction of CO₂ into Methylene: Formation

- of C–N, C–O, and C–C Bonds, *J. Am. Chem. Soc.*, 137, 9563–9566 (DOI: 10.1021/jacs.5b06077)
37. Vaidya P.D., Kenig E.Y. (2007), CO₂-Alkanolamine Reaction Kinetics: A Review of Recent Studies *Chem. Eng. Technol.*, 30, 1467–1474 (DOI: 10.1002/ceat.200700268)
 38. Conway W., Wang X., Fernandes D., Burns R. Lawrance, G., Puxty G., Maeder M. (2011), Comprehensive Kinetic and Thermodynamic Study of the Reactions of CO₂(aq) and HCO₃[−] with Monoethanolamine (MEA) in Aqueous Solution, *J. Phys. Chem. A*, 115, 14340–14349 (DOI: 10.1021/jp2081462)
 39. Shao R., Stangeland A. (2009), Amines Used in CO₂ Capture-Health and Environmental Impacts
 40. Khusnutdinova J.R., Garg J.A., Milstein D. (2015), Combining Low-Pressure CO₂ Capture and Hydrogenation To Form Methanol, *ACS Catal.*, 5, 2416–2422 (DOI: 10.1021/acscatal.5b00194)
 41. Arshadi S., Banaei A., Ebrahimiasl S., Monfared A., Vessally E. (2019), Solvent-free incorporation of CO₂ into 2-oxazolidinones: a review, *RSC Adv.*, 9, 19465–19482 (DOI: 10.1039/C9RA00551J)
 42. Brunel P., Monot J., Kefalidis C.E., Maron L., Martin-Vaca B., Bourissou D. (2017), Valorization of CO₂: Preparation of 2-Oxazolidinones by Metal–Ligand Cooperative Catalysis with SCS Indenediide Pd Complexes, *ACS Catal.*, 7, 2652–2660 (DOI: 10.1021/acscatal.7b00209)
 43. Juárez R., Concepción P., Corma A., García H. (2010), Ceria nanoparticles as heterogeneous catalyst for CO₂ fixation by ω-aminoalcohols, *Chem. Commun.*, 46, 4181–4183 (DOI: 10.1039/C001955K)
 44. Lin P.H., Wong D.S.H. (2014), Carbon dioxide capture and regeneration with amine/alcohol/water blends, *Int. J. Greenh. Gas Control*, 26, 69–75 (DOI: 10.1016/j.ijggc.2014.04.020)

45. Sheng Z.Z., Huang M.M., Xue T., Xia F., Wu H.H. (2020), Alcohol amine-catalyzed CO₂ conversion for the synthesis of quinazoline-2,4-(1H,3H)-dione in water, *RSC Adv.*, 10, 34910–34915 (DOI: 10.1039/D0RA06439D)
46. Foo S.W., Takada Y., Yamazaki Y., Saito S. (2013), Dehydrative synthesis of chiral oxazolidinones catalyzed by alkali metal carbonates under low pressure of CO₂, *Tetrahedron Lett.*, 54, 4717–4720.
47. Maneeintr K., Idem R.O., Tontiwachwuthikul P., Wee A.G.H. (2008), Synthesis, solubilities, and cyclic capacities of amino alcohols for CO₂ capture from flue gas streams, *Energy Procedia*, 1, 1327–1334 (DOI: 10.1016/j.egypro.2009.01.174)
48. Han Z., Rong L., Wu J., Zhang L., Wang Z., Ding K. (2012), Catalytic Hydrogenation of Cyclic Carbonates: A Practical Approach from CO₂ and Epoxides to Methanol and Diols, *Angew. Chem. Int. Ed.*, 51, 13041–13045 (DOI: 10.1002/anie.201207781)
49. Cabrero-Antonino J.R., Adam R., Papa V., Beller M. (2020), Homogeneous and heterogeneous catalytic reduction of amides and related compounds using molecular hydrogen, *Nat. Commun.*, 11, 3893 (DOI: 10.1038/s41467-020-17588-5)
50. Mandal S.C., Rawat K.S., Pathak B. (2019), A computational study on ligand assisted vs. ligand participation mechanisms for CO₂ hydrogenation: importance of bifunctional ligand based catalysts, *Phys. Chem. Chem. Phys.*, 21, 3932–3941 (DOI: 10.1039/C8CP06714G)
51. Elangovan S., Topf C., Fischer S., Jiao H., Spannenberg A., Baumann W., Ludwig R., Junge K., Beller M. (2016), Selective Catalytic Hydrogenations of Nitriles, Ketones, and Aldehydes by Well-Defined Manganese Pincer Complexes, *J. Am. Chem. Soc.*, 138, 8809–8814 (DOI: 10.1021/jacs.6b03709)

52. Frisch M.J. et al. (2013), Gaussian Revision D.01, Gaussian, Inc., Wallingford CT
53. Hehre W.J., Ditchfield R., Pople J.A. (1972), Self—Consistent Molecular Orbital Methods. XII. Further Extensions of Gaussian—Type Basis Sets for Use in Molecular Orbital Studies of Organic Molecules, *J. Chem. Phys.*, 56, 2257-2261 (DOI: 10.1063/1.1677527)
54. Hariharan P.C., Pople J.A. (1973), The influence of polarization functions on molecular orbital hydrogenation energies, *Theor. Chim Acta*, 28, 213-222 (DOI: 10.1007/BF00533485)
55. Krishnan R., Binkley J.S., Seeger R., Pople J.A. (1980), Self-consistent molecular orbital methods. XX. A basis set for correlated wave functions, *J. Chem. Phys.*, 72, 650–654 (DOI: 10.1063/1.438955)
56. Hay P.J., Wadt W.R. (1985), Ab initio effective core potentials for molecular calculations. Potentials for the transition metal atoms Sc to Hg, *J. Chem. Phys.*, 82, 270-283 (DOI: 10.1063/1.448799)
57. Hay P.J., Wadt W.R. (1985), Ab initio effective core potentials for molecular calculations. Potentials for K to Au including the outermost core orbitals, *J. Chem. Phys.*, 82, 299-310 (DOI: 10.1063/1.448975)
58. Becke A.D. (1988), Density-functional exchange-energy approximation with correct asymptotic behavior, *Phys. Rev. A*, 38, 3098–3100 (DOI: 10.1103/PhysRevA.38.3098)
59. Becke A.D. (1993), A new mixing of Hartree–Fock and local density-functional theories, *J. chem. Phys.*, 98, 1372–1377 (DOI: 10.1063/1.464304)
60. Becke A.D. (1997), Density-functional thermochemistry. V. Systematic optimization of exchange-correlation functionals *J. Chem. Phys.*, 107, 8554–8560 (DOI: 10.1063/1.475007)
61. Becke A.D. (1993), Density-functional thermochemistry. III. The role of exact exchange, *J. Chem. Phys.*, 98, 5648–5652 (DOI: 10.1063/1.464913)

62. Lee C., Yang W., Parr G. (1988), Development of the Colle-Salvetti correlation-energy formula into a functional of the electron density, *Phys.Rev. B*, 37, 785–789 (DOI: 10.1103/PhysRevB.37.785)
63. Rawat K.S., Mahata A., Choudhuri I., Pathak B. (2016), N-Heterocyclic Carbene-Based Mn Electrocatalyst for Two-Electron CO₂ Reduction over Proton Reduction, *J. Phys. Chem. C*, 120, 8821–8831 (DOI: 10.1021/acs.jpcc.6b02209)
64. Rawat K.S., Pathak B. (2018), Flexible proton-responsive ligand-based Mn(i) complexes for CO₂ hydrogenation: a DFT study, *Phys. Chem. Chem. Phys.*, 20, 12535–12542 (DOI: 10.1039/C7CP08637G)
65. Rawat K.S., Mahata A., Choudhuri I., Pathak B. (2016), Catalytic Hydrogenation of CO₂ by Manganese Complexes: Role of π -Acceptor Ligands, *J. Phys. Chem. C*, 120, 16478 –16488 (DOI: 10.1021/acs.jpcc.6b05065)
66. Cossi M., Rega N., Scalmani G., Barone V. (2003), Energies, structures, and electronic properties of molecules in solution with the C-PCM solvation model, *J. Comput. Chem.*, 24, 669 –681 (DOI: 10.1002/jcc.10189)
67. Barone V., Cossi M. (1998), Quantum Calculation of Molecular Energies and Energy Gradients in Solution by a Conductor Solvent Model, *J. Phys. Chem. A*, 102,1995–2001 (DOI: 10.1021/jp9716997)
68. Marenich A.V., Cramer C.J., Truhlar D.G. (2009), Universal Solvation Model Based on Solute Electron Density and on a Continuum Model of the Solvent Defined by the Bulk Dielectric Constant and Atomic Surface Tensions, *J. Phys. Chem. B*, 113, 6378–6396 (DOI: 10.1021/jp810292n)
69. Grimme S., Antony J., Ehrlich S., Krieg H. (2010), A consistent and accurate ab initio parametrization of density functional dispersion correction (DFT-D) for the 94 elements H-Pu, *J. Chem. Phys.*, 132, 154104-154123 (DOI: 10.1063/1.3382344)

70. Glendening E.D., Reed A.E., Carpenter J.E., Weinhold, F. NBO, Version 3.1.
71. Laidler K.J. (1987), *Chemical Kinetics*, 3rd ed., Harper & Row, New York, (ISBN 0060438622 9780060438623)
72. Hoops S., Sahle S., Gauges R., Lee C., Pahle J., Simus N., Singhal M., Xu L., Mendes P., Kummer U. (2006), COPASI—a COMplex PATHway Simulator, *Bioinformatics*, 22, 3067–3074 (DOI: 10.1093/bioinformatics/btl485)
73. Petzold L. (1983), Automatic Selection of Methods for Solving Stiff and Nonstiff Systems of Ordinary Differential Equations, *SIAM J. Sci. Stat Comput*, 4, 136–148 (DOI: 10.1137/0904010)
74. Canneaux S., Bohr F., Henon E. (2014), KiSTheIP: a program to predict thermodynamic properties and rate constants from quantum chemistry results, *J. Comp. Chem.*, 35, 82-93 (DOI: 10.1002/jcc.23470)
75. Filonenko G.A., Putten R.V., Hensen E.J.M., Pidko E.A. (2018), Catalytic (de)hydrogenation promoted by non-precious metals – Co, Fe and Mn: recent advances in an emerging field, *Chem. Soc. Rev.*, 47, 1459-1483 (DOI: 10.1039/C7CS00334J)
76. Zell T., Milstein D. (2015), Hydrogenation and Dehydrogenation Iron Pincer Catalysts Capable of Metal–Ligand Cooperation by Aromatization/Deaomatization, *Acc. Chem. Res.*, 48, 1979–1994 (DOI: 10.1021/acs.accounts.5b00027)
77. Dub P.A., Henson N.J., Martin R.L., Gordon J.C. (2014), Unravelling the Mechanism of the Asymmetric Hydrogenation of Acetophenone by [RuX₂(diphosphine)(1,2-diamine)] Catalysts *J. Am. Chem. Soc.*, 136, 3505–3521 (DOI: 10.1021/ja411374j)
78. Dub P.A., Gordon J.C. (2016), The mechanism of enantioselective ketone reduction with Noyori and Noyori–Ikariya bifunctional catalysts, *Dalton Trans.*, 45, 6756–6781 (DOI: 10.1039/C6DT00476H)

79. Dub P.A., Gordon J.C. (2017), Metal–Ligand Bifunctional Catalysis: The “Accepted” Mechanism, the Issue of Concertedness, and the Function of the Ligand in Catalytic Cycles Involving Hydrogen Atoms, *ACS Catal.*, 7, 6635–6655 (DOI: 10.1021/acscatal.7b01791)
80. Mandal S.C., Rawat K.S., Pathak B. (2019), A computational study on ligand assisted vs. ligand participation mechanisms for CO₂ hydrogenation: importance of bifunctional ligand based catalysts, *Phys. Chem. Chem. Phys.*, 21, 3932-3941 (DOI: doi.org/10.1039/C8CP06714G)
81. Bertini F., Glatz M., Gorgas N., Stoger B., Peruzzini M., Veiros L. Kirchner F., K., Gonsalvi L. (2017), A MOF-assisted phosphine free bifunctional iron complex for the hydrogenation of carbon dioxide, sodium bicarbonate and carbonate to formate, *Chem. Sci.*, 8, 5024–5029 (DOI: 10.1039/C8CC09771B)
82. Zhang Y., MacIntosh A.D., Wong J.L., Bielinski E.A., Williard P.G., Mercado B.Q., Hazari N., Bernskoetter W.H. (2015), *Chem. Sci.*, 6, 4291–4299 (DOI: 10.1039/C5SC01467K)
83. Kozuch S., Shaik S. (2011), *Acc. Chem. Res.*, 44, 101–110 (DOI: 10.1021/ar1000956)
84. Lu Y., Liu Z., Guo J., Qu S., Zhao R., Wang Z. (2017), *Chem. Commun.*, 53, 12148—12151 (DOI: 10.1039/C7CC06795J)
85. Bertini F., Glatz M., Stöger B., Peruzzini M., Veiros L.F., Kirchner K., Gonsalvi L. (2019), *ACS Catal.*, 9, 632–639 (DOI: 10.1021/acscatal.8b04106)
86. Zou Y.Q., Chakraborty S., Nerush A., Oren D., Diskin-Posner Y., Ben-David Y., Milstein D. (2018), Highly Selective, Efficient Deoxygenative Hydrogenation of Amides Catalyzed by a Manganese Pincer Complex via Metal–Ligand Cooperation, *ACS Catal.*, 8, 8014–8019 (DOI: 10.1021/acscatal.8b02902)
87. Suarez L.A., Culakova Z., Balcells D., Bernskoetter W.H., Eisenstein O., Goldberg K.I., Hazari N., Tilset M., Nova A. (2018), The Key

- Role of the Hemiaminal Intermediate in the Iron-Catalyzed Deaminative Hydrogenation of Amides, *ACS Catal.*, 8, 8751–8762 (DOI: 10.1021/acscatal.8b02184)
88. Morello G.R., Hopmann K.H. (2017), A Dihydride Mechanism Can Explain the Intriguing Substrate Selectivity of Iron-PNP-Mediated Hydrogenation, *ACS Catal.*, 7, 5847–5855 (DOI: 10.1021/acscatal.7b00764)
89. Sonnenberg J.F., Wan K.Y., Sues P.E., Morris R.H. (2017), Ketone Asymmetric Hydrogenation Catalyzed by P-NH-P' Pincer Iron Catalysts: An Experimental and Computational Study, *ACS Catal.*, 7, 316–326 (DOI: 10.1021/acscatal.6b02489)
90. Jiao H., Junge K., Alberico E., Beller M., (2016), A comparative computationally study about the defined M(II) pincer hydrogenation catalysts (M = Fe, Ru, Os), *J. Comput. Chem.*, 37, 168–176 (DOI: 10.1002/jcc.23944)
91. Rezayee N.M., Samblanet D.C., Sanford M.S. (2016), Iron-Catalyzed Hydrogenation of Amides to Alcohols and Amines, *ACS Catal.*, 6, 6377–6383 (DOI: 10.1021/acscatal.6b01454)
92. Jover J., Feytaud N., Purdie M., Lloyd-Jones G.C., Harvey J.N. (2010), A computational study of phosphine ligand effects in Suzuki-Miyaura coupling, *Journal of Molecular Catalysis A: Chemical*, 324, 39–47 (DOI: 10.1016/j.molcata.2010.02.021)
93. Gill D.S., Singh J., Ludwig R., Zeidler M.D. (1993), Nuclear magnetic resonance relaxation, permittivity, viscosity and ultrasonic velocity measurements in binary mixtures of methanol and tetrahydrofuran, *J. Chem. Soc. Faraday Trans.*, 89, 3955-3958 (DOI: 10.1039/FT9938903955)
94. Hull J.F., Balcells D., Sauer E.L.O., Raynaud C., Brudvig G.W., Crabtree R.H., Eisenstein O. (2010), Manganese Catalysts for C–H Activation: An Experimental/Theoretical Study Identifies the Stereoelectronic Factor That Controls the Switch between

Hydroxylation and Desaturation Pathways, *J. Am. Chem. Soc.*, 132, 7605–7616 (DOI: 10.1021/ja908744w)

95. Zhou J., Huang L., Yan W., Li J., Liu C., Lu X. (2018), Theoretical Study of the Mechanism for CO₂ Hydrogenation to Methanol Catalyzed by trans-RuH₂(CO)(dpa), *Catalysts*, 8, 244 (DOI: 10.3390/catal8060244)
96. Kar S., Sen R., Kothandaraman J., Goepfert A., Chowdhury R., Munoz S. B., Haiges R., Prakash G. K. S. (2019), *J. Am. Chem. Soc.*, 141, 3160-3170 (DOI: 10.1021/jacs.8b12763)

Chapter 5

*Selective CO₂ Hydrogenation to Methanol
Using Heterogeneous Based Cu
Nanocatalysts*

5.1. Introduction

The development of a sustainable energy source is one of the important alternative approaches for the replacement of the fossil fuel-based energies. The electrochemical CO₂ reduction is an imperative approach for the conversion of electrical energy into chemical energy [1]. Most of the reduced products (hydrocarbons and alcohols) are valuable chemicals for the generation of carbon-neutral fuels [1-3]. In this context, scientists have been working towards the development of efficient catalysts for CO₂ hydrogenation. The electrochemical CO₂ reduction has been identified as a promising approach, but it suffers from low conversion efficiency and product selectivity [4,5]. Hence, the development of an efficient and selective catalyst for the electrochemical CO₂ reduction to valuable products is highly demanding. In the case of electrochemical CO₂ hydrogenation, a series of different products can form, such as formate (HCOO⁻), methanol (CH₃OH), methane (CH₄) and so on [1,6-8]. Amongst all, methanol is one of the highly desirable products owing to its applications in industries and fuels [4,9]. Therefore, the selective electrochemical conversion of CO₂ to methanol is an important problem for researchers. Previous reports have concluded that, the catalysts for methanol formation process are very much temperature dependent [10]. In this regard, significant research progresses have been made for the development of the cost-effective and product selective electrochemical CO₂ reduction. In this context, both homogenous and heterogeneous catalysts have been investigated [11-25]. Though various transition metal-based heterogeneous catalysts have been studied, but copper-based catalysts have been identified as the most active metal-based catalysts for electrochemical CO₂ hydrogenation [17,26]. However, such Cu-based catalysts are not highly product selective as several other products, such as CO, formate, methane are formed during the catalytic reaction. On the other hand, methanol is produced industrially using the Cu/ZnO/Al₂O₃ catalyst, which operates at 50-100 atmosphere pressure and 473-573 K temperature

[27]. These catalysts show very low product selectivity as they are also used for reverse water gas shift reaction. Several experimental reports demonstrated that carbon monoxide (*CO), formaldehyde (*CH₂O) and methoxy (*H₃CO) are the three important intermediates for CO₂ hydrogenation to methanol [28,29]. So, the CO₂ hydrogenation to methanol reaction proceeds via CO, CH₂O, and CH₃O intermediates and therefore, we can say that it is a step by step hydrogenation process. However, it is very difficult for experimentalists to characterize all the intermediates and DFT studies have been found to be a reliable approach to characterize the underlying mechanism of CO₂ hydrogenation to CH₃OH formation [30,31]. On the other hand, the utilization of graphene has been very much inspiring for the scientific community to develop monolayer (ML) based catalysts. In this context, few layers of graphene, nitrogen doped graphene, metal doped graphene oxide, and N, Fe-decorated carbon nanosheets have been reported for electrochemical CO₂ hydrogenation [32-34]. Similarly, supported Cu monolayer based catalyst and Cu shell-based core-shell catalysts have been investigated [35,36]. Main group ML based catalysts have been reported for CO₂ hydrogenation [32,34]. However, the catalytic activity of such main group based ML improves upon metal atom doping. Therefore, we predict that pure metal based MLs can be more efficient catalyst compared to the main group based MLs. However, there are only a few reports of ultrathin metal-based CO₂ hydrogenation catalyst. Recently, an ultrathin bismuth nanosheet has been explored for CO₂ electroreduction to formate [37]. On the other hand, most of the monolayer based catalysts show higher catalytic activity compared to their pure bulk geometry [38-40]. In this context, Wang and co-workers have synthesized Pt-Cu nanosheet [38]. Our group has also investigated Pt monolayer based catalysts for similar type of reactions [39,40]. Inspired by these previous studies, we have modeled a series of Cu MLs. Earlier reports suggest that the synthesized Cu nanoclusters have highly exposed (110) and (111) surfaces as they are the most stable surfaces for Cu-based structures [41,42]. Based on this, we have

modelled four possible Cu MLs structures (Figure 5.1) using the face centered cubic Cu bulk structure along the (110) and (111) surface planes. Two six coordinated planar (hexagonal as well as orthorhombic) and two six coordinated buckled structures (hexagonal as well as orthorhombic) have been modelled. Amongst all, the most stable Cu ML has been considered for our study [43]. To find out the potential applicability of the Cu-ML catalyst, the results are then compared with the previous reports on electrochemical CO₂ reduction on the bulk Cu(111) surface as well as Cu-nanocluster based catalysts.

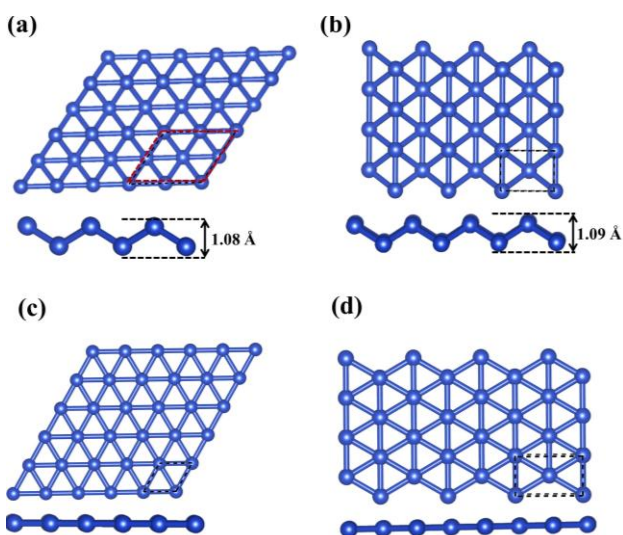


Figure 5.1: Different motifs of six coordinated Cu MLs: (a) hexagonal buckled, (b) orthorhombic buckled, (c) hexagonal planar, and (d) orthorhombic planar. The red dashed line indicates the unit cell of the respective monolayer.

Besides, Cu based single-atom catalysts (SAC) have also been identified as a promising catalyst for selective CH₃OH formation at low overpotential [44,45]. These SACs are highly beneficial due to their low metal uses that is maximum atom utilization efficiency. Different coordination number and unique electronic structure of SAC increase the catalytic activity in the reaction. In all the cases, the nature of the catalyst's active sites and the

reaction route are two important factors. Earlier studies have shown that the CO₂ hydrogenation to CH₃OH is obtained via two different pathways: (i) formate (HCOO) pathway and (ii) carboxyl (COOH) pathway [46,47]. Side by side, ZnO based nanostructures are highly abundant and non-toxic. On the other hand, various ZnO based nanostructures (such as nanocombs, nanosprings, nanorings, nanobows, nanobelts, nanocages and so on) have been synthesised very easily [48,49]. Most of these nanostructures are also found to be promising for hydrogenation reaction and more often than not, they have been identified as an efficient catalyst compared to their bulk catalysts [50,51]. Recently, Wu et al. have synthesised (ZnO)_n (n=1-15) based nanostructures [52]. Dmytruk et al., have shown that the (ZnO)₃₄, (ZnO)₆₀ and (ZnO)₇₀ nanostructures are highly stable [53]. Further to this, Tian and his co-workers have described that the (ZnO)₆₀ nanocluster is composed of (ZnO)₁₂ based structure where (ZnO)₁₂ acts as a basic unit for the formation of ZnO based nanocage (NC) structures [54]. Thus, we have considered Zn₁₂O₁₂ and Zn₂₄O₂₄ based NCs (Figure 5.2) for our study.

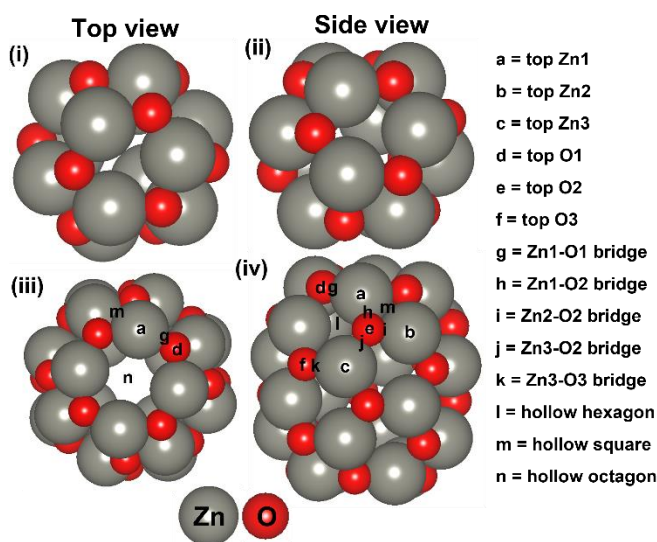


Figure 5.2: Top and side views of the considered NCs: (i, ii) Zn₁₂O₁₂, (iii, iv) Zn₂₄O₂₄.

Between these two NCs, the energetically most stable NC has been

considered for the CO₂ hydrogenation reaction. Our main objective in this study is to understand the catalytic activity of a single Cu-atom based catalyst compared to the previously reported Cu-bulk and Cu-nanostructure based catalysts. Therefore, we have investigated the CO₂ hydrogenation reaction over the Cu doped ZnO system and then compared our results with the previously reported Cu-bulk and Cu-nanostructure based catalysts (Cu(111), Cu ML, and Cu nanocluster). The most favourable pathways of the CO₂ hydrogenation reaction have been identified to gain insights towards the catalytic activity of the single Cu-atom based catalyst compared to the previously reported catalytic systems.

5.2. Computational Details

The first-principles calculations are carried out by using the projector augmented wave (PAW) as implemented in the Vienna Ab initio Simulation Package (VASP) [55-57]. The generalized gradient approximation of Perdew–Burke–Ernzerhof (GGA-PBE) has been used for the description of exchange correlation potential [58,59]. A ~15 Å vacuum space is kept along the z-direction for Cu-MLs to avoid the possible interactions between two successive periodic images whereas ~15 Å vacuum space is kept along all three directions for NCs. Furthermore, a 470 eV plane wave cutoff energy has been used to expand the electronic wave function. The convergence criteria are set to be 1×10^{-4} eV for electronic energy, and 0.02 eV/Å for force minimization. Grimme's D3-type of the semi-empirical method has also been included to calculate the van der Waals interactions and dispersion energy corrections [60]. We have used a 43×43×1 gamma centered k-point grid for Cu-based unit cell (one atom unit cell) optimization and density of states calculations. In case of NCs, we have calculated the energies at 3×3×3 and 1×1×1 gamma centred k-point and found that the difference in energy is negligible (~0.0009 eV). Hence, the plane-wave basis cutoff energy has been set to 470 eV with 1×1×1 gamma centred k-point for NCs. Adsorption energies (E_{ad}) of all the intermediates have been calculated using the

following equation (5.1):

$$E_{\text{ad}} = E_{\text{Cu ML/NCs+ads}} - (E_{\text{Cu ML/NCs}} + E_{\text{ads}}) \quad (5.1)$$

Here $E_{\text{Cu ML/NCs+ads}}$ is the total energy of the optimized Cu ML/NCs with adsorbate, $E_{\text{Cu ML/NCs}}$ and E_{ads} are the single point energies of the Cu ML/NCs, and adsorbed intermediate from the optimized geometry of the Cu ML/NCs+adsorbate. Here we have considered, adsorption energy is the difference between the total energy of the complex minus the energy of the isolated monomers in the geometry of the complex. If we consider the total energy of the fragment, then the fragmented structure is free to obtain their minima configuration whereas in case of single point energy the structure is freeze and it gives energy of its original form. Therefore, we have considered total energy of the Cu_{ML/NCs+adsorbate} and single point energies of $E_{\text{Cu ML/NCs}}$ and E_{ads} . All the reaction free energies (ΔG) and activation barriers (E_a) have been calculated using the computational hydrogen electrode (CHE) model as described by the Nørskov and co-workers [61]. The free energies (ΔG) and activation barriers (E_a) are calculated using the following equation (5.2):

$$\Delta G = \Delta E + \Delta ZPE - T\Delta S \quad (5.2)$$

where, ΔE is the total energy difference between initial and final states, ΔZPE is the change in zero-point energy, T is the temperature, and ΔS is the change in entropy of the reaction. The zero-point energy of the reaction is calculated by using $\sum \frac{1}{2} h\nu_i$, where h and ν_i denote the Planck's constant and vibrational frequency, respectively. Here total energy and frequency calculations are performed at 0 K temperature ($T = 0$ K). Therefore, $T\Delta S$ term becomes zero that is Gibbs free energy is equal to the $\Delta E + \Delta ZPE$. Hence, we have not considered the change in entropy during free energy calculation. On the other hand, if temperature is non-zero, entropy will have contributions from translation, rotational and vibrational degrees of freedom of each atom. Moreover, in the presence of an external potential (U), the chemical potential of the reaction shifts by $-eU$ where e is the

elementary potential charge of the considered step [62]. In general, translation and rotational entropies are negligible for catalyst with adsorbed intermediates whereas vibrational entropy contribution can be calculated from the standard thermochemistry calculation once vibrational frequencies are known [63]. This can be calculated using statistical thermodynamics equation as follow (5.3):

$$S_{\text{vib}} = R \sum \left(\frac{\hbar \nu_i}{k_B T \left(\exp\left(\frac{\hbar \nu_i}{k_B T}\right) - 1 \right)} - \ln \left(1 - \exp\left(\frac{-\hbar \nu_i}{k_B T}\right) \right) \right) \quad (5.3)$$

In the above equation, S_{vib} is vibrational entropy, R is gas constant, ν is vibrational frequency, k_B is Boltzmann constant, T is temperature and $\hbar = h/2\pi$, where h is Planck constant. From the above equation it is clear that the vibrational entropy will be less. Therefore, overall entropy will be very less for considered intermediates. Hence, change in entropy can be neglected during free energy calculation. Furthermore, the vibrational frequencies have been used to characterize the intermediates and transition states of the reaction. The transition states of the reaction have been searched using the six-climbing image nudged elastic band (CI-NEB) and dimer method [64,65]. Moreover, we have calculated Bader atomic charges using Henkelman code with near-grid algorithm refine-edge method [66,67]. From hereon, all the adsorbed species have been denoted by the asterisk sign (*) in this chapter.

5.3. Results and Discussion

At first, we have considered the Cu MLs for the investigation of CO₂ hydrogenation reaction. In the next part of this section, we have considered ZnO based NCs for CO₂ hydrogenation to methanol.

5.3.1. Cu MLs for CO₂ Hydrogenation Reaction

In the beginning, we have discussed the stability of the Cu MLs and NCs from the stability calculations we have investigated the catalytic activity of the most stable Cu ML and NC structure. Finally, we have compared our

results with the previously reported bulk Cu(111) surface and Cu nanocluster based catalysts.

5.3.1.1. Stability of the Cu MLs

The stability of the Cu ML based structures has been investigated in various ways. We find that the total energy remains same irrespective of their lattice symmetries. Our total energy calculations indicate that Cu(110) MLs are stable in the buckled form, whereas Cu(111) MLs are stable in the planar form. We have also calculated the formation and cohesive energies to understand the stability of such structures compared to the bulk structure [40]. In order to measure the energetic stability of the monolayer structures, we have calculated the cohesive (E_{coh}) and formation (E_f) energies of Cu MLs and bulk Cu(111) surface using the following equations (5.4 and 5.5) [68]:

$$E_{\text{coh}} = (E_{\text{Cu(ML/Cu(111))}} / N) - E_{\text{Cu}} \quad (5.4)$$

$$E_f = (E_{\text{Cu(ML/Cu(111))}} / N) - \mu_{\text{Cu}} \quad (5.5)$$

Here, $E_{\text{Cu(ML/Cu(111))}}$ is the total energy of the Cu(111) ML/bulk Cu(111) surface, N is the total number of atoms, E_{Cu} is the energy of an isolated Cu atom, and μ_{Cu} is the chemical potential of Cu atom. Here we have compared our calculated values with the reported experimental values for bulk Cu(111) to justify the GGA PBE level of theory is good enough to predict their energetic stability. The calculated formation and cohesive energy values are listed in Table 5.1, which shows that planar ML based structures are stable over buckled ML based structures. Therefore, hexagonal and orthorhombic planar Cu(111) ML structures are more stable compared to orthorhombic and hexagonal buckled (110) structures. It is noteworthy to mention that our calculated formation and cohesive energies of bulk Cu(111) surface are in good agreement with the experimental values [69]. Therefore, the level of theory is good enough for further study.

Table 5.1: Formation and cohesive energies of Cu MLs and bulk Cu(111)

surface. The experimental cohesive energy value of the bulk Cu(111) surface listed for comparison [69].

Cu ML and periodic systems	Formation energy (eV per atom)	Cohesive energy (eV per atom)
Orthorhombic buckled (110)	1.32	-2.79
Hexagonal buckled (110)	1.32	-2.79
Orthorhombic planar (111)	1.22	-2.90
Hexagonal planar (111)	1.21	-2.90
Bulk Cu(111) surface	0.26	-3.85
Bulk Cu(111) surface (experimental)	0.31	-3.49

The dynamic stability of the Cu MLs has been calculated using the density functional perturbation theory (DFPT) as implemented in VASP [70]. The phonon dispersions of the Cu MLs have been examined from their phonon dispersion plot using the phonopy code [71]. The phonon dispersion calculations are carried out in a 36-atom supercell geometry to reduce the constraints of the periodic boundary conditions. Our calculated phonon dispersion suggests that the modelled six coordinated hexagonal planar Cu ML is dynamically stable as there are no imaginary modes in the entire Brillouin zone (Figure 5.3a). On the other hand, the orthorhombic planar Cu ML shows two small imaginary frequencies in the order of $\sim 10i \text{ cm}^{-1}$ at the ($\Gamma \rightarrow X$ and $Y \rightarrow \Gamma$) high symmetry k-point path of the Brillouin zone (Figure 5.4a). Furthermore, the other modelled Cu(110) MLs are also dynamically unstable due to their large imaginary frequency in the order of $\sim 65\text{-}66 \text{ cm}^{-1}$ (Figure 5.4b and c).

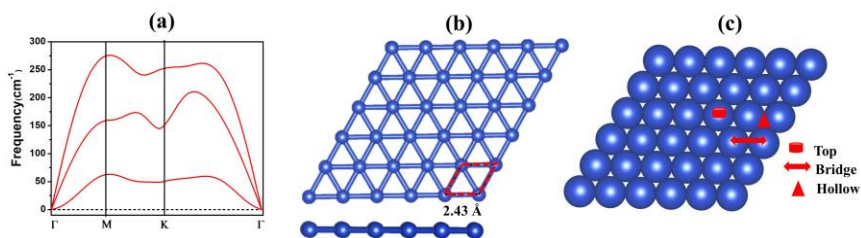


Figure 5.3: (a) The phonon dispersion plot of hexagonal Cu(111) ML, (b) top and side views of Cu(111) ML (where red dotted lines show the unit cell of the structure) and (c) the possible adsorption sites on Cu(111) ML.

Thus, hexagonal planar Cu(111) ML is dynamically stable compared to all the other modelled Cu MLs. Therefore, from hereon, we have used the term Cu(111) ML for the hexagonal planar Cu(111) monolayer structure and the structure (Figure 5.3) has been chosen for catalytic CO₂ hydrogenation reaction. The catalysts for CO₂ hydrogenation reaction mainly operate at 50-100 atmosphere (atm.) pressure and 473-573 K temperature [27]. Therefore, it is very crucial to find out whether the Cu(111) ML structure is stable at high temperature and pressure or if there is a chance of possible interconversion of Cu(111) ML to any other conformers.

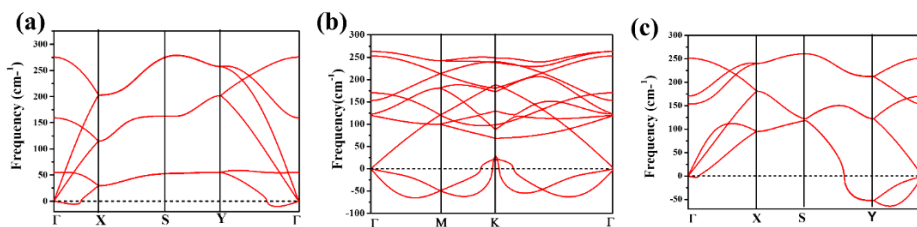


Figure 5.4: Dispersion of phonon modes for six-coordinated (a) orthorhombic planar Cu(111) ML, (b) orthorhombic buckled Cu(110) ML and (c) hexagonal buckled Cu(110) ML.

In this context, the thermal and mechanical stability of Cu(111) ML are investigated and our results suggest that the Cu(111) ML is thermally and mechanically stable. Therefore, we have performed ab initio molecular dynamics (AIMD) simulations using the Nosé thermostat model to check

the thermal stability of the Cu(111) ML [72]. The simulation has been carried out in a 6×6 supercell by using an NVT ensemble at 300-700 K temperature with a time step of 1 femtosecond (fs) for 20 picoseconds (ps) (Figure 5.5a). Our calculations confirm that there is not any appreciable energy change throughout the simulation at 300 K temperature. Furthermore, even at higher temperature (500 K - 700K) the overall energy fluctuation is not high and there is no structural reconstruction observed even after heating up to 700 K for 20 ps (Figure 5.6). Therefore, the possibility of interconversion of Cu(111) ML into other local minima energy structure is not possible in the 300-700 K temperature. Thus, we can say that our proposed Cu(111) ML is thermally stable structure and can be a potential catalyst for selective CO₂ hydrogenation.

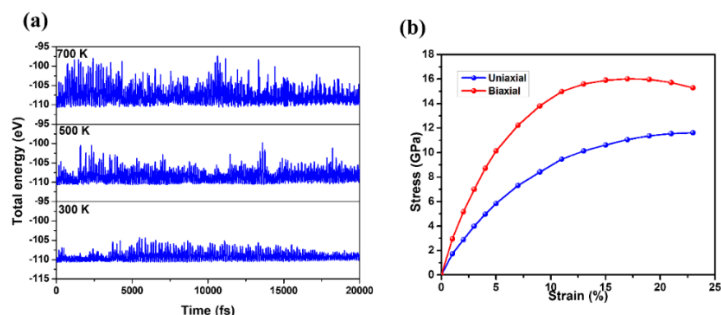


Figure 5.5: (a) The AIMD simulation of the Cu(111) ML at 300-700 K temperature for 20 ps. (b) Stress-strain relationship of the Cu(111) ML under in-plane uniaxial and biaxial direction.

Further to this, during intermediate adsorption on the Cu(111) ML, it may generate some distortion or strain in the structure. Thus, it is necessary to observe the effect of lattice deformation on the Cu(111) ML for structural stability. In this respect, strain technology is not only an appropriate technique to investigate their mechanical stability but also a very important tool to predict the possible synthesis of such structure. In this technique, the Cu(111) ML has been deformed by gradually increasing the lattice parameters along the in-plane uniaxial and biaxial directions, which is

referred as tensile strain. Thus, the % strain has been calculated by using the following formula (5.6) [73]:

$$\% \text{Strain} = \frac{a - a_1}{a} \times 100 \quad (5.6)$$

where a and a_1 are the lattice constants of the Cu(111) ML with and without strain. Each strained structure of the Cu(111) ML has been fully relaxed till the forces get minimized to 0.01 eV/\AA . However, the equivalent stress has been achieved by the rescaling the observed values of stress with Z/d_0 , where Z is the vacuum length in z -direction and d_0 is the thickness of the system. The observed stress value gives an elastic limit under the percentage of strain.

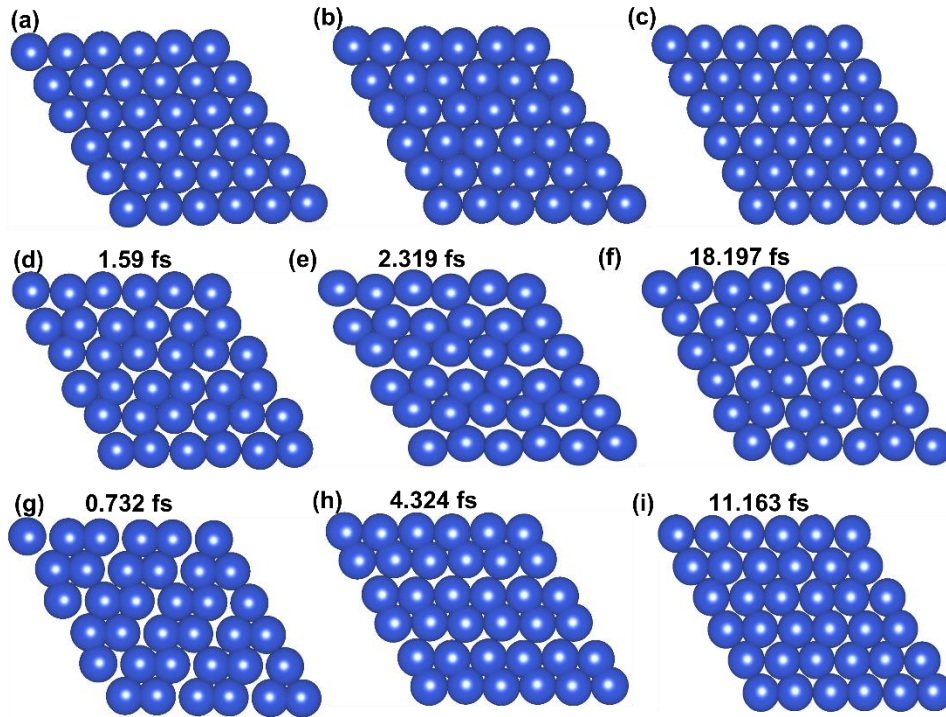


Figure 5.6: Snapshots of the Cu(111) ML at the end of the simulation with temperature (a) 300 K, (b) 500 K and (c) 700 K. Snapshots of the Cu(111) ML when the total energy fluctuation of the Cu(111) ML is around 10 eV during the simulation at 500K (d-f), and at 700 K (g-i).

The stress-strain relationship (Figure 5.5) indicates that maximum stress

limit occurs at the 21% and 23% in-plane biaxial and uniaxial direction, respectively. The maximum stress response of the Cu(111) ML is 16 GPa, interestingly this value is higher compared to platene [39]. Thus, we can say that the Cu(111) ML is mechanically a strong material. Moreover, we have also calculated the relative stiffness of the Cu(111) ML compared to other materials. For this, we have evaluated the change in energy after each successive strain, which is helpful to calculate the mechanical properties. Thus, the strain energy (U/unit cell) near the equilibrium position is calculated by using the following equation (5.7) [74,75]:

$$U = 1/2C_{11}\varepsilon_{xx}^2 + 1/2C_{22}\varepsilon_{yy}^2 + C_{12}\varepsilon_{xx}\varepsilon_{yy} + 2C_{44}\varepsilon_{xy}^2 \quad (5.7)$$

where C_{11} , C_{22} , C_{12} and C_{44} denote the linear elastic constants, whereas ε_{xx} , ε_{yy} , and ε_{xy} represent the in-plane stress along the uniaxial (-x, and -y) and biaxial direction (x-y), respectively. However, to calculate the elastic constants, we have done the polynomial fitting for strain *versus* energy (Figure 5.7).

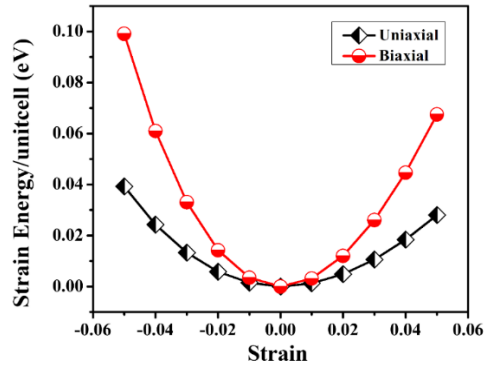


Figure 5.7: Strain energy under in plane uniaxial and biaxial strains of the Cu(111) ML.

Therefore, C_{11} and C_{12} have been calculated from the second order derivative of the polynomial fitting under uniaxial and biaxial deformations. The values of C_{11} , C_{12} , and C_{44} are calculated to be 73 GPa nm, 17 GPa nm, and 28 GPa nm respectively. The important feature of this part is $C_{11} > C_{12}$ and $C_{44} > 0$, which is an important thumb rule for mechanically stable 2D hexagonal system. Thus, all these results indicate that the Cu(111) ML is

mechanically stable material. Furthermore, the Young's modulus (Y) and Poisson's ratio (PR) have been calculated using the following equations.

$$Y = (C_{11}^2 - C_{12}^2) / C_{11} \quad (5.8)$$

$$PR = C_{12} / C_{11} \quad (5.9)$$

By using the above equation, we have calculated the values (in plane) of Y and PR, which are to be 69 GPa nm, and 0.23, respectively. However, Y of the Cu(111) ML is lower to that of graphene (340 GPa nm) [76] but significantly higher than stanene (24 GPa nm) [77]. Remarkably, the Cu(111) ML has a quite comparable PR to that of graphene (0.19) which shows that the Cu(111) ML has smaller shear motion similar to graphene, indicating that the Cu ML(111) is mechanically strong material like graphene [78]. Therefore, we have considered Cu(111) ML based on the highly exposed (111) surface. On the other hands, in recent times, there have been reports that metal-based MLs (along with NCs) have been synthesized [35,36,38]. Therefore, the interatomic attraction is good enough in case of metal-based MLs too. Similarly, we wanted to see whether the interatomic attraction in Cu ML is strong enough for to hold the structure or not. Based on our total energy, AIMD, and phonon calculations, we find that the attraction is strong enough to hold the structure. Based on our energetic, thermal, dynamic and mechanical stability calculations, we have found that Cu(111) ML is stable. However, without any detailed investigations, it's very difficult to comment whether the Cu ML structure will be sintering into bulk Cu(111) surface or not.

5.3.1.2. Adsorption of Intermediates

In this section, the applicability of the Cu(111) ML for CO₂ hydrogenation has been investigated in detail. Three possible catalytic sites (top, bridge, and hollow; Figure 5.3c) have been considered for adsorption of all the reaction intermediates. All the preferred adsorption sites (most stable sites,) and their respective geometries and adsorption energies are given in Figure 5.8 and Table 5.2, respectively.

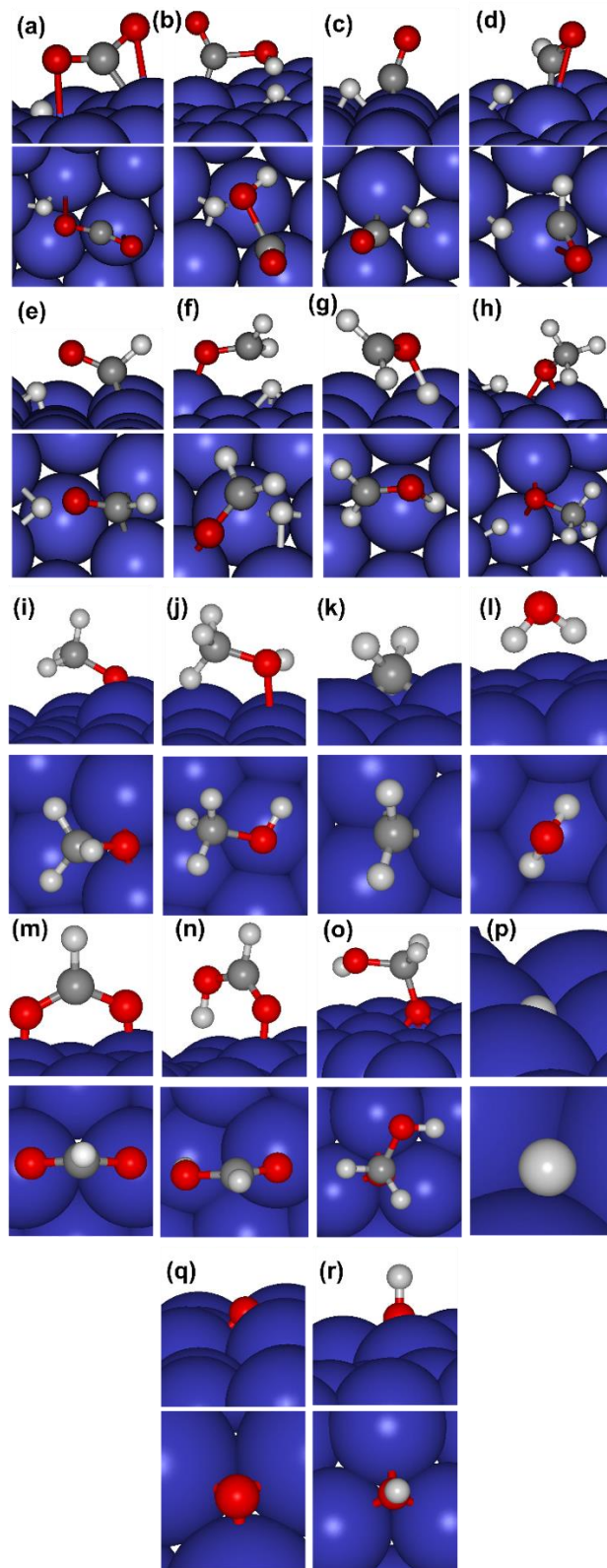


Figure 5.8: Adsorption patterns of the intermediates on the Cu(111) ML surface: (a) *CO_2 , (b) *COOH , (c) *CO , (d) *CHO , (e) *COH , (f) *CHOH ,

(g) *CH₂O, (h) *CH₂OH, (i) *CH₃O, (j) *CH₃OH, (k) *CH₂, (l) *H₂O, (m) *HCOO, (n) *HCOOH (o) *H₂COOH (p) *H, (q) *O and (r) *OH.

Table 5.2: Preferred adsorption sites (top, bridge and hollow) and adsorption energies of all the CO₂ hydrogenation intermediates on Cu(111) ML. The preferred site and adsorption energies of the respective adsorbates are compared with our earlier report on the bulk Cu(111) surfaces [79].

Intermediates (Preferred site)	Adsorption Energy (eV)	
	Cu(111) ML	Bulk Cu(111)
CO ₂ (bridge)	-0.21	Not adsorbed
*COOH (bridge)	-1.84	-1.72
*HCOO (bridge)	-3.60	-
*HCOOH (top)	-0.70	-
*H ₂ COOH (hollow)	-3.16	-
*CO (top)	-0.98	-0.91
*CHO (bridge)	-1.57	-1.44
*COH (hollow)	-2.97	-2.89
*CHOH (bridge)	-2.41	-2.00
*CH ₂ O (bridge)	-0.35	-0.04
*CH ₂ OH (bridge)	-1.54	-1.24
*CH ₃ O (bridge)	-2.62	-2.41
*CH ₃ OH (top)	-0.39	-0.12
*CH ₂ (bridge)	-3.58	-3.37
*H ₂ O	-0.33	-0.16
*H (hollow)	-3.52	-2.50
*O (hollow)	-5.26	-4.79
*OH (hollow)	-3.83	-3.10

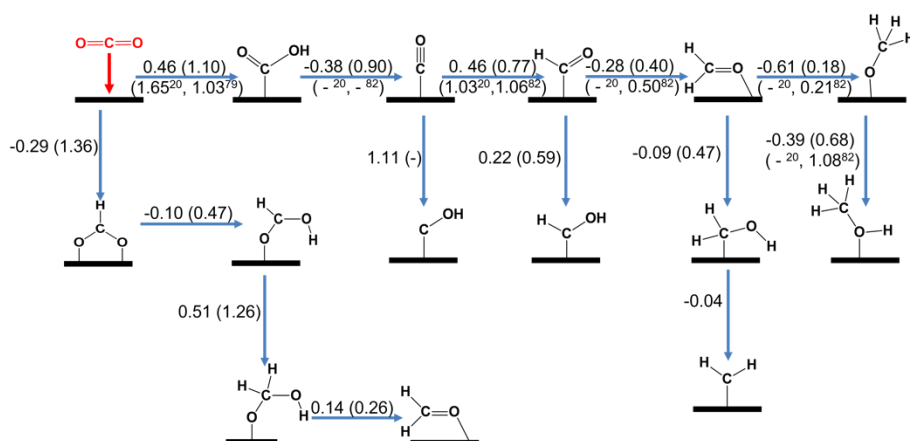
For comparisons, we have compared our calculated adsorption energies of intermediates with that on the bulk Cu(111) surface [79]. We find that CO₂ interacts very weakly on the Cu(111) ML surface, which is very much

similar with the previous experimental and theoretical reports, where they found that CO₂ interacts weakly on the bulk Cu(111) surface [80,81]. On the other hand, we find that the most preferred adsorption sites of all the intermediates are same on the Cu(111) ML and bulk Cu(111) though the calculated adsorption energies of the intermediates are higher on the Cu(111) ML compared to that on the bulk Cu(111) surface. Interestingly, *CHO and *COH are the two important intermediates for the formation of CH₃OH and CH₄, respectively. We find that *CHO binds weakly on the Cu(111) ML compared to *COH on the Cu(111) ML surface. We also find that the *CH₂O (another important intermediate for CH₃OH formation) binds strongly on the Cu(111) ML compared to that on the bulk Cu(111) surface [79]. In the presence of adsorbed species, the structure does not distort. Rather, it retains its planarity. This indicates that the attraction between Cu-atoms is quite strong in Cu(111) ML. We have not considered the adsorption of adsorbates on both sides of the surface as such metal-based ML structures have been synthesized on supported materials [35,36].

5.3.1.3. CO₂ Hydrogenation Mechanisms

The CO₂ gas molecule can interact with the adsorbed hydrogen atom on the surface. In such cases, the strong C=O bond of CO₂ molecule can be weakened, which in turn can be dissociated into other intermediates. Therefore, direct activation of CO₂ may be difficult, though indirect activation of CO₂ can be possible via hydrogenation. Hydrogen can react via Langmuir-Hinshelwood (LH) or Eley-Rideal (ER) mechanism. In case of Langmuir-Hinshelwood (LH) mechanism, hydrogen is adsorbed on the surface whereas in case of Eley-Rideal (ER) mechanism, hydrogen remains in the gas phase. However, earlier reports have shown that CO₂ hydrogenation reaction proceeds via Langmuir-Hinshelwood (LH) mechanism [20,35,79]. Therefore, we have considered only Langmuir-Hinshelwood mechanism for our study. Moreover, previous reports have shown that the gas phase calculation of CO₂ hydrogenation reaction can

reproduce the experimental trend [81]. Therefore, we have not used solvent model in our calculations as these calculations are computationally expensive. The *CO_2 hydrogenation will lead to the formation of *COOH and *HCOO , and the formation of these two products can be highly dependent on the source of the proton and its transfer mechanism [81]. Earlier reports suggest that the hydrogenation of CO_2 occurs via proton transfer mechanism for the formation of O-H bond to form *COOH [20,23]. Therefore, we have proposed proton-transfer mechanisms (Scheme 5.1) for CO_2 hydrogenation to *COOH and *HCOO . The Cu(111) ML surface has been modelled using a (6×6) supercell ($a=14.6 \text{ \AA}$ and $b=14.6 \text{ \AA}$) of 36 Cu atoms to investigate the CO_2 hydrogenation reaction mechanism.



Scheme 5.1: The calculated reaction free energies (eV) and activation barriers (values in parenthesis, eV) for electrochemical CO_2 reduction on the Cu(111) ML. Our calculated activation barriers are compared that with the previous reports on the bulk Cu(111) surface [20,79,82]. Here (-) represents data is not available for this step.

Our calculated surface coverage is 0.028 ML (as $1/36=0.0277$). Here, we have considered a low surface coverage to avoid any periodic interactions between adsorbed intermediates. Scheme 5.1 shows the calculated reaction free energy and activation barrier values for CO_2 hydrogenation on Cu(111) ML with respect to the previous reports on the bulk Cu(111). Figure 5.9

shows the corresponding potential energy surface, whereas Figure 5.10 and Table 5.3 show the corresponding structures and imaginary frequencies of the transition states. Previously, Asthagiri and co-workers have reported a barrier of 1.65 eV for *COOH formation when catalyzed by the bulk Cu(111) surface [20].

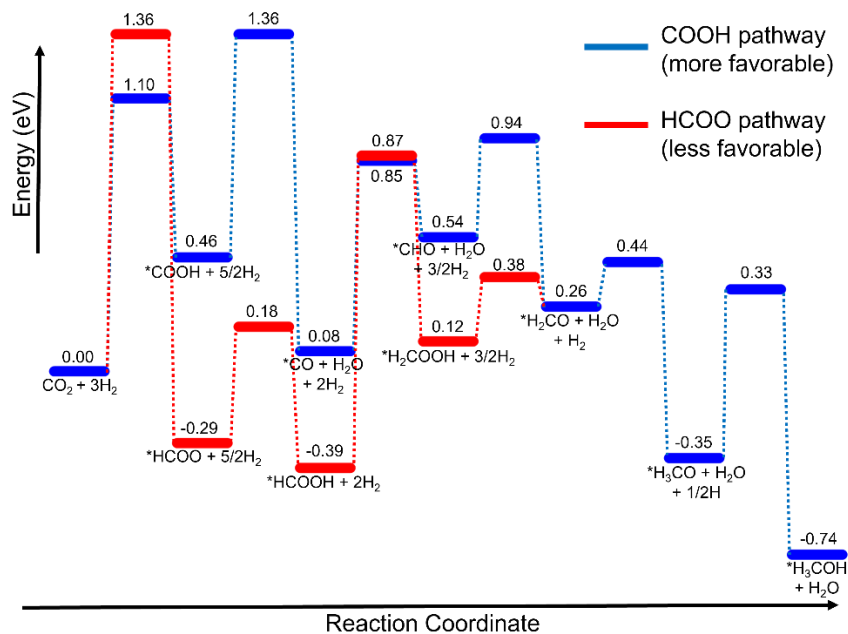


Figure 5.9: Potential energy surface for CO₂ hydrogenation to methanol via different possible pathways on the Cu(111) ML. All the calculated reaction free energies and activation barriers are in eV.

The calculated activation barrier (E_a) for CO₂ hydrogenation to *COOH is 1.03 eV on the surface of Cu nanocluster [79]. These suggests that the activation barrier for *COOH formation on Cu(111) ML is lower compared to that on the bulk Cu(111) surface and very much comparable to the Cu nanocluster based catalyst. Moreover, our calculated activation barrier of *HCOO formation from CO₂ shows that the step is kinetically unfavourable. Furthermore, the *CO₂ hydrogenated product *COOH can be protonated for the dissociation of water and formation of *CO. Side by side, intermediate *HCOO can also be hydrogenated for the formation of

*HCOOH. These steps are reported to be very important for the CH₃OH formation as it is associated with *CO and *HCOOH formation. However, *CO can be desorbed from the catalyst surface, thus inhibiting further hydrogenation on *CO. The *COOH hydrogenation to CO proceeds through a proton–electron transfer step.

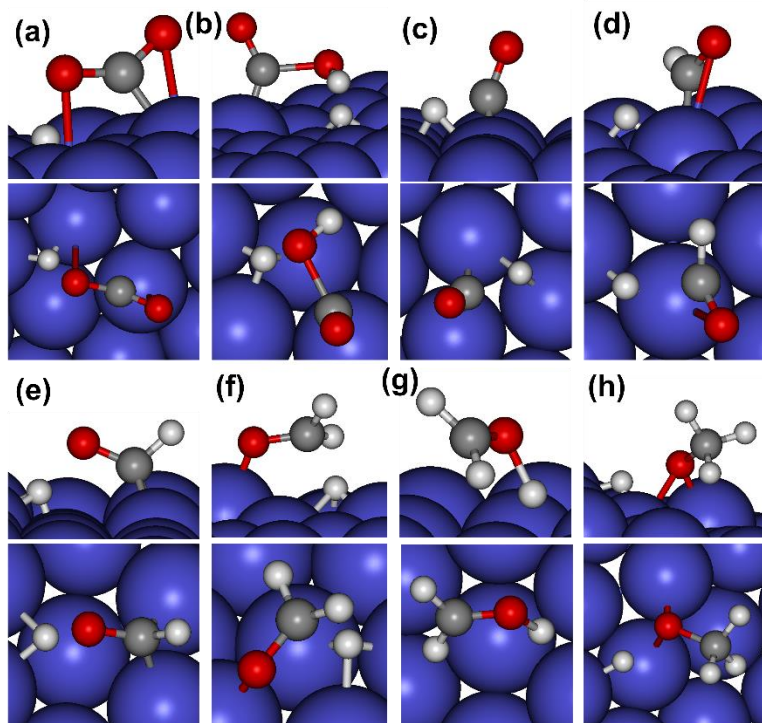


Figure 5.10: Optimized structure of the transition states on the Cu(111) ML: (a) $*\text{CO}_2 + *H \rightarrow *\text{COOH}$, (b) $*\text{COOH} + *H \rightarrow *\text{CO} + *\text{H}_2\text{O}$, (c) $*\text{CO} + *H \rightarrow *\text{CHO}$, (d) $*\text{CHO} + *H \rightarrow *\text{CH}_2\text{O}$, (e) $*\text{CHO} + *H \rightarrow *\text{CHOH}$, (f) $*\text{CH}_2\text{O} + *H \rightarrow *\text{CH}_3\text{O}$, (g) $*\text{CH}_2\text{O} + *H \rightarrow *\text{CH}_2\text{OH}$, and (h) $*\text{CH}_3\text{O} + *H \rightarrow *\text{CH}_3\text{OH}$.

The hydrogenation of *COOH to *CO step is calculated to be a highly favourable on the Cu(111) ML surface compared to that of *HCOOH formation. Furthermore, the hydrogenation of *CO can be initiated at C or O centre, which leads to the formation of *CHO and *COH, respectively. Besides, *HCOOH can also be hydrogenated at the C centre and form *H₂COOH. The intermediate *CHO leads to the formation of CH₃OH while

*COH is responsible for the formation of CH₄. We show that the product selectivity (i.e., CH₃OH vs. CH₄) can be very high on the Cu(111) ML catalyst compared to the previously reported catalysts as the product selectivity depends on the *CO hydrogenated products (*CHO and *COH) [20,23,83,84]. For example, CHO formation favours methanol formation, whereas *COH favours methane.

Table 5.3: All imaginary frequencies of the corresponding transition states.

Steps	Imaginary frequencies (cm ⁻¹)
CO ₂ + *H → *COOH	1269.0
CO ₂ + *H → *HCOO	697.2
*COOH + *H → *CO + *H ₂ O	1042.8
*HCOO + *H → *HCOOH	892.2
*CO + *H → *CHO	837.4
*HCOOH + *H → *H ₂ COOH	1085.4
*CHO + *H → *CH ₂ O	653.0
*HCOOH + *H → *CH ₂ O + H ₂ O	1109.6
*CHO + *H → *CHOH	1125.3
*CH ₂ O + *H → *CH ₃ O	840.4
*CH ₂ O + *H → *CH ₂ OH	1235.4
*CH ₃ O + *H → *CH ₃ OH	881.4

Our calculated reaction free energies (0.46 eV for *CHO and 1.11 eV, for *COH) clearly show that the Cu(111) ML is highly selective towards methanol formation compared to the bulk Cu(111) surface [20,79,82]. We find that *CHO binds weakly compared to the intermediate *COH on the Cu(111) ML surface, which is again different compared to that on the bulk Cu(111) surface. Moreover, to understand the reason behind the weak *CHO and strong *COH adsorption, we have calculated Bader atomic charges of *CHO and *COH. Our calculated Bader charge analysis shows that 0.10 |e| and 0.11 |e| charges are transferred from the Cu(111) ML to the

C atom of *CHO whereas 0.16 |e|, 0.15 |e| and 0.17 |e| charges are transferred from the Cu(111) ML to the C atom of *COH. Therefore, transferred charge from Cu(111) ML is more to the C atom of *COH compared to the *CHO. Hence, adsorption of *COH is more compared to the adsorption of *CHO on the Cu(111) ML. Hence, Cu(111) ML can be highly selective for CO₂ hydrogenation to methanol compared to the bulk Cu(111) catalysts. The previously calculated activation barriers for *CHO formation are 1.06 eV and 1.03 eV on the bulk Cu(111) surface [20,82]. On the other hand, the previously calculated activation barrier on the Cu nanocluster is 0.87 eV [79]. This suggests that the formation of *CHO on the Cu(111) ML surface is more favourable than that on the bulk Cu(111) and Cu nanocluster surface. We have also tried to find out the activation barrier for *COH formation, but it forms *CHO during dimer optimisation. Therefore, it is clear that the reaction will proceed via *CHO intermediate from *CO. In the next step the hydrogenation of *CHO occurs for the formation of *CH₂O and *CHOH based on the hydrogenation at C and O sites of the *CHO. Here, *H₂COOH can also be protonated for the formation of *CH₂O and *H₂O. The reaction free energies suggest that the formation of *CH₂O from *CHO is 0.50 eV more favourable compared to the formation of *CHOH from *CHO. Similarly, formation of *CH₂O from *CHO is 0.42 eV more favourable compared to that from *CH₂OH. All these calculated activation barrier values indicate that the CO₂ hydrogenation reaction favoured through *COOH over *HCOO intermediate. To find out whether the formation of *CHOH and *CH₂O is kinetically favourable from *CHO, we have calculated the activation barrier for hydrogenation of *CHO. Our calculated results show that the formation of *CH₂O is more favourable over formation of *CHOH. Previous report concludes that the formation of *CH₂O requires an activation barrier of 0.50 eV on the bulk Cu (111) surface [82]. Therefore, Cu(111) ML requires lower activation barrier for *CH₂O formation. Previous studies have shown that the *CH₂O intermediate interacts weakly on the bulk Cu(111) surface.

However, our calculated adsorption energy value of $*CH_2O$ show that $*CH_2O$ binds strongly on the Cu(111) ML compared to that on the bulk Cu(111) surface (-0.35 eV on Cu(111) ML and -0.04 eV on bulk Cu(111) surface). Therefore, formation of $*CH_2O$ followed by $*CH_3O$ and $*CH_3OH$ becomes exergonic. To understand the reason behind this, we have calculated Bader atomic charges of $*CH_2O$ intermediate on the bulk Cu(111) surface and ML. Our calculated Bader charge analysis shows that 0.03 |e| and 0.10 |e| amounts of charges are transferred from the Cu(111) surface and Cu(111) ML, respectively to the O atom of the $*CH_2O$. Owing to the excellent nucleophilicity (electron donating ability) of Cu(111) ML, charge transfer from Cu(111) ML to the O atom of $*CH_2O$ is more compared to that on the bulk Cu(111) surface. Hence, $*CH_2O$ binds strongly on the Cu(111) ML surface. Therefore, desorption of such adsorbed intermediate is difficult, whereas formation of other intermediates ($*CH_3O$, $*CH_3OH$ etc.) may be possible from $*CH_2O$. On the other hand, $*CH_2O$ is a very important intermediate for product selectivity. Hence, electron donating ability of Cu(111) ML indicates that Cu(111) ML can be a promising catalyst for selective CO_2 hydrogenation reaction. Moreover, owing to the excellent nucleophilicity of Cu(111) ML, charge transfer from Cu(111) ML to the other intermediates is more in most of the cases, that is intermediates bind strongly on Cu(111) ML compared to that on the bulk Cu(111) surface. Furthermore, the hydrogenation of $*CH_2O$ may lead to the formation of C–H or O–H bond for the formation of $*CH_3O$ and $*CH_2OH$, respectively. The calculated reaction free energies show that $*CH_2O$ prefers to be formed over $*CH_3O$ on the Cu(111) ML surface. The calculated activation barrier for $*CH_3O$ (0.18 eV) formation is comparable with the previously reported activation barrier on the bulk Cu(111) surface (0.21 eV) [82]. Furthermore, we have calculated the reaction free energy of the $*CH_2$ formation from $*CH_2OH$. The calculated reaction free energy for the step is -0.04 eV i.e., the formation of $*CH_2$ from the intermediate $*CH_2OH$ is possible. But due to the less favourable reaction free energy for $*CH_2O$ to

*CH₂OH, formation of *CH₂ may not be preferable. Hence, the formation of *CH₄ may not be favourable on the Cu(111) ML as CH₄ is formed via *CH₂ intermediate. In the last step, hydrogenation of *CH₃O occurs, which leads to the formation of final product that is *CH₃OH via O-H bond formation. The calculated activation barrier for *CH₃OH formation is 0.40 eV lower compared to that on the bulk Cu(111) surface (1.08 eV) [82]. This suggests that the formation of *CH₃OH is more favourable on the Cu(111) ML surface compared to that on the bulk Cu(111) surface. Thus, our calculated reaction free energies and activation barriers values suggest that the Cu(111) ML can be selective for the formation of CH₃OH compared to the bulk catalyst. In this report, we show that rate determining steps (RDS) of CO₂ hydrogenation to *CH₃OH are different from the previous reports on bulk or any other Cu-based catalysts. For example, we find that indirect CO₂ hydrogenation to *COOH can be a RDS for CO₂ hydrogenation to *CH₃OH, which is different from the previous reports, where they show that *CO to *CHO is the only RDS [20,79]. Such finding can be instrumental towards designing of CO₂ hydrogenation based catalysts for methanol production. Our previous report suggests that the *CO to *CHO is the potential limiting step for CO₂ hydrogenation reaction on the Cu nanocluster surface for the formation of CH₃OH, where the required potential is 0.53 V [79]. On the other hand, the bulk Cu(111) surface requires a working potential of 0.71 V for CH₃OH formation [20]. In this case, our considered Cu(111) ML surface requires lower working potential (0.46 V) compared to the earlier reports and thus, is a promising catalyst for selective CO₂ hydrogenation to methanol. To understand this, we have calculated d-band centre energies of the bulk Cu(111) surface and Cu(111) ML. Our calculated d-band centre energies for the bulk Cu(111) surface, and Cu(111) ML are -1.59 and -1.35 eV, respectively. Therefore, Cu(111) ML can bind strongly with the adsorbates, which indicates that it can be better catalyst compared to that of the bulk Cu(111) catalyst. We have also studied whether the ML structure can be easily oxidized compared to the

bulk Cu(111) structure [85]. For this, we have calculated the free energy change for $*+1/2\text{O}_2 \rightarrow *\text{O}$ and the calculated free energy values are -1.76 and -1.75 eV for Cu(111) ML and bulk Cu(111) surface, [86] respectively. This indicates that antioxidant nature of the ML surface is very much comparable to the bulk Cu(111) catalyst. Therefore, Cu(111) ML can also be used for CO_2 hydrogenation reaction.

5.3.1.4. Working Potential for CO_2 Hydrogenation

The working potential is very important for CO_2 hydrogenation reaction as at this potential all the steps of the CO_2 hydrogenation reaction become exergonic. Therefore, the most endergonic elementary step of the reaction is considered as a potential limiting step or working potential of the electrode [87]. In this study, we have considered several mechanistic pathways for CH_3OH formation. Considering $\text{CO}_2 \rightarrow *\text{HCOO} \rightarrow *\text{HCOOH} \rightarrow *\text{H}_2\text{COOH} \rightarrow *\text{CH}_2\text{O} \rightarrow *\text{CH}_3\text{O} \rightarrow *\text{CH}_3\text{OH}$, formation of $*\text{H}_2\text{COOH}$ from $*\text{HCOOH}$ is the most endergonic step with a reaction free energy of 0.51 eV whereas in case of $\text{CO}_2 \rightarrow *\text{COOH} \rightarrow *\text{CO} \rightarrow *\text{CHO} \rightarrow *\text{CH}_2\text{O} \rightarrow *\text{CH}_3\text{O} \rightarrow *\text{CH}_3\text{OH}$, formation of $*\text{COOH}$ from $*\text{CO}_2$ and $*\text{CHO}$ from $*\text{CO}$ are the most endergonic steps with a reaction free energy of 0.46 eV. Therefore, $\text{CO}_2 \rightarrow *\text{COOH} \rightarrow *\text{CO} \rightarrow *\text{CHO} \rightarrow *\text{CH}_2\text{O} \rightarrow *\text{CH}_3\text{O} \rightarrow *\text{CH}_3\text{OH}$ steps are considered to find out working potential of CO_2 hydrogenation to CH_3OH on the Cu(111) ML surface (Figure 5.11). At 0.46 V, all the elementary steps of the CO_2 hydrogenation reaction become thermodynamically favourable. Our calculated adsorption energy values show that most of the considered intermediates bind strongly on the Cu(111) ML compared to the bulk Cu and Cu nanocluster. This may be due to the highly exposed surface of Cu(111) ML compared to the bulk Cu and Cu nanocluster. Our previous report suggests that the $*\text{CO}$ to $*\text{CHO}$ is the potential limiting step for CO_2 hydrogenation reaction on the Cu nanocluster surface for the formation of CH_3OH , where the required potential is 0.53 V [79]. On the other hand, the bulk Cu(111) surface requires a working

potential of 0.71 V for CH₃OH formation [20]. Therefore, our considered Cu(111) ML surface requires lower working potential (0.46 V) compared to the earlier reports and thus, is a promising catalyst for selective CO₂ hydrogenation to methanol.

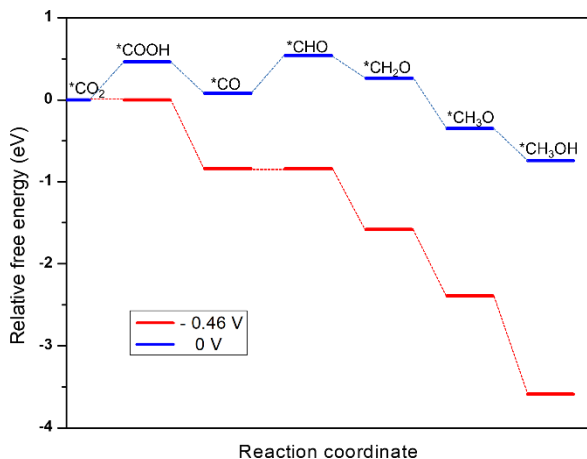
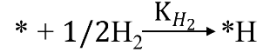
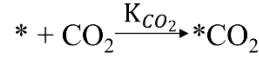


Figure 5.11: Relative reaction free energies and their dependencies on the applied electrode potential.

5.3.1.5. Microkinetic Analysis

From the elementary reaction pathways (Scheme 5.1), it is clear that the various products can be synthesized through CO₂ hydrogenation reaction. Our calculated ΔG gives an idea about the desired product. However, surface coverage, partial pressure of the reactants, and temperature of the reaction cannot be fully understood from the ΔG value. Therefore, we have performed a detailed microkinetic analysis on the basis of our DFT results [88]. In this context, we have calculated forward (k_i) and backward rate (k_{-i}) constants using transition state theory at 500 K as such reaction occurs in the 473-573 K temperature range [27]. We find that adsorption of CO₂ and H₂ are highly exothermic that is CO₂ and H₂ adsorptions can be in equilibrium and K_{eq} can be calculated from $K_{eq} = \exp[-(\Delta E_{ads} - T\Delta S)/k_B T]$. Here, ΔE_{ads} is the adsorption energy of CO₂ and H₂, ΔS is the entropy change of CO₂ and H₂, k_B is Boltzmann's Constant and T is 500 K. The

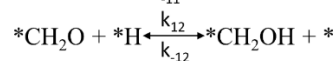
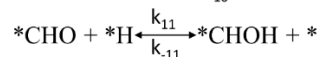
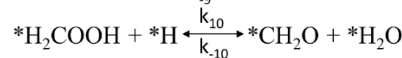
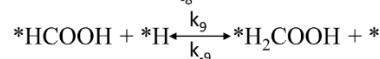
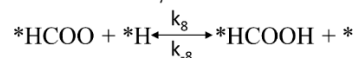
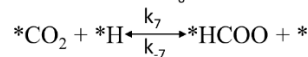
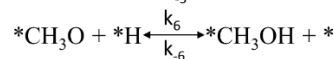
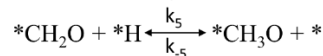
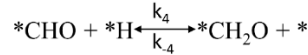
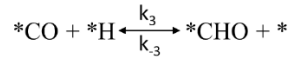
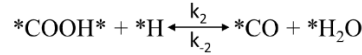
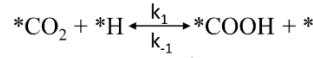
coverage of CO₂ and H₂ can be obtained using the following equations (5.10 and 5.11):



$$\Theta_{\text{CO}_2} = p_{\text{CO}_2} K_{\text{CO}_2} \Theta^* \quad (5.10)$$

$$\Theta_{\text{H}} = p_{\text{H}_2}^{1/2} K_{\text{H}_2} \Theta^* \quad (5.11)$$

We have calculated the rate constants at 500 K (Table 5.4) using transition state theory and the coverage can be obtained from the steady-state approximations.



Now, applying steady state approximation, we get:

$$\frac{d\Theta_{\text{COOH}}}{dt} = k_1 \Theta_{\text{CO}_2} \Theta_{\text{H}} - k_{-1} \Theta_{\text{COOH}} \Theta^* - k_2 \Theta_{\text{COOH}} \Theta_{\text{H}} + k_{-2} \Theta_{\text{CO}} \Theta_{\text{H}_2\text{O}} \quad (5.12)$$

$$\frac{d\Theta_{\text{HCOO}}}{dt} = k_7 \Theta_{\text{CO}_2} \Theta_{\text{H}} - k_{-7} \Theta_{\text{HCOO}} \Theta^* - k_8 \Theta_{\text{HCOO}} \Theta_{\text{H}} + k_{-8} \Theta_{\text{HCOOH}} \Theta^* \quad (5.13)$$

$$\frac{d\Theta_{\text{CO}}}{dt} = k_2 \Theta_{\text{COOH}} \Theta_{\text{H}} - k_{-2} \Theta_{\text{CO}} \Theta_{\text{H}_2\text{O}} - k_3 \Theta_{\text{CO}} \Theta_{\text{H}} + k_{-3} \Theta_{\text{CHO}} \Theta^* \quad (5.14)$$

$$\frac{d\Theta_{\text{HCOOH}}}{dt} = k_8 \Theta_{\text{HCOO}} \Theta_{\text{H}} - k_{-8} \Theta_{\text{HCOOH}} \Theta^* - k_9 \Theta_{\text{HCOOH}} \Theta_{\text{H}} + k_{-9} \Theta_{\text{H}_2\text{COOH}} \Theta^* \quad (5.15)$$

$$\frac{d\theta_{\text{H}_2\text{COOH}}}{dt} = k_9\theta_{\text{HCOOH}}\theta_{\text{H}} - k_{-9}\theta_{\text{H}_2\text{COOH}}\theta^* - k_{10}\theta_{\text{H}_2\text{COOH}}\theta_{\text{H}} + k_{-10}\theta_{\text{CH}_2\text{O}}\theta_{\text{H}_2\text{O}} \quad (5.16)$$

$$\frac{d\theta_{\text{CHO}}}{dt} = k_3\theta_{\text{CO}}\theta_{\text{H}} - k_{-3}\theta_{\text{CHO}}\theta^* - k_4\theta_{\text{CHO}}\theta_{\text{H}} + k_{-4}\theta_{\text{CH}_2\text{O}}\theta^* - k_{11}\theta_{\text{CHO}}\theta_{\text{H}} + k_{-11}\theta_{\text{CHOH}}\theta^* \quad (5.17)$$

$$\frac{d\theta_{\text{CH}_2\text{O}}}{dt} = k_4\theta_{\text{CHO}}\theta_{\text{H}} - k_{-4}\theta_{\text{CH}_2\text{O}}\theta^* - k_5\theta_{\text{CH}_2\text{O}}\theta_{\text{H}} + k_{-5}\theta_{\text{CH}_3\text{O}}\theta^* + k_{10}\theta_{\text{H}_2\text{COOH}}\theta_{\text{H}} - k_{-10}\theta_{\text{CH}_2\text{O}}\theta_{\text{H}_2\text{O}} - k_{12}\theta_{\text{CH}_2\text{O}}\theta_{\text{H}} + k_{-12}\theta_{\text{CH}_2\text{OH}}\theta^* \quad (5.18)$$

$$\frac{d\theta_{\text{CHOH}}}{dt} = k_{11}\theta_{\text{CHO}}\theta_{\text{H}} - k_{-11}\theta_{\text{CHOH}}\theta^* \quad (5.19)$$

$$\frac{d\theta_{\text{CH}_3\text{O}}}{dt} = k_5\theta_{\text{CH}_2\text{O}}\theta_{\text{H}} - k_{-5}\theta_{\text{CH}_3\text{O}}\theta^* - k_6\theta_{\text{CH}_3\text{O}}\theta_{\text{H}} + k_{-6}\theta_{\text{CH}_3\text{OH}}\theta^* \quad (5.20)$$

$$\frac{d\theta_{\text{CH}_2\text{OH}}}{dt} = k_{12}\theta_{\text{CH}_2\text{O}}\theta_{\text{H}} - k_{-12}\theta_{\text{CH}_2\text{OH}}\theta^* \quad (5.21)$$

Now, it is obvious that $\frac{d\theta_{\text{CH}_3\text{O}}}{dt}$ is responsible for CH_3OH , whereas $\frac{d\theta_{\text{CH}_2\text{OH}}}{dt}$ is responsible for CH_2 followed by CH_3 and CH_4 . Therefore, $\theta_{\text{CH}_3\text{O}}$ and $\theta_{\text{CH}_2\text{OH}}$ are highly important for the selectivity of the products (CH_3OH vs. CH_4).

From equation 5.20 and 5.21, we can get:

$$\frac{d\theta_{\text{CH}_3\text{O}}}{dt} = k_5\theta_{\text{CH}_2\text{O}}\theta_{\text{H}} - k_{-5}\theta_{\text{CH}_3\text{O}}\theta^* - k_6\theta_{\text{CH}_3\text{O}}\theta_{\text{H}} + k_{-6}\theta_{\text{CH}_3\text{OH}}\theta^* = 0$$

$$k_5\theta_{\text{CH}_2\text{O}}p_{\text{H}_2}^{1/2}K_{\text{H}_2}\theta^* - k_{-5}\theta_{\text{CH}_3\text{O}}\theta^* - k_6\theta_{\text{CH}_3\text{O}}p_{\text{H}_2}^{1/2}K_{\text{H}_2}\theta^* + k_{-6}\theta_{\text{CH}_3\text{OH}}\theta^* = 0$$

$$k_{-5}\theta_{\text{CH}_3\text{O}} + k_6\theta_{\text{CH}_3\text{O}}p_{\text{H}_2}^{1/2}K_{\text{H}_2} = k_5\theta_{\text{CH}_2\text{O}}p_{\text{H}_2}^{1/2}K_{\text{H}_2} + k_{-6}\theta_{\text{CH}_3\text{OH}}$$

$$\theta_{\text{CH}_3\text{O}} = \frac{k_5\theta_{\text{CH}_2\text{O}}p_{\text{H}_2}^{1/2}K_{\text{H}_2} + k_{-6}\theta_{\text{CH}_3\text{OH}}}{k_{-5} + k_6p_{\text{H}_2}^{1/2}K_{\text{H}_2}} \quad (5.22)$$

Similarly,

$$\frac{d\theta_{\text{CH}_2\text{OH}}}{dt} = k_{12}\theta_{\text{CH}_2\text{O}}\theta_{\text{H}} - k_{-12}\theta_{\text{CH}_2\text{OH}}\theta^* = 0$$

$$\begin{aligned}
k_{12}\theta_{\text{CH}_2\text{O}}p_{\text{H}_2}^{1/2}K_{\text{H}_2}\theta^* - k_{-12}\theta_{\text{CH}_2\text{OH}}\theta^* &= 0 \\
k_{-12}\theta_{\text{CH}_2\text{OH}} &= k_{12}\theta_{\text{CH}_2\text{O}}p_{\text{H}_2}^{1/2}K_{\text{H}_2} \\
\theta_{\text{CH}_2\text{OH}} &= \frac{k_{12}\theta_{\text{CH}_2\text{O}}p_{\text{H}_2}^{1/2}K_{\text{H}_2}}{k_{-12}} \quad (5.23)
\end{aligned}$$

The adsorption of H₂ and CO₂ are exergonic, that is H₂ is the most abundant intermediate in the reaction medium. Our microkinetic analysis also shows that the adsorbed H is the most abundant intermediate in the reaction medium which is produced from H₂. Our calculated rate constant value shows that k₋₆ is less compared to the k₅ (Table 5.4). Therefore, we can neglect k₋₆θ_{CH₃OH}; hence the equation 5.22 will be as follow:

$$\theta_{\text{CH}_3\text{O}} = \frac{k_5\theta_{\text{CH}_2\text{O}}p_{\text{H}_2}^{\frac{1}{2}}K_{\text{H}_2}}{k_{-5} + k_6p_{\text{H}_2}^{\frac{1}{2}}K_{\text{H}_2}} \quad (5.24)$$

The ratio between the coverage of CH₃O and CH₂OH can explain the selectivity of the product.

Therefore,

$$\begin{aligned}
\frac{\theta_{\text{CH}_3\text{O}}}{\theta_{\text{CH}_2\text{OH}}} &= \frac{k_5\theta_{\text{CH}_2\text{O}}p_{\text{H}_2}^{\frac{1}{2}}K_{\text{H}_2}}{k_{-5} + k_6p_{\text{H}_2}^{\frac{1}{2}}K_{\text{H}_2}} \times \frac{k_{-12}}{k_{12}\theta_{\text{CH}_2\text{O}}p_{\text{H}_2}^{1/2}K_{\text{H}_2}} \\
\frac{\theta_{\text{CH}_3\text{O}}}{\theta_{\text{CH}_2\text{OH}}} &= \frac{k_5k_{-12}}{k_{12}(k_{-5} + k_6p_{\text{H}_2}^{\frac{1}{2}}K_{\text{H}_2})} \quad (5.25)
\end{aligned}$$

Here, we would like to find out the role of partial pressure towards the product selectivity. Earlier reports have shown that the *CH₂OH and *CH₃O are the two important intermediates for the selectivity of CO₂ hydrogenated product [89]. Therefore, we would like to understand the role of hydrogen partial pressure (equation 5.25) towards CH₃OH formation. At 500 K, the ratio between *CH₃O and *CH₂OH rate constants (k₅/k₁₂ = 1.52×10¹¹/1.98×10⁸) is ~10³.

Table 5.4: Reaction mechanisms elementary step's reaction free energy

barrier and rate constant. All activation energy barriers are in kcal/mol and rate constants are in $M^{-1}S^{-1}$.

Steps	Barrier (kcal/mol)	Rate constant (500 K)
$*CO_2 + *H = *COOH$	25.4	$k_1 = 8.21E+01$
$*COOH* = *CO_2 + *H$	14.8	$k_{-1} = 3.53E+06$
$*COOH* + *H = *CO + *H_2O$	20.7	$k_2 = 9.31E+03$
$*CO + *H_2O* = *COOH* + *H$	29.5	$k_{-2} = 1.33E+00$
$*CO + *H = *CHO$	17.7	$k_3 = 1.91E+05$
$*CHO = *CO + *H$	7.1	$k_{-3} = 8.21E+09$
$*CHO + *H = *CH_2O$	9.2	$k_4 = 9.91E+08$
$*CH_2O = *CHO + *H$	15.7	$k_{-4} = 1.43E+06$
$*CH_2O + *H = *CH_3O$	4.2	$k_5 = 1.52E+11$
$*CH_3O = *CH_2O + *H$	18.2	$k_{-5} = 1.15E+05$
$*CH_3O + *H = *CH_3OH$	15.7	$k_6 = 1.43E+06$
$*CH_3OH = *CH_3O + *H$	24.7	$k_{-6} = 1.66E+02$
$*CO_2 + *H = *HCOO$	31.4	$k_7 = 1.96E-01$
$*HCOO = *CO_2 + *H$	38.1	$k_{-7} = 2.31E-04$
$*HCOO + *H = *HCOOH$	10.8	$k_8 = 1.98E+08$
$*HCOOH = *HCOO + *H$	13.1	$k_{-8} = 1.96E+07$
$*HCOOH + *H = *H_2COOH$	29.1	$k_9 = 1.98E+00$
$*H_2COOH = *HCOOH + *H$	17.3	$k_{-9} = 2.85E+05$
$*H_2COOH + *H = *CH_2O + *H_2O$	6.0	$k_{10} = 2.48E+10$
$*CH_2O + *H_2O = *H_2COOH + *H$	2.8	$k_{-10} = 6.22E+11$
$*CHO + *H = *CHOH$	13.6	$k_{11} = 1.18E+07$
$*CHOH = *CHO + *H$	8.5	$k_{-11} = 2.01E+09$
$*CH_2O + *H = *CH_2OH$	10.8	$k_{12} = 1.98E+08$
$*CH_2OH = *CH_2O + *H$	12.9	$k_{-12} = 2.39E+07$

Based on our rate constant value, we can say that *CH₃O formation is highly favourable compared to the *CH₂OH. This can be further assessed from the surface coverage study too. Here, surface coverage ratio is inversely proportional to the partial pressure of hydrogen. Different hydrogen partial pressures ($p_{\text{H}_2}^{1/2}$) have been considered to understand the effect of hydrogen partial pressure towards the product selectivity. Our calculated ratios between the coverage of CH₃O and CH₂OH ($\frac{\theta_{\text{CH}_3\text{O}}}{\theta_{\text{CH}_2\text{OH}}}$) are 1.06×10⁵, 2.62×10⁴, 3.08×10³, 6.25×10², 1.25×10², 6.28×10¹, 1.26×10¹, 6.28, 4.19, 3.14, 2.51, 2.09, 1.79, 1.57 and 1.26 for 0.002, 0.02, 0.2, 1, 5, 10, 50, 100, 150, 200, 250, 300, 350, 400 and 500 atmospheres of H₂ partial pressure ($p_{\text{H}_2}^{1/2}$), respectively.

5.3.1.6. Conclusions

Here, Cu(111) ML has been studied for CO₂ hydrogenation reaction. Various possible CO₂ hydrogenation mechanisms and their different adsorption possibilities of intermediates have been considered to understand the activity of Cu ML compared to that on the bulk Cu(111) catalyst. We find that the adsorption energies of different intermediates are relatively higher on the Cu(111) ML surface than that on the bulk Cu(111) surface. Furthermore, our calculated adsorption energies show that *CO binds strongly on the Cu(111) ML surface, which in turn indicates that the CO₂ hydrogenation reaction prefers to proceed for selective hydrogenation. For example, the most important intermediate *CHO binds weakly on the Cu(111) ML surface compared to the *COH. Our calculated reaction free energies show that the formation of *CHO intermediate is 0.65 eV more favourable compared to the formation of *COH intermediate. Hence, the reaction will proceed for selective hydrogenation to CH₃OH via *CHO intermediate over CH₄ formation via *COH intermediate. Our applied potential studies show that the CO₂ hydrogenation to *COOH and *CO hydrogenation to *CHO steps are the two potential-limiting steps for CO₂

hydrogenation. Moreover, the calculated working potential for selective CO₂ hydrogenation to CH₃OH is 0.46 V on the Cu(111) ML surface, which is lower compared to the bulk Cu (0.71 V) and Cu nanocluster (0.53 V) based catalysts. Therefore, our detailed investigations show that the Cu(111) ML can be a highly efficient and selective catalyst for CO₂ hydrogenation to CH₃OH owing to its strong nucleophilic nature compared to the previously studied Cu-based bulk catalysts.

5.3.2. ZnO Based NCs for CO₂ Hydrogenation Reaction

In this section of the thesis, we have discussed the CO₂ hydrogenation reaction in detail using ZnO based NCs.

5.3.2.1. Stability of the NCs

The stability of the considered NC based structures has been explored in various ways. In this context, we have considered the energetic stability of Zn₁₂O₁₂ and Zn₂₄O₂₄ NCs through the calculation of formation and cohesive energies which are listed in Table 5.5.

Table 5.5: Formation and cohesive energies of Zn₁₂O₁₂, Zn₂₄O₂₄ NCs and bulk ZnO. Previously calculated formation energy value for the bulk ZnO is also listed in the parenthesis for comparison [90].

ZnO systems	Formation energy (eV/formula unit)	Cohesive energy (eV/formula unit)
Zn ₁₂ O ₁₂	-1.70	-6.39
Zn ₂₄ O ₂₄	-1.90	-6.59
bulk ZnO	-2.96 (-3.04)	-7.64 (-)

Our calculated formation energy values indicate that the formation of Zn₂₄O₂₄ NC is 0.2 eV more favourable compared to the formation of Zn₁₂O₁₂ NC. Similarly, cohesive energy values also show that the Zn₂₄O₂₄ NC is more stable compared to the Zn₁₂O₁₂ NC. For this reason, we have

considered $\text{Zn}_{24}\text{O}_{24}$ NC for further studies. Moreover, it is noteworthy to mention that the formation energy of the bulk ZnO has been calculated and found to be -2.96 eV/formula unit which is comparable to the earlier report -3.04 eV/formula unit [90]. Therefore, the level of theory used in this study is good enough for further study. Now energetically stable $\text{Zn}_{24}\text{O}_{24}$ NC has been considered for further study. Hereafter, all the possible Zn sites of $\text{Zn}_{24}\text{O}_{24}$ NC have been substituted by the Cu atoms to understand the effect of Cu doping on ZnO for CO_2 hydrogenation reaction. The $\text{Zn}_{24}\text{O}_{24}$ NC has three different Zn sites which have been replaced by Cu atoms (Figure 5.12a-f) and the energetically stable structure has been considered. Here, Figure 5.12a-b, Figure 5.12c-2 and Figure 5.12e-f have been considered as first, second- and third-layer Cu doped structures, respectively.

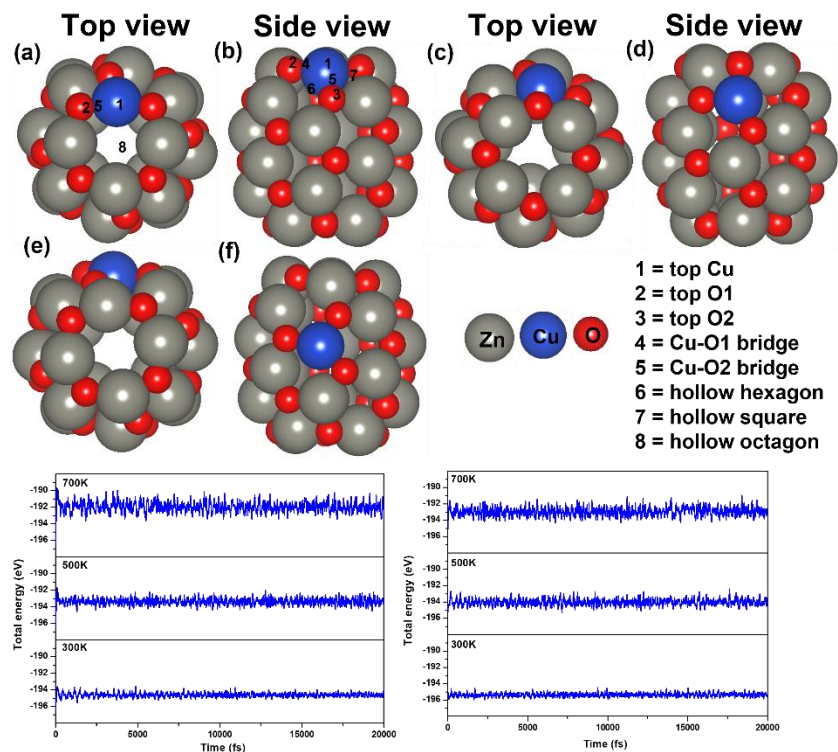


Figure 5.12: Top and side views of considered Cu doped ZnO NCs: (a, b) first layer Cu doped $\text{Zn}_{24}\text{O}_{24}$, (c, d) second layer Cu doped $\text{Zn}_{24}\text{O}_{24}$, (e, f) third layer Cu doped $\text{Zn}_{24}\text{O}_{24}$. (g, h) Ab initio molecular dynamics simulations of (g) ZnO and (h) Cu@ZnO NCs at 300, 500 and 700 K.

We have considered all the three possible Zn sites for Cu doping in the modelled ZnO NC. The calculated total energies show that the Cu doping at the top layer is 0.02 and 0.19 eV more stable compared to the doping in the second- and third layer, respectively. Moreover, we have noticed that the doping of Cu atom in the ZnO NC does not change the skeleton of the nanocage which could be due to the similar atomic radius of Cu and Zn atoms (Cu:1.28 and Zn:1.34 Å). This also could be one of the reasons that Cu/ZnO/Al₂O₃ based catalysts have been one of the best catalysts for such reaction. So, first layer Cu doped ZnO NC has been considered for CO₂ hydrogenation reaction. From here on, Zn₂₄O₂₄ NC and the most stable Cu doped Zn₂₃CuO₂₄ NC have been represented as ZnO NC and Cu@ZnO NC. Furthermore, dynamic stability calculations are performed for ZnO and Cu@ZnO using the phonon calculation as implemented in VASP [70]. Our phonon results show small imaginary frequency up to 9i cm⁻¹ for ZnO NC and up to 7i cm⁻¹ for Cu@ZnO NC. Previous studies have reported that the clusters showing very small imaginary frequencies can be called as a dynamically stable structure [39]. In general, CO₂ hydrogenation reactions are carried out at 473-573 K temperatures [27]. Hence the catalyst must be stable in this temperature range. So, we have performed the thermal stability calculations of ZnO and Cu@ZnO to find out the structural stability at the operational temperature. Ab initio molecular dynamics (AIMD) simulations with Nosé thermostat model have been used to check the thermal stability of the considered NCs [72]. The simulations have been performed with NVT ensemble at temperatures 300 K, 500 K and 700 K, with a time step of 1 femtosecond (fs) for 20 picoseconds (ps). Our simulations show that there are no significant changes in the energy throughout the simulation at 300 K for both the NCs (Figure 5.12g-h). At temperature 500 K and 700 K also, overall energy fluctuation is less for the considered NCs. So, the possibility of interconversion of ZnO and Cu@ZnO NCs into other local minima energy structure is not possible within 300-700 K temperature.

Thus, we can say that ZnO and Cu@ZnO NCs are thermally stable up to 700 K and can be used for the CO₂ hydrogenation reaction.

5.3.2.2. Adsorption of Different Intermediates

The applicability of ZnO and Cu@ZnO NCs has been investigated in detail through the adsorption of different CO₂ hydrogenation reaction intermediates on the NCs. We have considered all the possible adsorption sites on the ZnO NC (Figure 5.2) and also adsorption sites close to the Cu atom on the Cu@ZnO NC (Figure 5.12a-b). We have chosen adsorption sites close to the Cu atom to check the role of single atom catalyst on the catalytic activity. Therefore, all the possible top, bridge and hollow sites of the ZnO NC and Cu@ZnO have been taken into consideration. We could not compare our calculated results with the Cu/ZnO/Al₂O₃ catalyst as the previously reported values are not calculated using the same level of theory. For example, Liu and his co-workers have theoretically investigated CO₂ hydrogenation reaction on Cu/ZnO/Al₂O₃ based catalyst to support their experimental findings. However, they have used the GGA/PW91 level of theory for their theoretical calculations [81]. Therefore, we have compared our results only with the Cu-based catalytic systems which are calculated at GGA/PBE level of theory. Therefore, the adsorption energies of the intermediates on ZnO and Cu@ZnO NCs have been compared with the adsorption energies of the intermediates on bulk Cu(111), hexagonal Cu(111) monolayer (Cu(111) ML), Cu nanocluster and compared our results with the synergistic effects of the Cu/ZnO based catalyst [79,81]. The most stable adsorption patterns of the intermediates on ZnO and Cu@ZnO NCs are given in Figure 5.13-5.14 and their respective adsorption energies are given in Table 5.6. We find that the most stable adsorption sites of the considered intermediates are different on both the NCs. Here, the first intermediate that is CO₂ molecule adsorbs strongly on both the NCs whereas CO₂ interacts weakly on the extensively studied Cu based materials [20,79]. Therefore, the considered NCs can be promising for the activation

of CO₂ molecule such that the following reaction steps are facilitated.

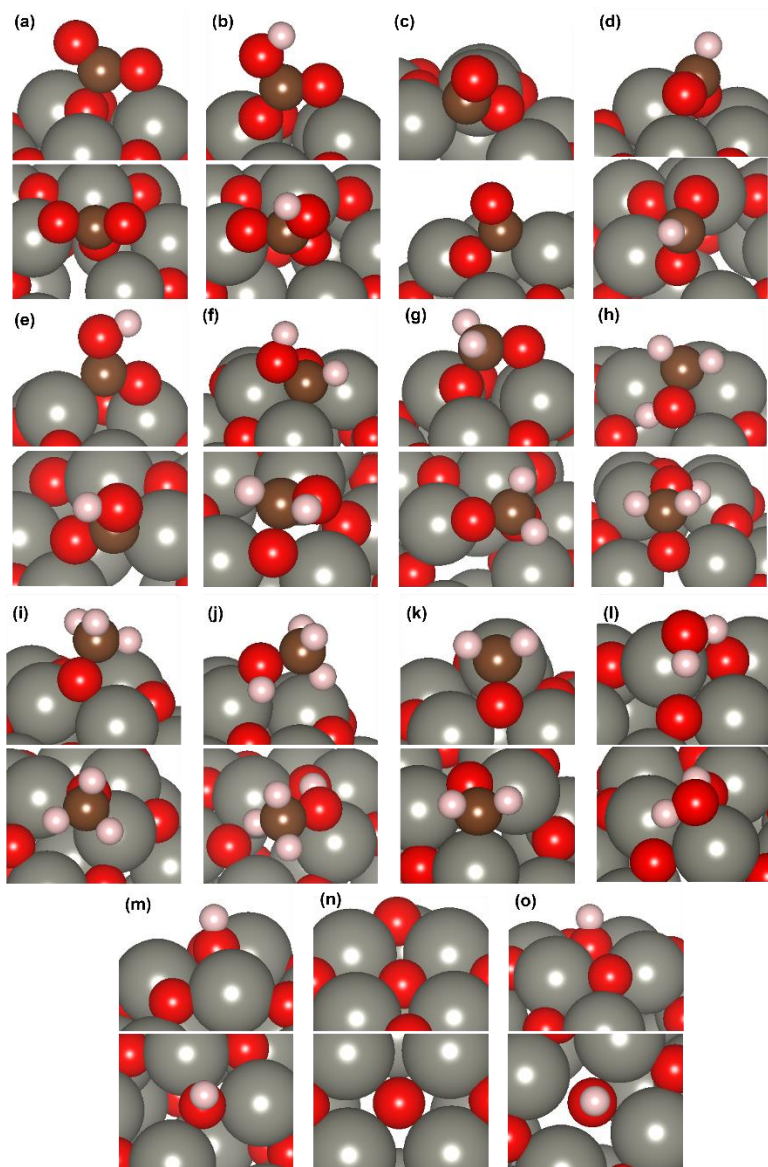


Figure 5.13: Adsorption patterns of the considered CO₂ hydrogenation reaction intermediates on ZnO NC: (a) *CO₂, (b) *COOH, (c) *CO, (d) *CHO, (e) *COH, (f) *CHOH, (g) *CH₂O, (h) *CH₂OH, (i) *CH₃O, (j) *CH₃OH, (k) *CH₂, (l) *H₂O, (m) *H, (n) *O and (o) *OH.

Besides, we find that the calculated adsorption energies of the considered intermediates are higher on the ZnO and Cu@ZnO NCs compared to the bulk Cu(111), Cu(111) ML, Cu nanocluster and Cu-ZnO based catalysts

[79,81].

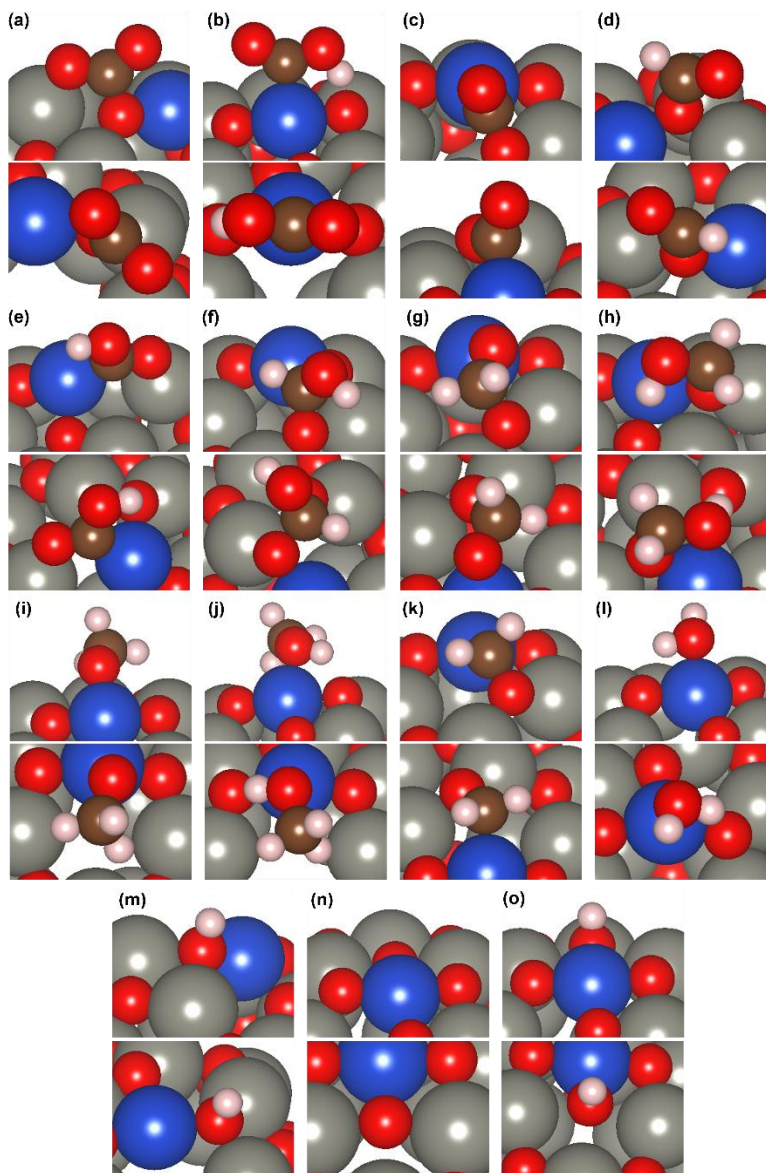


Figure 5.14: Adsorption patterns of the considered CO₂ hydrogenation reaction intermediates on Cu@ZnO NC: (a) *CO₂, (b) *COOH, (c) *CO, (d) *CHO, (e) *COH, (f) *CHOH, (g) *CH₂O, (h) *CH₂OH, (i) *CH₃O, (j) *CH₃OH, (k) *CH₂, (l) *H₂O, (m) *H, (n) *O and (o) *OH.

Table 5.6: Adsorption energies of all the intermediates of CO₂ hydrogenation reaction with their most favourable adsorption sites (in the parenthesis) on ZnO and Cu@ZnO NCs. The adsorption energies of all the

considered adsorbates have been compared with the previous reports on the bulk Cu(111), Cu(111) ML and Cu nanocluster [79].

Adsorbates	ZnO NC	Cu@ZnO NC	Bulk Cu(111)	Cu(111) ML	Cu nanocluster
*CO ₂	-3.27 (e)	-3.83 (2)	not adsorbed	-0.21	-1.14
*COOH	-5.28 (i)	-2.45 (1)	-1.72	-1.84	-2.29
*CO	-2.06 (g)	-2.05 (5)	-0.91	-0.98	-1.10
*CHO	-4.63 (h)	-3.79 (2)	-1.44	-1.57	-2.21
*COH	-6.86 (i)	-7.80 (4)	-2.89	-2.97	-3.10
*CHOH	-4.99 (h)	-6.56 (7)	-2.00	-2.41	-2.35
*CH ₂ O	-3.79 (i)	-3.27 (5)	-0.04	-0.35	-1.66
*CH ₂ OH	-3.48 (h)	-3.28 (2)	-1.24	-1.54	-1.85
*CH ₃ O	-2.77 (l)	-1.92 (1)	-2.41	-2.62	-2.88
*CH ₃ OH	-0.87 (b)	-0.78 (1)	-0.12	-0.39	-0.49
*CH ₂	-5.02 (h)	-4.82 (5)	-3.37	-3.58	-3.87
*H ₂ O	-0.71 (a)	-0.35 (1)	-0.16	-0.33	-0.38
*H	-3.13 (e)	-3.48 (2)	-2.50	-3.52	-2.71

*O	-3.28 (n)	-4.07 (8)	-4.79	-5.26	-5.21
*OH	-2.28 (n)	-3.06 (8)	-3.10	-3.83	-3.84

Furthermore, our calculated adsorption energy values show that the *COOH intermediate adsorbs strongly on the ZnO NC compared to that on the Cu@ZnO NC, whereas other considered intermediates adsorption energies are almost similar on ZnO and Cu@ZnO NCs. To understand the reason behind the strong *COOH adsorption on ZnO NC compared to the Cu@ZnO NC, we have calculated Bader atomic charges which shows that 0.03 |e| charge is transferred from the Zn atom of ZnO NC to the O of *COOH whereas 0.06 |e| charge is gained by the O atom of ZnO NC from the C atom of *COOH. Moreover, there is no charge transfer from Cu of the Cu@ZnO NC to the C atom of *COOH whereas 0.05 |e| charge is gained by the O atom of Cu@ZnO NC from the H atom of *COOH. The amount of transferred charge is more in the case of ZnO NC compared to the Cu@ZnO NC. So, the adsorption energy of *COOH intermediate is more on the ZnO NC compared to the Cu@ZnO NC. However, intermediates *COOH, *CO, *CHO, *CH₂O, *CH₂OH, *CH₃O, *CH₃OH, *CH₂ and *H₂O adsorb strongly on the ZnO NC compared to the Cu@ZnO NC whereas intermediates *CO₂, *COH, *CHOH, *H, *O and *OH adsorb strongly on the Cu@ZnO NC compared to the ZnO NC. On the other hand, the adsorption energies of the products should be less so that it can be removed easily from the catalytic surface for the further steps. In our study, *CH₃OH and *CH₂ are two expected products and the calculated adsorption energy values of *CH₃OH and *CH₂ intermediates are -0.87 eV and -5.02 eV on the ZnO NC whereas -0.78 eV and -4.82 eV are the adsorption energies on the Cu@ZnO NC. As a result, the removal of *CH₃OH is easier compared to the *CH₂.

unfavourable whereas, indirect *CO₂ reduction to *CO is favourable via *COOH intermediate. Therefore, we have studied indirect CO₂ reduction procedure for further study. In the indirect mechanism, *CO₂ interacts with the adsorbed/free H atom for the hydrogenation, which forms *COOH via weakening one of the C=O bond. This hydrogenation step is highly dependent on the proton source and transfer mechanism of the proton. Most of the cases, hydrogen can react via Langmuir-Hinshelwood (LH) or Eley-Rideal (ER) type of mechanism. In general, CO₂ hydrogenation reaction proceeds via Langmuir-Hinshelwood (LH) mechanism [20,79]. Therefore, we have considered Langmuir-Hinshelwood mechanism for the *CO₂ hydrogenation to *COOH.



Our calculated ZPE corrected reaction energies for the formation of *COOH intermediate are lower compared to that on the bulk Cu(111) surface and Cu(111) ML [79]. However, these values are the calculated ZPE corrected reaction energy values suggest that the formation of *COOH is more favourable on the ZnO NC compared to that on the Cu@ZnO NC. In the next step, the *COOH intermediate reacts with *H atom and may form *CO and *H₂O. Earlier reports have suggested that the CH₃OH formation is associated with the *CO intermediate [81]. Sometimes *CO desorbs from the catalytic surface which decreases the overall product formation. In this case, the adsorption energy of *CO is -2.06 and -2.05 eV on ZnO and Cu@ZnO NCs. Therefore, the considered NCs may be promising for CH₃OH formation.



In most of the cases, the formation of *CO from *COOH is a downhill process. In this case, calculated ZPE corrected reaction energies are endergonic compared to the Cu nanocluster and Cu(111) ML-based catalyst for the formation of *CO from *COOH [79]. This may be due to the strong adsorption energy of *COOH on the ZnO NC compared to the Cu@ZnO

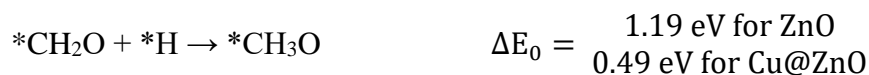
NC which makes the step endergonic for ZnO NC and reversible for Cu@ZnO. Further to this, intermediate *CO can be hydrogenated to *CHO and *COH via hydrogenation at the C and O centres of *CO. Earlier reports have concluded that *CHO forms CH₃OH whereas *COH forms CH₄ [20,23,79]. Hence, this step is highly important for the selective product formation (CH₃OH vs. CH₄).



The calculated ZPE corrected reaction energies are -0.41 and -0.43 eV on ZnO and Cu@ZnO NCs, respectively for the formation of the *CHO intermediate. Side by side, the calculated ZPE corrected reaction energies for *COH formation are 0.37 and -0.22 eV on ZnO and Cu@ZnO NCs, respectively. Therefore, the formation of *CHO intermediate is highly favourable compared to the formation of *COH intermediate on both the NCs. Thus, we have considered *CHO as an important intermediate for our further study. Furthermore, *CHO can be converted to *CH₂O and *CHOH through hydrogenation at the C and O centres of *CHO, respectively.



Our calculated ZPE corrected reaction energies suggest that the formation of *CH₂O is 0.83 and 0.27 eV more favourable compared to the formation of *CHOH on the ZnO and Cu@ZnO NCs, respectively. The calculated ZPE corrected reaction energies reveal that the *CH₂O formation is exergonic on ZnO NC and endergonic on Cu@ZnO NC. Therefore, the reaction will proceed via *CH₂O intermediate which is in agreement with the earlier reports [20,23,79]. Afterwards, *CH₂O can form *CH₂OH and *CH₃O via hydrogenation at the O and C centres of *CH₂O for the formation of O–H and C–H bond, respectively.



In this case, the formation of $*CH_2OH$ is 0.92 and 0.78 eV more favourable on ZnO and Cu@ZnO NCs compared to the $*CH_3O$. Besides, it is also clear that the formation of O–H bond is 0.56 eV more favourable on the ZnO NC compared to the Cu@ZnO NC. Earlier reports have suggested that the formation of $*CH_3O$ is more favourable on the Cu(111) ML, whereas the formation of $*CH_2OH$ is more favourable on the Cu nanocluster [79]. However, our calculated ZPE corrected reaction energies show that the Cu@ZnO NC can be considered as an efficient catalyst for $*CH_2OH$ formation.



These steps are highly important for the formation of selective CO_2 hydrogenated products like CH_3OH and CH_4 . Here CH_2OH may react with the $*H$ at C and O centre of $*CH_2OH$ for the formation of $*CH_3OH$ via hydrogenation at the C centre of $*CH_2OH$ or $*CH_2$ and $*H_2O$ via cleavage of C–O bond, followed by O–H bond formation. If the formation of $*CH_2$ is favourable, the final product will be CH_4 . The calculated ZPE corrected reaction energies show that the formation of $*CH_3OH$ intermediate is highly exergonic on both the NCs and formation of $*CH_2$ intermediate is reversible on the ZnO NC and endergonic on the Cu@ZnO NC. Moreover, the $*CH_3OH$ formation on the ZnO NC is 0.66 eV more favourable compared to the Cu@ZnO NC. This can also be explained by the adsorption energies of $*CH_3OH$ and $*CH_2$. Therefore, the formation of CH_4 is not favourable on both the considered NCs.



In the last step, $*CH_3OH$ desorbs from the catalytic surface and NCs are

regenerated for further catalytic cycle. The calculated ZPE corrected reaction energies for this desorption steps are 0.65 and 0.55 eV on ZnO and Cu@ZnO NCs, respectively. Hence the desorption of *CH₃OH intermediate is 0.10 eV more favourable on the Cu@ZnO NC compared to the ZnO NC. Thus, our calculated ZPE corrected reaction energy values suggest that the ZnO and Cu@ZnO NCs can be considered as a highly active and selective catalyst for CH₃OH formation. Moreover, the CO₂ hydrogenation reaction to CH₃OH on ZnO and Cu@ZnO NCs proceeds via * → *CO₂ → *COOH → *CO → *CHO → *CH₂O → *CH₂OH → *CH₃OH → CH₃OH. Here, *CO₂ + *H → *COOH, *CHO + *H → *CH₂O and *CH₂OH + *H → *CH₃OH steps are favourable on ZnO NC whereas * + CO₂ → *CO₂, *COOH + *H → *CO + *H₂O, *CO + *H → *CHO, *CH₂O + *H → *CH₂OH and *CH₃OH → * + CH₃OH steps are favourable on the Cu@ZnO NC. In this study, we have calculated the Bader atomic charges of Zn and Cu atoms in ZnO and Cu@ZnO NCs to understand the role of the single atom catalyst. Our calculated Bader atomic charges show that the charge on the Zn atom of ZnO NC is +1.16 |e| whereas the charge on the Cu atom of Cu@ZnO NC is +0.90 |e|. Therefore, the Zn atom in the ZnO NC contains highly positive charge compared to the Cu atom in Cu@ZnO. So, this indicates that the single Cu atom is available for the CO₂ reduction reaction compared to the Zn site as Cu can be oxidised easily compared to the Zn atom. Therefore, Cu doping on the ZnO NC increases the catalytic activity, which could be due to the synergistic effects between the metal atoms. Similarly, Wang and his co-workers have reported that the synergetic effects between Cu and zinc oxides are responsible for the efficient CO₂ hydrogenation to methanol [91]. Several other previous studies have shown that synergic effect plays an important role for high methanol production [81,92].

5.3.2.4. Comparison between ZnO and Cu@ZnO NCs

Our considered ZnO and Cu@ZnO NCs can selectively hydrogenate CO₂

for the formation of CH₃OH. In this context, the potential of the most endergonic elementary step of the reaction is the potential limiting step [87]. These potential limiting steps are highly important to find out the applied electrode potential of the reaction. On the basis of the energies obtained above, Figure 5.15 represents the calculated ZPE corrected reaction energies of the intermediates and their dependencies on the applied electrode potential. Considering the electrochemical steps of CO₂ hydrogenation reaction to CH₃OH, the formation of *CO from *COOH is the potential limiting step (Figure 5.15) for ZnO NC and *COOH formation from *CO₂ is the potential limiting step for Cu@ZnO NC.

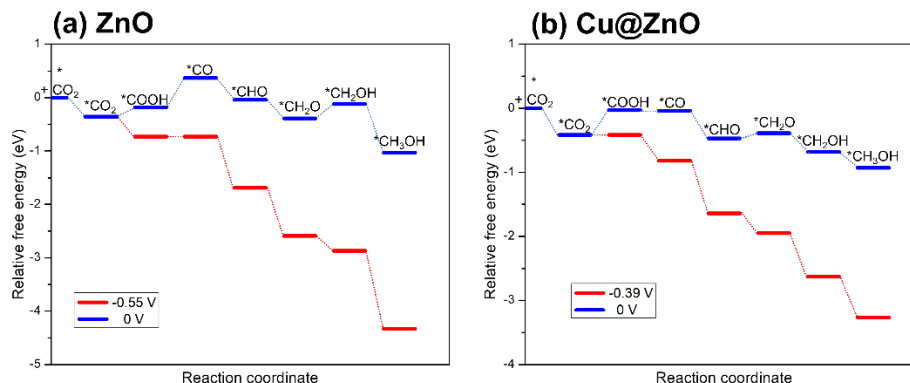


Figure 5.15: Relative CO₂ hydrogenation ZPE corrected reaction energies and their dependencies on the applied electrode potential on (a) ZnO NC, and (b) Cu@ZnO NC.

The calculated ZPE corrected reaction energies of the considered potential limiting steps are 0.55 and 0.39 eV on ZnO and Cu@ZnO NCs, respectively. Therefore, at applied potentials of 0.55 V for ZnO NC and 0.39 V for Cu@ZnO NC, all the CO₂ hydrogenation reaction steps become exergonic/reversible. Hence, Cu@ZnO NC requires 0.16 V less potential compared to the ZnO NC for CH₃OH formation. Our earlier reports have concluded that *CO to *CHO is the potential limiting step for Cu nanocluster with applied electrode potential of 0.53 V whereas *CO₂ to *COOH and *CO to *CHO are the potential limiting steps for Cu(111) ML

with applied electrode potential of 0.46 V [79]. Besides, bulk Cu(111) surface has been reported with 0.71 V applied electrode potential [20]. Therefore, the calculated results show that the Cu@ZnO NC can be a very active catalyst for CH₃OH formation compared to the previously reported bulk Cu(111), Cu nanocluster, Cu(111) ML, ZnO NC and Cu@ZnO NC. Besides, the catalytic performance shown by the ZnO NC is comparable with the Cu nanocluster. In this study, we have considered the intermediate coverages on the ZnO and Cu@ZnO based NCs. We have focused on the coverage study of *COOH and *COH intermediates on ZnO NC, whereas *COH and *CHOH intermediates on Cu@ZnO NC based on their respective adsorption energy values. Here, the average adsorption energies of the important intermediates are calculated at different coverages and the calculated adsorption energies are summarised in Table 5.7.

Table 5.7: Average adsorption energies per ZnO unit on the ZnO and Cu@ZnO NCs.

Coverages (ML) on ZnO NC		Average adsorption energy (eV)	Coverages (ML) on Cu@ZnO NC		Average adsorption energy (eV)
*COOH	0.042	-5.28	*COH	0.042	-7.80
	0.083	-4.72		0.083	-6.83
	0.125	-5.40		0.125	-6.95
	0.167	-5.41		0.167	-4.89
*COH	0.042	-6.86	*CHOH	0.042	-6.56
	0.083	-4.04		0.083	-5.44
	0.125	-5.38		0.125	-4.95
	0.167	-4.02		0.167	-4.84

Our calculated results show that the average adsorption energy value mostly reduces at high coverage. However, the adsorption energy values are still significant at high surface coverage, which indicates the catalytic activity

of the NCs may not change significantly due to surface coverages. The skeleton of the NCs also remain same even at high surface coverage that is there are no surface reconstruction. This indicates that the attraction between Zn and O atoms is quite strong in the NC for the CO₂ hydrogenation reaction even at high surface coverage. Therefore, the NCs can be used as an active catalyst for CO₂ hydrogenation reaction even at high surface coverage.

5.3.2.5. Conclusions

In conclusion, DFT calculations have been performed for the CO₂ hydrogenation reaction to CH₃OH on ZnO and Cu@ZnO NCs. Different adsorption possibilities of all the considered intermediates and various possible reaction pathways have been considered to understand the catalytic activity of ZnO and Cu@ZnO NCs. Our calculated adsorption energy values show that the considered intermediates bind strongly on both the NCs. However, intermediate *COOH binds strongly on ZnO NC compared to that on the Cu@ZnO NC. Moreover, *CHO formation is favourable over *COH on both the considered NCs for selective CO₂ hydrogenation to CH₃OH via *CHO intermediate. Our calculated ZPE corrected reaction energy values show that the *CHO formation is 0.78 and 0.21 eV more favourable over *COH on ZnO and Cu@ZnO NCs, respectively. Hence, the catalysts are selective for CH₃OH formation. Furthermore, our considered reaction mechanisms show that the *CO₂ hydrogenation to *COOH is the potential limiting step for ZnO NC whereas formation of *CO from *COOH is the potential limiting step for Cu@ZnO NC. Here, the calculated applied electrode potential to make all the steps exergonic and/or reversible are 0.55 and 0.39 V for ZnO and Cu@ZnO NCs, respectively which is lower compared to earlier Cu based catalysts. Moreover, increasing the surface coverage of the important intermediates on the ZnO NC surface increase the applied potential of the reaction. However, the applied potential values do not increase to a prohibitive range with respect to the surface coverage.

Therefore, our detailed mechanistic study shows that the ZnO and Cu@ZnO NCs can be efficient and selective catalyst for the CO₂ hydrogenation reaction to CH₃OH. Moreover, Cu@ZnO NC calculated to be more promising catalyst compared to the ZnO NC.

5.4. References

1. Kuhl K.P., Cave E.R., Abram D.N., Jaramillo T.F. (2012), New Insights into the Electrochemical Reduction of Carbon Dioxide on Metallic Copper Surfaces, *Energy Environ. Sci.*, 5, 7050-7059 (DOI: 10.1039/C2EE21234J).
2. Olah G.A., Prakash G.K.S., Goepfert A. (2011), Anthropogenic Chemical Carbon Cycle for a Sustainable Future, *J. Am. Chem. Soc.*, 133, 12881–12898 (DOI: 10.1021/ja202642y).
3. Song Q.-W., Zhou Z.-H., He L.-N. (2017), Efficient, Selective and Sustainable Catalysis of Carbon Dioxide, *Green Chem.*, 19, 3707–3728 (DOI: 10.1039/C7GC00199A).
4. Baiker A. (2000), Utilization of Carbon Dioxide in Heterogeneous Catalytic Synthesis, *Appl. Organomet. Chem.*, 14, 751–762 (DOI: 10.1002/1099-0739(200012)14:12<751::AID-AOC85>3.0.CO;2-J).
5. Rosen B.A., Salehi-Khojin A., Thorson M.R., Zhu W., Whipple D.T., Kenis P.J.A., Masel R.I. (2011), Ionic Liquid-Mediated Selective Conversion of CO₂ to CO at Low Overpotentials, *Science*, 334, 643–644 (DOI: 10.1126/science.1209786).
6. Kuhl K.P., Hatsukade T., Cave E.R., Abram D.N., Kibsgaard J., Jaramillo T.F. (2014), Electrocatalytic Conversion of Carbon Dioxide to Methane and Methanol on Transition Metal Surfaces, *J. Am. Chem. Soc.*, 136, 14107–14113 (DOI: 10.1021/ja505791r).
7. Hori Y., Kikuchi K., Suzuki S. (1985), Production of CO and CH₄ in Electrochemical Reduction of CO₂ at Metal Electrodes in Aqueous Hydrogencarbonate Solution, *Chem. Lett.*, 1695–1698 (DOI: 10.1246/cl.1985.1695)

8. Lee C.W., Hong J.S., Yang K.D., Jin K., Lee J.H., Ahn H.-Y., Seo H., Sung N.-E., Nam K.T. (2018), Selective Electrochemical Production of Formate from Carbon Dioxide with Bismuth-Based Catalysts in an Aqueous Electrolyte, *ACS Catal.*, 8, 931–937 (DOI: 10.1021/acscatal.7b03242)
9. Xiaoding X., Moulijn J.A. (1996), Mitigation of CO₂ by Chemical Conversion: Plausible Chemical Reactions and Promising Products, *Energy Fuels*, 10, 305–325 (DOI: 10.1021/ef9501511)
10. Torrente-Murciano L., Mattia D., Jones M.D., Plucinski P.K. (2014), Formation of Hydrocarbons via CO₂ Hydrogenation – A Thermodynamic Study, *J. CO₂ Util.*, 6, 34–39 (DOI: 10.1016/j.jcou.2014.03.002)
11. Kar S., Sen R., Goeppert A., Prakash G.K.S. (2018), Integrative CO₂ Capture and Hydrogenation to Methanol with Reusable Catalyst and Amine: Toward a Carbon Neutral Methanol Economy, *J. Am. Chem. Soc.*, 140, 1580–1583 (DOI: 10.1021/jacs.7b12183)
12. Mandal S.C., Rawat K.S., Nandi S., Pathak B. (2019), Theoretical insights into CO₂ hydrogenation to methanol by a Mn–PNP complex, *Catal. Sci. Technol.*, 9, 1867–1878 (DOI: 10.1039/C9CY00114J)
13. Kothandaraman J., Goeppert A., Czaun M., Olah G.A., Prakash G.K.S. (2016), Conversion of CO₂ from Air into Methanol Using a Polyamine and a Homogeneous Ruthenium Catalyst, *J. Am. Chem. Soc.*, 138, 778–781 (DOI: 10.1021/jacs.5b12354)
14. Kar S., Goeppert A., Kothandaraman J., Prakash G.K.S. (2017), Manganese-Catalyzed Sequential Hydrogenation of CO₂ to Methanol via Formamide, *ACS Catal.*, 7, 6347–6351 (DOI: 10.1021/acscatal.7b02066)
15. Lam E., Larmier K., Wolf P., Tada S., Safonova O.V., Copéret C. (2018), Isolated Zr Surface Sites on Silica Promote Hydrogenation of CO₂ to CH₃OH in Supported Cu Catalysts, *J. Am. Chem. Soc.*, 140, 10530–10535 (DOI: 10.1021/jacs.8b05595)

16. Kattel S., Yan B., Yang Y., Chen J.G., Liu P. (2016), Optimizing Binding Energies of Key Intermediates for CO₂ Hydrogenation to Methanol over Oxide-Supported Copper, *J. Am. Chem. Soc.*, 138, 12440–12450 (DOI: 10.1021/jacs.6b05791)
17. Liu C., Yang B., Tyo E., Seifert S., DeBartolo J., von Issendorff B., Zapol P., Vajda S., Curtiss L.A. (2015), Carbon Dioxide Conversion to Methanol over Size-Selected Cu₄ Clusters at Low Pressures. *J. Am. Chem. Soc.*, 137, 8676–8679 (DOI: 10.1021/jacs.5b03668)
18. Tada S., Kayamori S., Honma T., Kamei H., Nariyuki A., Kon K., Toyao T., Shimizu K., Satokawa S. (2018), Design of Interfacial Sites between Cu and Amorphous ZrO₂ Dedicated to CO₂ -to-Methanol Hydrogenation, *ACS Catal.*, 8, 7809–7819 (DOI: 10.1021/acscatal.8b01396)
19. Nie X., Jiang X., Wang H., Luo W., Janik M.J., Chen Y., Guo X., Song C. (2018), Mechanistic Understanding of Alloy Effect and Water Promotion for Pd-Cu Bimetallic Catalysts in CO₂ Hydrogenation to Methanol, *ACS Catal.*, 8, 4873–4892 (DOI: 10.1021/acscatal.7b04150)
20. Nie X., Luo W., Janik M.J., Asthagiri A. (2014), Reaction Mechanisms of CO₂ Electrochemical Reduction on Cu(111) Determined with Density Functional Theory, *J. Catal.*, 312, 108–122 (DOI: 10.1016/j.jcat.2014.01.013)
21. Wu P., Yang B. (2017), Significance of Surface Formate Coverage on the Reaction Kinetics of Methanol Synthesis from CO₂ Hydrogenation over Cu, *ACS Catal.*, 7, 7187–7195 (DOI: 10.1021/acscatal.7b01910)
22. Ro I., Liu Y., Ball M.R., Jackson D.H.K., Chada J.P., Sener C., Kuech T.F., Madon R.J., Huber G.W., Dumesic J.A. (2016), Role of the Cu-ZrO₂ Interfacial Sites for Conversion of Ethanol to Ethyl Acetate and Synthesis of Methanol from CO₂ and H₂, *ACS Catal.*, 6, 7040–7050 (DOI:10.1021/ACSCATAL.6B01805)

23. Nie X., Esopi M.R., Janik M.J., Asthagiri A. (2013), Selectivity of CO₂ Reduction on Copper Electrodes: The Role of the Kinetics of Elementary Steps, *Angew. Chem. Int. Ed.*, 52, 2459–2462 (DOI: 10.1002/anie.201208320)
24. Bahruji H., Bowker M., Jones W., Hayward J., Ruiz Esquiús J., Morgan D.J., Hutchings G.J. (2017), PdZn Catalysts for CO₂ Hydrogenation to Methanol Using Chemical Vapour Impregnation (CVI), *Faraday Discuss.*, 197, 309–324 (DOI: 10.1039/C6FD00189K)
25. Tuci G., Rossin A., Luconi L., Pham-Huu C., Cicchi S., Ba H., Giambastiani G. (2017), Pyridine-Decorated Carbon Nanotubes as a Metal-Free Heterogeneous Catalyst for Mild CO₂ Reduction to Methanol with Hydroboranes, *Catal. Sci. Technol.*, 7, 5833–5837 (DOI: 10.1039/C7CY01772C)
26. Hussain J., Skúlason E., Jónsson H. (2015), Computational Study of Electrochemical CO₂ Reduction at Transition Metal Electrodes, *Procedia Comput. Sci.*, 51, 1865–1871
27. Waugh K.C. (1992), Methanol Synthesis, *Catal. Today*, 15, 51-75 (DOI: 10.1016/0920-5861(92)80122-4)
28. Chinchén G.C., Waugh K.C. (1986), The Chemical State of Copper during Methanol Synthesis, *J. Catal.*, 97, 280-283 (DOI: 10.1016/0021-9517(86)90063-1)
29. Chinchén G.C., Waugh K.C., Whan D.A. (1986), The Activity and State of the Copper Surface in Methanol Synthesis Catalysts, *Appl. Catal.*, 25, 101–107 (DOI: 10.1016/S0166-9834(00)81226-9)
30. Grabow L.C., Mavrikakis M. (2011), Mechanism of Methanol Synthesis on Cu through CO₂ and CO Hydrogenation, *ACS Catal.*, 1, 365–384 (DOI: 10.1021/cs200055d)
31. Behrens M. (2014), Heterogeneous Catalysis of CO₂ Conversion to Methanol on Copper Surfaces, *Angew. Chem. Int. Ed.*, 53, 12022–12024 (DOI: 10.1002/anie.201409282)

32. Pan F., Zhao H., Deng W., Feng X., Li Y. (2018), A Novel N,Fe-Decorated Carbon Nanotube/Carbon Nanosheet Architecture for Efficient CO₂ Reduction, *Electrochim. Acta*, 273, 154–161 (DOI:10.1016/J.ELECTACTA.2018.04.047)
33. Chai G.-L., Guo Z.-X. (2016), Highly Effective Sites and Selectivity of Nitrogen-Doped Graphene/CNT Catalysts for CO₂ Electrochemical Reduction, *Chem. Sci.*, 7, 1268–1275 (DOI: 10.1039/C5SC03695J)
34. Li P., Wang F., Wei S., Lia X., Zhou Y. (2017), Mechanistic insights into CO₂ reduction on Cu/Mo-loaded two-dimensional g-C₃N₄(001), *Phys. Chem. Chem. Phys.*, 19, 4405—4410 (DOI: 10.1039/C6CP08409E)
35. Behrens M., Studt F., Kasatkin I., Kuhl S., Havecker M., Abild-Pedersen F., Zander S., Girgsdies F., Kurr P., Knief B.-L., Tovar M., Fischer R.W., Nørskov J.K., Schlögl R. (2012), The Active Site of Methanol Synthesis over Cu/ZnO/Al₂O₃ Industrial Catalysts, *Science*, 336, 893–897 (DOI: 10.1126/science.1219831)
36. Tsai C.-H., Chen S.-Y., Song J.-M., Chen I.-G., Lee H.-Y. (2013), Thermal Stability of Cu@Ag Core–Shell Nanoparticles, *Corros. Sci.*, 74, 123–129 (DOI: 10.1016/j.corsci.2013.04.032)
37. Han N., Wang Y., Yang H., Deng J., Wu J., Li Y., Li Y. (2018), Ultrathin Bismuth Nanosheets from in Situ Topotactic Transformation for Selective Electrocatalytic CO₂ Reduction to Formate, *Nat. Commun.*, 9, 1320–1328 (DOI: 10.1038/s41467-018-03712-z)
38. Saleem F., Zhang Z., Xu B., Xu X., He P., Wang X. (2013), Ultrathin Pt–Cu Nanosheets and Nanocones, *J. Am. Chem. Soc.*, 135, 18304–18307 (DOI: 10.1021/ja4101968)
39. Mahata A., Garg P., Rawat K.S., Bhauriyal P., Pathak B. (2017), A Free-Standing Platinum Monolayer as an Efficient and Selective

- Catalyst for the Oxygen Reduction Reaction, *J. Mater. Chem. A*, 5, 5303–5313 (DOI: 10.1039/C7TA00685C)
40. Mahata A., Rawat K.S., Choudhuri I., Pathak B. (2016), Single-Layered Platinum Nanocage: A Highly Selective and Efficient Catalyst for Fuel Cells, *J. Mater. Chem. A*, 4, 12756–12767 (DOI: 10.1039/C6TA03245A)
 41. Gawande M.B., Goswami A., Felpin F.-X., Asefa T., Huang X., Silva R., Zou X., Zboril R., Varma R.S. (2016), Cu and Cu-Based Nanoparticles: Synthesis and Applications in Catalysis, *Chem. Rev.*, 116, 3722–3811 (DOI: 10.1021/acs.chemrev.5b00482)
 42. Ghosh R., Sahoo A.K., Ghosh S.S., Paul A., Chattopadhyay A. (2014), Blue-Emitting Copper Nanoclusters Synthesized in the Presence of Lysozyme as Candidates for Cell Labeling, *ACS Appl. Mater. Interfaces*, 6, 3822–3828 (DOI: 10.1021/am500040t)
 43. Yang L.-M., Frauenheim T., Ganz E. (2016), Properties of the Free-Standing Two-Dimensional Copper Monolayer, *J. Nanomater.*, 1–6 (DOI: 10.1155/2016/8429510)
 44. Back S., Lim J., Kim N.-Y., Kim Y.-H., Jung Y. (2017), Single-atom catalysts for CO₂ electroreduction with significant activity and selectivity improvements, *Chem. Sci.*, 8, 1090–1096 (DOI: 10.1039/C6SC03911A).
 45. Zhao Z., Lu G. (2019), Cu-Based Single-Atom Catalysts Boost Electroreduction of CO₂ to CH₃OH: First-Principles Predictions, *J. Phys. Chem. C*, 123, 4380–4387 (DOI: 10.1021/acs.jpcc.8b12449).
 46. Nakano H., Nakamura I., Fujitani T., Nakamura J. (2001), Structure-Dependent Kinetics for Synthesis and Decomposition of Formate Species over Cu(111) and Cu(110) Model Catalysts, *J. Phys. Chem. B*, 105, 1355–1365 (DOI: 10.1021/jp002644z).
 47. Nakamura I., Nakano H., Fujitani T., Uchijima T., Nakamura J. (1999), Growth kinetics of GaN and effects of flux ratio on the properties of GaN films grown by plasma-assisted molecular beam

- epitaxy, *J. Vac. Sci. Technol. A*, 17, 1592–1595 (DOI: 10.1116/1.581975)
48. Wang Z.L. (2004), Nanostructures of zinc oxide, *Mater. Today*, 7, 26-33 (DOI: 10.1016/S1369-7021(04)00286-X)
 49. Özgür Ü., Alivov Y.I., Liu C., Teke A., Reshchikov M.A., Doğan S., Avrutin V., Cho S.-J., Morkoç H. (2005), A comprehensive review of ZnO materials and devices, *J. Appl. Phys.*, 98, 041301-103 (DOI: 10.1063/1.1992666)
 50. Dent A.L., Kokes R.J. (1969), Hydrogenation of ethylene by zinc oxide. I. Role of slow hydrogen chemisorption, *J. Phys. Chem.*, 73, 3772–3780 (DOI: 10.1021/j100845a035)
 51. Liu X., Ye L., Liu S., Li Y., Ji X. (2016), Photocatalytic Reduction of CO₂ by ZnO Micro/nanomaterials with Different Morphologies and Ratios of {0001} Facets, *Sci. Rep.*, 6, 38474 (DOI: 10.1038/srep38474)
 52. Wu S., Yuan N., Xu H., Wang X., Schelly Z.A. (2006), Synthesis and bandgap oscillation of uncapped, ZnO clusters by electroporation of vesicles, *Nanotechnology*, 17, 4713–4718 (DOI: 10.1088/0957-4484/17/18/031)
 53. Dmytruk A., Dmitruk I., Shynkarenko Y., Belosludovc R., Kasuyad A. (2017), ZnO nested shell magic clusters as tetrapod nuclei, *RSC Adv.*, 7, 21933–21942 (DOI: 10.1039/C7RA01610G)
 54. Zhang S., Zhang Y., Huang S., Liu H., Wang P., Tian H. (2011), Theoretical investigation of growth, stability, and electronic properties of beaded ZnO nanoclusters, *J. Mater. Chem.*, 21, 16905–16910 (DOI: 10.1039/C1JM12061A)
 55. Blochl P.E. (1994), Projector augmented-wave method, *Phy. Rev. B*, 50, 17953 (DOI: 10.1103/PhysRevB.50.17953)
 56. Kresse G., Joubert D. (1999), From Ultrasoft Pseudopotentials to the Projector Augmented-Wave Method, *Phys. Rev. B*, 59, 1758–1775 (DOI: 10.1103/PhysRevB.59.1758)

57. Kresse G., Furthmüller J. (1996), Efficient Iterative Schemes for Ab Initio Total-Energy Calculations Using a Plane-Wave Basis Set, *Phys. Rev. B*, 54, 11169–11186 (DOI: 10.1103/PhysRevB.54.11169)
58. Perdew J.P., Burke K., Ernzerhof M. (1996), Generalized gradient approximation made simple, *Phys. Rev. Lett.*, 77, 3865-3868. (DOI: 10.1103/PhysRevLett.77.3865)
59. Perdew J.P., Burke K., Ernzerhof M. (1997), Generalized Gradient Approximation Made Simple [*Phys. Rev. Lett.* 77, 3865 (1996)]. *Phys. Rev. Lett.*, 78, 1396–1396 (DOI: 10.1103/PhysRevLett.78.1396)
60. Grimme S., Antony J., Ehrlich S., Krieg H. (2010), A consistent and accurate ab initio parametrization of density functional dispersion correction (DFT-D) for the 94 elements H-Pu, *J. Chem. Phys.*, 132, 154104 (DOI: 10.1063/1.3382344)
61. Nørskov J.K., Rossmeisl J., Logadottir A., Lindqvist L., Kitchin J. R., Bligaard T., Jónsson H. (2004), Origin of the Overpotential for Oxygen Reduction at a Fuel-Cell Cathode, *J. Phys. Chem. B*, 108, 17886–17892 (DOI: 10.1021/jp047349j)
62. Sanville E., Kenny S.D., Smith R., Henkelman G. (2007), Improved grid-based algorithm for Bader charge allocation, *J. Comput. Chem.*, 28, 899– 908 (DOI: 10.1002/jcc.20575)
63. McQuarrie D.A. (1973) *Statistical Mechanics*, Harper & Row
64. Henkelman G., Uberuaga B.P., Jónsson H. (2000), A Climbing Image Nudged Elastic Band Method for Finding Saddle Points and Minimum Energy Paths. *J. Chem. Phys.*, 113, 9901–9904 (DOI: 10.1063/1.1329672)
65. Henkelman G., Jónsson H. (1999), A Dimer Method for Finding Saddle Points on High Dimensional Potential Surfaces Using Only First Derivatives, *J. Chem. Phys.*, 111, 7010–7022 (DOI: 10.1063/1.480097)

66. Tang W., Sanville E., Henkelman G. (2009), A grid-based Bader analysis algorithm without lattice bias, *J. Phys.: Condens. Matter*, 21, 084204 (DOI: 10.1088/0953-8984/21/8/084204)
67. Sanville E., Kenny S.D., Smith R., Henkelman G. (2007), Improved grid-based algorithm for Bader charge allocation, *J. Comput. Chem.*, 28, 899-908 (DOI: 10.1002/jcc.20575)
68. Garg P., Kumar S., Choudhuri I., Mahata A., Pathak B. (2016), Hexagonal Planar CdS Monolayer Sheet for Visible Light Photocatalysis, *J. Phys. Chem. C*, 120, 7052–7060 (DOI: 10.1021/acs.jpcc.6b01622)
69. Feibelman P.J. (1999), First-Principles Step- and Kink-Formation Energies on Cu(111), *Phys. Rev. B*, 60, 11118–11122 (DOI: 10.1103/PhysRevB.60.11118)
70. Baroni S., Giannozzi P., Testa A. (1987), Green's-Function Approach to Linear Response in Solids, *Phys. Rev. Lett.*, 58, 1861–1864 (DOI: 10.1103/PhysRevLett.58.1861)
71. Togo A., Oba F., Tanaka I. (2008), First-Principles Calculations of the Ferroelastic Transition between Rutile-Type and CaCl₂-Type SiO₂ at High Pressures, *Phys. Rev. B*, 78, 134106-9 (DOI: 10.1103/PhysRevB.78.134106)
72. Nosé S. (1994), A unified formulation of the constant temperature molecular dynamics methods, *J. Chem. Phys.*, 81, 511–519 (DOI: 10.1063/1.447334)
73. Zhang J., Gong X., Xu B., Xia Y., Yin J., Liu Z. (2014), Half-metallicity in graphitic C₃N₄ nanoribbons: An ab initio study, *Phys. Status Solidi B*, 251, 1386-1392 (DOI: 10.1002/pssb.201451110)
74. Zhang S., Zhou J., Wang Q., Chen X., Kawazoe Y., Jena P. (2015), Penta-graphene: A new carbon allotrope, *Proc. Natl. Acad. Sci. U. S. A.*, 112, 2372-2377 (DOI: 10.1073/pnas.1416591112)
75. Mannix A.J., Zhou X., Kiraly B. Wood J. D., Alducin D., Myers B. D., Liu X., Fisher B.L., Santiago U., Guest J.R., Yacaman M.J.,

- Ponce A., Oganov A.R., Hersam M.C., Guisinger N.P. (2015), Synthesis of borophenes: Anisotropic, two-dimensional boron polymorphs, *Science*, 350, 1513-1516 (DOI: 10.1126/science.aad1080)
76. Lee C., Wei X., Kysar J. W., Hone J. (2008), Measurement of the Elastic Properties and Intrinsic Strength of Monolayer Graphene, *Science*, 321, 385-388 (DOI: 10.1126/science.1157996)
77. Tao L., Yangy C., Wu L., Han L., Songz Y., Wangz S., Lu P. (2016), Tension-induced mechanical properties of stanine, *Mod. Phys. Lett. B*, 30, 1650146 (DOI: 10.1142/S0217984916501463)
78. Politano A., Chiarello G. (2015), Probing the Young's modulus and Poisson's ratio in graphene/metal interfaces and graphite: a comparative study, *Nano Research*, 8, 1847–1856 (DOI: 10.1007/s12274-014-0691-9)
79. Rawat K.S., Mahata A., Pathak B. (2017), Thermochemical and Electrochemical CO₂ Reduction on Octahedral Cu Nanocluster: Role of Solvent towards Product Selectivity, *J. Catal.*, 349, 118–127 (DOI: 10.1016/j.jcat.2017.03.011)
80. Hadenfeldt S., Benndorf C., Stricker A., Töwe M. (1996), Adsorption of CO₂ on K-Promoted Cu(111) Surfaces, *Surf. Sci.*, 352–354, 295–299 (DOI: 10.1016/0039-6028(95)01150-1)
81. Kattel S., Ramírez P.J., Chen J.G., Rodriguez J.A., Liu P. (2017), Active sites for CO₂ hydrogenation to methanol on Cu/ZnO catalysts, *Science*, 355, 1296–1299 (DOI: 10.1126/science.aal3573)
82. Zhang X., Liu J.-X., Zijlstra B., Filot I.A.W., Zhou Z., Sun S., Hensen E.J.M. (2018), Optimum Cu Nanoparticle Catalysts for CO₂ Hydrogenation towards Methanol, *Nano Energy*, 43, 200–209 (DOI: 10.1016/j.nanoen.2017.11.021)
83. Luo W., Nie X., Janik M.J., Asthagiri A. (2016), Facet Dependence of CO₂ Reduction Paths on Cu Electrodes *ACS Catal.*, 6, 219–229 (DOI: 10.1021/acscatal.5b01967)

84. Montoya J.H., Shi C., Chan K., Nørskov J.K. (2015), Theoretical Insights into a CO Dimerization Mechanism in CO₂ Electroreduction, *J. Phys. Chem. Lett.*, 6, 2032–2037 (DOI: 10.1021/acs.jpcllett.5b00722)
85. Shin D., Sinthika S., Choi M., Thapa R., Park N. (2014), Ab Initio Study of Thin Oxide–Metal Overlayers as an Inverse Catalytic System for Dioxygen Reduction and Enhanced CO Tolerance, *ACS Catal.*, 4, 4074–4080 (DOI: 10.1021/cs501153p)
86. Lide D.R. (2005) *CRC Handbook of Chemistry and Physics*, Internet version, CRC Press, Boca Raton, FL
87. Karamad M., Hansen H.A., Rossmeisl J., Nørskov J.K. (2015), Mechanistic Pathway in the Electrochemical Reduction of CO₂ on RuO₂, *ACS Catal.*, 5, 4075–4081 (DOI: 10.1021/cs501542n)
88. Mahata A., Rawat K.S., Choudhuri I., Pathak B. (2016), Octahedral Ni-nanocluster (Ni₈₅) for Efficient and Selective Reduction of Nitric Oxide (NO) to Nitrogen (N₂), *Sci. Rep.*, 6, 25590 (DOI: 10.1038/srep25590)
89. Ou L. (2018), New Insights into the Pt-Catalyzed CH₃OH Oxidation Mechanism: First-Principle Considerations on Thermodynamics, Kinetics, and Reversible Potentials, *ACS Omega*, 3, 886–897 (DOI: 10.1021/acsomega.7b01725)
90. Fang D.Q., Zhang R.O. (2011), Size effects on formation energies and electronic structures of oxygen and zinc vacancies in ZnO nanowires: A first-principles study, *J. Appl. Phys.*, 109, 044306 (DOI: 10.1063/1.3549131)
91. Wang Y., Kattel S., Gao W., Li K., Liu P., Chen J.G., Wang H. (2019), Exploring the ternary interactions in Cu–ZnO–ZrO₂ catalysts for efficient CO₂ hydrogenation to methanol, *Nat Commun.*, 10, 1166 (DOI: 10.1038/s41467-019-09072-6)
92. Kuld S., Thorhauge M., Falsig H., Elkjær C.F., Helveg S., Chorkendorff I., Sehested J. (2016), Quantifying the promotion of Cu

catalysts by ZnO for methanol synthesis, *Science*, 352, 969-974
(DOI: 10.1126/science.aaf0718)

Chapter 6

Electrocatalytic CO₂ Hydrogenation to C₂ Based Products through C–C Coupling over Heterogenous Based Cu Nanocatalysts

6.1. Introduction

Electrocatalytic CO₂ hydrogenation reaction can be a promising approach for renewable energy production through conversion of CO₂ to liquid fuel and such hydrogenation reactions are also very important for fundamental chemistry such as C-C coupling as well as C-H bond formation reactions [1-3]. Among various metals in heterogenous electrocatalytic CO₂ hydrogenation reaction, Cu has been found as an effective electrocatalyst for CO₂ hydrogenation [4]. In the case of other electrodes, Ti, Fe, Ni, or Pt-based electrodes are found to be promising for hydrogen productions [5] whereas Ag, Au or Zn based electrodes are efficient for CO productions [6,7] and Pb, Pd, Au, Cd, In, Sn, or Ru-based electrodes favor formate [8-10] productions. Hori and co-workers have shown two major products (CH₄ and C₂H₄) on Cu based catalysts with high current density and Faradic efficiency (FE) [4,10,11]. However, the required potential for CO₂ hydrogenation is relatively high (~1.0 V) and therefore, the efficiency of Cu based catalysts is less for such reaction [12]. Further to this, the selectivity of the product is less as various products can be achieved at comparable potential. Hence, the major difficulties in the electrochemical CO₂ hydrogenation reaction are high overpotential and low product selectivity which hamper the development and application of CO₂ hydrogenation reaction. Several research groups have revealed that the selectivity and activity of CO₂ reduction reactions are highly affected by the morphology of Cu surface. Hori and co-workers have demonstrated that CH₄ is the main product on Cu(111) surface whereas C₂H₄ is the major product on the (100) facet of Cu [13-15]. In this context, Koper and co-workers have shown two different pathways on periodic Cu(100) surface for the origination of C₂ based product [16-18]. Both the pathways have some common intermediates which can form CH₄ at -0.8 to -0.9 V vs reversible hydrogen electrode (RHE). In this case, the most important step for C₂ based products is the dimerization of CO at ~-0.4 V vs RHE. After these reports, Calle-Vallejo et al. have investigated the C₂ production mechanism using DFT

calculations on periodic Cu(100) surface [19]. Nørskov and co-workers have also explored the CO₂ hydrogenation mechanism and shown that the CO dimerization barrier is less on the periodic Cu(100) surface compared to that on the periodic Cu(111) surface [20]. Recently a detailed mechanistic pathways, required potentials, and various product selectivity have been investigated by Asthagiri and co-workers on periodic Cu(100) surface [21]. After this, Head-Gordon and co-workers have shown the mechanism of various C₂ based products on the periodic Cu(100) surface and compared that with the periodic Cu(111) surface [22]. All of these reports indicate the favorability of C–C bond formation steps on the Cu(100) facet than that on the Cu(111) facet. However, the activity and selectivity of the products are the major concerns on periodic Cu(100) surface. Even though several reports are available on CO₂ hydrogenation to C₂ based products formation, the selectivity of the products (C₁ vs. C₂ based products) is still the major challenge as there are some common intermediates which can lead to various products and hence several products can be obtained at comparable potential. Along with these, the C–C coupling steps are highly important for C₂ based product formation. Therefore, finding out the most important steps controlling the above mentioned aspects and identifying the origin of these factors will be highly beneficial to the theoreticians as well as experimentalists for the designing of efficient and selective catalyst towards CO₂ hydrogenation to selective C₂-based product formation. Therefore, the strategies to achieve low potential and selectivity need to be developed. In an effort to produce highly selective C₂ based products, Cu nanoparticles have been used in earlier studies [23-25]. In the case of nanoparticles, exposed (100) facet surface area is more than that of the periodic Cu(100) surface i.e., catalytic activity is more. Recently, Nilsson and co-workers have reported that Cu nanocube exposed with (100) facet shows more selectivity towards C₂ based product at a very low overpotential [26]. Their report shows that C₂H₄ can be formed at –0.60 V and CH₄ can be formed at –0.93 V vs. RHE. However,

C₂ based products, C₂H₄ and C₂H₅OH is obtained along with some undesired H₂, HCOO⁻, CH₃OH and CH₄ products. Besides, experimental mechanistic studies of CO₂ hydrogenation reaction are very challenging due to the complexities of spectroscopic operation on the reactants and intermediates. Even though several experimentalists have shown via in situ IR spectroscopy and confirmed CO₂, CO, and formate are important intermediates, this cannot identify all the surface species during the reaction specially for two carbon atoms-based products [27,28]. Besides, Koper and co-workers have proposed a CO₂ hydrogenation mechanism, but it does not include all the possible pathways of CO₂ hydrogenation reaction [16]. Their study can identify only the stable intermediates and it is obtained after observing the product only. So, the theoretical free energy calculations of all the possible pathways are very promising in terms of identifying the reaction pathways. In an effort to this, Rossmeisl and co-workers have shown various important intermediates for alcohol formation [29]. Hence, it is highly essential to theoretically investigate the full mechanistic pathways due to the limitation in experimental studies. However, C₂H₄ and C₂H₅OH are highly useful C₂ based CO₂ hydrogenated product along with various C₁ based products (HCOOH, CH₃OH and CH₄) [30-34]. For example, C₂H₄ is an important feedstock in chemical industries as C₂H₄ oligomerization can produce highly valuable ethylene oxide, polyethylene, and diesel. Besides, C₂H₅OH can also be used as a feedstock for C₂H₄, glycol ether, amines, and esters formation. Even though several reports are available on CO₂ hydrogenation to C₂ based products formation there has been no concise study addressing the selectivity of the products (C₁ vs. C₂ based products), which is still the major challenge in this area as there are some common intermediates which can lead to various products at comparable potential. Though CO₂ hydrogenation to C₂ products have been studied on Cu(100) surface, there has been no attempt to study this in the nano dimension. As it is well-known that confining to nano regime brings out significant activity changes, in our work, we study computational CO₂

hydrogenation to C₁ as well as C₂ products in copper based nanocube. Therefore in this work, we have considered all the important factors and identified the most important steps as well as dependence of these steps on the Cu nanoparticle based catalytic surface. Specifically, the most favourable pathways of various products with their adsorption energy and reaction free energy are not fully understood. Therefore, finding out the most favourable mechanisms for all C₁ and C₂ based products are highly essential to get the idea about the product selectivity of any catalyst. Hence, the present study investigates the development of CO₂ hydrogenation reaction mechanistic pathways for the formation of C₁ as well as C₂ based products. For this, we have modelled a Cu nanocube (Cu-NC) exposed with Cu(100) facets (Figure 6.1), as such nanocube has been experimentally reported to be more efficient and selective catalyst compared to the periodic Cu(100) surface/facet for C–C coupling and therefore production of C₂ based products.

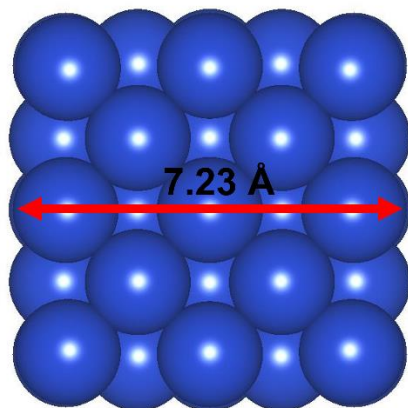


Figure 6.1: Modelled Cu nanocube (Cu-NC) exposed with Cu(100) surface for CO₂ hydrogenation reaction.

The Cu-NC is constructed from the Cu FCC bulk by selectively terminating along the (100) directions as it is known to be the highest active Cu facet for CO₂ hydrogenation to C₂-based product formation. The NC such constructed consists of 63 Cu atoms. As a part of the attempt, Cu-NC

stability, adsorption energy of all the considered intermediates and reaction free energy of each elementary steps have been calculated. These adsorptions and reaction free energy information can give a quantitative idea of the Cu electrode for CO₂ hydrogenation reaction based on the surface morphology, and which can guide the future direction of modelling efficient catalyst. Shortly, we have computationally investigated the most plausible pathways of C₁ and C₂ based CO₂ hydrogenated products (such as CH₃OH, HCOOH, CH₄, C₂H₄ and C₂H₅OH) on the Cu-NC and found out the factors responsible for favoring those reaction pathways.

6.2. Computational Details

The first principles calculations have been implemented using the projector augmented wave (PAW) method as employed in the Vienna Ab initio Simulation Package (VASP) [35-37]. The description of the exchange-correlation interaction during all the calculations has been incorporated with the Perdew–Burke–Ernzerhof (PBE) functional [38-40]. The Grimme’s D3 semiempirical dispersion energy corrections have also been incorporated in the calculations for the considerations of the non-covalent interactions [41]. In the case of the H atom energy, we have used the computational hydrogen electrode (CHE) model concept as reported by Nørskov and co-workers [42]. During an external applied potential (U) in the reaction, the chemical potential of each step changes by eU (e is the electronic charge transferred in each elementary step) [43,44]. Moreover, we have checked transition states and calculated the energy barriers for some of the important steps using the nudged elastic band (CI-NEB, six climbing-image) and dimer methods [45,46]. Besides, the some of the intermediates Bader atomic charges have been calculated using the Henkelman code using near-grid algorithm refine-edge method [47-49]. The adsorbed intermediates have been represented by an asterisk sign (*) throughout the chapter. Moreover, more than 15 Å vacuum has been added in all the three directions to avoid any periodic image interactions. We have tested the plane wave basis set

energy cutoff for various values and found that energy change is minimal after 470 eV cutoff (Table 6.1). Therefore, the plane-wave basis cutoff energy in our study is set to 470 eV. Here all the structures were optimized until the convergence criteria of energy becomes less than that of 1×10^{-4} eV and forces become less than 0.02 eV/\AA . We have calculated the total energies of the Cu-NC using a series of gamma centered k-points grid. The calculated results show a little improvement of 9.2×10^{-4} and 7.1×10^{-4} eV in the total energy using $3 \times 3 \times 3$ and $5 \times 5 \times 5$ gamma centered k-points, respectively compared to $1 \times 1 \times 1$ gamma centered k-points. Besides, a gamma centered k-points grid reduces computation cost and can give the important information regarding the structure and energy of the system. Therefore, all the calculations have been performed using $1 \times 1 \times 1$ gamma centered k-points. Moreover, we have calculated adsorption energies of the considered CO_2 hydrogenation intermediates using following equation (6.1):

$$E_{\text{ad}} = E_{\text{NC+adsorbate}} - (E_{\text{adsorbate}} + E_{\text{NC}}) \quad (6.1)$$

In the above equation (6.1), E_{ad} is the adsorption energy of any intermediate, $E_{\text{NC+adsorbate}}$ is the total electronic energy of the optimized NC in the presence of adsorbate whereas $E_{\text{adsorbate}}$ and E_{NC} are single point energies of adsorbate and Cu-NC (within the optimized geometry of NC+adsorbate) respectively. We have taken the single point energies of the NC and the intermediate within the optimized geometry of adsorbed system owing to the fact that during adsorption, the structures of both the NC and the intermediates are observed to undergo local structural changes from their pristine forms. Hence, consideration of single point energies give a more accurate adsorption energies by taking account of these structural changes. Moreover, the reaction free energies of all the considered steps have been computed using the following equation (6.2):

$$\text{DG} = \text{DE} + \text{DZPE} - \text{TDS} \quad (6.2)$$

In equation (6.2), DG, DE, DZPE and DS are the reaction free energy, change in total energy, change in zero-point energy, change in entropy of

the particular elementary step, respectively whereas T is the temperature. The zero-point energy has been calculated using $\sum \frac{1}{2} h\nu_i$ where h and ν_i are the Planck's constant and vibrational frequency, respectively. Here, we have neglected the entropy term during reaction free energy calculation. A set of $3 \times 3 \times 3$ k-point grid has been used for some of the important intermediates to explore the electronic structures. We have also characterized all the intermediates by examining the absence of vibrational frequency.

Table 6.1: The convergence calculation for Cu-NC using various plane wave basis set cutoff.

Plane wave basis set cutoff (in eV)	Computed energy of Cu-NC (in eV)
400	-202.034
450	-201.925
470	-201.937
500	-201.941

6.3. Results and Discussion

In this segment, the stability of the Cu-NC has been explored using energetic, dynamic, and thermal stability analysis. After stability analysis, we have considered the stable form of the Cu-NC for the investigation of CO_2 hydrogenation reaction catalytic activity using adsorption energy of each considered intermediates and reaction free energy of every elementary step for C_1 and C_2 based product formation.

6.3.1. Stability Analysis

At first, we have explored the energetic stability through formation as well as cohesive energies analysis of the Cu-NC to check the stability of the considered NC than that of bulk Cu structure. We have used equation 6.3 and equation 6.4 for the calculation of cohesive energy (E_{coh}) as well as

formation energy (E_{for}) of the considered Cu-NC respectively [50,51].

$$E_{\text{coh}} = E_{\text{Cu-NC}}/N - E_{\text{Cu}} \quad (6.3)$$

$$E_{\text{for}} = E_{\text{Cu-NC}}/N - \mu_{\text{Cu}} \quad (6.4)$$

In the above equations, $E_{\text{Cu-NC}}$, E_{Cu} , μ_{Cu} , and N are the total electronic energy of the nanocube, isolated Cu atom energy, chemical potential of a Cu atom and total number of atoms present in the Cu-NC, respectively. The calculated results show that the chemical potential of bulk Cu is -4.24 eV per atom. The chemical potentials of Cu atom in periodic Cu(100) surface, Cu-NC and Cu-dNC are -3.78, -3.21 and -3.25 eV, respectively. Since, the chemical potentials are found to be different for these systems, their catalytic activities can also be expected to be distinct. For comparisons, we have analyzed formation as well as cohesive energies of the periodic Cu(100) and Cu(111) surfaces and then compared with the available experimental values. Our computed formation as well as cohesive energies are tabulated in Table 6.2. The computed formation and cohesive energy values for periodic Cu(111) surface are close to the experimental formation and cohesive energy values on periodic Cu(111) surface [52]. Hence, the considered level of theory is acceptable for the adsorption and reaction free energies calculations. Further to this, the dynamic stability of the considered catalysts has been examined by adopting density functional perturbation theory (DFPT). By using DFPT method, we have calculated the lattice vibrations of the catalyst systems and confirmed the stability by verifying the imaginary modes. Our calculated, dynamic stability analysis shows that there is an imaginary frequency of $\sim 40i \text{ cm}^{-1}$. Several earlier reports have shown that the systems can be considered as stable if the imaginary frequency is below $35i \text{ cm}^{-1}$ [53,54]. Therefore, the considered Cu-NC is dynamically unstable structure that is Cu-NC has a possibility of interconversion to other form. Even though our considered approach is electrochemical there will be some nonelectrochemical steps which can be performed at experimental thermal condition. In general, thermal CO_2 hydrogenation reaction is performed at 473–573 K temperature [55]. So, it

is highly important to check the stability of the considered Cu-NC at that temperature range for the operation of the reaction. To investigate these aspects, we have examined the ab initio molecular dynamics (AIMD) simulations with 1 femtosecond (fs) time step at 300, 400 and 500 K of the Cu-NC (Figure 6.2a) using the Nose' thermostat model and NVT ensemble for 20 picoseconds (ps) [56]. We find that there is no significance change in the energy as well as structure throughout the simulation of the Cu-NC at 300 K. However, we have noticed fluctuation in energy at 400 K after 13 ps. The same has been observed at 500 K after 10 ps. Therefore, we have checked the structure of the Cu-NC after the completion of the simulation at 400 and 500 K. The radial distribution functions of the Cu-NC also show a significant change in the Cu-Cu bond length from 300 to 400 and 500 K (Figure 6.3a). The structures obtained after completion of the AIMD simulation have shown a significant change in the Cu-NC structure at 400 and 500 K. The Cu-NC is now converted into another geometry, where the structure looks like an octahedral structure (Figure 6.2b).

Table 6.2: Formation and cohesive energies of Cu-NC, Cu-dNC, periodic Cu(100) and Cu(111) surface. The experimental formation and cohesive energy values for the periodic Cu(111) surface are given in parenthesis for comparisons.⁵²

Cu-NC and periodic systems	Formation energy (eV/atom)	Cohesive energy (eV/atom)
Cu-NC	1.03	-2.96
Cu-dNC	0.99	-3.01
periodic Cu(100) surface	0.46	-3.54
periodic Cu(111) surface	0.26 (0.31) ⁵²	-3.85 (-3.49) ⁵²

Therefore, there is a possibility of interconversion of the Cu-NC during the

operation of the CO₂ hydrogenation reaction. Hence, we have considered the distorted Cu-NC (Cu-dNC) and checked its stability using energetic, dynamic, and thermal stability analysis. Our calculated cohesive and formation energy values indicated that the simulated Cu-dNC is more stable than the Cu-NC. Furthermore, we have checked the dynamic stability of Cu-dNC using phonon calculations. Our study shows very small (up to 10i cm⁻¹) imaginary frequency. Hence, the Cu-dNC structure is dynamically more stable compared to the Cu-NC structure.

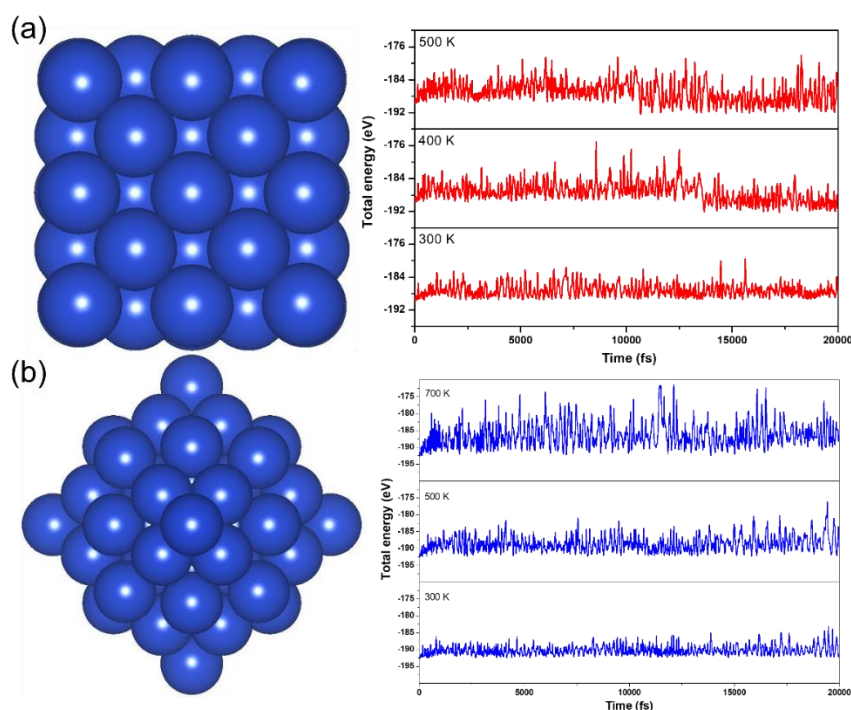


Figure 6.2: (a) Optimized structures of the Cu-NC and ab initio molecular dynamics (AIMD) simulations of Cu NC at 300, 400 and 500 K. (b) Optimized structures of the Cu-dNC and AIMD simulations of Cu-dNC at 300, 500 and 700 K.

After confirmation of energetic and dynamic stability of the Cu-dNC, we have examined the Cu-dNC thermal stability of at 300, 500 and 700 K for 20 ps with 1 fs time step (Figure 6.2b). Our AIMD simulations show no significant change in the energy as well as structure throughout the

calculation at 300 K. The overall energy change is minimal even at 500 K throughout the calculation. Though the energy fluctuation is relatively larger at 700 K, no significant structural reconstruction is obtained even at 700 K for 20 ps. Hence, the Cu-dNC structure is thermally stable even at high temperature. Even though the radial distribution functions of the Cu-dNC show a relatively higher change in the Cu-Cu bond length distribution at 700 K (Figure 6.3b), there are no significant structural reconstruction within the Cu-dNC. Such structural transformations towards distorted geometry have been recently reported for electrocatalysts [57]. Hence, the interconversion possibility to other local minimum energy structure of the Cu-dNC during the reaction is not expected in the 300 to 700 K temperature. So, we can say Cu-dNC is a stable structure and therefore considered as a model catalyst for the CO₂ hydrogenation reaction.

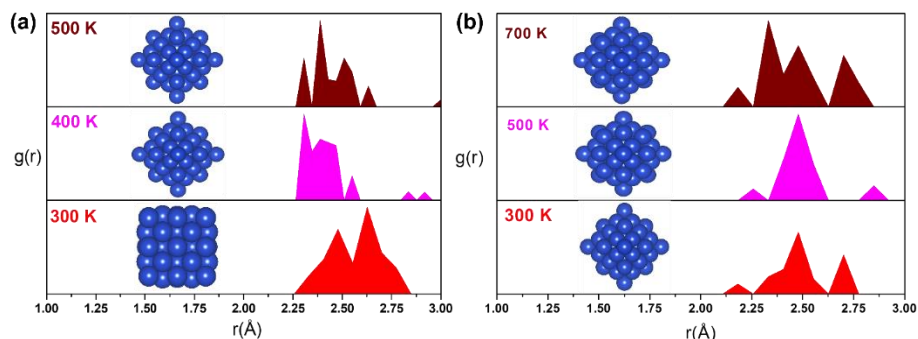


Figure 6.3: The radial distribution functions ($g(r)$) of (a) Cu-NC and (b) Cu-dNC calculated from AIMD simulation at different temperatures. The structure obtained at the end of the simulation is attached with $g(r)$.

6.3.2. Adsorption of Different Intermediates

Here, we have checked the applicability of Cu-dNC for CO₂ hydrogenation reaction in detail. At first, all the possible intermediates are identified, which can be formed during the CO₂ hydrogenation for the formation of C₁ and C₂ based products. All the possible adsorption sites on the Cu-dNC have been identified for all the considered intermediates as shown in Figure 6.4.

On the Cu-dNC surface, four top, four bridge and three possible hollow sites are available. Therefore, all these adsorption sites have been taken into account for the adsorption energy calculations of the intermediates. The preferred adsorption sites as well as adsorption energies are listed in Table 6.3 whereas the respective geometries for C₁, H, O and H₂O intermediates are shown in Figure 6.5 and the respective geometries for C₂ based intermediates are shown in Figure 6.6.

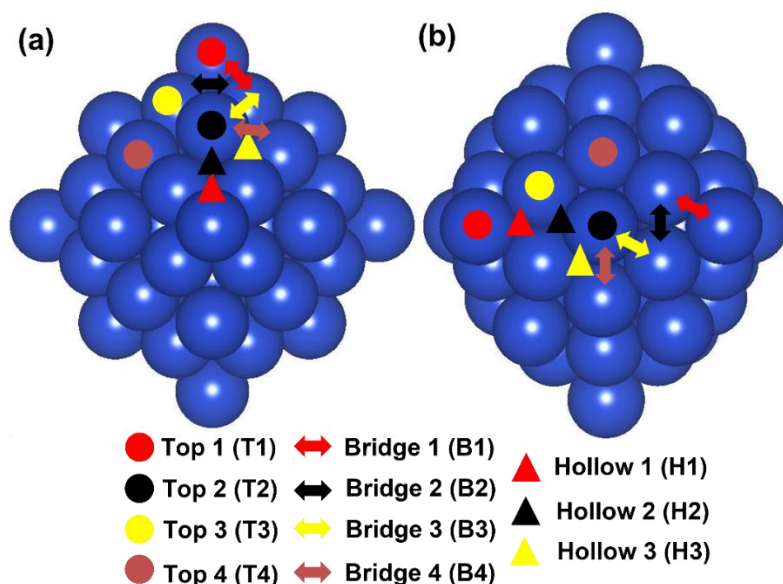


Figure 6.4: (a) Side and (b) top views of the considered Cu-dNC with all possible adsorption sites.

Most of the C₁ based intermediates adsorption energies are higher on Cu-dNC surface compared to that on the periodic Cu(111) surface [58]. However, CO₂ interacts very weakly with -0.19 eV adsorption energy on the Cu-dNC surface. The same has been observed in several experimental and theoretical studies [58-60]. The *COOH intermediate also binds weakly on whereas *HCOO binds strongly on the catalytic surface. This may be due to the presence of two strong Cu–O bonds in case of *HCOO whereas one Cu–C and one Cu–O bonds are present in *COOH. Furthermore, to understand the reason behind the trends of adsorption

energy, we have checked the projected density of states (PDOS) for *COOH and *HCOO. From Figure 6.7a-b, it is obvious that the overlap among Cu-d orbitals and C+O-p orbital is less compared to the overlap among Cu-d orbitals and 2O-p orbital.

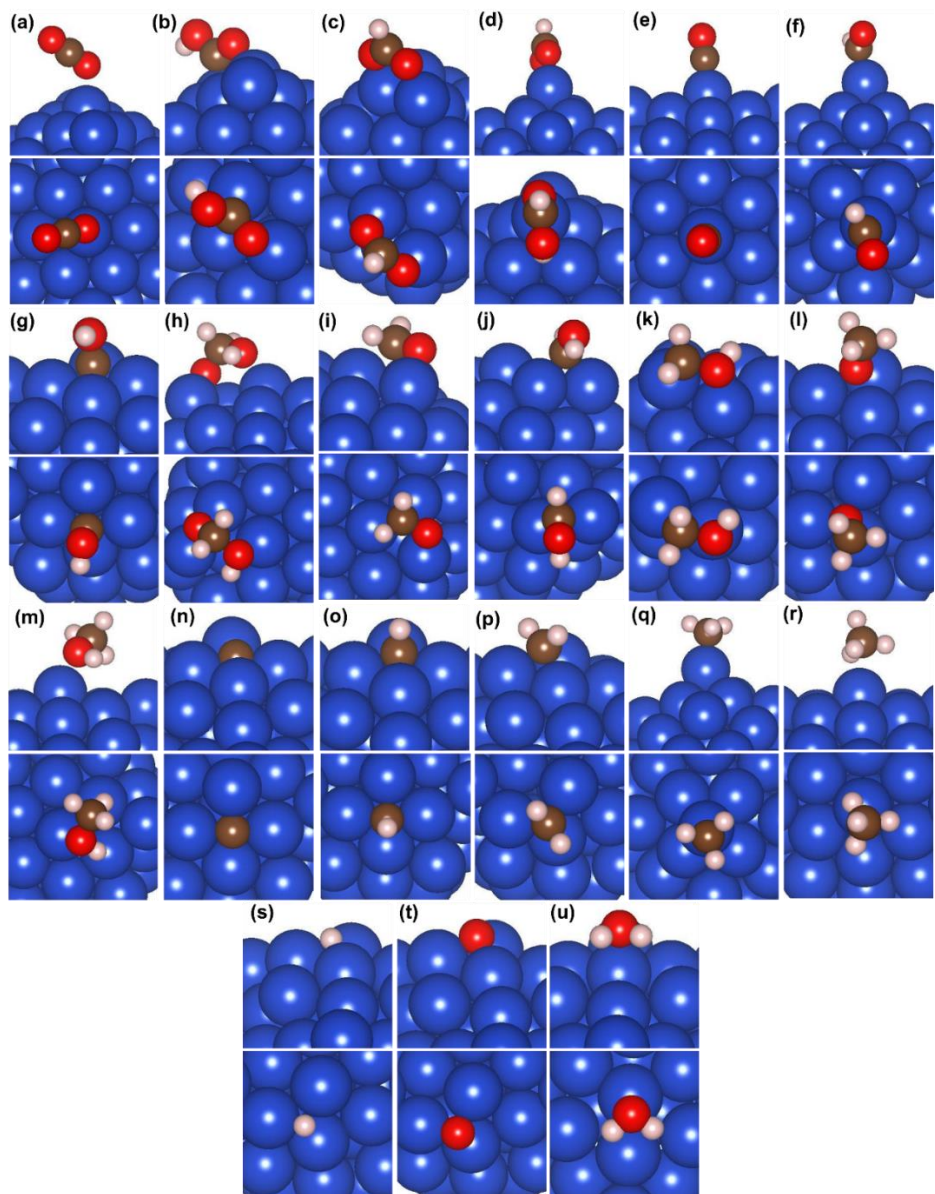


Figure 6.5: Adsorption patterns of the considered CO₂ hydrogenation to C₁ based intermediates on Cu-dNC: (a) *CO₂, (b) *COOH, (c) *HCOO, (d) *HCOOH, (e) *CO, (f) *HCO, (g) *COH, (h) *H₂COOH, (i) *H₂CO, (j) *HCOH, (k) *H₂COH, (l) *H₃CO, (m) *H₃COH, (n) *C, (o) *HC, (p) *H₂C,

(q) *H₃C, (r) *H₄C, (s) *H, (t) *O and (u) *H₂O.

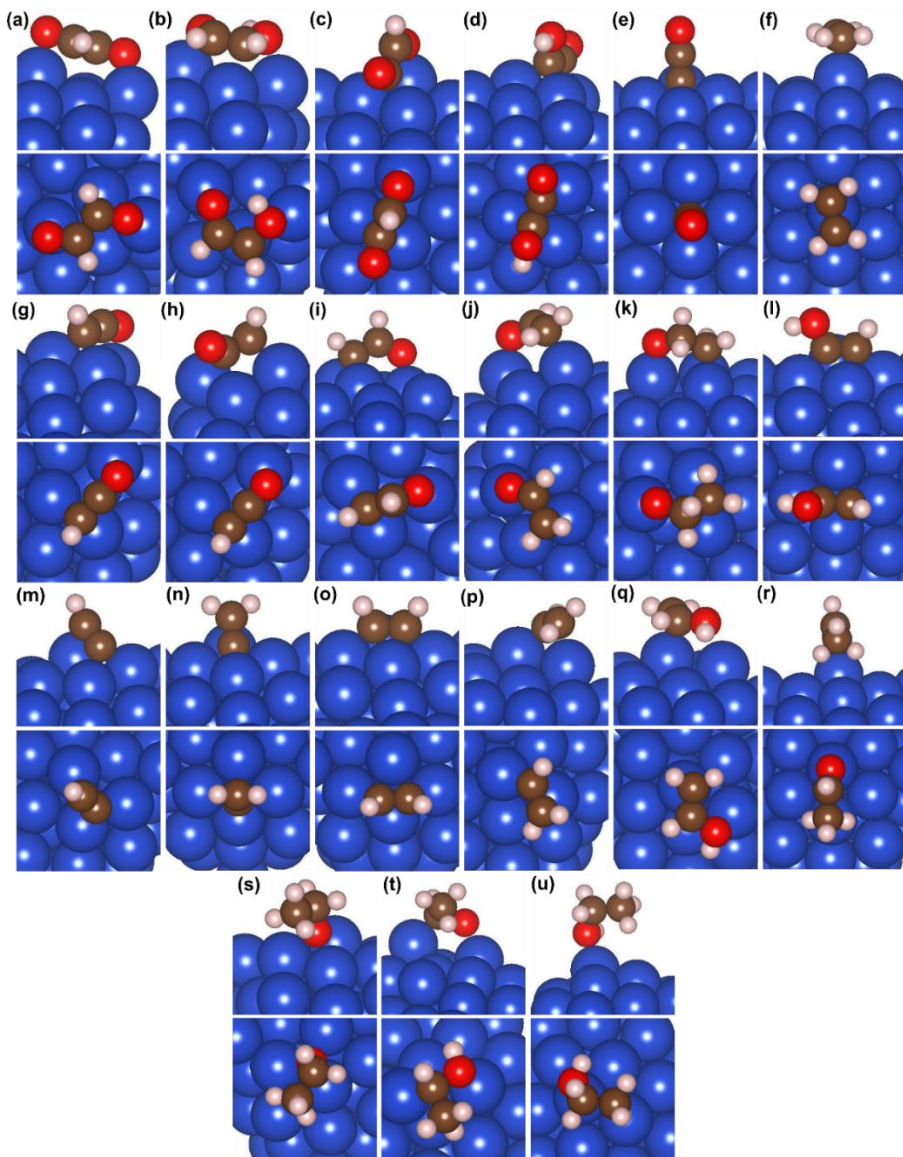


Figure 6.6: Adsorption patterns of the considered CO₂ hydrogenation to C₂ based intermediates on Cu-dNC: (a) *HCO-HCO, (b) *HCO-HCOH, (c) *HCO-CO, (d) *COH-CO, (e) *C-CO, (f) *C₂H₄, (g) *HC-CO, (h) *H₂C-CO, (i) *HC-HCO, (j) *H₂C-HCO, (k) *H₂C-H₂CO, (l) *HC-COH, (m) *C-HC, (n) *C-H₂C, (o) *HC-HC, (p) *HC-H₂C, (q) *H₂C-HCOH, (r) *H₃C-HCO, (s) *H₃C-H₂CO, (t) *H₃C-HCOH and (u) *H₃C-H₂COH.

Moreover, our computed Bader atomic charges show that 0.29 |e| and 0.25

|e| charges shift from the Cu surface to the two O atoms of *HCOO, respectively whereas 0.26 |e| and 0.12 |e| charges shift from Cu surface to the O and C-atom of *COOH. So, the amount of charge transfer is more for *HCOO compared to that for *COOH.

Table 6.3: Favored adsorption sites and all the CO₂ hydrogenation related intermediates adsorption energies on the Cu-dNC surface.

C ₁ based, H, O and H ₂ O intermediates		C ₂ based intermediates	
Intermediates	Adsorption energy on Cu-dNC (eV)	Intermediates	Adsorption energy on Cu-dNC (eV)
*CO ₂ (T2)	-0.19	*HCO-HCO (B3)	-2.35
*COOH (B3)	-2.84	*HCO-HCOH (B3)	-2.59
*HCOO (B1)	-4.09	*HCO-CO (B3)	-3.14
*HCOOH (T1)	-1.04	*COH-CO (B1)	-3.67
*CO (T2)	-1.28	*C-CO (B4)	-5.40
*HCO (T1)	-1.96	*C ₂ H ₄ (T2)	-1.19
*COH (B4)	-3.71	*HC-CO (B3)	-3.55
*H ₂ COOH (B3)	-3.53	*H ₂ C-CO (B3)	-3.15
*H ₂ CO (B1)	-1.94	*HC-HCO (H3)	-4.99
*HCOH (B1)	-2.72	*H ₂ C-HCO (H2)	-3.20
*H ₂ COH (B1)	-2.37	*H ₂ C-H ₂ CO (B1)	-4.64
*H ₃ CO (H3)	-3.12	*HC-COH (H3)	-5.78
*H ₃ COH (T2)	-0.76	*C-HC (H3)	-4.81
*C (B4)	-6.24	*C-H ₂ C (B4)	-3.95
*CH (B4)	-6.02	*HC-HC (H3)	-4.85
*CH ₂ (H3)	-4.21	*HC-H ₂ C (B3)	-3.26

*CH ₃ (T1)	-2.38	*H ₂ C-HCOH (T2)	-1.16
*CH ₄ (T2)	-0.25	*H ₃ C-HCO (B4)	-0.95
*H (H3)	-2.70	*H ₃ C-H ₂ CO (H3)	-3.19
*O (H3)	-5.60	*H ₃ C-HCOH (T1)	-2.41
*H ₂ O (T4)	-0.44	*H ₃ C-H ₂ COH (T3)	-0.77

The adsorption energy of any species on the surface is highly dependent on the charge transfer between the surface as adsorption energy is dependent to the polarizability of the adsorbate. In case of higher charge transfer, the surface is polarized and can induce polarization on the adsorbates, that is a better adsorption. Also, the charge transfer from the electron rich metal towards the unoccupied electronic energy levels of adsorbate species strengthens the binding and hence result in a higher adsorption energy. Hence, adsorption energy is more in case of *HCOO on Cu-dNC compared to that for the *COOH. Another two important intermediates of CO₂ hydrogenation to C₁ based product formation are *HCO and *COH. In general, *COH and *HCO are two crucial intermediates for the selective C₁ based product formation of CH₄ and CH₃OH, respectively [58,61-63]. Our calculated results show that *HCO adsorption energy is less on the catalytic surface compared to the *COH. The calculated Bader atomic charges show that Cu surface transfer 0.13 |e| charges to the C atom of *HCO whereas the Cu surface transfer 0.15 |e| charges to the C atom of *COH. So, the amount of charge transfer is more for *COH compared to the *HCO from Cu-dNC that is adsorption energy is more for *COH compared to the *HCO. Besides, the *H₂CO binds effectively on the catalytic surface than that of periodic Cu(111) surface [58] i.e., the *H₂CO can be hydrogenated further for CH₃OH formation rather than desorption from the catalytic surface. In

case of C₂ based products, intermediates adsorption energies are more compared to the adsorption energies of C₁ based intermediates. However, *HC-HCO adsorption energy is more compared to the *H₂C-CO adsorption energy as one extra strong Cu–O bond (1.936 Å) is present in case of *HC-HCO (Figure 6.6).

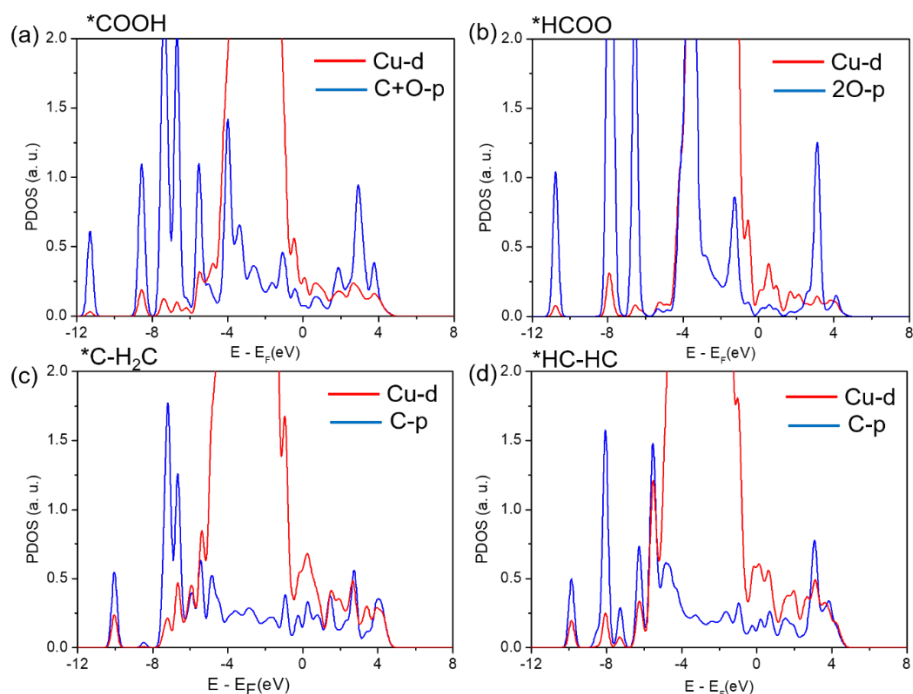


Figure 6.7: Projected density of states plot of (a) *COOH, (b) *HCOO, (c) *C-H₂C, and (d) *HC-HC intermediates on Cu-dNC.

The same has been observed in case of *H₂C-H₂CO (Cu–O bond length is 1.843 Å) where adsorption energy is 3.48 and 3.69 eV high compared to the *H₂C-HCOH and *H₃C-HCO adsorption energy, respectively. Moreover, the adsorption energy of *H₃C-H₂CO is 0.78 eV more compared to the adsorption energy of *H₃C-HCOH. In this case also higher adsorption energy is due to the O binding with the active surface. Besides, the adsorption energy of *HC-HC is 0.90 eV higher than that of *C-H₂C. This may be due to the presence of two single Cu-C in *HC-HC. To understand the reason behind the trends of adsorption energy we have checked the

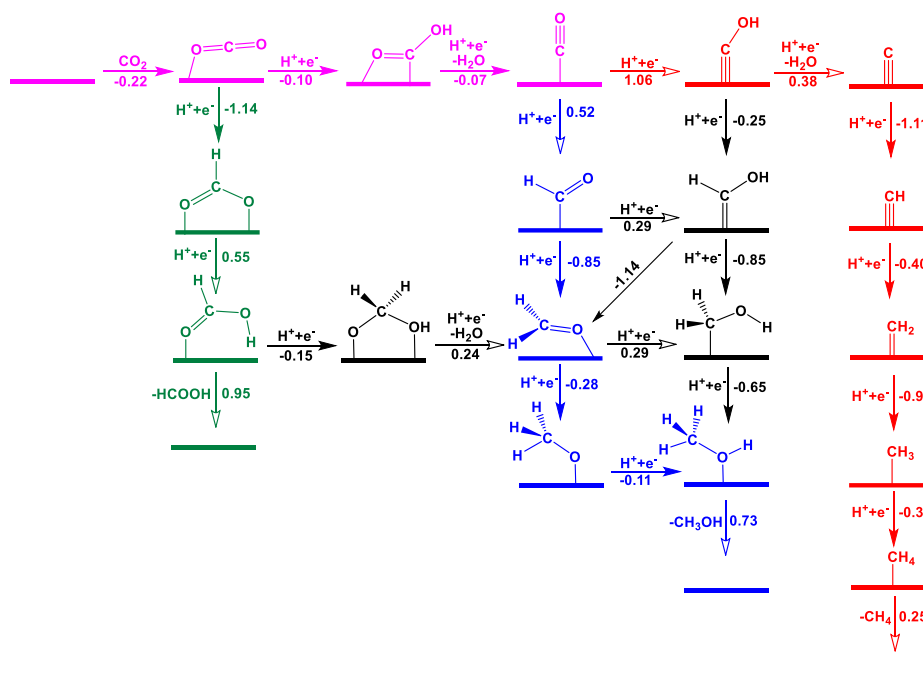
PDOS for *C-H₂C and *HC-HC. From Figure 6.7c and 6.7d it is clear that the overlap between Cu-d orbitals with C-p orbital is less for *C-H₂C compared to the overlap between Cu-d orbitals with C-p orbital of *HC-HC. Hence, adsorption energy is more in case of *HC-HC on Cu-dNC compared to that for *C-H₂C. Further to this, we have noticed that presence of adsorbate on the catalytic surface does not distort the catalyst. Therefore, the nano catalyst is stable even in the presence of adsorbates.

6.3.3. CO₂ Hydrogenation to C₁ Based Product Formation

In this section, we have studied all the possible mechanistic pathways for C₁ based product formation from CO₂ and identified the most plausible pathways along with the potential determining steps (PDS) responsible for such reaction on the Cu-dNC. All the considered mechanistic pathways for CO₂ hydrogenation to HCOOH, CH₃OH and CH₄ along with the calculated reaction free energies associated for each of those mechanistic steps are shown in Scheme 6.1.

6.3.3.1. Formation of HCOOH: Several earlier studies have confirmed that HCOOH is a common CO₂ hydrogenated product. Hence, we have started our discussion of mechanistic investigation from CO₂ to HCOOH. The adsorption energy analysis shows that CO₂ interacts weakly with the Cu-dNC surface. However, the computed reaction free energy value indicates that the CO₂ adsorption process is exergonic by 0.22 eV. Our earlier report has also shown that the reaction free energy of CO₂ adsorption step is exergonic on ZnO and Cu doped ZnO based nanocages [62]. In the presence of H, the C=O bonds of *CO₂ can be weakened due to the hydrogenation at the C-center for the formation of *HCOO. Moreover, the *HCOO intermediate can be hydrogenated further at the O-center of *HCOO for the production of *HCOOH. Lastly, the HCOOH can be separated from the Cu-dNC catalytic surface and the removal of HCOOH is 0.95 eV endergonic in nature. So, a massive input of energy is required

for the of separation of HCOOH from the catalytic surface. The formation of *HCOOH from *HCOO is calculated to be the potential rate determining step along with a reaction free energy of 0.55 eV and the favourable pathway for HCOOH formation from CO₂ on the Cu-dNC is * + CO₂ → *CO₂ → *HCOO → *HCOOH → * + HCOOH.



Scheme 6.1: All possible mechanistic pathways with reaction free energies (in eV) for CO₂ hydrogenation reaction to HCOOH, CH₃OH and CH₄ on Cu-dNC. The common intermediates of most favourable pathways are highlighted in magenta color and the intermediates determine the selectivity of HCOOH, CH₃OH and CH₄ are highlighted in green, blue and red colors, respectively. The hollow and solid arrow heads represent the endergonic and exergonic steps, respectively.

6.3.3.2. Formation of CH₃OH: The CH₃OH is another important C₁ based CO₂ hydrogenated product. In this context several experimental studies have reported that *CO is an essential intermediate for the formation of CH₃OH [27,28]. The adsorbed *CO₂ can be hydrogenated at the O-center for the formation of *CO. Our computed results demonstrate that

*COOH→*CO is very much reversible where the computed reaction free energy is 0.07 eV. Subsequently, *CO can form *HCO/*COH via hydrogenation. Several earlier reports have shown that the *HCO is responsible for CH₃OH formation whereas *COH is responsible for CH₄ [58,62-64]. Therefore, the product selectivity is very much dependent on the *CO hydrogenation step. Scheme 6.1 shows that the formation of *HCO is 0.54 eV more preferable than that of *COH formation. Hence, we can conclude that the formation of CH₃OH is more over CH₄ formation on the Cu-dNC. We have also found out that *HCO formation is 0.10 eV more preferable on the Cu-dNC surface compared to the *HCO formation on the periodic Cu(100) surface as reported by Asthagiri and co-workers using the same level of theory [21]. Besides, *COH formation is 0.32 eV is less favourable on the Cu-dNC than that of the periodic Cu(100) surface as reported by Asthagiri and co-workers [21]. All these results indicate that formation of CH₃OH on the Cu-dNC surface can be more selective compared to that on the periodic Cu(100) surface. In the next step, *HCO can be hydrogenated for the formation of *H₂CO/*HCOH. Besides, *H₂CO/*HCOH can be produced via other pathways as shown in scheme 6.1. The computed results reveal that the formation of *H₂CO is 1.14 eV more favourable than that of *HCOH formation. Subsequently, *H₂CO can also be hydrogenated to *H₃CO/*H₂COH. The *H₃CO formation is exergonic whereas *H₂COH formation is endergonic from *H₂CO that is the reaction will proceed via *H₃CO. Further to this, *H₃CO and *H₂COH can be hydrogenated for the formation of *CH₃OH. Moreover, our calculated adsorption energies of *H₂CO, *H₃CO and *H₂COH show that these intermediates adsorb strongly on the Cu-dNC surface compared to *H₃COH. Therefore, it is expected that *H₂CO will not desorb from the catalyst surface after combining with one H whereas *H₃CO or *H₂COH will easily desorb from the catalyst surface after combining with one H by forming *H₃COH. Eventually, CH₃OH can be separated, and the calculated results show that the removal of CH₃OH requires an amount of 0.73 eV

energy. Considering all the above pathways and the most favourable CO₂ hydrogenation to CH₃OH pathway is * + CO₂ → *CO₂ → *COOH → *CO → *HCO → *H₂CO → *H₃CO → *H₃COH → * + CH₃OH, where the formation of the *CO → *HCO is the PDS with 0.52 eV reaction free energy. The previous reports on various Cu based surfaces [Cu(100) surface [21], Cu₈₅ nanocluster [58], periodic Cu(111) surface [64] and Cu(111) monolayer [63]] have also reported that *CO → *HCO is the PDS for CO₂ hydrogenation to CH₃OH reaction. However, the computed reaction free energy value of the PDS indicates that Cu-dNC can be used as an active catalyst compared to the periodic Cu(100), Cu(111) surface and Cu₈₅ nanocluster for CH₃OH formation [21,58,64].

6.3.3.3. Formation of CH₄: Along with HCOOH and CH₃OH, we have also investigated the mechanistic pathways of CO₂ hydrogenation to CH₄ formation via *COH intermediate. Here, *COH can be hydrogenated at the O-center followed by removal of H₂O and produce *C. Subsequent hydrogenations of *C would lead to the formation of *HC, *H₂C, *H₃C and *H₄C. The computed reaction free energy values indicate that all these subsequent hydrogenation steps are exergonic. In the final step, CH₄ can be separated from the catalytic surface of Cu-dNC. The calculated reaction free energy of PDS for CH₄ formation (*CO → *COH) is 1.06 eV. Hence the selectivity towards CH₄ formation would be less on the Cu-dNC. Several previous reports have also demonstrated that the reaction free energy of *CO → *COH step is 0.74, 1.11 and 0.71 eV on periodic Cu(100) surface [21], Cu(111) monolayer [63] and Cu₈₅ nanocluster [58], respectively (Table 6.4). Hence, formation of CH₄ is highly unfavourable on the Cu-dNC compared to the periodic Cu(111) surface and Cu₈₅ nanocluster and therefore, Cu-dNC can be very much selective towards CH₃OH compared to CH₄.

Table 6.4: Stepwise CO₂ hydrogenation reaction free energies on Cu-dNC,

periodic Cu(100) surface, Cu(111) monolayer and Cu nanocluster based surfaces. All reaction free energies are in eV. Here, (-) means that the reaction free energy is not available for this step. The stepwise reaction free energies of Cu(100) surface, Cu(111) monolayer and Cu₈₅ nanocluster have been taken from references [9,18,19].

Steps	Cu-dNC	Cu(100) Surface [18]	Cu(111) monolayer [9]	Cu nanocluster [19]
* + CO ₂ → *CO ₂	-0.22	-	-	-
*CO ₂ + (H ⁺ +e ⁻) → *COOH	-0.10	-	0.46	-0.17
*COOH + (H ⁺ +e ⁻) → *CO + H ₂ O	-0.07	-	-0.38	-0.29
*CO + (H ⁺ +e ⁻) → *HCO	0.52	0.62	0.46	0.53
*CO + (H ⁺ +e ⁻) → *COH	1.06	0.74	1.11	0.71
*CO ₂ + (H ⁺ +e ⁻) → *HCOO	-1.14	-	-0.29	-
*HCOO + (H ⁺ +e ⁻) → *HCOOH	0.55	-	-0.10	-
*HCOOH → * + HCOOH	0.95	-	-	-
*HCOOH + (H ⁺ +e ⁻) → *H ₂ COOH	-0.15	-	0.51	-
*H ₂ COOH + (H ⁺ +e ⁻) → *H ₂ CO + H ₂ O	0.24	-	0.14	-
*HCO + (H ⁺ +e ⁻) → *H ₂ CO	-0.85	-0.23	-0.28	-0.10
*HCO + (H ⁺ +e ⁻) → *HCOH	0.29	0.39	0.22	0.18
*COH + (H ⁺ +e ⁻) → *HCOH	-0.25	-	-	-
*H ₂ CO + (H ⁺ +e ⁻) → *H ₃ CO	-0.28	-0.40	-0.61	-0.40
*H ₂ CO + (H ⁺ +e ⁻) → *H ₂ COH	0.29	0.28	-0.09	-0.42
*HCOH + (H ⁺ +e ⁻) → *H ₂ COH	-0.85	-	-	-
*H ₃ CO + (H ⁺ +e ⁻) → *H ₃ COH	-0.11	-0.09	-0.39	-
*H ₂ COH + (H ⁺ +e ⁻) → *H ₃ COH	-0.65	-	-	-0.66
*H ₃ COH → * + H ₃ COH	0.73	-	-	-
*COH + (H ⁺ +e ⁻) → *C + H ₂ O	0.38	-0.16	-	-
*C + (H ⁺ +e ⁻) → *HC	-1.11	-0.36	-	-
*HC + (H ⁺ +e ⁻) → *H ₂ C	-0.40	0.08	-	-

$*\text{H}_2\text{C} + (\text{H}^+ + \text{e}^-) \rightarrow *\text{H}_3\text{C}$	-0.90	-0.56	-	-
$*\text{H}_3\text{C} + (\text{H}^+ + \text{e}^-) \rightarrow *\text{H}_4\text{C}$	-0.38	-1.57	-	-
$*\text{H}_4\text{C} \rightarrow * + \text{H}_4\text{C}$	0.25	-	-	-
$*2\text{H}_2\text{C} \rightarrow *\text{H}_2\text{C}-\text{H}_2\text{C}$	-1.25	-1.56	-	-
$*\text{H}_2\text{C}-\text{H}_2\text{C} \rightarrow * + \text{H}_2\text{C}-\text{H}_2\text{C}$	1.08	-	-	-
$*2\text{HCO} \rightarrow *\text{HCO}-\text{HCO}$	-0.81	-1.19	-	-
$*(\text{HCO} + \text{CO}) \rightarrow *\text{CO}-\text{HCO}$	0.24	-	-	-
$*(\text{COH} + \text{CO}) \rightarrow *\text{CO}-\text{COH}$	0.03	-	-	-
$*\text{CO}-\text{COH} + (\text{H}^+ + \text{e}^-) \rightarrow *\text{C}-\text{CO} + \text{H}_2\text{O}$	-0.89	-	-	-
$*\text{CO}-\text{HCO} + (\text{H}^+ + \text{e}^-) \rightarrow *\text{HCO}-\text{HCO}$	-0.70	-	-	-
$*\text{HCO}-\text{HCO} + (\text{H}^+ + \text{e}^-) \rightarrow *\text{HCO}-\text{HCOH}$	-0.47	0.35	-	-
$*\text{C}-\text{CO} + (\text{H}^+ + \text{e}^-) \rightarrow *\text{HC}-\text{CO}$	-0.52	-	-	-
$*\text{HC}-\text{CO} + (\text{H}^+ + \text{e}^-) \rightarrow *\text{HC}-\text{COH}$	0.51	-	-	-
$*\text{HC}-\text{COH} + (\text{H}^+ + \text{e}^-) \rightarrow *\text{HC}-\text{C} + \text{H}_2\text{O}$	0.35	-	-	-
$*\text{HC}-\text{C} + (\text{H}^+ + \text{e}^-) \rightarrow *\text{HC}-\text{HC}$	-0.83	-	-	-
$*\text{HC}-\text{C} + (\text{H}^+ + \text{e}^-) \rightarrow *\text{H}_2\text{C}-\text{C}$	-0.45	-	-	-
$*\text{HC}-\text{HC} + (\text{H}^+ + \text{e}^-) \rightarrow *\text{H}_2\text{C}-\text{HC}$	-1.40	-	-	-
$*\text{H}_2\text{C}-\text{C} + (\text{H}^+ + \text{e}^-) \rightarrow *\text{H}_2\text{C}-\text{HC}$	-1.78	-	-	-
$*\text{H}_2\text{C}-\text{HC} + (\text{H}^+ + \text{e}^-) \rightarrow *\text{H}_2\text{C}-\text{H}_2\text{C}$	0.34	-0.96	-	-
$*\text{HC}-\text{CO} + (\text{H}^+ + \text{e}^-) \rightarrow *\text{H}_2\text{C}-\text{CO}$	0.21	-	-	-
$*\text{H}_2\text{C}-\text{CO} + (\text{H}^+ + \text{e}^-) \rightarrow *\text{H}_2\text{C}-\text{HCO}$	-1.33	-	-	-
$*\text{HCO}-\text{HCOH} + (\text{H}^+ + \text{e}^-) \rightarrow *\text{HC}-\text{HCO}$	-0.59	-0.85	-	-
$*\text{HC}-\text{HCO} + (\text{H}^+ + \text{e}^-) \rightarrow *\text{H}_2\text{C}-\text{HCO}$	-0.44	-0.10	-	-
$*\text{H}_2\text{C}-\text{HCO} + (\text{H}^+ + \text{e}^-) \rightarrow *\text{H}_2\text{C}-\text{H}_2\text{CO}$	0.57	0.06	-	-
$*\text{H}_2\text{C}-\text{HCO} + (\text{H}^+ + \text{e}^-) \rightarrow *\text{H}_3\text{C}-\text{HCO}$	0.44	-	-	-
$*\text{H}_2\text{C}-\text{HCO} + (\text{H}^+ + \text{e}^-) \rightarrow *\text{H}_2\text{C}-\text{HCOH}$	-0.28	0.44	-	-
$*\text{H}_2\text{C}-\text{HCOH} + (\text{H}^+ + \text{e}^-) \rightarrow *\text{H}_2\text{C}-\text{HC} + \text{H}_2\text{O}$	0.02	0.11	-	-
$*\text{H}_2\text{C}-\text{H}_2\text{CO} + (\text{H}^+ + \text{e}^-) \rightarrow *\text{H}_3\text{C}-\text{H}_2\text{CO}$	-0.64	-0.47	-	-
$*\text{H}_3\text{C}-\text{HCO} + (\text{H}^+ + \text{e}^-) \rightarrow *\text{H}_3\text{C}-\text{H}_2\text{CO}$	-0.51	-	-	-
$*\text{H}_2\text{C}-\text{HCOH} + (\text{H}^+ + \text{e}^-) \rightarrow *\text{H}_3\text{C}-\text{HCOH}$	0.94	-	-	-

$*\text{H}_3\text{C-HCO} + (\text{H}^+ + \text{e}^-) \rightarrow *\text{H}_3\text{C-HCOH}$	0.22	-	-	-
$*\text{H}_3\text{C-HCOH} + (\text{H}^+ + \text{e}^-) \rightarrow *\text{H}_3\text{C-H}_2\text{COH}$	-1.32	-	-	-
$*\text{H}_3\text{C-H}_2\text{CO} + (\text{H}^+ + \text{e}^-) \rightarrow *\text{H}_3\text{C-H}_2\text{COH}$	-0.59	0.11	-	-
$*\text{H}_3\text{C-H}_2\text{COH} \rightarrow * + \text{H}_3\text{C-H}_2\text{COH}$	1.30	-	-	-

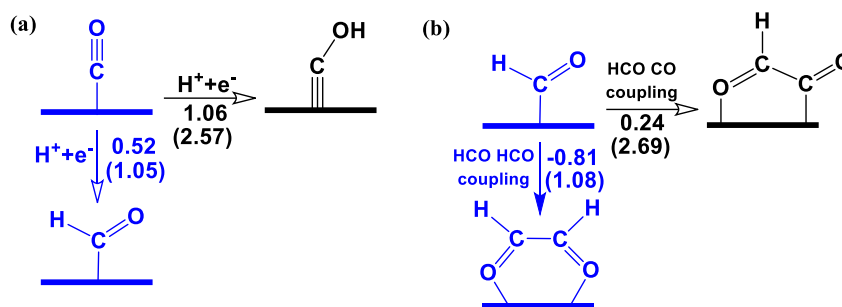
6.3.4. CO₂ Hydrogenation to C₂ Based Product Formation

Here we have considered all the possible mechanistic pathways for C₂ based products formation from CO₂ and identified the most plausible pathways with minimum applied potential on the Cu-dNC. It has been revealed in the former section that at first CO₂ is converted to CO and several studies have shown that by CO₂ hydrogenation to C₂ based products formation proceeds via CO [17,65]. Hence, we have considered all the mechanistic pathways from *CO as shown in Scheme 6.2.

6.3.4.1. Formation of C₂H₄: The C₂H₄ is the simplest and highly useful C₂ based hydrocarbon which can be obtained from CO₂. Various mechanistic pathways have been investigated via *HCO and *COH pathways as illustrated in Scheme 6.2. As shown in Scheme 6.2, *CO can be hydrogenated to *HCO and *COH and can be dimerized to form C₂ based intermediates. There can be various nonelectrochemical steps to obtain C₂ based intermediates like *COH-CO, *HCO-HCO, *HCO-CO and *CO-CO. We have not discussed the *CO dimerization step as we could not able to optimize the *CO-CO intermediate on the Cu-dNC catalytic surface. However, we have considered one explicit water molecule for the optimization of *CO-CO intermediate on the Cu-dNC catalytic surface and unfortunately, we are further unable to detect any *CO-CO intermediate on the Cu-dNC surface as it was shown to undergo dissociation into two *CO species on the surface. Thus, we believe that the nonavailability of *CO-CO intermediate on the Cu-dNC in our study is not due to the absence of solvent effects, rather it is driven by the destabilization of this intermediate owing to the very high stability of an adsorption configuration with two

proceed via *HCO-HCO intermediates. After the nonelectrochemical dimerization steps, subsequent proton transfer directs to the formation of various intermediates like *C-CO from *COH-CO, *HCO-HCO from *HCO-CO and *HCO-HCOH from *HCO-HCO. All of these proton transfer steps are exergonic in nature. Subsequently, *HCO-HCOH can be hydrogenated at the OH-center for the formation of *HC-HCO. Subsequent hydrogenation at the CH-center of the *HC-HCO can form *H₂C-HCO where the computed reaction free energy is -0.44 eV. Then, *H₂C-HCO can form *H₂C-HCOH which is also an exergonic step. The successive hydrogenation and removal of water will form *HC-H₂C which can be a reversible step (0.02 eV). The additional hydrogenation of *HC-H₂C would lead to the formation of *C₂H₄.

Moreover, we have calculated the kinetic barriers for some of the important intermediates for the conforming the most favourable pathways. The overall scheme shows that the most important steps are hydrogenation of *CO to *HCO or *COH. Our computed reaction free energies indicate the preferred *HCO formation over *COH formation. The same can also be also confirmed from the kinetic barriers of these two important steps (Scheme 6.3a). Another important step for C₂ based products are the C-C coupling steps. The kinetic barriers of the important C-C coupling steps reveal that dimerization of *HCO is 1.61 eV more favourable compared to *HCO and *CO coupling (Scheme 6.3b). Therefore, kinetic barriers of C-C coupling steps follow a similar trend as that of free energy change within the catalyst. Recent report by Asthagiri and co-workers have also shown that the kinetic barrier of the CO₂ hydrogenation reaction follow a similar trend as that of reaction free energy [21]. Moreover, we have investigated the further hydrogenation of *C-CO even though this pathway is unfavourable. The subsequent hydrogenation of *C-CO would result in the formation of *C₂H₄ via *HC-CO, *HC-COH, *C-HC, *C-H₂C/*HC-HC and *HC-H₂C intermediates. We have also identified the *C₂H₄ formation pathway via nonelectrochemical *H₂C dimerization step.



Scheme 6.3: Possible mechanistic pathways of (a) $^*\text{CO}$ to $^*\text{HCO}$ vs. $^*\text{COH}$ formation and (b) C–C coupling steps with reaction free energies (in eV) on Cu-dNC. The values given in the parenthesis are the activation barriers in eV at 0 V vs. RHE. The common favourable intermediates of most favourable pathways are highlighted in blue color. The hollow and solid arrow heads represent the endergonic and exergonic steps, respectively.

Ultimately, C_2H_4 can be removed from the surface for the regeneration of the catalyst. This step requires an amount of 1.08 eV energy. Among all the probable pathways, the most favourable pathway for CO_2 hydrogenation to C_2H_4 is $^* + \text{CO}_2 \rightarrow ^*\text{CO}_2 \rightarrow ^*\text{COOH} \rightarrow ^*\text{CO} \rightarrow ^*\text{HCO} \rightarrow ^*\text{HCO-HCO} \rightarrow ^*\text{HCO-HCOH} \rightarrow ^*\text{HC-HCO} \rightarrow ^*\text{H}_2\text{C-HCO} \rightarrow ^*\text{H}_2\text{C-HCOH} \rightarrow ^*\text{HC-H}_2\text{C} \rightarrow ^*\text{C}_2\text{H}_4 \rightarrow ^* + \text{C}_2\text{H}_4$ with a reaction total free energy of -1.02 eV. Hence, CO_2 hydrogenation to C_2H_4 is thermodynamically favourable. Nørskov and co-workers have also shown that C_2H_4 pathways proceeds via $^*\text{CHO}$ and $^*\text{HCO-HCO}$ intermediates at -0.74 V [44]. Moreover, our investigated route for C_2H_4 formation is similar as reported by Asthagiri and co-workers on the periodic Cu(100) surface [21]. Conversely, the most favourable pathway is different from Head-Gordon's report as they have shown $^*\text{COCHO}$ formation is exergonic for C_2 based products formation [22]. Moreover, our calculated results show that $^*\text{CO} \rightarrow ^*\text{HCO}$ is the PDS for C_2H_4 formation. Besides, the $^*\text{CO} \rightarrow ^*\text{HCO}$, $^*\text{H}_2\text{C-HCOH} \rightarrow ^*\text{HC-H}_2\text{C}$, $^*\text{HC-H}_2\text{C} \rightarrow ^*\text{C}_2\text{H}_4$ and $^*\text{C}_2\text{H}_4 \rightarrow ^* + \text{C}_2\text{H}_4$ steps are endergonic which can be downhill at applied potential of -0.52 V. Asthagiri and co-workers have

also shown that the $*\text{CO} \rightarrow *\text{HCO}$ step is most endergonic step and the reported reaction free energy is 0.62 eV on the periodic Cu(100) surface for C_2H_4 formation [21]. Along with this, Nilsson and co-workers have reported that CO_2 can be converted to C_2H_4 at -0.60 V on the Cu cube [26]. Hence, formation of C_2H_4 is highly desirable on the Cu-dNC compared to that on the periodic Cu(100) surface.

6.3.4.2. Formation of $\text{C}_2\text{H}_5\text{OH}$: Along with C_2H_4 another important C_2 based CO_2 hydrogenated product is $\text{C}_2\text{H}_5\text{OH}$. Therefore, we have investigated the CO_2 hydrogenation to $\text{C}_2\text{H}_5\text{OH}$ mechanistic pathways. There are some common intermediates for $\text{C}_2\text{H}_5\text{OH}$ and C_2H_4 formations. The common intermediates of most favourable pathway for C_2H_4 formation are $*\text{CO}$, $*\text{HCO}$, $*\text{HCO-HCO}$, $*\text{HCO-HCOH}$, $*\text{HC-HCO}$, and $*\text{H}_2\text{C-HCO}$. In case of $\text{C}_2\text{H}_5\text{OH}$, the formation of $*\text{HCO-HCO}$ is more favourable as it can be reduced to $\text{C}_2\text{H}_5\text{OH}$. The $*\text{HCO-HCO}$ intermediate has also been identified for $\text{C}_2\text{H}_5\text{OH}$ formation by several groups on periodic Cu(100) surfaces [21,22]. After identifying the common intermediates, possible pathways for $\text{C}_2\text{H}_5\text{OH}$ formation have been investigated by computing the reaction free energy of all the probable elementary step. The $*\text{H}_2\text{C-HCO}$ can form $\text{C}_2\text{H}_5\text{OH}$ via hydrogenation at three different positions and may form $*\text{H}_2\text{C-HCOH}$, $*\text{H}_3\text{C-HCO}$ and $*\text{H}_2\text{C-H}_2\text{CO}$. The reaction free energies reveal that the hydrogenation step of $*\text{H}_2\text{C-HCO}$ is exergonic if protonation occurs only at the O-center of the $*\text{H}_2\text{C-HCO}$. Then, further hydrogenation at the H_2C -center of $*\text{H}_2\text{C-HCOH}$ and hydrogenation at the O-center of the $*\text{H}_3\text{C-HCO}$ may form $*\text{H}_3\text{C-HCOH}$. Besides, hydrogenation at the HC-center of $*\text{H}_3\text{C-HCO}$ and hydrogenation at the H_2C -center of $*\text{H}_2\text{C-H}_2\text{CO}$ produce $*\text{H}_3\text{C-H}_2\text{CO}$ with the reaction free energies of -0.51 and -0.64 eV, respectively. In the next step, $*\text{H}_3\text{C-HCOH}$ and $*\text{H}_3\text{C-H}_2\text{CO}$ can be converted to $*\text{H}_3\text{C-H}_2\text{COH}$. Eventually, $\text{C}_2\text{H}_5\text{OH}$ can be removed from the catalytic surface of Cu-dNC. This step requires 1.30 eV energy. Therefore, the amount of $\text{C}_2\text{H}_5\text{OH}$ production is expected

to be less. However, the most favourable pathway for CO₂ hydrogenation to C₂H₅OH is * + CO₂ → *CO₂ → *COOH → *CO → *HCO → *HCO-HCO → *HCO-HCOH → *HC-HCO → *H₂C-HCO → *H₃C-HCO → *H₃C-H₂CO → *H₃C-H₂COH → * + C₂H₅OH with -1.54 eV total reaction free energy. Besides, *CO → *HCO is the PDS where the computed reaction free energy is 0.52 eV. Recently, Yeo and co-workers have shown C₂H₅OH pathway via *CH and *CO coupling on Cu(111) surface which are different than that of our favourable pathway on the Cu-dNC [67]. However, the *CO → *HCO has also been reported to be the PDS by several other studies on periodic Cu(100) surface but the required reaction free energy of the PDS step is higher in those studies than that on the Cu-dNC for C₂H₅OH formation [21,22]. Therefore, Cu-dNC can be an efficient catalyst for C₂H₅OH formation from CO₂.

6.4. Comparison among C₁ and C₂ Based Products

In this section, we have compared the C₁ and C₂ based products based on the computed working potential. The working potential is the minimum required potential upon which all the favourable elementary reaction steps become exergonic or reversible [43].⁴³ Hence, the required working potential is the most endergonic step's potential i.e., PDS. In this case we have considered the most plausible mechanistic pathway for HCOOH, CH₃OH, CH₄, C₂H₄ and C₂H₅OH formation from CO₂. The comparative reaction free energies and effect of applied potentials on the reaction free energies are shown in Figure 6.8 and 6.9. Further to this, we have correlated our reaction energetics with that of previously reported periodic Cu(100) surface, Cu(111) monolayer and Cu₈₅ nanocluster (Table 6.4). From the table 6.4, it can be understood that the reaction energetics of Cu-dNC follows a similar trend as that of these systems with *CO hydrogenation to *HCO being the PDS for the most favourable pathways of CH₃OH formation and *CO to *COH being the potential determining step for CH₄ formation. Similarly, *CO→*HCO is the PDS for Cu-dNC as well as

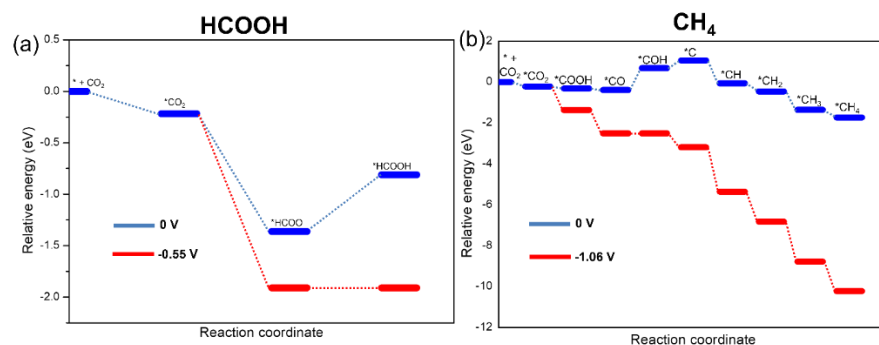


Figure 6.9: Reaction free energies of CO₂ hydrogenation to (a) HCOOH, and (b) CH₄ and their dependencies on the applied potentials.

Earlier reports also suggest that on the Cu₈₅ nanocluster and periodic Cu(111) surface, *CO to *HCO is the potential limiting step with required -0.53 and -0.71 V potential, respectively for CH₃OH formation [58,64]. Moreover, earlier reports have reported the most endergonic step (*CO → *HCO) with 0.62 and 0.65 eV on periodic Cu(100) surface for C₂ based product formation from CO₂ [21,22]. Thus, Cu-dNC can be considered as an effective and promising catalyst for CO₂ hydrogenation reaction to C₂ based product formation. To realize the reason behind the superior catalytic activity of the Cu(100) facet of the Cu-dNC compared to periodic Cu(100) surface, we have investigated the d-band-center energies. The calculated d-band-center energies are -2.45 and -2.43 eV for periodic Cu(100) surface and Cu(100) facet, respectively. Therefore, the computed d-band-center energies of the Cu(100) and Cu(100) facet are more or less same. On the other hand, the Cu-Cu bond distances are 2.47 Å on the periodic Cu(100) surface whereas the Cu-Cu average bond distance is 2.52 Å as various Cu-Cu bond lengths are observed (2.56, 2.76, 2.42 and 2.35 Å) on the Cu-dNC surface. So, Cu-dNC is highly distorted than that of periodic Cu(100) surface. Our calculated strain value shows that Cu-dNC is under tensile strain (10.99%) compared to the periodic Cu(100) surface. Hence, the formation of *HCO from *CO is preferred on the Cu-dNC as distorted surface can stabilize the intermediates as also reported by Rojas and co-

workers, who have shown that the lattice distortion of the catalyst can influence the activity, higher distortion results higher catalytic activity [68]. Moreover, the average coordination number (CN) of Cu-dNC (CN=7) is less than that of the periodic Cu(100) surface (CN=8). This is due to the higher extent of deformation within Cu-dNC. Hence, this less coordination causes an unsaturation on the catalytically active surface which leads to the high catalytic activity compared to the periodic Cu(100) surface. Even though increase in the exposure ratio is one of the obvious consequences of transforming to the nano form, there are other catalytically relevant factors which are unique in the nano regime. These include the local surface structure, coordinative unsaturation (edge and vertex atom), strain effects (due to enclosed by various facets) and modulated metal-metal bonding (compared to bulk) which are critical in determining the interaction with reaction intermediates and hence affecting the catalytic activity. Since generally the theoretical simulation is carried out on a single facet in both Cu(100) surface and Cu(100) based nanostructures, only finite-size effects cause catalytic activity differences in nanocube. However, in our study, we clearly notice the structural transformation from a (100) facet derived Cu-NC to more stable Cu-dNC which features all the aforementioned effects such as local surface structure, coordinative unsaturation, strain effects. Hence, we take account of many plausible factors which could be determining the Cu-dNC activity which cannot be ascribed for Cu(100) periodic surface.

6.5. Conclusions

We have used DFT studies for the investigation of the most favourable pathways of CO₂ hydrogenation to various C₁ and C₂ based products on the Cu(100) facet of a Cu-NC based nanocluster. At first, the stability of the modelled Cu-NC has been examined and we have found out that the structure is not thermally and dynamically stable as Cu-NC converts to a minimum energy structure at higher temperatures. The structure distorts to

another structure (Cu-dNC) which is calculated to be stable. Hence, the CO₂ hydrogenation reaction to C₁ and C₂ based products has been studied on the Cu-dNC catalyst. Our calculated adsorption energies and mechanistic pathways explains various important observations including the reason behind the superior activity of Cu-dNC for product selectivity towards C₂ based products. The adsorption energies of most of the studied intermediates on the Cu-dNC are high compared to that on the periodic Cu(111) surface. The trend in adsorption energies of the intermediate can be supported using the PDOS and Bader charge analysis. Moreover, we have investigated the effect of applied potential on the product formation steps and the calculated results indicate that the formation of CH₃OH, C₂H₄ and C₂H₅OH are favourable at -0.52 V. Besides, our computed reaction energy values (-0.38 eV for CH₃OH, -1.02 eV for C₂H₄, and -1.54 eV C₂H₅OH) show that the formation of C₂ based products are highly exergonic compared to C₁ (CH₃OH) formation. Hence, Cu-dNC can be considered as efficient catalyst for the C₂ based products than that of the periodic Cu(100) surface. This may be due to the distorted surface of Cu-dNC which stabilize the intermediates responsible for C₂ based products formation. To the best of our knowledge, this is the first theoretical reports of CO₂ hydrogenation reaction for various C₁ and C₂ based product formation on a Cu-NC based model. We believe that these finding will be helpful for theorists as well as experimentalists working on the CO₂ hydrogenation reaction for the designing of efficient and selective catalyst.

6.6. References

- (1) Olah G. A., Prakash G.K.S., Goepfert A. (2011), Anthropogenic Chemical Carbon Cycle for a Sustainable Future, *J. Am. Chem. Soc.*, 133, 12881–12898 (DOI: 10.1021/ja202642y)
- (2) Ghadimkhani G., Tacconi N.R.de, Chanmanee W., Janaky C., Rajeshwar K. (2013), Efficient solar photoelectrosynthesis of methanol from carbon dioxide using hybrid CuO–Cu₂O

- semiconductor nanorod arrays, *Chem. Commun.*, 49, 1297–1299 (DOI: 10.1039/C2CC38068D)
- (3) Yin L., Liebscher J. (2007), Carbon–Carbon Coupling Reactions Catalyzed by Heterogeneous Palladium Catalysts, *Chem. Rev.*, 107, 133–173 (DOI: 10.1021/cr0505674)
 - (4) Vayenas C.G., White R.E., Gamboa-Aldeco M.E. (2008), In *Modern Aspects of Electrochemistry*, Eds.; Springer: New York, Vol. 42, pp 89–189 (ISBN: 978-0-387-49489-0)
 - (5) Sapountzi F.M., Gracia J.M., Weststrate C.J., Fredriksson H.O.A., Niemantsverdriet J.W. (2017), Electrocatalysts for the generation of hydrogen, oxygen and synthesis gas, *Prog. Energy Combust. Sci.*, 58, 1-35 (DOI: 10.1016/j.peccs.2016.09.001)
 - (6) Luo W., Zhang J., Li M., Züttel A. (2019), Boosting CO Production in Electrocatalytic CO₂ Reduction on Highly Porous Zn Catalysts, *ACS Catal.*, 9, 3783–3791 (DOI: 10.1021/acscatal.8b05109)
 - (7) Lamaison S., Wakerley D., Blanchard J., Montero D., Rouse G., Mercier D., Marcus P., Taverna D., Giaume D., Mougel V., Fontecave M. (2020), High-Current-Density CO₂-to-CO Electroreduction on Ag-Alloyed Zn Dendrites at Elevated Pressure, *Joule*, 4, 395–406 (DOI: 10.1016/j.joule.2019.11.014)
 - (8) Sun R., Liao Y., Bai S.-T., Zheng M., Zhou C., Zhang T., Sels B.F. (2021), Heterogeneous catalysts for CO₂ hydrogenation to formic acid/formate: from nanoscale to single atom, *Energy Environ. Sci.*, 14, 1247–1285 (DOI: 10.1039/D0EE03575K)
 - (9) Gunasekar G.H., Park K., Jung K.-D., Yoon S. (2016), Recent developments in the catalytic hydrogenation of CO₂ to formic acid/formate using heterogeneous catalysts, *Inorg. Chem. Front.*, 3, 882–895 (DOI: 10.1039/C5QI00231A)
 - (10) Hori Y., Kikuchi K., Suzuki S. (1985), Production of CO and CH₄ in Electrochemical Reduction of CO₂ at Metal Electrodes in

- Aqueous Hydrogencarbonate Solution, *Chem. Lett.*, 14, 1695–1698 (DOI: 10.1246/cl.1985.1695)
- (11) Hori Y., Kikuchi K., Murata A., Suzuki S. (1986), Production of Methane and Ethylene in Electrochemical Reduction of Carbon Dioxide at Copper Electrode in Aqueous Hydrogencarbonate Solution, *Chem. Lett.*, 15, 897–898 (DOI: 10.1246/CL.1986.897)
- (12) Hori. Y., Murata A., Takahashi R.J. (1989), Formation of hydrocarbons in the electrochemical reduction of carbon dioxide at a copper electrode in aqueous solution, *Chem. Soc., Faraday Trans. 1*, 85, 2309–2326 (DOI: 10.1039/F19898502309)
- (13) Hori Y., Wakebe H., Tsukamoto T., Koga O. (1995), Adsorption of CO accompanied with simultaneous charge transfer on copper single crystal electrodes related with electrochemical reduction of CO₂ to hydrocarbons, *Surf. Sci.*, 335, 258–263 (DOI: 10.1016/0039-6028(95)00441-6)
- (14) Takahashi I., Koga O., Hoshi N., Hori Y. (2002), Electrochemical reduction of CO₂ at copper single crystal Cu(S)-[n(111)×(111)] and Cu(S)-[n(110)×(100)] electrodes, *J. Electroanal. Chem.*, 533, 135–143 (DOI: 10.1016/S0022-0728(02)01081-1)
- (15) Hori Y., Takahashi I., Koga O., Hoshi N. (2003), Electrochemical reduction of carbon dioxide at various series of copper single crystal electrodes, *J. Mol. Catal. A: Chem.*, 199, 39–47 (DOI: 10.1016/S1381-1169(03)00016-5)
- (16) Schouten K.J.P., Kwon Y., van der Ham C.J.M., Qin Z., Koper M.T.M. (2011), A new mechanism for the selectivity to C₁ and C₂ species in the electrochemical reduction of carbon dioxide on copper electrodes, *Chem. Sci.*, 2, 1902–1909 (DOI: 10.1039/C1SC00277E)
- (17) Schouten K.J.P., Qin Z.S., Gallent E.P., Koper M.T.M. (2012), Two Pathways for the Formation of Ethylene in CO Reduction on Single-Crystal Copper Electrodes, *J. Am. Chem. Soc.*, 134, 9864–9867 (DOI: 10.1021/ja302668n)

- (18) Kortlever R., Shen J., Schouten K.J.P., Calle-Vallejo F., Koper, M.T.M. (2015), Catalysts and Reaction Pathways for the Electrochemical Reduction of Carbon Dioxide, *J. Phys. Chem. Lett.*, 6, 4073–4082 (DOI: 10.1021/acs.jpcllett.5b01559)
- (19) Calle-Vallejo F., Koper M.T.M. (2013), Theoretical Considerations on the Electroreduction of CO to C₂ Species on Cu(100) Electrodes, *Angew. Chem. Int. Ed.*, 52, 7282–7285 (DOI: 10.1002/anie.201301470)
- (20) Montoya J.H., Shi C., Chan K., Nørskov J.K. (2015), Theoretical Insights into a CO Dimerization Mechanism in CO₂ Electroreduction, *J. Phys. Chem. Lett.*, 6, 2032–2037 (DOI: 10.1021/acs.jpcllett.5b00722)
- (21) Luo W., Nie X., Janik M.J., Asthagiri A. (2016), Facet Dependence of CO₂ Reduction Paths on Cu Electrodes *ACS Catal.*, 6, 219–229 (DOI: 10.1021/acscatal.5b01967)
- (22) Garza A.J., Bell A.T., Head-Gordon M. (2018), Mechanism of CO₂ Reduction at Copper Surfaces: Pathways to C₂ Products, *ACS Catal.*, 8, 1490–1499 (DOI: 10.1021/acscatal.7b03477)
- (23) Mangione G., Huang J., Buonsanti R., Corminboeuf C. (2019), Dual-Facet Mechanism in Copper Nanocubes for Electrochemical CO₂ Reduction into Ethylene *J. Phys. Chem. Lett.*, 10, 4259–4265 (DOI: 10.1021/acs.jpcllett.9b01471)
- (24) Gregorio G.L.D., Burdyny T., Loiudice A., Iyengar P., Smith W.A., Buonsanti R. (2020), Facet-Dependent Selectivity of Cu Catalysts in Electrochemical CO₂ Reduction at Commercially Viable Current Densities, *ACS Catal.*, 10, 4854–4862 (DOI: 10.1021/acscatal.0c00297)
- (25) Todorova T.K., Schreiber M.W., Fontecave M. (2020), Mechanistic Understanding of CO₂ Reduction Reaction (CO₂RR) Toward Multicarbon Products by Heterogeneous Copper-Based Catalysts, *ACS Catal.*, 10, 1754–1768 (DOI: 10.1021/acscatal.9b04746)

- (26) Roberts F.S., Kuhl K.P., Nilsson A. (2015), High Selectivity for Ethylene from Carbon Dioxide Reduction over Copper Nanocube Electrocatalysts, *Angew. Chem. Int. Ed.*, 54, 5179–5182 (DOI: 10.1002/anie.201412214)
- (27) Baruch M.F., Pander J.E., White J.L., Bocarsly A.B. (2015), Mechanistic Insights into the Reduction of CO₂ on Tin Electrodes using in Situ ATR-IR Spectroscopy, *ACS Catal.*, 5, 3148–3156 (DOI: 10.1021/acscatal.5b00402)
- (28) Figueiredo M.C., Ledezma-Yanez I., Koper M.T.M. (2016), In Situ Spectroscopic Study of CO₂ Electroreduction at Copper Electrodes in Acetonitrile, *ACS Catal.*, 6, 2382–2392 (DOI: 10.1021/acscatal.5b02543)
- (29) Bagger A., Ju W., Varela A.S., Strasser P., Rossmeisl J. (2017), Electrochemical CO₂ Reduction: A Classification Problem, *ChemPhysChem*, 18, 3266–3273 (DOI: 10.1002/cphc.201700736)
- (30) Lin Z., Zhong S., Grierson D. (2009), Recent advances in ethylene research, *J. Exp. Bot.*, 60, 3311–3336 (DOI: 10.1093/jxb/erp204)
- (31) Goldemberg J. (2007), Ethanol for a Sustainable Energy Future, *Science*, 315, 808-810 (DOI: 10.1126/science.1137013)
- (32) Badwal S.P.S., Giddey S., Kulkarni A., Goel J., Basu S. (2015), Direct ethanol fuel cells for transport and stationary applications – A comprehensive review, *Appl. Energy*, 145, 80–103 (DOI: 10.1016/j.apenergy.2015.02.002)
- (33) Wang W., Wang S., Ma X., Gong J. (2011), Recent advances in catalytic hydrogenation of carbon dioxide, *Chem. Soc. Rev.*, 40, 3703–3727 (DOI: 10.1039/C1CS15008A)
- (34) Fukuzumi S. (2017), Production of Liquid Solar Fuels and Their Use in Fuel Cells, *Joule*, 1, 689–738 (DOI: 10.1016/j.joule.2017.07.007)
- (35) Blöchl P.E. (1994), Projector augmented-wave method, *Phys. Rev. B: Condens. Matter Mater. Phys.*, 50, 17953–17979 (DOI: 10.1103/PhysRevB.50.17953)

- (36) Kresse G., Joubert D. (1999), From ultrasoft pseudopotentials to the projector augmented-wave method, *Phys. Rev. B: Condens. Matter Mater. Phys.*, 59, 1758–1775 (DOI: 10.1103/PhysRevB.59.1758)
- (37) Kresse G., Furthmüller J. (1996), Efficient iterative schemes for ab initio total-energy calculations using a plane-wave basis set, *Phys. Rev. B: Condens. Matter Mater. Phys.*, 54, 11169–11186 (DOI: 10.1103/PhysRevB.54.11169)
- (38) Perdew J.P., Burke K., Ernzerhof M. (1996), Generalized Gradient Approximation Made Simple, *Phys. Rev. Lett.*, 77, 3865–3868 (DOI: 10.1103/PhysRevLett.77.3865)
- (39) Perdew J.P., Burke K., Ernzerhof M. (1997), Generalized Gradient Approximation Made Simple [*Phys. Rev. Lett.* 77, 3865 (1996)], *Phys. Rev. Lett.*, 78, 1396 (DOI: 10.1103/PhysRevLett.78.1396)
- (40) Perdew J.P., Chevary J.A., Vosko S.H., Jackson K.A., Pederson M.R., Singh D.J., Fiolhais C. (1992), Atoms, molecules, solids, and surfaces: Applications of the generalized gradient approximation for exchange and correlation, *Phys. Rev. B: Condens. Matter Mater. Phys.*, 46, 6671–6687 (DOI: 10.1103/physrevb.46.6671)
- (41) Grimme S., Antony J., Ehrlich S., Krieg H. (2010), A consistent and accurate ab initio parametrization of density functional dispersion correction (DFT-D) for the 94 elements H-Pu, *J. Chem. Phys.*, 132, 154104 (DOI: 10.1063/1.3382344)
- (42) Nørskov J.K., Rossmeisl J., Logadottir A., Lindqvist L., Kitchin J.R., Bligaard T., Jonsson H. (2004), Origin of the Overpotential for Oxygen Reduction at a Fuel-Cell Cathode, *J. Phys. Chem. B*, 108, 17886–17892 (DOI: 10.1021/jp047349j)
- (43) Karamad M., Hansen H.A., Rossmeisl J., Nørskov J.K. (2015), Mechanistic Pathway in the Electrochemical Reduction of CO₂ on RuO₂, *ACS Catal.*, 5, 4075–4081 (DOI: 10.1021/cs501542n)
- (44) Peterson A.A., Abild-Pedersen F., Studt F., Rossmeisl J., Nørskov J.K. (2010), How copper catalyzes the electroreduction of carbon

- dioxide into hydrocarbon fuels, *Energy Environ. Sci.*, 3, 1311–1315 (DOI: 10.1039/C0EE00071J)
- (45) Henkelman G., Uberuaga B.P., Jónsson H. (2000), A climbing image nudged elastic band method for finding saddle points and minimum energy paths, *J. Chem. Phys.*, 113, 9901–9904 (DOI: 10.1063/1.1329672)
- (46) Henkelman G., Jónsson H. (1999) A dimer method for finding saddle points on high dimensional potential surfaces using only first derivatives, *J. Chem. Phys.*, 111, 7010–7022 (DOI: 10.1063/1.480097)
- (47) Tang W., Sanville E., Henkelman G. (2009), A grid-based Bader analysis algorithm without lattice bias, *J. Phys.: Condens. Matter*, 21, 084204 (DOI: 10.1088/0953-8984/21/8/084204)
- (48) Sanville E., Kenny S.D., Smith R., Henkelman G. (2007), Improved grid-based algorithm for Bader charge allocation, *J. Comput. Chem.*, 28, 899–908 (DOI: 10.1002/jcc.20575)
- (49) Henkelman G., Arnaldsson A., Jónsson H. (2006), A fast and robust algorithm for Bader decomposition of charge density, *Comput. Mater. Sci.*, 36, 354–360 (DOI: 10.1016/j.commatsci.2005.04.010)
- (50) Shi Z., Zhang Z., Kutana A., Yakobson B.I. (2015), Predicting Two-Dimensional Silicon Carbide Monolayers, *ACS Nano*, 9, 9802–9809 (DOI: 10.1021/acs.nano.5b02753)
- (51) Garg P., Kumar S., Choudhuri I., Mahata A., Pathak B. (2016), Hexagonal Planar CdS Monolayer Sheet for Visible Light Photocatalysis, *J. Phys. Chem. C*, 120, 7052–7060 (DOI: 10.1021/acs.jpcc.6b01622)
- (52) Feibelman P.J. (1999), First-principles step- and kink-formation energies on Cu(111), *Phys. Rev. B: Condens. Matter Mater. Phys.*, 60, 11118–11122 (DOI: 10.1103/PhysRevB.60.11118)

- (53) Zhang Z., Liu X., Yakobson B.I., Guo W. (2012), Two-Dimensional Tetragonal TiC Monolayer Sheet and Nanoribbons, *J. Am. Chem. Soc.*, 134, 19326–19329 (DOI: 10.1021/ja308576g)
- (54) Zhou J., Huang J., Sumpter B.G., Kent P.R.C., Xie Y., Terrones H., Smith S.C. (2014), Theoretical Predictions of Freestanding Honeycomb Sheets of Cadmium Chalcogenides, *J. Phys. Chem. C*, 118, 16236–16245 (DOI: 10.1021/jp504299e)
- (55) Waugh K.C. (1992) Methanol Synthesis, *Catal. Today*, 15, 51–75 (DOI: 10.1016/0920-5861(92)80122-4)
- (56) Nosé S. (1984), A unified formulation of the constant temperature molecular dynamics methods *J. Chem. Phys.*, 81, 511–519 (DOI: 10.1063/1.447334)
- (57) Liu L., Corma A. (2021), Structural transformations of solid electrocatalysts and photocatalysts, *Nat. Rev. Chem.*, 5, 256–276 (DOI: 10.1038/s41570-021-00255-8)
- (58) Rawat K.S., Mahata A., Pathak B. (2017), Thermochemical and electrochemical CO₂ reduction on octahedral Cu nanocluster: Role of solvent towards product selectivity, *J. Catal.*, 349, 118–127 (DOI: 10.1016/j.jcat.2017.03.011)
- (59) Muttaqien F., Hamamoto Y., Inagaki K., Morikawa Y. (2014), Dissociative adsorption of CO₂ on flat, stepped, and kinked Cu surfaces, *J. Chem. Phys.*, 141, 034702 (DOI: 10.1063/1.4887362)
- (60) Grabow L.C., Mavrikakis M. (2011), Mechanism of Methanol Synthesis on Cu through CO₂ and CO Hydrogenation, *ACS Catal.*, 1, 365–384 (DOI: 10.1021/cs200055d)
- (61) Zhang X., Liu J.-X., Zijlstra B., Filot I.A.W., Zhou Z., Sun S., Hensen E.J.M. (2018), Optimum Cu nanoparticle catalysts for CO₂ hydrogenation towards methanol, *Nano Energy*, 43, 200–209 (DOI: 10.1016/j.nanoen.2017.11.021)
- (62) Mandal S.C., Pathak B. (2020), Computational insights into selective CO₂ hydrogenation to CH₃OH catalysed by ZnO based

- nanocages, *Mater. Adv.*, 1, 2300-2309 (DOI: 10.1039/D0MA00208A)
- (63) Mandal S.C.; Rawat K.S., Garg P., Pathak B. (2019), Hexagonal Cu(111) Monolayers for Selective CO₂ Hydrogenation to CH₃OH: Insights from Density Functional Theory, *ACS Appl. Nano Mater.*, 2, 7686–7695 (DOI: 10.1021/acsnm.9b01751)
- (64) Nie X., Luo W., Janik M.J., Asthagiri A. (2014), Reaction mechanisms of CO₂ electrochemical reduction on Cu(111) determined with density functional theory, *J. Catal.*, 312, 108-122 (DOI: 10.1016/j.jcat.2014.01.013)
- (65) Hori Y., Takahashi R., Yoshinami Y., Murata A. (1997), Electrochemical Reduction of CO at a Copper Electrode. *J. Phys. Chem. B*, 101, 7075-7081 (DOI: 10.1021/jp970284i)
- (66) Ma W., Xie S., Liu T., Fan Q., Ye J., Sun F., Jiang Z., Zhang Q., Cheng J., Wang Y. (2020), Electrocatalytic reduction of CO₂ to ethylene and ethanol through hydrogen-assisted C–C coupling over fluorine-modified copper, *Nat. Catal.*, 3, 478–487 (DOI: 10.1038/s41929-020-0450-0)
- (67) Ting L.R.L., Piqué O., Lim S.Y., Tanhaei M., Calle-Vallejo F., Yeo B.S. (2020), Enhancing CO₂ Electroreduction to Ethanol on Copper–Silver Composites by Opening an Alternative Catalytic Pathway, *ACS Catal.*, 10, 4059–4069 (DOI: 10.1021/acscatal.9b05319)
- (68) Retuerto M., Pascual L., Pique O., Kayser P., Salam M.A., Mokhtar M., Alonso J.A., Pena M., Calle-Vallejo F., Rojas S. (2021), How oxidation state and lattice distortion influence the oxygen evolution activity in acid of iridium double perovskites, *J. Mater. Chem. A*, 9, 2980–2990 (DOI: 10.1039/D0TA10316K)

Chapter 7

Scope for Future Work

7.1. Scope for Future Work

This thesis presents the CO₂ hydrogenation reactions mechanisms along with designing of various homogeneous and heterogeneous catalysts for the finding of efficient catalysts to convert CO₂ to CO, HCOOH, CH₃OH, C₂H₄ and C₂H₅OH. As we know, the catalytic activity can be tuned by altering the ligand sphere of the homogeneous catalysts and alloying as well as support of the heterogeneous catalysts. So, future scope of this field can be the finding of efficient ligand sphere with earth abundant metal based catalysts for homogeneous catalysts whereas in case of heterogeneous catalysts finding out the most appropriate alloy or support of the catalytic system for the enhancement of the catalytic activity. In this regard, there are huge scopes in this field via screening of huge number of catalytic systems using machine learning approaches for the investigation of efficient catalysts of CO₂ hydrogenation reactions where the rate determining steps/descriptors of these reactions can be used from this thesis. Besides, CO₂ can be hydrogenated to higher hydrocarbons and alcohols including jet fuels and gasoline. Therefore, finding out the most important steps along with the explanation of the key affecting factors during the reaction is also another future scope of this topic. In this context, it will be highly interesting to see whether direct conversion of CO₂ to higher hydrocarbons and alcohols as well as jet fuels and gasoline is plausible or not. Therefore, it will be highly interesting to screen the earth abundant metal-based for CO₂ hydrogenation to higher hydrocarbons and alcohols including jet fuels and gasoline using machine learning based studies. In all the above mentioned cases, selectivity of the products and conversion efficiency of the reactants are the main challenges. Hence, computational designing of the efficient catalysts with detailed mechanistic investigations of the reactions is highly instrumental during CO₂ hydrogenation to higher carbon-based fuels, which can then be used as inputs for machine learning based screening of efficient catalysts.